

This file is part of the following work:

Alancherry, Surjith (2018) *Development of carbon nanostructures from non-conventional resources*. PhD Thesis, James Cook University.

Access to this file is available from:

<https://doi.org/10.25903/5d479a9e35ad7>

Copyright © 2018 Surjith Alancherry.

The author has certified to JCU that they have made a reasonable effort to gain permission and acknowledge the owners of any third party copyright material included in this document. If you believe that this is not the case, please email

researchonline@jcu.edu.au

Development of Carbon Nanostructures from Non-conventional Resources

Thesis submitted by

Surjith Alancherry

In December 2018

For the Degree of Doctor of Philosophy

In College of Science and Engineering

James Cook University

Supervisors: Prof. Mohan V. Jacob, Dr. Kateryna Bazaka

DECLARATION

I hereby declare that the work presented in this thesis entitled “*Development of Carbon Nanostructures from Non-conventional Resources*” is my own work and has not been submitted in any form for another degree or diploma at any university or institute of territory education. Information derived from the published and unpublished work of others have been acknowledged in the text and a list of references is given.

Surjith Alancherry

December 2018

STATEMENT OF ACCESS TO THIS THESIS

I, the undersigned, the author of this work, understand that James Cook University will make this work available for use within the University, and via the Australian Digital Thesis Network, for use elsewhere.

I understand that as an unpublished work, a thesis has significant protection under the Copyright Act. I do not wish to place any restriction on access to this thesis. However, any use of its content must be acknowledged and could be potentially be restricted by future patents.

Surjith Alancherry

December 2018

ACKNOWLEDGMENTS

I would like to thank my research supervisor, Prof. Mohan V. Jacob for the innovative suggestions, encouragement, editing on my writings and excellent guidance throughout this work. I would also like to thank my co-supervisor Dr. Kateryna Bazaka for the inventive thoughts, recommendations and valuable feedback on my writings. I believe that their help and support was priceless and lead to the successful completion of this thesis.

I am grateful to Prof. Oomman Varghese, University of Houston, USA, for the sensor fabrication and testing and for helping me to characterize my samples using Transmission electron microscopy and X-ray photoelectron spectroscopy techniques.

I thank Dr. R. Ratheesh, Director, C-MET Hyderabad, India, for the constant motivation and helping me to characterize my samples with Scanning electron microscopy.

Thank you to John Renehan and Lloyd Baker electrical engineering supporting crew for their assistance in setting up the experimental system and troubleshooting.

I would like to thank the College of Science and Engineering academic staffs Melissa Norton, Rebecca Steel for their help and support in all aspects during these years.

I would like to acknowledge the financial support from James Cook University, through James Cook University Postgraduate Research fellowship (JCUPRS) and Graduate Research School funding.

Special thanks to my fellow researchers Dr. Daniel Grant, Ahmed Al-jumaili and Avishek Kumar for providing me a good and healthy laboratory atmosphere.

Finally, thanks to my loving family and friends for their love, care and inspiration.

STATEMENT OF CONTRIBUTION OF OTHERS

This thesis included the following contribution from others:

Financial assistance: The financial assistance to cover the tuition fees and living cost over the duration of this course was provided by James Cook University, Australia, through James Cook University Post Graduate Research Fellowship (JCUPRS). Additional funding received from Graduate Research School and College of Science and Engineering to support the procurement of consumables and advanced characterizations.

Editorial assistance: Prof. Mohan V. Jacob and Dr. Kateryna Bazaka provided the editorial assistance for all chapters and journal articles included in this thesis.

Experimental assistance and data analysis: Throughout the duration of this thesis, Prof. Mohan V. Jacob assisted to plan and design the experimental procedures and Dr. Kateryna Bazaka assisted the data analysis.

Contribution to co-authored publications: I have received assistance in terms of access to advanced characterizations that is not available in James Cook University, partial assistance in editing, theoretical modeling and analysis to which a co-authorship was given. Co-authors of published and submitted papers that constitute chapter 3-5 include Kartika Prasad (QUT), Jickson Joseph (QUT), Dr. Olga Bazaka (JCU), Dr. Ram Neupane (University of Houston), Dr. Oleg Baranov (National Aerospace University), Prof. Oomman. K. Varghese (University of Houston), Dr. S.Xu (Nanyang Technological University) and Prof. Igor Levchenko (Nanyang Technological University). Assistance was provided by the co-authors in theoretical modelling/analysis and access to facilities (chapter 4-5).

ABSTRACT

Carbon nanostructures (CNSs) perpetuate the scientific interest over decades due to their remarkable properties and emerging technological applications. The development of sustainable technologies for the synthesis of CNSs from natural resources grabbed immense research attention aiming to implement these high-end materials in wide range of nano electronic devices through safe and environmentally friendly routes. Even though a number of top down and bottom up approaches have been developed for the production of CNSs, most of them either aided by catalysts or involved solvent assisted multi-step process that considerably increase the cost of production and hinders the realization of low cost CNSs based commercial devices. In addition, vast majority of these techniques use high pure petroleum derived hydrocarbon gas precursors that are non-renewable and expensive. Hence, it is imperative to develop scalable techniques that can derive high quality CNSs directly on arbitrary substrates from naturally derived carbon feed stocks. This work aims to develop an environmentally benign plasma enhanced chemical vapor deposition technique for fabricating CNSs from *Citrus sinensis* essential oil, a bio renewable precursor, and explored the potential of these nanostructures for gas sensing application.

C. sinensis essential oil, obtained through cold extraction of orange peels is a rich source of non-synthetic hydrocarbon compounds principally limonene. Inherently volatile in nature, *C. sinensis* essential oil can serve as an ideal candidate material compatible to plasma enhanced chemical vapor deposition. This thesis investigated the fabrication of vertically-oriented graphene nanostructures from *C.sinensis* essential oil through radio frequency plasma enhanced chemical vapor deposition process, the fundamental properties, extend to which the process parameters influenced the structure and morphological features, and the suitability of the developed vertical graphene arrays for gas sensing applications. Special attention is paid to probe deep into the morphological evolution with the help of a set of advanced analytical characterization methods and multi-parameter model simulations.

In the first phase, *C.sinensis* vapors were subjected to low RF power glow discharge that resulted in the formation of plasma polymer thin films, and the material properties were studied as a function of input RF energy. The fundamental properties of plasma polymer thin films fabricated at

different RF power level (10–75 W) were characterized with variable angle spectroscopic ellipsometry, UV-visible spectroscopy, Fourier transform infrared spectroscopy X-ray photoelectron spectroscopy and atomic force microscopy. Optical characterization showed that independent of deposition power films exhibited good transparency (~90 %) in the visible region and a refractive index of 1.55 at 500nm. The optical band gap measured around 3.60 eV and falls within the insulating region. The atomic force microscopic (AFM) images revealed that the surface is pinhole-free and smooth at nanoscale, with average surface roughness dependent on the deposition power. Film hardness increased from 0.50 GPa to 0.78 GPa as applied power increased from 10 to 75 W.

In the second phase, experiments were modified by redesigning the experimental set up in order to eliminate hydrogen from the deposits leaving only crystalline carbon. The RF power deliberately kept high, substrate temperature was raised and hydrogen gas fed into the reactor in controlled manner. A sequence of experiments were carried out by systematically changing the process parameters such as input RF power (300-500W), hydrogen flow rate (10-50 sccm) and deposition duration (2-8 min) and analysed the structural and morphological evolution of the resulted vertical graphene nanostructure.

The structure-property correlation of vertical graphene arrays with the plasma process parameters was performed. The Raman spectra ascertained the formation of less defected multilayered graphene nanostructures and scanning electron microscopic images provided the primary evidences of morphological evolution. The potential of the novel analytical techniques such as Hough transformations, fractal dimension distributions and Minkowski connectivity for the analysis of graphene array morphology was then successfully demonstrated. Worth noting that, these advanced techniques displayed significant changes and revealed the complex morphological transformation of *C. sinensis* derived vertical graphene subjected to change in process conditions. Precisely, vertical graphene nanowalls obtained at 300 and 500W presented a narrow height distribution profile but much wider array formed at 400 W. Fourier and Hough transformation spectra showed a prominent change with an increase in power, thus highlighted change in the morphology with the density of nanoflakes. Similarly, 2D FFT transform spectra of vertical graphene samples also presented notable changes with increasing hydrogen flux. The most narrow height distributions, well-shaped Hough transformation

spectra and distribution of fractal dimensions obtained for structures formed at 20 and 50 sccm of hydrogen flow rate. In addition to this, the principal characteristics of thus fabricated vertical graphene such as flake length (L_{vg}) and flake half width (W_{vg}) are theoretically modelled by an ad hoc model based on a large number of interaction elemental processes and correlated with the experimental results. The combination of the experimental and simulation results ensured important insights and deeper understanding of the processes that govern formation of the vertical graphene morphology. Vertical graphene nanostructures having superior structural and morphological properties were successfully fabricated at an input RF energy of 500W, hydrogen flow rate of 30 sccm and deposition duration of 6 minutes.

The third phase presented an in-depth study of the properties of *C.sinensis* oil derived graphene over a set of conducting (copper and nickel) and insulating substrates (silicon and quartz). The SEM images of thus fabricated graphene patterns showed the unique feature of vertically interconnected and non-agglomerated carbon nanowall structures having maze-like and petal-like networks. Moreover, the normalized height distribution function and 2-D FFT spectra analysis ascertained that vertical graphene formed on silicon substrates displayed the most uniform distribution. X-ray photoelectron spectroscopy spotted only the presence of carbon and the transmission electron microscopic studies revealed the formation of unique onion-like closed loops. The 3-D nanoporous structure of *C.sinensis* oil derived graphene showed high hydrophobicity and measured a water contact angle of 129°. The surface energy studies were performed using Neumann model, Owens-Wendt-Kaelble approach and van Oss-Chaudhury-Good relation and estimated within the range 35–41 mJ/m².

Finally, plasma reformed vertical graphene from *C. sinensis* was integrated into a sensor device prototype to evaluate the performance in gas sensing. The chemiresistive type sensor exhibited sensing activity towards acetone.

In summary, this thesis has identified a viable renewable resource and successfully developed a process that transform them into vertical graphene nanostructures. Furthermore, the fabricated graphene was integrated to real world devices and evaluated the performance. The outcomes of this investigation add knowledge base to the state-of-the-art of green chemistry approach for the synthesis of vertical graphene carbon nanostructures.

CONTENTS

DECLARATION	I
STATEMENT OF ACCESS TO THIS THESIS	II
ACKNOWLEDGMENTS	III
STATEMENT OF CONTRIBUTION OF OTHERS	IV
ABSTRACT	V
LIST OF FIGURES	XIII
LIST OF TABLES	XIX
LIST OF PUBLICATIONS	XX
CHAPTER 1 INTRODUCTION	1
1.1 Rational	1
1.2 Research objectives.....	3
1.3 Thesis organization.....	4
CHAPTER 2 LITERATURE REVIEW	7
2.1 Introduction	8
2.1.1 Fullerene	8
2.1.2 Carbon nanotubes	9
2.1.3 Graphene	9
2.1.4 Vertical graphene nanostructures	10
2.2 Reactive plasma: Direct current, Radio frequency and Microwave frequency discharges	11
2.2.1 Reactive plasma and nanostructure growth	13
2.2.2 PECVD: Growth of various CNSs	14
2.3. PECVD growth of graphene and its significance	16
2.3.1 Vertical alignment	16
2.3.2 Catalyst-free growth	16
2.3.3 Non-Precursor specific nature	16
2.3.4 Easy tailoring of properties	17

2.4. Influence of various plasma process parameters on the growth of graphene	18
2.4.1 Precursors and precursor concentration	18
2.4.2 Growth temperature	19
2.4.3 Deposition power and pressure	21
2.5 PECVD and mechanism of VG growth	23
2.6 Break down and rebuild of natural precursors into various CNSs	24
2.7. Significance of plasma in deriving CNSs from natural resources	27
2.8. Conclusion	30
CHPATER 3 RF PLASMA POLYMERIZATION OF ORANGE OIL AND	
CHARTERIZATION OF POLYMER THIN FILMS	44
3.1 Introduction	45
3.2 Experimental	46
3.3 Results and Discussion	48
3.3.1 Film thickness	49
3.3.2 Chemical characterization	49
3.3.3 Optical properties	54
3.3.4 Optical band gap	55
3.3.5 Surface topography	57
3.3.6 Nanoindentation	59
3.4 Conclusion	61
CHAPTER 4 TOWARDS SOPHISTICATED MORPHOLOGY CONTROL OF NATURAL	
RESOURCE-DERIVED VERTCAL GRAPHENE : EXPERIMENTAL NAD	
SIMULATION INSIGHTS	67
4.1 Introduction	68
4.2 Methods	70
4.2.1 Framework for growth processes in plasmas	70
4.2.2 Experimental	73
4.3 Experimental Results and Discussion	76

4.3.1. Effect of RF power, gas flux and growth time on structure of graphene	75
4.3.2. Effect of RF power on the morphological characteristics of graphene array	80
4.3.3. Effect of hydrogen flow rate on the morphological characteristics of graphene array...	86
4.3.4. Effect of deposition time on the morphological characteristics of graphene array	89
4.4 Simulations: Insights into Growth Process	91
4.4.1. Model and technique	91
4.4.2 Density of radicals of the precursor gas on a substrate surface	95
4.4.3 Density of hydrocarbon radicals and atomic hydrogen on substrate surfaces	96
4.4.4 Ion energy and density of ion current as the factors determining surface sputtering	97
4.4.5 Rate of vertical graphene growth	98
4.4.6 Numerical Procedure	101
4.4.7 Numerical results	102
4.4.8 Simulation results	104
4.5 Conclusion	109
CHAPTER 5 ONE-STEP PLASMA-ASSITED SYNTHESIS OF GRAPHENE	
FROM CITRUS SINESIS OIL: ACETONE SENSORS AND EVIDENCE OF	
ONION-LIKE STRUCTURES	
	119
5.1 Introduction	120
5.2 Experimental	122
5.3 Results and Discussion	124
5.3.1 Raman characterization of plasma derived vertically oriented graphene	124
5.3.2 Morphological features of vertically oriented graphene arrays on different substrates	126
5.3.3 Transmission electron microscopic studies	129
5.3.4 Plausible mechanism on nano-onions and nano-rings formation	130
5.3.5 Elemental analysis of plasma synthesized vertical graphene	132
5.3.6 Contact angle measurements and surface energy studies	133
5.4 <i>C. sinensis</i> derived vertically oriented graphene and gas sensing properties	140
5.5 Conclusion	142

CHAPTER 6 CONCLUSION AND FUTURE WORK	151
6.1 Fabrication of Plasma polymer thin films and fundamental properties	152
6.2 One-step plasma fabrication of vertical graphene: Characterization and control of morphology .	152
6.3 One-step plasma fabrication of vertical graphene: Growth on different substrates, properties and acetone gas sensing	154
6.4 Supplementary future work	156
Appendix A.....	158

LIST OF FIGURES

Figure 3.1 FTIR spectra of orange oil and plasma polymerized orange oil thin films fabricated at different RF input powers	51
Figure 3.2 (a) XPS survey spectrum of orange oil polymer thin film fabricated at 10W RF power (b) Curve fitting for the high-resolution C 1 s spectrum.....	54
Figure 3.3 Refractive index (a), extinction coefficient (b), and (c) transmittance of polymer thin films derived from orange oil within the range 200-1000nm	55
Figure 3.4 UV-vis absorption spectra of orange oil polymer thin films	56
Figure 3.5 Representative AFM images ($3\mu\text{m} \times 3\mu\text{m}$) of plasma derived orange oil thin films deposited at different RF powers (a) 10 W, (b) 25 W, (c) 50 W and (d) 75 W	58
Figure 3.6 Typical loading and unloading curve (maximum load $1000\ \mu\text{N}$) and AFM image of orange oil polymer thin film fabricated at 25 W and indented with different loads	60
Figure 4.1 A strategy for growing complex nanostructures based on a step-by-step transition from plasma-enhanced treatment of millimetre- through micrometre- to nanometre-size areas. Each stage comprises three main phases classified according to the rate of change in the geometrical shape of the treated surface. The first phase is associated with that transform the base surface into a substrate suitable for material growth; the second stage covers all the processes of additive growth of structures on the base surface. For the case of vertically-oriented graphenes, this phase describes the growth of graphene sheets orthogonal to the surface of the substrate. The third phase, denoted as “trimming”, includes processes that result in removal of excess material, such as atoms of amorphous carbon ($\alpha\text{-C}$). Then, next cycle of the construction can begin, and the possible transition is shown by the arrow pointed from the stage 1 to stage 2	72
Figure 4.2 Top panel: Experimental set-up for growth of networks of vertically-oriented graphene nanosheets in low-temperature plasmas. Surface characterization was performed using	

traditional suit of microscopy and spectroscopy methods, and analytical approaches to investigate various morphological characteristics such as fractal dimensions, Minkowski connectivity, and others. Bottom panel: Three-dimensional morphology patterns of the dense (left) and rarefied (right) arrays of vertical graphenes75

Figure 4.3 Raman characterization of vertically-oriented graphene nanoflakes synthesizes in plasma. (a-c) Raman spectra of graphene samples fabricated at different RF power (300, 400, and 500 W), hydrogen flow rates (10, 20, 30, and 50 sccm), and time of deposition (2, 4, 6, and 8 min). (d-f) Peak intensity ratios from the Raman spectra for the same samples, fabricated at different RF power, hydrogen flow rate, and time of deposition77

Figure 4.4 XPS spectra of vertically-oriented graphenes produced in PECVD (a) survey scan and (b) C1s high resolution scan fitted with sp^2 , sp^3 and shake-up features79

Figure 4.5 Control of the graphene patterns morphology by varying input power. Image illustrates (from top to bottom) SEM images, 3D reconstructions, 2D FFT transforms, Hough transformation spectra and heights distributions of the arrays of graphene nanoflakes grown at 300 W (a), 400 W (b), and 500 W (c) discharge power. Low density of graphene nanoflakes can be observed for 300 W, with much higher density obtained for 400 W, and even higher density of flakes for samples fabricated at 500 W. Fourier and Hough transformation spectra show a notable change with an increase in power, thus highlighting a change in the morphology with the density of nanoflakes. Growth at 10 sccm, 750 °C, 4 min. Bottom images show the spectra of heights distributions, with notably wider distribution obtained at 400 W80

Figure 4.6 Fractal dimensions calculated as a power spectrum [70] (a) and by triangulation [68] (b). (c, d): Minkovski boundaries distribution (c) and Minkovski connectivity (d) as morphological descriptors85

Figure 4.7 Evolution of graphene morphology as a function of gas flux (see caption of similar figure 4.5 for more details). SEM images, 3D reconstruction, and 2D FFT transform of the arrays

of graphene nanoflakes grown at 20 sccm (a), 30 sccm (b), and 50 sccm (c) gas flux. Low density of graphene nanoflakes for 20 sccm, much higher density for 30 sccm, and even lower density for 50 sccm is noted. 2D FFT transform spectra show notable changes with increasing hydrogen flux, thus highlighting a change in morphology with the density of nanoflakes. Very narrow height distributions were obtained for 20 and 50 sccm (lower histograms). Growth at 500 W, 750 °C, 4 min86

Figure 4.8 Spectrum of the fractal dimensions (power spectrum) does not significantly depend on the reactive gas supply (a); complex dependence of a triangulation-calculated fractal dimension on gas flux (b), with the highest values reached at 30 sccm (b). Indeed, the relevant SEM images shows simple-shaped nanoflakes. Insets illustrates the dependence of maximum values of fractal dimension on gas flow. Minkovski boundaries distribution (c) and Minkovski connectivity (d) show narrow spectra for 50 sccm, and well-developed patterns for 30 sccm of hydrogen flow88

Figure 4.9 Influence of growth time on evolution of morphology (see caption of similar figure 5 for more details). SEM images, 3D-reconstruction, and 2D FFT transform of the arrays of graphene nanoflakes grown at 2 min (a), 6 min (b), and 8 min (c). The density of graphene flakes increases with time. 2D FFT transform spectra show a notable change with deposition time increasing from 2 to 5 min, thus highlighting change of the morphology with the density of nanoflakes. Growth at 500 W, 750 °C, 30 sccm89

Figure 4.10 Spectrum of fractal dimensions (power spectrum) does not significantly depend on the time of deposition (a); complex dependence of fractal dimension (calculated by triangulation) on time of deposition (b), with the lowest values obtained after 2 min (b). Minkovski boundaries distribution (c) and Minkovski connectivity (d) show the widest distribution for the longer (8 minutes) process91

Figure 4.11 Schematics of the energies and processes involved in the simulations. Dependencies of the growth characteristics on the control parameters through the microscopic quantities. Complex interrelation of many elemental processes were taken into account in the model,

to ensure detailed simulations of the graphene nucleation and growth, and formation of the array morphology	93
Figure 4.12 Schematic of the mechanisms and reactions involved in vertical graphene growth. Motion of species involved into the reactions about the surface of growing graphene flake (a); list of chemical reactions taken into account in the model (b); schematic of the reactions (c)..	94
Figure 4.13 Dependence of a vertical graphene length on time under various growth conditions (a); time evolution of the vertical graphene shape at $T_s = 750\text{ }^\circ\text{C}$	102
Figure 4.14 Surface plots $L_{vg}(P, T_s)$ of the vertical graphene length for the growth time $t = 6\text{ min}$ and for different ratios of carbon precursor-to-total gas pressure: total gas pressure P is varied at a fixed pressure $P_{C_xH_y} = 3\text{ Pa}$ of the carbon precursor (a), P is varied at a fixed ratio $P_{C_xH_y} : P = 0.1$ (b)	103
Figure 4.15 Surface plots $L_{vg}(j_i, T_s)$ of the vertical graphene flake length for different operation modes and moments of time t : a – hydrogen pressure 18 Pa (corresponds to hydrogen flow of 20 sccm), carbon precursor gas pressure 3 Pa, total gas pressure 21 Pa, time of growth 6 min; b – hydrogen pressure 27 Pa (hydrogen flow of 30 sccm), carbon precursor gas pressure 3 Pa, total gas pressure 30 Pa, time of growth 6 min; c – hydrogen pressure 45 Pa (hydrogen flow of 50 sccm), carbon precursor gas pressure 3 Pa, total gas pressure 48 Pa; time of growth 6 min; d – Hydrogen pressure 45 Pa (hydrogen flow of 50 sccm); carbon precursor gas pressure 3 Pa, total gas pressure 48 Pa, time of growth 20 min	105
Figure 4.16 Relative densities of adsorbed species as a function of growth temperature at a fixed density of the ion current $j_i = 50\text{ A/m}^2$ (a), and the relative densities as a function of density of the ion current at the fixed growth temperature $T_s = 750\text{ }^\circ\text{C}$ (b); other parameters are: $P_{H_2} = 30\text{ Pa}$; $P_{C_xH_y} = 3\text{ Pa}$	106
Figure 5.1 Custom-made quartz tube plasma enhanced chemical vapor deposition system	122
Figure 5.2 Raman characterization of plasma synthesized vertically oriented graphene samples (a) Raman spectra of graphene deposited on copper, nickel, Si/SiO ₂ and quartz substrates, (b)	

Band intensity ratios and (c) FWHM for D, D and 2D Raman bands for the same set of samples	124
Figure 5.3 Morphological features of plasma derived vertically oriented graphene nanostructures fabricated over different substrates. Scanning electron microscopic images (left column), three-dimensional representation of the relief (central column), and the energy dispersive X-ray diffraction spectrum (right column) for graphene patterns grown on (a) copper, (b) nickel, (c) Si/SiO ₂ and (d) quartz substrates, respectively	127
Figure 5.4 Morphological analysis of the four samples shown in Figure 5.3. Normalized height distribution functions of the vertically oriented graphene patterns on different substrates: (a) copper, (b) nickel, (c) Si/SiO ₂ and (d) quartz. The pattern on Si/SiO ₂ (c) demonstrates the most uniform distribution, followed by the array formed on quartz (d)	128
Figure 5.5 Morphological analysis of the four samples shown in Figure 5.3. 2D Fast Fourier Transform (2d FFT) spectra of the vertically oriented graphene patterns on different substrates: (a) copper, (b) nickel, (c) Si/SiO ₂ and (d) quartz. The pattern on Si/SiO ₂ (c) demonstrates the most ordered (less noised) structure	128
Figure 5.6 Representative transmission electron microscopic (TEM) images of graphene samples deposited on quartz substrates	130
Figure 5.7 (a) Formation carbon rings on surface. This system is a combination of the topside monolayer graphene domain (gray) and the bottom side few-layer graphene ribbons (blue), are synthesized on Cu foils by heating in a H ₂ /CH ₄ atmosphere at 1074 °C. Reprinted from [55]. Note that our structures were synthesized at much lower temperatures, due to strong activation by plasma-accelerated ions. (b) A model of three-dimensional onion-like structure. Reprinted from [51]. According to TEM observations (see also Figure S1 in the Supporting Information available), the structures close to onions shown in (b) were synthesized in this work	131

Figure 5.8 XPS spectra of vertically-oriented graphene samples grown on Copper, Nickel and Silicon substrates (a) survey scan, (b-d) high resolution C1s scan	132
Figure 5.9 Contact angle measurements on vertical graphene patterns formed on Si/SiO ₂ substrates for six different test liquids, (a) water (129.04°), (b) glycerol (107.03°), (c) formamide (94.54°), (d) ethylene glycol (81.39°), (e) DSMO (64.40°) and (f) DIM (39.50°).....	135
Figure 5.10 Surface energy studies of vertically oriented graphene samples fabricated on silicon substrates. Surface energy plots obtained from (a) calculated by Neumann surface energy model and (b) Owens, Wendt, Rabel and Kaelble (OWRK) Approach	140
Figure 5.11 The response of the orange oil reformed graphene chemiresistive device towards acetone (a) and the selectivity of the device towards various gases (b)	141

LIST OF TABLES

Table.2.1 Over view of PECVD fabrication of various CNSs	15
Table.2.2 An overview of synthesis of CNSs using bio-renewable resources through conventional techniques	27
Table 2.3 PECVD growth of graphene from natural precursors: plasms parameters, properties and applications	29
Table 3.1 Vibrational band assignments. Vibrational modes: ν_s = symmetric stretching, ν_a = asymmetric stretching, ν = stretching, δ_s =symmetric bending, δ_a =asymmetric bending, ω = out of plane bending	52
Table 3.2 Surface properties of orange oil thin films	58
Table 3.3 Mechanical properties of orange oil thin films	60
Table 5.1 Polar and dispersive surface energy components and average contact angle measured for different solvents	135
Table 5.2 Surface tension components graphene nanosheets using OCG method for different liquid combinations	138

LIST OF PUBLICATIONS

Candidate prepared the following publications during the course of this thesis:

1. S. Alancherry, K. Bazaka and M.V. Jacob, “*RF plasma polymerization of orange oil and characterization of polymer thin films*”, *J. Polymers and the environment*, (2018), 26 (7), 2925-33.
2. S. Alancherry, M. Jacob, K. Prasad, J. Joseph, O. Bazaka, R. Neupane, O. Varghese, O. Baranov, S. Xu, I. Levchenko, and K. Bazaka, “*Towards Sophisticated Morphology Control of Natural Resource-derived Vertical Graphenes: Experimental and Simulation Insights*”, submitted to *Journal of Materials Chemistry A*.
3. S. Alancherry, K. Bazaka, I. Levchenko, A. Al-Jumaili, O. K. Varghese and M. V. Jacob, “*One-step plasma assisted synthesis of graphene from Citrus sinensis oil for acetone gas sensors*”, submitted to *Carbon*.

Candidate contributed to additional publications that is not related to this thesis:

4. A. Al-Jumaili, S. Alancherry, K. Bazaka, M.V. Jacob, “*Review on the antimicrobial properties of carbon nanostructures*”, *Materials*. 10 (2017) 1066.
5. A. Al-Jumaili, S. Alancherry, K. Bazaka, M.V. Jacob, “*The electrical properties of plasma-deposited thin films derived from Pelargonium graveolens*”, *Electronics*. 6 (2017) 86.
6. K. Bazaka, D.S. Grant, S. Alancherry, M.V. Jacob, “*Plasma-Assisted Fabrication and Processing of Biomaterials*”, *Biomedical Applications of Polymeric Material and Applications*, Wiley-VCH: Heidelberg, GmbH & Co. KGaA, Weinheim, Germany (2016).
7. A. Kumar, D. Grant, S. Alancherry, A. Al-Jumaili, K. Bazaka, M.V. Jacob, “*Plasma Polymerization: Electronics and Biomedical Application*”, *Plasma Science and Technology for Emerging Economies*, Springer (2017).

8. A. Al-Jumaili, S. Alancherry, D. Grant, A. Kumar, K. Bazaka, M.V. Jacob, “*Plasma Treatment of Polymeric Membranes*”, Non-Thermal Plasma Technology for Polymeric Materials, Elsevier (2019).

Chapter 1

Introduction

1.1 Rational

The advent in nanotechnology spearheaded the ongoing developments in modern electronics that paved the way for device miniaturization and improved the device performance many-fold. Carbon nanostructures (CNSs) are vital part of this technological breakthrough owing to its remarkable combination of material properties ideally suit them to serve various domains of nanoelectronics, energy conversion and storage, gas and bio sensing and environmental science. As one of the potential candidate material for swiftly emerging organic electronics industry, CNSs have been widely investigated for tailoring their properties, deterministic growth and large-scale production [1, 2]. The ever-increasing energy demand and environmental concerns put forwarded by the growing population tremendously increased CNSs demand. For instance, the global market for graphene is expected to hit US\$349 million by 2025 which was just US\$12 million during 2013 [3, 4]. Such a colossal demand necessitates the need for sustainable development of these high-end materials through “green” synthesis routes.

The fabrication of CNSs through scalable, sustainable and cost effective techniques become the most crucial part of CNSs research from both the developmental and application point of view. One of the major challenge encountered by the material scientists and industrialists in the production of CNSs is the high manufacturing cost predominantly imposed by the energy intensive and resource consuming nature of the existing fabrication processes (e.g. Thermal CVD, arc discharge, epitaxial growth etc.) [5]. The large energy consumption arises from the stringent process requisites such as high temperature, high vacuum, catalyst-assistance and long lasting deposition durations. In the meantime, the resource exploitation mainly associated with the incomplete conversion of the precursors, extensive use of catalysts and toxic organic solvents (e.g. N-methyl-pyrrolidone, sodium dodecylbenzene sulfonate etc.) and post-synthesis process for catalyst removal, purification and CNSs transfer.

The huge demand for CNSs anticipates the rapid exhaustion of commonly used synthetic non-renewable hydrocarbon resources like methane, acetylene, xylene and toluene etc. Besides, these high pure hydrocarbons are refined from petroleum and hence are expensive sources and explosive in nature. Even though naturally existing graphite can serve as another carbon feed stock, but mostly employed in top down approach like mechanical exfoliation that is limited to laboratory scale production. In this regard, it is imperative to pinpoint cheap, naturally derived renewable precursors that are plentiful and can be transformed to CNSs at low cost and minimal environmental damage.

The reformation of natural precursors into useable nanostructures using conventional techniques is complex as most of them are catalyst assisted, precursor-specific and require high temperature [6, 7]. On the other hand, PECVD, since the first study by Wang et al. [8] for fabricating few layered graphene acknowledged as much more efficient technique that address almost all the aforementioned issues and extensively used for converting both conventional and non-conventional precursors to high-value added carbon nano materials. The supremacy of PECVD over other methods mainly ascribed to the ability of plasma to create a highly reactive environment with exceptionally high amount of reactive species, featured by the collision assisted molecular dissociation unique to plasma [9]. The capability of PECVD to rebuild a wide range of precursors to functional nanomaterials, growth/patterning on arbitrary substrates, catalyst-free nature, and low process temperature benchmarked the PECVD technique as the most proficient compared to the conventional methods. In addition, the plasma sheath and the intense ion fluxes that originate at the sheath region, which is exclusive to plasma, enable the growth of vertically aligned novel nanostructures and facilitate much easier way to control the properties through independent control of the process parameters [10]. Therefore, the selection of an abundant and cheap renewable precursor in combination with PECVD technique provide far more efficient way to achieve the goal of implementing green chemistry approach (precursor-process-nanomaterial) for the fabrication of CNSs.

In this view, to develop an environmentally friendly and economically viable synthesis of high pure CNSs having well defined properties, *Citrus sinensis* essential oil (Australian Botanical Products, Australia), a by-product from juicing industry was used with PECVD. As-extracted *C. sinensis* oil is

abundant, inexpensive, self-volatile and serve as rich source of hydrocarbon compounds primarily composed limonene (>94 %) and several other monoterpenes like myrcene , α -pinene, sabinene etc. in trace amounts. The fabrication of CNSs from *C.sinensis* oil derive novel nano material for advanced applications like environmental sensing, developed from a low cost environmentally friendly approach. In brief, a process was developed for synthesizing CNSs, the process was optimized, properties were investigated, and the device performance was evaluated.

1.2 Research objectives

This research aimed to develop environmentally friendly and low cost method for the growth of high purity CNSs from a bio-renewable precursor, *C.sinensis* essential oil with minimal energy and resource consumption and to explore its performance in environmental monitoring applications. In order to achieve this aim a set of research goals are formed and given below:

- Develop RF-PECVD technique for the synthesis of CNSs from *C.sinensis* essential oil precursor source.
- Optimize the RF-PECVD process by varying the discharge parameters and to identify the most favorable deposition conditions that produce high quality CNSs.
- Determine the material's fundamental properties (structural, morphological, chemical and surface properties) using appropriate characterization techniques and to deduce structure/process/property relation.
- Investigate the structural and morphological evolution through theoretical modelling.
- Identify a particular application in the field of carbon-based nanoelectronics and evaluate the performance of CNSs thus developed by integrating into device structure.

Achieving these objectives would significantly contribute to the current research activities in environmentally benign production of CNSs from non-conventional resources for advanced applications. This project would demonstrate an efficient methodology for the fabrication of CNSs based on essential oil i.e. *C.sinensis* oil for environmental applications, potentially for gas sensors.

Furthermore, the knowledge base produced out of this project shed light into new application areas like advanced electronics for Australian essential oils.

1.3 Document organization

This thesis comprises six chapters, each of which intended to address the abovementioned research objectives.

Chapter 1 introduces the motivation and the research context of this work, outlines the research objectives to be formed to accomplish the aim of the project.

Chapter 2 presents a literature review that describes the relevant studies detailing the CNSs and their properties, significance of plasma in the growth of CNSs, the effect of various plasma process parameters on the growth and properties of CNSs, and the importance of plasma-assisted techniques in deriving CNSs from natural resources.

Chapter 3 details the low power plasma deposition of *C. sinensis* vapours and studies the fundamental properties of the resultant plasma polymer thin films as a function of RF power. The optical properties were investigated using variable angle spectroscopic ellipsometry and UV-visible spectroscopy. The chemical properties were revealed through Fourier transform infrared spectroscopy (FITR) and X-ray photoelectron spectroscopy (XPS). The morphological and mechanical properties were probed through atomic force microscopy (AFM) and nano-indentation measurements. The results were reported in the journal article *S. Alancherry, K. Bazaka, M.V. Jacob, RF Plasma Polymerization of Orange Oil and Characterization of the Polymer Thin Films, J. Polymers and the Environment, 2018, 26 (7), 2925-33.*

Chapter 4 presents the development of vertical graphene nanostructures from *C. sinensis* essential oil through RF-PECVD technique. This chapter principally focussed on the process optimization for the fabrication of vertical graphene nanosheets having well defined structural and morphological properties by varying the input RF energy, hydrogen flow rate and deposition time. The structural features and chemical properties of thus developed graphene were described with the help of laser Raman spectroscopy. A comprehensive characterization of morphological features of graphene arrays fabricated at various plasma process parameters were revealed through scanning electron microscope

(SEM), Fourier and Hough transformation profiles. In addition, the degree of connectivity and randomness of the resulted vertical graphene geometry and morphology was probed through Minkowski connectivity and fractal dimension (FD). Finally, the vertical graphene growth was simulated through theoretical modelling. The results has been communicated *S. Alancherry, M. Jacob, K. Prasad, J. Joseph, O. Bazaka, R. Neupane, O. Varghese, O. Baranov, S. Xu, I. Levchenko, and K. Bazaka, "Towards Sophisticated Morphology Control of Natural Resource-derived Vertical Graphenes: Experimental and Simulation Insights", to Journal of Materials Chemistry A.*

Chapter 5 illustrates the growth of vertical graphene nanosheets from *C. sinensis* over a range of four different conducting and insulating substrates (copper, nickel, quartz and silicon) and investigated the material properties. The structural and morphological evolution of thus formed vertical graphene arrays on different substrates was probed at length using Laser Raman spectroscopy, scanning and transmission electron microscopies, as well as sophisticated statistical and morphological analyses. X-ray photoelectron spectroscopy was then employed to perform the chemical composition analysis. The surface properties of as-fabricated graphene nanosheets was measured using contact angle measurement and the surface energy was estimated through Neumann model, Owens-Wendt-Kaelble approach and van Oss-Chaudhury-Good relation. Finally, a sensor device was fabricated and demonstrated the sensing activity towards acetone gas. The results has been communicated *S. Alancherry, K. Bazaka, I. Levchenko, A. Al-Jumaili, O. K. Varghese and M. V. Jacob. One-step plasma assisted synthesis of graphene from Citrus sinensis oil for acetone gas sensors, to Carbon.*

Chapter 6 provides an overall summary of the research work undertaken in this research. This chapter also highlighted the major results and recommendations for future work.

REFERENCES:

- [1] R. Zhang, Y. Zhang, and F. Wei, "Horizontally aligned carbon nanotube arrays: growth mechanism, controlled synthesis, characterization, properties and applications," *Chemical Society Reviews*, vol. 46, pp. 3661-3715, 2017.
- [2] V. Georgakilas, J. A. Perman, J. Tucek, and R. Zboril, "Broad family of carbon nanoallotropes: classification, chemistry, and applications of fullerenes, carbon dots, nanotubes, graphene, nanodiamonds, and combined superstructures," *Chemical reviews*, vol. 115, pp. 4744-4822, 2015.
- [3] M. Peplow, "Graphene booms in factories but lacks a killer app," *Nature*, vol. 522, p. 268, 2015.
- [4] K. S. Siow, "Graphite Exfoliation to Commercialize Graphene Technology," *SAINS MALAYSIANA*, vol. 46, pp. 1047-1059, 2017.
- [5] I. Levchenko, K. Ostrikov, J. Zheng, X. Li, M. Keidar, and K. Teo, "Scalable graphene production: perspectives and challenges of plasma applications," *Nanoscale*, 2016.
- [6] S. Ravi and S. Vadukumpully, "Sustainable carbon nanomaterials: recent advances and its applications in energy and environmental remediation," *Journal of Environmental Chemical Engineering*, vol. 4, pp. 835-856, 2016.
- [7] J. Deng, Y. You, V. Sahajwalla, and R. K. Joshi, "Transforming waste into carbon-based nanomaterials," *Carbon*, vol. 96, pp. 105-115, 2016.
- [8] J. Wang, M. Zhu, R. A. Outlaw, X. Zhao, D. M. Manos, and B. C. Holloway, "Synthesis of carbon nanosheets by inductively coupled radio-frequency plasma enhanced chemical vapor deposition," *Carbon*, vol. 42, pp. 2867-2872, // 2004.
- [9] K. Bazaka, M. V. Jacob, and K. Ostrikov, "Sustainable Life Cycles of Natural-Precursor-Derived Nanocarbons," *Chemical reviews*, 2016.
- [10] S. Ghosh, S. Polaki, M. Kamruddin, S. M. Jeong, and K. K. Ostrikov, "Plasma-electric field controlled growth of oriented graphene for energy storage applications," *Journal of Physics D: Applied Physics*, vol. 51, p. 145303, 2018.

Chapter 2

Literature Review

This chapter summarizes the literature relevant to plasma-assisted synthesis of carbon nanostructures (CNSs). Principally, the review focused on two areas: CNSs and PECVD growth of CNSs. The first section, Section 2.1, scrutinises important CNSs such as fullerene, carbon nanotubes (CNTs), graphene and their fundamental properties. The second section, Section 2.2, covers the important studies describing different type of plasma discharges and PECVD growth of various type of CNSs. The significance of PECVD in growing CNSs especially graphene and the role of various plasma process parameters on the structure and properties of graphene were discussed in depth. Additionally, special focus was given to studies explaining conventional and plasma-assisted reformation of renewable resources into various type of CNSs.

2.1 Carbon nanostructures

Among nanomaterials, CNSs, the group of carbon allotropes in the nano regime having different size, shape and dimensionality grabbed immense research interest owing to their structural diversity, remarkable material properties and huge application potentials [1-4]. Until now, different types of CNSs were developed and intensive efforts have been in progress to tailor their properties and large-scale production [5-8]. With regards to the material properties, CNSs are widely reorganized for their excellent electrical conductivity, supreme mechanical strength, high thermal conductivity, extraordinary high surface area, good transparency and structural stability [9, 10]. Featured by the unique combination of properties, CNSs have been widely employed in a range of advanced applications stretching from thin film transistors [11], transparent conducting electrodes [12], photovoltaics [13], supercapacitors [14], hydrogen storage [15] and sensors [16]. Perhaps most importantly, CNSs are considered as an integral part of organic electronics and hold the potential to substitute the silicon semiconductor technology currently used by the modern microelectronics [17]. Compared to the silicon-based technology, carbon nanoelectronics have many advantages such as low cost, low energy consumption, superior performance, device flexibility and environmental friendliness. In order to cater the huge demand put forwarded by the modern technologies enormous attention is being paid for the large-scale development of CNSs through simple, cost effective and “clean” approaches.

2.1.1 Fullerene

The advent of CNSs began during 1985's with the discovery of fullerenes, zero dimensional (0-D) allotrope of carbon [18]. Fullerenes are carbon clusters comprised of pentagonal and hexagonal rings of sp^2 hybridized carbon atoms self-assembled to spherical shape. They can be generally represented by the formula C_{20+m} (m is an integer) and consist of wide range of structures and isomers [19]. The most abundant and stable fullerene is C_{60} which exhibits a close-packed face centered cubic (FCC) structure with lattice constant 14.17 \AA [20]. C_{60} behaves as an n-type semiconductor having direct band gap [21]. Also, fullerene possesses high electron affinity, large surface to volume ratio and

a hydrophobic surface [22]. Highly resistant to compression (compressed up to 75% of the original shape), fullerenes exhibited a bulk moduli of 665 GPa [23]. Fullerenes have gained immense attention for organic photovoltaics as the active layer (fullerene/polymer blend) to create heterojunction polymer solar cells [24]. In addition, fullerene find extensive usage in nonlinear optics, surface coatings, biology and medicine [25-27].

2.1.2 Carbon nanotubes

The pioneering work of Iijima [28] led to the discovery of CNT, the one dimensional (1-D) allotrope of carbon. CNT represents the cylindrically arranged structures of carbon atoms, typically a few nanometers in diameter and micro/millimeters in length. Strongly dependent to number of layers, CNTs exhibit different properties, and mainly classified as single and multi-walled depending on the number of concentric layers. The charge transport through CNTs is ballistic in nature and hence showed remarkably high carrier mobility ($1,00,000 \text{ cm}^2\text{V}^{-1}\text{s}^{-1}$) and large current density (10^9 A/cm^2) [29, 30]. They exhibit supreme mechanical strength with Young's modulus 100 times greater than steel. A Young's modulus of 0.27-0.95 TPa measured for individual SWCNT whereas 0.32-1.47 TPa reported for MWCNT [31, 32]. In addition, CNTs showed excellent photo transparency higher than 90% [33]. With its large surface to volume ratio, CNTs measured a surface area as high as $1315 \text{ m}^2/\text{g}$ [34]. A number of fabrication techniques such as arc discharge, laser ablation, chemical vapor deposition (CVD), electrolysis and spray pyrolysis etc. have been used for the synthesis of CNTs [35].

2.1.3 Graphene

Graphene, the two dimensional (2-D) allotrope of carbon represents the one atom thick atomic layer of sp^2 hybridized carbon atoms arranged in a hexagonal honeycomb lattice. To date, graphene represents the most promising nano material having unparalleled physicochemical properties. Graphene is a zero band gap semiconductor with exceptional carrier mobility of $2,00,000 \text{ cm}^2\text{V}^{-1}\text{s}^{-1}$ and current density 10^{13} A/cm^2 indicating the lowest resistivity material at room temperature [36, 37]. However, a range of carrier mobility have been reported for this technological material and mainly affected by the number of layers, defects, ripples and the deposition process [38-40]. The presence of delocalized

electrons having very high Fermi velocity give rise to the phenomenon of ballistic transport which make them an ideal material for Terahertz devices [37]. A monolayer of graphene possesses excellent transmittance of 97.3% over the entire wavelength region and widely recognized for transparent electrode applications. It is also noticed that the transmittance is a function of number of layers (N) which varies as $T \sim 100 - 2.3 N(\%)$ [41]. Mechanically, graphene is the stiffest material ever found with Young's modulus 1 ± 0.1 TPa and tensile strength 130 ± 10 GPa [42]. Also, graphene is renowned for the extra ordinarily high surface area ($2630 \text{ m}^2/\text{g}$) and super hydrophobicity [43]. It exhibits an intrinsic capacitance of $21 \mu\text{F}/\text{cm}^2$ and denote the highest capacitance among the carbon based materials [44]. The major synthesis routes for graphene include PECVD, thermal CVD, epitaxial growth on SiC, micromechanical cleavage and chemical reduction of graphene oxide (GO) [45].

2.1.4 Vertical graphene nanostructures

Vertical graphene nanosheets are the 3-D interconnected network of self-supported graphene layers typically composed of 1 to 3 layers on the top and several layers at the bottom arranged perpendicular to the substrates [46, 47]. The vertical alignment make vertical graphene a unique material with distinguished material properties. Intrinsically graphene, vertically-oriented graphene exhibits distinctive characteristic properties such as, non-agglomerated free standing interconnected structure, long exposed thin reactive edges, high mechanical stability, superior in-plane conductivity and exceptionally high specific surface area all resulted from the perpendicular orientation [48, 49]. The spacing between adjacent graphene walls varied from few nanometers to few hundreds of nanometers and observed to be dependent to the deposition conditions [50]. With its exclusively defined surface features forming electrochemically active reactive edges, vertical graphene electrodes provide large accessible area for ion diffusion and swift ion transport and widely employed for the development of high performing supercapacitors [51]. In addition, highly reactive edges can immobilize biomolecules and rapidly respond to various gases hence implemented for gas and bio sensing applications [16]. Morphologically, vertical graphene exhibited a variety of an interconnected 3-D porous structure having leaf-like [47], petal-like [52], tree-like [53] and turnstile-like [54] topographies.

2.2 Suitable techniques for vertical graphene fabrication - Reactive plasma:

Direct current, Radio frequency and Microwave frequency discharges

Plasma represents partially or fully ionized state of a gas comprised of free electrons, ions, free radicals, photons, atoms in the ground and excited states. In general, plasma can be generated through the dissociation of neutral gas molecules by providing an energy greater than the ionization energy. For creating plasma and disintegrate gas molecules a number of ways is used such as thermal excitation, adiabatic compression, excitation using charged beams or an electric field [55]. Nevertheless, the most convenient way of generating and sustaining plasma in laboratory is through a glow discharge produced by applying an electric field to a neutral gas. Usually, the glow discharge plasma operates at a lower pressure and uses a direct current (DC), radio frequency (RF), or microwave (MW) frequency signal for triggering the plasma [56]. Upon excitation, the reactant molecules dissociate into smaller molecular fragments by the inelastic collisions with the free electrons, and subsequently recombine with the other species in the plasma volume and dissociate further to sustain the plasma [57]. The plasma produced by such means are categorized as “cold” (i.e. $T < 5000\text{K}$), possesses low degree of ionization and low ion temperature ranges from fractions to few tens of electron volt. The other category is termed as “hot” (i.e. $T > 5000\text{K}$), display very high degree of ionization and high electron and ion temperature [58]. The cold plasma can be further divided in to thermal plasma and non-thermal plasma with respect to their electron, ion and neutral particle temperatures. The former exhibits a thermal equilibrium in electron, ion and neutral particle temperatures (i.e. $T_e \sim T_i \sim T_n$) whereas the latter possesses a higher electron temperature than others [59].

The conventional DC plasma reactor consisted two parallel plate electrodes arranged inside a vacuum chamber powered with DC electric signal. By regulating the voltage and current of the input signal, various discharges such as Townsend discharge, subnormal glow discharge, normal discharge and arc discharge could be created inside the discharge tube [55]. A DC discharge at lower pressure produces characteristic luminous bands such as cathode dark space, negative glow, Faraday dark space, positive column and anode glow inside the discharge volume [60]. However, DC glow discharge is not

commonly used in applications due to the following reasons. Firstly, in a DC discharge more energy is consumed for accelerating ion than creating reactive species [61]. Secondly, DC discharge with high energy ion collisions damages the substrate as well as the growing structure [62].

A typical RF plasma system should have three necessary components: the RF generator, impedance matching network and reactor. The matching network minimises the reflected RF power by matching the impedance of the generator to that of the discharge [63]. In order to sustain an RF plasma the wavelength of the exciting signal should be comparable with the dimensions of the plasma reactor. The most commonly used excitation signal frequency for RF plasma is 13.56 MHz, restricted by the International Telecommunications Union-approved, Industrial, Scientific and Medical (ISM) frequencies [64]. There are mainly two types of RF-discharges, such as capacitively coupled (CCP) and inductively coupled configuration (ICP), classified based on the nature of coupling of RF power to the reactor. The CCP configuration uses either internal parallel electrodes or external electrodes to deliver RF power into the reactor. The presence of “self-bias” field is the unique feature of CCP discharge [65]. The self-bias is created by the higher mobility of electrons compared to the ions in an RF field which create large difference in the electron current and ion current formed on an electrode in successive half cycles of the RF field. To balance the positive ion flow and electron charge flow, the surface of the electrode become negative self-biased with respect to the plasma potential [56]. The CCP configuration can generate electron densities up to 10^9 – 10^{10} cm^{-3} and plasma density 10^{11} cm^{-3} [66]. The ICP uses electric field generated by RF current in a conductor to excite the plasma [55]. Noteworthy is that, ICP have high electron density (10^{12} cm^{-3}) and plasma density (10^{14} cm^{-3}) than CCP [61, 66].

The MW plasma systems use electromagnetic signals within the microwave regime (frequency above 300 MHz) to generate the plasma discharge. The ISM accepted excitation frequency for microwave discharge is 2.45 GHz. The MW discharge are electrodeless and can operate at pressure ranges from 10^{-5} Torr to atmospheric pressure and power ranging from several watts to hundreds of kilowatts. Compared to low frequency plasma MW can deliver high electron densities of the order of 10^{13} cm^{-3} and high degree of ionization [67]. Apart from this, MW plasma exhibits intense emission in near ultra violet region which triggers the simultaneous action of plasma-chemical and photo-chemical

process which realize high growth rate and remarkable properties [68]. In fact, the absorbed power in a plasma system depends on the electron neutral collision frequency, and is very high (up to 90%) of the incident power in MW plasma systems [69]. Wertheimer and Moisan [70] compared the behavior of microwave and lower frequency plasma and reported that the former have significantly higher fraction of high energy electrons and very high deposition rate (about ten times higher) compared to the latter. According to Musil et al. [68] the electron energy distribution and activation of plasma particles inside the plasma volume is determined by the ratio ν/ω , where ν is the electron-neutral collisional frequency and ω is the angular frequency of the applied electromagnetic field. It was observed that, the plasma created by the low frequency and microwave have entirely different ν/ω and electron energy distribution. For $\nu/\omega \geq 1$ (RF and ac region) many collisions occurs per oscillations whereas when $\nu/\omega \geq 1$ (MW region) many oscillations of the electron occurs before collision [56]. The theoretical studies of Ferreira and Loureiro proposed that the electron energy distribution of microwave plasmas is Maxwellian ($\nu/\omega \leq 1$) where as others are not Maxwellian distribution ($\nu/\omega \geq 1$) [71]. Hence, it is generally considered that microwave plasma is different from other plasmas.

2.2.1 Reactive plasma and nanostructure growth

Reactive plasma serves as an excellent tool for the fabrication of nanostructures. For the creation of any nanoassemblies, there exists mainly four different stages such as (a) creation of building units, (b) preparation of substrate surface to initiate the growth, (c) transport of building unit on to the substrate and (d) appropriate stacking of building unit [72]. It is important to note that, plasma have significant influence over each of these phases and hence considered superior to other techniques for nanostructure growth [59]. Firstly, reactive plasma exhibits the unique ability to generate a large number of building units ranging from simple elementary units such as atoms, ions and free radicals to complex macromolecules or nanoclusters. It is worth noting that, plasma can offer different ways like gas phase inelastic electronic and ionic collisions, physical sputtering and complex gas phase recombination for the formation of building units [72]. In addition to this, the plasma sheath effectively trap electrons and negatively charged ions inside the plasma volume thereby enable the rapid dissociation and reintegration of plasma species that can form huge number of building units [73]. To exemplify the

efficacy of plasma, Hash and Meyyappan [74] demonstrated that, compared to thermal dissociation of CH_4/H_2 feedstock, plasma dissociation produced several other hydrocarbon (benzene, acetylene etc.), huge variety of C_xH_y radicals and ions that favours the enhanced growth of nanostructure at lower temperature. Secondly, reactive plasma facilitates the substrate surface preparation through the inherent mechanism of physical sputtering (PS) and reactive chemical etching (RCE) via the intensive collisions of large fluxes of ions and neutrals [75]. Lee et al. [76] observed that the cobalt and nickel catalyst layers can be converted into densely distributed small island of diameter 4 to 6 nm with a 10 minute H_2 (100 sccm), 200W RF-plasma pre-treatment at 700°C . Likewise, a number of studies have reported regarding the substrate surface preparation using intense collisions of plasma species [77-80]. Thirdly, the plasma sheath enables the transport of selective building units from the plasma bulk to the specific growth sites on the substrate and provide many-fold enhancement in the growth rate. Fourthly, during plasma assisted deposition the ion fluxes are focussed towards the sharp tips of growing nanostructure on the substrate that facilitated the appropriate stacking of building unit with excellent orientation [72]. This enhances the vertical alignment of growing structure and further increase the quality of the structure produced [78, 81]. Due to above-mentioned advantageous, plasma assisted synthesis became the most attracted fabrication technique for growing CNSs.

2.2.2 PECVD: Growth of various CNSs

PECVD have been used for fabricating various CNSs since decades [48, 61, 82-84]. The first report on the synthesis of CNSs through PECVD technique was appeared in 1989 by Amaratunga et al. [82], reported the room temperature growth of nanodiamond crystal using low pressure RF-PECVD from CH_4/Ar gas mixture. The process has employed a RF power of 275–350W, pressure of 200 mTorr, and CH_4/Ar mixture to produce nanocrystalline diamond film. Soon after the discovery, the technique gained enormous attention among researchers for producing high-value added CNSs owing to its simplicity, reproducibility, low deposition temperature and high yield. The most popular and widely studied among them are CNTs. PECVD growth of CNTs was extensively reviewed by Meyyappan et al. [61, 85] and majority of studies has employed $\text{C}_2\text{H}_2/\text{NH}_3$ and CH_4/H_2 precursor, temperature between $500\text{--}800^\circ\text{C}$ and deposition pressure within 5–10 mbar. The first study on the plasma fabrication of

carbon nanofiber was published by Chen and coworkers [86] using CH₄/N₂ feedstock on Ni (100) substrate maintained at a temperature 800°C and pressure 50 Torr. Wu and colleagues [87] for the first time reported the fabrication of carbon nanowall using MW-PECVD, operated at 500W using CH₄/H₂ gases on different substrates kept at 650–700°C temperature and 1 Torr pressure. The first report on the preparation of few layers of graphene through RF-PECVD was published by Wang and coworkers [83]. Graphene sheet of less than 1 nm thicknesses synthesized without the aid of any catalysts on a wide variety of substrates (Si, W, Mo, Zr, Ti, Hf, Nb, Ta, Cr, stainless steel, SiO₂ and Al₂O₃). The process employed a gas mixture of CH₄/H₂, deposition pressure of 12 Pa, deposition temperature 680°C and a RF power of 900W. The study by Tsakadze et al. [75] fabricated aligned carbon nanotips on Si (100) substrates kept at low temperature 350°C through an inductively coupled RF-PECVD from Ar/H₂/CH₄ gas mixture. From the foregoing discussion, it is clearly understood that by the by appropriate selection of the precursors and plasma process parameters any form of CNSs can be created using PECVD and the properties can be easily tailored. Hence, PECVD is considered as the most versatile technique for the synthesis of CNSs.

Table.2.1 Over view of PECVD fabrication of various CNSs

Carbon nanostructure	Precursors	Ratio	Temperature (°C)	Pressure (mbar)	Power (W)	Ref
Nanodiamond	CH ₄ /Ar	2/98	30	0.2	275–350	[82]
Carbon nanotube	C ₂ H ₂ /NH ₃	–	750	0.01	1000	[88]
Graphene	CH ₄ /H ₂	5/100	680	0.12	900	[83]
Carbon nanotip	CH ₄ /H ₂ /Ar	–	350	0.13	2000	[75]
Carbon nanowall	CH ₄ /H ₂	10/40	650–700	1.3	500	[87]
Carbon nanofiber	C ₂ H ₂ /NH ₃	40/50	700	2	550	[86]

2.3. PECVD growth of graphene and its significance

2.3.1 Vertical alignment

Vertical orientation is the most striking feature of plasma-derived graphene, exclusively provided by the plasma field. The vertical alignment was driven by the combined action of plasma-induced field, stress effect, anisotropic effects and lattice mismatch [81, 89, 90]. The influence of plasma field on the vertical growth is detailed in the coming section 2.5.

2.3.2 Catalyst-free growth

As in any other process, the catalysts activate the surface diffusion of carbon bearing moieties and facilitate faster growth of CNSs. However, the use of catalyst is generally less entertained due to its high cost and limited availability. Moreover, catalyst free techniques eliminate all intricacies (i.e. formation of wrinkles, cracks and unintentional doping) associated with the post-synthesis process to remove the catalyst and transfer graphene into desired substrate for device fabrication. In this regard, plasma being a highly reactive environment facilitate alternate reaction mechanisms that enable the growth of graphene without the aid of catalysts on wide variety of substrates [7, 54, 91-96]. With regard to the substrates, PECVD offers compatibility to a wide spectrum of substrates (i.e. metallic, dielectric and insulating). Chugh et al. [93] observed that the substrate has no effect on the decomposition of hydrocarbon species in PECVD, but the adsorption and diffusion of carbon bearing species during the process is different for each substrates caused variation in the growth rate of graphene. It can also be noticed that substrate-plasma interaction and the subsequent nanographitic layer formation is dissimilar for different substrates which lead to divergence in morphology and growth rate of graphene with respect to substrates [97].

2.3.3 Non-Precursor specific nature

The PECVD is widely noted for its excellent compatibility with diverse range of precursors in any form such as solid (e.g. sugarcane bagasse, food waste and insect waste), liquid (plant extracts) gaseous (e.g. hydrocarbons and fluorocarbons) for growing graphene nanostructures [98-100]. Unlike

conventional techniques plasma have the capability to reform precursors into analogous structures irrespective of their state [16, 90].

2.3.4 Easy tailoring of the properties

PECVD offers a number of independent process parameters such as deposition power, pressure, temperature and reactant gas concentration, each of which have significant effect on governing the growth process and final properties of the generated nanostructure. The following section 2.4 presented an in-depth discussion on the influence of various plasma process parameters on graphene growth. Seo et al. [54] reported that by simply changing the pre-treatment conditions, vertical graphene topography could be switched from a turnstile-like to maze-like morphology and the electrical properties from strongly dielectric to semiconducting nature within the same plasma unit under the same process conditions. It can also be noticed that PECVD is capable of generating a wide variety of morphologies such as leaf-like [47], petal-like [52], tree-like [53] and turnstile-like [54] and excitingly different properties. The recent literature by Shuai et al. [50] identified that by changing the plasma source (DC, RF-ICP and MW) the wettability of the vertical graphene nanostructure can be tailored from hydrophilic to hydrophobic nature. The study pointed out that, graphene morphologies formed under the experimental condition were noticeably different and measured with different inter-sheet spacing. The distance between neighboring walls and WCA decreased in the order $306.2 > 102.7 > 14.5$ nm and $110^\circ > 72^\circ > 34.5^\circ$ for DC, RF-ICP and MW plasma respectively. As plasma is compatible with all precursors, it became so easy to dope graphene and alter the properties. For instance, Wei et al. [101] reported the nitrogen doping to modulate the electronic properties of graphene without metal-catalyst by simple incorporating 30% NH_3 along with CH_4 gas. Considering the above factors, it can be understood that PECVD have significant advantages over other techniques in terms of the simplicity, purity, short deposition durations, and energy efficiency.

2.4. Influence of various plasma process parameters on the growth of graphene

2.4.1 Precursors and precursor concentration

The most common and widely used precursor for the development of graphene nanostructure through PECVD is purified hydrocarbon gases (e.g. methane, ethane, acetylene, benzene, toluene and xylene) and fluorocarbon gases [48, 102]. In general, a mixture of hydrocarbon gas with appropriate percentage of inert gas like argon or hydrogen-bearing gases (hydrogen, ammonia etc.) were used to minimize the co-deposition of amorphous carbon. The hydrogen molecules when subjected to electric field dissociate into atomic hydrogen and contribute to the etching of co-deposited amorphous carbon [103-105]. On the other hand, inert gases help to maintain the discharge and enhances the ionization and dissociation capacity within the plasma volume [106, 107]. For the successful growth of graphene and other CNSs, optimal hydrogen flow rate should be used because a low flow rate induces the co-deposition of amorphous carbon, while the high flow rate caused dominant etching of the deposited carbon [108]. In fact, the precursor gas chemistry and concentration significantly change the plasma chemistry, density of reactive species within the plasma volume and the final properties of the growing nanostructure [109-112]. For instance, the study conducted by Zhu et al. [109] revealed that vertical graphene produced from different precursors exhibited different growth rate. In a comparison, the authors observed that vertical graphene were produced at rate 16 $\mu\text{m/h}$ with acetylene, which is 8 times higher than that of methane. Similar observation was noticed by Cai et al. [110], where vertical graphene nanosheets grown from C_2H_2 feedstock exhibited faster growth rate (2.7 times) and higher specific capacitance than those obtained from CH_4 gas under the same growth conditions. The difference in properties with respect to feedstock was mainly associated with the bond dissociation energies of a particular reactant molecule and the creation different reactive species especially C_2 dimer, the most important growth component for the growth of carbon nanostructure [113]. With the help of optical emission spectroscopy, Teii et al. [114] traced the difference in plasma species formed by $\text{Ar/N}_2/\text{C}_2\text{H}_2$ and $\text{Ar/N}_2/\text{CH}_4$ gas mixtures. It was confirmed that, the former creates the C_2 dimer through direct

dissociation and hence have higher percentage of C₂ dimer than the latter where the disintegration mechanism is indirect. Consequently, acetylene exhibited higher growth rate than methane and the resulted nanostructure was morphologically different. It is worth noting that there should be a minimum concentration of the carbon bearing gas, otherwise resulted with amorphous carbon [115]. In an attempt to grow nitrogen doped graphene on dielectric substrates, Wei et al. [101] noticed that the growth temperature was precursor dependent. Interestingly, hydrocarbon gases with higher hydrogen content like CH₄ required more substrate temperature compared to C₂H₄ or C₂H₂ when diluted with 15% NH₃ gas. The study successfully developed graphene at lower temperatures 435°C>475°C>600°C with gas compositions that contain acetylene, ethane and methane respectively. In a recent study, Gosh et al. [111] detected that the growth and orientation of graphene in PECVD using a CH₄ plasma could be flipped by diluting with different concentration of hydrogen and argon gases. While the hydrogen-rich CH₄ plasma preferred the horizontal growth, argon-rich plasma favored the vertical growth. Another study by Yue et al. [112] reported the tuning of the vertical graphene morphology within the same plasma reactor. In a typical gas mixture of CH₄/H₂/Ar, 30:40:50 composition formed petal-like morphology whereas 44:11:45 lead to tree-like morphology. Therefore, it is clear that the precursor gas chemistry play vital part in the growth and properties of graphene nanostructures.

2.4.2 Growth temperature

The substrate temperature is another critical process parameter that significantly affect the physical and chemical properties of graphene and other CNSs fabricated through PECVD [115, 116]. In a catalyst assisted PECVD, the growth temperature determines the size, shape and number density of catalyst nano-islands and regulate the size, shape and properties of the growing nanostructure [117, 118]. On the other hand, in catalyst-free PECVD, the temperature influences the surface diffusion of reactant species as well as the purity and the alignment of the resulted structure [54, 88, 119, 120]. In contradiction to thermal CVD, PECVD offers relatively low growth temperature due to its capability to fragment the reactant molecules through inelastic collisions, not by the substrate temperature [121-123]. In addition, PECVD capable of heating the substrates through the inherent mechanism of physical sputtering (PS) and reactive chemical etching (RCE) [75]. Kim et al. [107] published the large area

(23cm X 20cm) growth of graphene through MW-PECVD from a mixture of CH₄/Ar/H₂ gases at a temperature of 400°C one of the lowest growth temperature reported for graphene growth. Similarly, there are published reports on the development of graphene from hydrocarbon plasma at a substrate temperature well below 680°C [83, 124]. A recent, report by Pineda et al. [125] discussed the extremely low temperature (i.e. at 200 °C) synthesis of graphene micro-islands on copper foil through inductively coupled RF-PECVD process using CH₄/Ar/H₂ gas mixtures. It is noteworthy that plasma alone is capable of providing sufficient heat environment for the nanostructure growth [126]. Nevertheless, majority of PECVD process employ a conventional heating along with plasma in order to change the plasma independent of the substrate temperature [48]. Generally, an enhanced growth rate was suggested with increase in substrate temperature due to the improved surface diffusion of adsorbed carbon species. The surface diffusion time and substrate temperature is related as [103, 127]

$$\tau_d = \nu_1^{-1} \text{Exp} \left[\frac{E_d}{(kT_s)} \right] \quad (2.1)$$

where τ_d is the mean diffusion time, ν_1 is the lattice vibrational constant, k is the Boltzmann constant and T_s is the substrate temperature. It is also observed that a higher substrate temperature lead to a higher impingement rate that further improve the deposition rate [103]. In an ICP configured plasma system, Tsakadze and coworkers [117] measured the same ion current at the substrate surface at lower and higher temperatures and therefore claimed that neutral free radicals predominantly contribute to the enhanced growth rate than ions. In addition, the higher substrate temperature cause larger pressure gradient at near substrate region and increased thermophoresis forces that improves the diffusion flow of neutral species.

In MW-PECVD, Kim and coworkers [128] demonstrated that temperature was very critical in determining the microstructure, nanowall height, surface density and the crystallinity of carbon nanowall. In their work, lower temperature (700°C) failed to form the characteristic nanowall microstructure whereas the higher temperature (950°C) resulted in microstructure collapse. Similar observations were made in a RF-PECVD process by Wang et al. [120] during the development of carbon nanowalls at four different temperatures 630, 680, 730 and 830°C. Well-separated and densely packed

nanowalls were formed only at 680°C, which gradually turned into a corrugated and agglomerated form with further increase in temperature. Another study by Raut et al. [129] showed that within the same plasma system and under the same process conditions, by solely controlling the substrate temperature (950–1150°C) nanostructures with different dimensions and properties can be synthesized. Interestingly, the authors could form 1-D CNT at lower temperature (~950°C), 2-D graphenated CNT at intermediate temperature (1050°C) and 3-D vertical graphene sheets at higher temperature (1150°C). Therefore, the optimization of the deposition temperature become essential for the successful growth of the growth of graphene and other CNSs with well-defined properties. From the above discussion, it is evident that with the incredible properties of plasma, property-tailored CNSs can be grown at lower temperature on arbitrary substrates, which significantly reduced the energy and resource consuming.

2.4.3 Deposition power and pressure

The deposition power is an important plasma tool in PECVD to engineer the CNSs properties. Most significantly, deposition power influences the dissociation of reactant molecules and determine the ion, neutral and radical densities inside the bulk plasma. More the power higher the molecular fragmentation, density, momentum and energy of the plasma species (ions, electrons and neutral species). Denysenko and coworkers [130] studied the effect of RF-power on the dissociation of Ar/CH₄/H₂ gas mixture and observed that the concentration of electron, Ar⁺, H⁺ densities inside the plasma increased with increase in the RF power whereas concentration of Ar, H₂, CH₄ and higher hydrocarbons (C_xH_y, x≥2) decreased. The study by Zhu et al. [103] revealed that vertical graphene nanosheets formed at higher RF power (1200 W) have smooth morphology, increased growth rate and high degree of order compared to samples made at lower RF power (800 W). Moreover, an increase in the atomic hydrogen percentage was noticed with respect to the increase in RF power caused enhanced etching of amorphous carbon. Kim et al. [104] in an effort to grow graphene from methane gas on copper substrate at different RF power (50–120W) observed that the RF power can effectively tune the hydrogen partial pressure and thereby control the grain size and nucleation density during the early phase growth of graphene. Another study from Yang et al. [119] attempted growing vertical graphene nanosheets at different RF power ranging from 50–200W reported that the lower power only resulted

sparingly distributed vertically erected graphene flakes. Gosh et al. [131] reported the mechanism of growth of vertical graphene fabricated at different microwave powers, 200–475W, from CH₄/Ar plasma. The study revealed that the microwave power controlled the growth rate and areal density of vertical graphene and found to be high at intermediate power 375W, but decreased thereafter.

The effect of pressure on the PECVD growth of CNSs is complex and controlled by Paschen's law. For a particular gas composition, it was observed that the breakdown voltage is directly proportional to the product of the system pressure (p) and the inter-electrode distance (d). Therefore, pressure became a critical factor deciding the molecular fragmentation as the electrode distance is a fixed variable for a particular system. In addition, the mean free path for inelastic collisions is inversely proportional to the pressure which provide higher dissociation and increased ionization rate inside bulk plasma at lower pressure [48]. Furthermore, pressure also affects the number of collisions ($n \propto P^{1/2}$) within the sheath region and the mean energy per ion ($E \propto P^{-1/2}$) [132, 133]. Most importantly, the deposition pressure influences the growth rate as well as the defects formed within the growing nanostructure. It is observed that lowering the pressure inside the chamber resulted with increased deposition rate and defects in the structure. An increase in the deposition rate could be ascribed to increased fragmentation of the reactant molecules [103]. In the above study, the calculated mean ion energy near sheath region is varied from 2 to 8 eV as the pressure varied from 400 to 20 mTorr. Apart from this, in hydrogen rich plasma the lower pressure leads to the increased concentration of atomic hydrogen that predominate the etching effects. To illustrate, Wei et al. [134] reported a drastic increase in the H_α concentration within the plasma created from C₂H₂/H₂/Ar mixture with decrease in chamber pressure from 350 mTorr to 50 mTorr. The Raman characterization of PECVD deposited graphene films at a various pressure 0.8 to 1.5 Torr indicated that I_D/I_G ratio increased with increase in pressure and hence the samples became more defected at higher pressure [135]. In an attempt to study the effect of pressure (0.4 – 50 mbar) and argon flow rate (350–1400 sccm) on the properties of carbon nanowalls, Vizireau et al. [118] found that well distinguished carbon nanowall with good length /thickness ratio and surface density could only be grown at lower pressure (1 mbar) and high argon flow rate (1400 sccm). Recent study by Gao et al. [136] explored the effect of deposition pressure (30, 40 and 50 Pa)

on the structural and morphological properties of carbon nanowalls prepared through RF-PECVD. The key finding was that an increase in working pressure increased the surface roughness and decreased the surface free energy of graphene samples. The water contact angle measurements conducted revealed that all samples exhibited super hydrophobic behavior and noticed with a steady increase in WCA, showed a maximum value of 152.1° for sample formed at 50 Pa.

2.5 PECVD and mechanism of vertical graphene growth

Over other techniques, PECVD is widely recognized for producing individual, free-standing vertically aligned structures. The growth mechanism for vertical graphene was discussed in detail in the review article by Bo et al. [84] and the references therein. According to Malesevic and coworkers [137] the growth comprises three phases. During the first stage, a discontinuous graphitic buffer layer formed parallel to the substrate. These layers consisted of several cracks and dangling bonds that act as the nucleation sites to receive the incoming carbon bearing species and initiate the formation of freestanding few layers of graphene in the second stage. Finally, the process terminated by the accumulation of carbon moieties, strongly determined by the competitive deposition and etching of plasma process. The early stage buffer layer formed before the onset of vertical growth mainly composed of amorphous carbon, defective nanographitic islands, nanodiamond particles and carbon onions [46, 97, 103, 138]. Ghosh et al. [97] further investigated the phase prior to buffer layer formation and revealed that hot spots were formed on the substrate surface through the energetic plasma bombardment which is followed by the rapid nucleation of the nano graphitic islands that coalesce to the form the buffer layer. There are several mechanisms such as surface electric field interactions, stress induced effects etc. that govern the vertical growth from the parallel buffer layers. The effect of local electric field in the growth and alignment of vertical graphene was explained by Zhu et al. [103]. It was postulated that the local electric field produced by the plasma induces the bending of the nucleating layer by providing sufficient energy to overcome the activation energy barrier (∇E) of the sp^2 bonded graphene network layer. In addition, by making the electric field radially oriented, the authors further observed that the nanosheet growth predominantly oriented radially in the local electric field direction and therefore confirmed the correlation between the direction of electric field and alignment. It was also interpreted that as a result

of the existence of plasma sheath electric field, on the substrate region the ion fluxes are focussed towards the sharp tips of growing nanostructure that efficiently direct the carbon bearing radicals on to the tip of the developing structure that predominate the growth in vertical direction than horizontal direction [72]. Similar observation have been reported for CNTs. By running PECVD and thermal CVD consecutively within the same apparatus, Bower et al. [81] showed that the plasma induced self-bias field has major role in controlling the vertical growth and alignment of CNTs. The authors noticed a switching between aligned nanotubes to curly nanotubes when the process shifted from PECVD to thermal CVD. The study conducted by Yu et al. [139] revealed that the electric field near the substrate is critical to graphene growth and coverage. The work pointed out that under same experimental conditions the electric field intensity near grounded gold substrate is higher than the dielectric SiO₂ substrate. As a result, the reactant gas was ionized more efficiently over gold substrate and provide better coverage. Another study attributes the vertical growth to the accumulation of compressive strain energy that transform the continuous 2-D intermediate few layers of graphene film into discontinues 3-D clusters [140]. In addition, the high-energy ion bombardment from the plasma creates defects, which act as the nucleation spots for the carbon bearing species and further accelerate the vertical growth. In a recent study, Zhao et al. [46] demonstrated that the vertical growth starts either from the mismatches and curved areas of the graphitic layers or from the carbon onions that formed on the substrate surface.

2.6 Break down and rebuild of natural precursors into various CNSs

Fabrication of CNSs from natural precursors gained immense research attention among material scientists. In general, the non-renewable resources for producing CNSs includes graphite, purified hydrocarbon gases and several other organic compounds [141-143]. Among the conventional precursors, purified hydrocarbon gases such as methane, acetylene, xylene, toluene benzene etc. are extensively used owing to the popularity of chemical vapor deposition for synthesizing CNSs. However, hydrocarbon gases are refined from petroleum and hence are expensive. In addition, the dissociation of hydrocarbon gases produce harmful mixtures of volatile organic compounds and polycyclic aromatic hydrocarbons as by-products that contribute to the greenhouse gas emission [144]. In this context, natural resources gained considerable impetus as carbon sources due to its abundance, renewability,

low cost and environmental friendliness. The recent advancements in the development of CNSs from sustainable materials were detailed in review articles by Soumya et al. [145], Titirici et al. [146] and Deng et al. [147] and the references therein. Until now, renewable feedstock like biomass [148], waste plastics [149], plant extracts [91], oils [150], proteins[151] etc. have been successfully employed to develop diverse functional carbon based nano structures. For instance, Sun et al. [148] reported the preparation of porous graphene-like nanosheet from a biomass, coconut shell. The procedure employed the simultaneous activation and graphitization process by mixing FeCl₃ catalyst and ZnCl₂ activation agent with the coconut shell and heating to a temperature of 900°C under N₂ atmosphere. During the pyrolytic process FeCl₃ catalyst generates a carburized phase from the rest of the reactants which govern the graphene formation. Similarly, Ruiz et al. [151] published the production of graphene from sucrose and gelatine protein through thermal treatment at N₂ atmosphere. The study by Kumar et al. [152] described the synthesis of single and multi-walled CNTs from a botanical hydrocarbon: camphor (C₁₀H₁₆O) through pyrolysis method. The process has used a temperature of 800–1050°C, Fe catalyst and argon atmosphere to grow high purity CNTs with good yield as high as 90%. Camphor was also identified as an excellent precursor for fabricating few layers of graphene through two-step thermal CVD technique. Initially, camphor was vaporized by heating up to 180°C in the first chamber and carried to the second chamber using argon gas to undergo thermal decomposition over nickel substrate maintained at a temperature 700–850°C, yielded few layered planar graphene [153]. In liquid precursors, turpentine oil, a plant extract derived from the oleoresin of pinus species served as an excellent renewable resource for CNTs [150, 154, 155]. Gosh et al. [156] converted eucalyptus oil to single walled CNT through catalyst decomposition process at a temperature 850°C under the presence of Fe/Co catalyst. Kawale et al. [157] demonstrated the fabrication and electrical characterizations of CNTs through hot wire chemical vapour deposition using a wide range of naturally derived materials such as camphor, mustard oil, castor oil, coconut oil, turpentine oil and menthol. Noteworthy is that, the process provided excellent yield and resulted nanostructures displayed comparable properties with that of the hydrocarbon equivalent. A two-step dissolution-precipitation process for developing graphitic carbon nanostructures from celluloses was described by Sevilla and Fuertes [158]. The cellulose was first treated by a hydrothermal process at 250°C and then subjected to the impregnation

with nickel nitrate solution followed by a thermal treatment at 900°C to form the graphitic nanostructures. The yielded nanostructures exhibited coiled morphology, high crystallinity and accessible surface area and hence proposed for electrochemical applications. In an attempt to utilize negatively valued precursors, Ruan et al. [99] explored six different waste carbon-containing materials such as chocolate, cookies, grass, polystyrene, dog feces and cockroach leg for monolayer graphene synthesis through thermal CVD. The growth was carried out on copper substrate heated to 1050°C at lower pressure under H₂/Ar gas flow. This method produced high quality pristine monolayer graphene having excellent transparency (97%) on the backside of the copper foil. Likewise, there are several studies reported employing other waste plastics such as polypropylene (PP), polyethylene-polystyrene, polytetrafluoroethylene (PTFE), polymethylmethacrylate (PMMA) for deriving single layer and multilayer graphene [149, 159, 160]. Lotus and hibiscus flower petals was the carbon source for Ray and co-workers [161]. Pure graphene was obtained through thermal exfoliation method by heating the petals to a very high temperature of 1600°C in argon atmosphere for half an hour. The cellulose and hemicellulose present in the petals acted as the carbon supplier, which undergo bond scission at elevated temperature and rearranged to form graphene. The study noticed that the quality of graphene was poor at lower temperature (800°C) but improved with the increase in temperature. The foregoing discussion clearly states that the conversion of bio-renewable resources into CNSs require high temperature catalyst assisted multi-step process. Therefore, it is essential to develop single-step, catalyst-free low temperature techniques that transform precursors of any kind to different forms of CNSs.

Table.2.2 An overview of synthesis of CNSs using bio-renewable resources through conventional techniques

Precursor	Synthesise technique	Temperature/Catalyst	Carbon nanostructure Type	Reference
Camphor	Pyrolysis	800–1050°C Fe	single, multi-walled CNTs	[152]
Coconut shell	Simultaneous activation-graphitisation (SAG)	900°C/ FeCl ₃	Graphene-like nanosheets	[148]
Turpentine oil	spray pyrolysis	500–900°C Fe/Co	CNTs	[150]
cellulose	Hydrothermal carbonization	900°C/Ni	Graphitic carbon	[158]
Camphor	Thermal CVD	700–850°C/Ni	Few-layered planar graphene	[153]
Food waste and insect waste	Thermal CVD	1050°C/Cu	monolayer graphene	[99]
Hibiscus/lotus petals	Thermal exfoliation	1600°C	graphene/ Ni-decorated graphene	[161]

2.7. Significance of plasma in deriving CNSs from natural resources

The advantage of PECVD in the growth of graphene and other CNSs were detailed in section 2.3. However, it can also be mentioned that PECVD offer significant advantages in converting bio-renewable carbon sources into diverse high-value-added nanostructures [162]. Most importantly, PECVD recognized as non-precursor specific technique that allows the use of virtually any type of carbon containing sources (solid, liquid and gaseous) to derive potential nanostructures with minimal

consumption of time, precursor and energy. To illustrate, with the aid of plasma Seo and colleagues [90] reformed a range of natural resources such as honey, table sugar, butter, milk and methane into vertical graphene nanostructures and evidenced that plasma is capable of converting diverse precursors to functional nanostructures under the same process conditions. By successively running PECVD and thermal CVD with these sources, the authors ascertained that only PECVD could successfully produce graphene, and thermal CVD resulted in the formation of amorphous carbon. In contrast to plasma-derived structures, thermal reformed samples were different in structure and morphology (indicated by the SEM and Raman studies) due to the precursor specific nature of thermal CVD. However, the use of plasma for reforming naturally derived precursors into novel CNSs like vertical graphene gained attention recently, and hence only less explored. Recent literature by Mohan et al. [91] reported the catalyst-free growth of high quality graphene from the volatile extract of tea tree (*Melaleuca alternifolia*). The 3-D nanostructured surface found to be highly hydrophobic (WCA of 135°) and possessed high degree of structural order ($I_D/I_G=0.63$ and $I_{2D}/I_G=3.32$). In addition, no elemental impurities detected on the XPS spectrum (even for very short duration of deposition of 2m) though tea tree oil is a multicomponent system. Furthermore, the film showed excellent memristive behaviour and proved to be promising for RRAM applications. The synthesis of graphene through a scalable RF-PECVD from honey and its by-product honeycomb was demonstrated by Seo et al. [16, 163]. Both studies obtained few-atomic-layer thick vertical graphene nanosheets having exceptional material properties suitable for bio-sensing and supercapacitor electrode applications. The former showed potential sensing towards hydrogen and Au tagged antibodies whereas the latter to neurotoxic Amyloid-beta ($A\beta$), biomarker for Alzheimer's disease. Furthermore, the cost calculation revealed a substantial reduction of production cost (about 100 times lower) for honey based graphene compared to that produced from purified methane. Similar studies have been reported from other bio-renewable resources like cheese and butter and demonstrated the supercapacitor electrode applications [92, 164]. Interestingly, cheese derived graphene electrodes possessed a very high areal capacitance of 0.46 F cm^{-2} owing to the high mass loading of 3.2 mg cm^{-2} . The recent work by Shah et al. [165] described the successful fabrication of single layer and few layers of graphene from waste mango peels, a biomass rich in heteropolysaccharide pectin. The process first ground mango peels into powders (particle size \approx

1 nm) and uniformly distributed over copper a substrate. The samples were then placed inside reaction chamber and heated up to 750°C under vacuum. An argon/hydrogen plasma (RF power 300W) was ignited then for one hour to deposit graphene. It was noticed that multilayer graphene was formed for plasma exposure time ≤ 30 min and single layer was obtained at one hour. Another work by Karthika et al. [98] revealed effective use of sugarcane bagasse to produce vertical graphene for antifouling coatings. Similar to previous case, grounded sugarcane bagasse powder was evenly loaded on porous nickel substrate and exposed to Ar/H₂ (50:15 sccm) plasma generated at 760W for 10 minutes. The TEM analysis revealed the formation of multilayer system having 15-20 layers. The coatings exhibited reasonably good antifouling characteristics against gram-positive bacteria *Escherichia coli* and gram-negative bacteria *Staphylococcus aureus*.

Table 2.3 PECVD growth of graphene from natural precursors: plasms parameters, properties and applications

Precursor	Process parameters Power (P), pressure (p), temperature (T)	Properties	Application	Reference
Tea tree oil	P –500W p–0.20 mbar T–800°C	$I_{2D}/I_G=3.32$, $I_D/I_G=0.63$ 3–4 layers	Random access memory (RRAM)	[91]
Honey	P– 1000W p– 2 Pa T–400°C	$I_{2D}/I_G=1.4$, $I_D/I_G=0.63$ 5–6 layers	Biosensing (Au-antibodies) and gas sensing (Hydrogen)	[163]
Mango peel	P –300W p–0.2 Torr T– 750°C	$I_{2D}/I_G= 2.78$ Single layer	-	[165]
Honeycomb	P –1000W p–2 Pa T– No external heating	$I_{2D}/I_G=0.45$, $I_D/I_G=0.72$ Specific capacitance 240 Fg^{-1}	Biosensing (A β) and supercapacitor electrode	[16]
Sugarcane bagasse	P –760W p–2 Pa T– 400°C	$I_{2D}/I_G=0.38$, $I_D/I_G= 1.52$ 15-20 layers	Antifouling coatings	[98]

2.8 Conclusion

In summary, this chapter overviewed various type of CNSs such as fullerene, CNTs and graphene and their properties. Then the significance of plasma assisted synthesis over other techniques for the fabrication of CNSs reviewed succinctly. PECVD employed with DC, RF and MW sources for the synthesis of CNSs was demonstrated. With special focus on graphene, the significance of PECVD and the influence of process parameters such as precursor gas, gas concentration, temperature, power and pressure were discussed. The important studies unveiling the mechanism of vertical graphene growth was then comprehended. Finally, different types of non-conventional resources and currently existing techniques for their conversion to various CNSs with special focus to PECVD process was established.

REFERENCES:

- [1] J. Peng, W. Gao, B. K. Gupta, Z. Liu, R. Romero-Aburto, L. Ge, *et al.*, "Graphene quantum dots derived from carbon fibers," *Nano letters*, vol. 12, pp. 844-849, 2012.
- [2] M. G. Hahm, A. Leela Mohana Reddy, D. P. Cole, M. Rivera, J. A. Vento, J. Nam, *et al.*, "Carbon nanotube–nanocup hybrid structures for high power supercapacitor applications," *Nano letters*, vol. 12, pp. 5616-5621, 2012.
- [3] K. S. Novoselov, V. Fal, L. Colombo, P. Gellert, M. Schwab, and K. Kim, "A roadmap for graphene," *Nature*, vol. 490, pp. 192-200, 2012.
- [4] X. Cao, Y. Shi, W. Shi, G. Lu, X. Huang, Q. Yan, *et al.*, "Preparation of novel 3D graphene networks for supercapacitor applications," *Small*, vol. 7, pp. 3163-3168, 2011.
- [5] C.-M. Yang, Y.-J. Kim, M. Endo, H. Kanoh, M. Yudasaka, S. Iijima, *et al.*, "Nanowindow-regulated specific capacitance of supercapacitor electrodes of single-wall carbon nanohorns," *Journal of the American Chemical Society*, vol. 129, pp. 20-21, 2007.
- [6] G.-L. Chen, S.-H. Fan, C.-L. Li, W.-C. Gu, W.-R. Feng, G.-L. Zhang, *et al.*, "A Novel Atmospheric Pressure Plasma Fluidized Bed and Its Application in Mutation of Plant Seeds," *Chinese Physics Letters*, vol. 22, p. 1980, 2005.
- [7] M. Hiramatsu, K. Shiji, H. Amano, and M. Hori, "Fabrication of vertically aligned carbon nanowalls using capacitively coupled plasma-enhanced chemical vapor deposition assisted by hydrogen radical injection," *Applied Physics Letters*, vol. 84, pp. 4708-4710, 2004.
- [8] K. Novoselov, A. K. Geim, S. Morozov, D. Jiang, M. Katsnelson, I. Grigorieva, *et al.*, "Two-dimensional gas of massless Dirac fermions in graphene," *nature*, vol. 438, pp. 197-200, 2005.
- [9] Q. Cao and J. A. Rogers, "Ultrathin Films of Single-Walled Carbon Nanotubes for Electronics and Sensors: A Review of Fundamental and Applied Aspects," *Advanced Materials*, vol. 21, pp. 29-53, 2009.
- [10] W. Choi, I. Lahiri, R. Seelaboyina, and Y. S. Kang, "Synthesis of Graphene and Its Applications: A Review," *Critical Reviews in Solid State and Materials Sciences*, vol. 35, pp. 52-71, 2010/02/11 2010.
- [11] Y. Wu, X. Lin, and M. Zhang, "Carbon nanotubes for thin film transistor: fabrication, properties, and applications," *Journal of Nanomaterials*, vol. 2013, p. 64, 2013.
- [12] D. S. Hecht, L. Hu, and G. Irvin, "Emerging Transparent Electrodes Based on Thin Films of Carbon Nanotubes, Graphene, and Metallic Nanostructures," *Advanced Materials*, vol. 23, pp. 1482-1513, 2011.

- [13] X. Wang, L. Zhi, and K. Müllen, "Transparent, conductive graphene electrodes for dye-sensitized solar cells," *Nano letters*, vol. 8, pp. 323-327, 2008.
- [14] D. H. Seo, Z. J. Han, S. Kumar, and K. Ostrikov, "Structure-Controlled, Vertical Graphene-Based, Binder-Free Electrodes from Plasma-Reformed Butter Enhance Supercapacitor Performance," *Advanced Energy Materials*, vol. 3, pp. 1316-1323, 2013.
- [15] G. K. Dimitrakakis, E. Tylianakis, and G. E. Froudakis, "Pillared graphene: a new 3-D network nanostructure for enhanced hydrogen storage," *Nano letters*, vol. 8, pp. 3166-3170, 2008.
- [16] D. H. Seo, S. Pineda, S. Yick, J. Bell, Z. J. Han, and K. K. Ostrikov, "Plasma-enabled sustainable elemental lifecycles: honeycomb-derived graphenes for next-generation biosensors and supercapacitors," *Green Chemistry*, 2015.
- [17] N. P. Guisinger and M. S. Arnold, "Beyond silicon: carbon-based nanotechnology," *MRS bulletin*, vol. 35, pp. 273-279, 2010.
- [18] W. Krätschmer, L. D. Lamb, K. Fostiropoulos, and D. R. Huffman, "C60: a new form of carbon," *Nature*, vol. 347, pp. 354-358, 1990.
- [19] T. C. Dinadayalane and J. Leszczynski, "Remarkable diversity of carbon-carbon bonds: structures and properties of fullerenes, carbon nanotubes, and graphene," *Structural Chemistry*, vol. 21, pp. 1155-1169, 2010/12/01 2010.
- [20] W. I. David, R. M. Ibberson, J. C. Matthewman, K. Prassides, T. J. S. Dennis, J. P. Hare, *et al.*, "Crystal structure and bonding of ordered C60," *Nature*, vol. 353, pp. 147-149, 1991.
- [21] G. G. Wallace, J. Chen, D. Li, S. E. Moulton, and J. M. Razal, "Nanostructured carbon electrodes," *Journal of Materials Chemistry*, vol. 20, pp. 3553-3562, 2010.
- [22] B.-T. Zhang, X. Zheng, H.-F. Li, and J.-M. Lin, "Application of carbon-based nanomaterials in sample preparation: A review," *Analytica Chimica Acta*, vol. 784, pp. 1-17, 6/19/ 2013.
- [23] R. S. Ruoff and A. L. Ruoff, "The bulk modulus of C60 molecules and crystals: a molecular mechanics approach," *Applied physics letters*, vol. 59, pp. 1553-1555, 1991.
- [24] D. M. Guldi and V. Sgobba, "Carbon nanostructures for solar energy conversion schemes," *Chemical Communications*, vol. 47, pp. 606-610, 2011.
- [25] R. Bakry, R. M. Vallant, M. Najam-ul-Haq, M. Rainer, Z. Szabo, C. W. Huck, *et al.*, "Medicinal applications of fullerenes," *International journal of nanomedicine*, vol. 2, p. 639, 2007.
- [26] R. C. Hollins, "Materials for optical limiters," *Current opinion in solid state and materials science*, vol. 4, pp. 189-196, 1999.

- [27] E. Castro, A. H. Garcia, G. Zavala, and L. Echegoyen, "Fullerenes in biology and medicine," *Journal of Materials Chemistry B*, vol. 5, pp. 6523-6535, 2017.
- [28] S. Iijima, "Helical microtubules of graphitic carbon," *nature*, vol. 354, pp. 56-58, 1991.
- [29] T. Dürkop, S. Getty, E. Cobas, and M. Fuhrer, "Extraordinary mobility in semiconducting carbon nanotubes," *Nano letters*, vol. 4, pp. 35-39, 2004.
- [30] Z. Yao, C. L. Kane, and C. Dekker, "High-field electrical transport in single-wall carbon nanotubes," *Physical Review Letters*, vol. 84, p. 2941, 2000.
- [31] M.-F. Yu, O. Lourie, M. J. Dyer, K. Moloni, T. F. Kelly, and R. S. Ruoff, "Strength and breaking mechanism of multiwalled carbon nanotubes under tensile load," *Science*, vol. 287, pp. 637-640, 2000.
- [32] M.-F. Yu, B. S. Files, S. Arepalli, and R. S. Ruoff, "Tensile loading of ropes of single wall carbon nanotubes and their mechanical properties," *Physical review letters*, vol. 84, p. 5552, 2000.
- [33] Z. Wu, Z. Chen, X. Du, J. M. Logan, J. Sippel, M. Nikolou, *et al.*, "Transparent, conductive carbon nanotube films," *Science*, vol. 305, pp. 1273-1276, 2004.
- [34] A. Peigney, C. Laurent, E. Flahaut, R. Bacsas, and A. Rousset, "Specific surface area of carbon nanotubes and bundles of carbon nanotubes," *Carbon*, vol. 39, pp. 507-514, 2001.
- [35] M. Terrones, "Science and technology of the twenty-first century: synthesis, properties, and applications of carbon nanotubes," *Annual review of materials research*, vol. 33, pp. 419-501, 2003.
- [36] L. Ma, J. Wang, and F. Ding, "Recent progress and challenges in graphene nanoribbon synthesis," *ChemPhysChem*, vol. 14, pp. 47-54, 2013.
- [37] K. S. Novoselov, A. K. Geim, S. Morozov, D. Jiang, Y. Zhang, S. Dubonos, *et al.*, "Electric field effect in atomically thin carbon films," *science*, vol. 306, pp. 666-669, 2004.
- [38] J.-H. Chen, C. Jang, S. Xiao, M. Ishigami, and M. S. Fuhrer, "Intrinsic and extrinsic performance limits of graphene devices on SiO₂," *Nature nanotechnology*, vol. 3, pp. 206-209, 2008.
- [39] S. Morozov, K. Novoselov, M. Katsnelson, F. Schedin, D. Elias, J. Jaszczak, *et al.*, "Giant intrinsic carrier mobilities in graphene and its bilayer," *Physical Review Letters*, vol. 100, p. 016602, 2008.
- [40] F. Schwierz, "Graphene transistors," *Nature nanotechnology*, vol. 5, pp. 487-496, 2010.

- [41] R. Nair, P. Blake, A. Grigorenko, K. Novoselov, T. Booth, T. Stauber, *et al.*, "Fine structure constant defines visual transparency of graphene," *Science*, vol. 320, pp. 1308-1308, 2008.
- [42] C. Lee, X. Wei, J. W. Kysar, and J. Hone, "Measurement of the Elastic Properties and Intrinsic Strength of Monolayer Graphene," *Science*, vol. 321, pp. 385-388, July 18, 2008 2008.
- [43] F. Bonaccorso, L. Colombo, G. Yu, M. Stoller, V. Tozzini, A. C. Ferrari, *et al.*, "Graphene, related two-dimensional crystals, and hybrid systems for energy conversion and storage," *Science*, vol. 347, p. 1246501, 2015.
- [44] J. Xia, F. Chen, J. Li, and N. Tao, "Measurement of the quantum capacitance of graphene," *Nature nanotechnology*, vol. 4, pp. 505-509, 2009.
- [45] W.-W. Liu, S.-P. Chai, A. R. Mohamed, and U. Hashim, "Synthesis and characterization of graphene and carbon nanotubes: a review on the past and recent developments," *Journal of Industrial and Engineering Chemistry*, vol. 20, pp. 1171-1185, 2014.
- [46] J. Zhao, M. Shaygan, J. r. Eckert, M. Meyyappan, and M. H. R. mmeli, "A growth mechanism for free-standing vertical graphene," *Nano letters*, vol. 14, pp. 3064-3071, 2014.
- [47] K. Davami, M. Shaygan, N. Kheirabi, J. Zhao, D. A. Kovalenko, M. H. Rümmele, *et al.*, "Synthesis and characterization of carbon nanowalls on different substrates by radio frequency plasma enhanced chemical vapor deposition," *Carbon*, vol. 72, pp. 372-380, 2014.
- [48] Z. Bo, Y. Yang, J. Chen, K. Yu, J. Yan, and K. Cen, "Plasma-enhanced chemical vapor deposition synthesis of vertically oriented graphene nanosheets," *Nanoscale*, vol. 5, pp. 5180-5204, 2013.
- [49] J. Chen, Z. Bo, and G. Lu, "The Properties of Vertically-Oriented Graphene," in *Vertically-Oriented Graphene*, ed: Springer, 2015, pp. 11-18.
- [50] X. Shuai, Z. Bo, J. Kong, J. Yan, and K. Cen, "Wettability of vertically-oriented graphenes with different intersheet distances," *RSC Advances*, vol. 7, pp. 2667-2675, 2017.
- [51] Y.-W. Chi, C.-C. Hu, H.-H. Shen, and K.-P. Huang, "New approach for high-voltage electrical double-layer capacitors using vertical graphene nanowalls with and without nitrogen doping," *Nano letters*, vol. 16, pp. 5719-5727, 2016.
- [52] L. Zhang, Z. Sun, J. L. Qi, J. Shi, T. Hao, and J. Feng, "Understanding the growth mechanism of vertically aligned graphene and control of its wettability," *Carbon*, vol. 103, pp. 339-345, 2016.
- [53] Y. Ma, M. Wang, N. Kim, J. Suhr, and H. Chae, "A flexible supercapacitor based on vertically oriented 'Graphene Forest' electrodes," *Journal of Materials Chemistry A*, vol. 3, pp. 21875-21881, 2015.

- [54] D. Seo, S. Kumar, and K. Ostrikov, "Control of morphology and electrical properties of self-organized graphenes in a plasma," *Carbon*, vol. 49, pp. 4331-4339, 2011.
- [55] H. Conrads and M. Schmidt, "Plasma generation and plasma sources," *Plasma Sources Science and Technology*, vol. 9, p. 441, 2000.
- [56] Y. Osada, *Plasma polymerization processes* vol. 3: Elsevier Science Ltd, 1992.
- [57] K. Ostrikov, *Plasma nanoscience*: John Wiley & Sons, 2008.
- [58] Q. Wang, X. Wang, Z. Chai, and W. Hu, "Low-temperature plasma synthesis of carbon nanotubes and graphene based materials and their fuel cell applications," *Chemical Society Reviews*, vol. 42, pp. 8821-8834, 2013.
- [59] K. Ostrikov and A. Murphy, "Plasma-aided nanofabrication: where is the cutting edge?," *Journal of Physics D: Applied Physics*, vol. 40, p. 2223, 2007.
- [60] G. Francis, "The glow discharge at low pressure," *Handbuch der Physik*, vol. 22, pp. 53-208, 1956.
- [61] M. Meyyappan, "A review of plasma enhanced chemical vapour deposition of carbon nanotubes," *Journal of Physics D: Applied Physics*, vol. 42, p. 213001, 2009.
- [62] A. Bogaerts, E. Neyts, R. Gijbels, and J. van der Mullen, "Gas discharge plasmas and their applications," *Spectrochimica Acta Part B: Atomic Spectroscopy*, vol. 57, pp. 609-658, 2002.
- [63] M. Hirose, "Plasma-deposited films: kinetics of formation, composition, and microstructure," *Plasma Deposited Films*, 1986.
- [64] M. Moisan and M. Wertheimer, "Comparison of microwave and RF plasmas: fundamentals and applications," *Surface and Coatings Technology*, vol. 59, pp. 1-13, 1993.
- [65] H. Butler and G. Kino, "Plasma Sheath Formation by Radio-Frequency Fields," *Physics of Fluids (1958-1988)*, vol. 6, pp. 1346-1355, 1963.
- [66] O. A. Popov, *High density plasma sources: design, physics and performance*: Elsevier, 1996.
- [67] J. Musil, "Microwave plasma: its characteristics and applications in thin film technology," *Vacuum*, vol. 36, pp. 161-169, 1986.
- [68] J. Musil, "Deposition of thin films using microwave plasmas: present status and trends," *Vacuum*, vol. 47, pp. 145-155, 2// 1996.
- [69] Y. A. Lebedev, "Microwave discharges: generation and diagnostics," in *Journal of Physics: Conference Series*, 2010, p. 012016.

- [70] M. Moisan, C. Barbeau, R. Claude, C. M. Ferreira, J. Margot, J. Paraszczak, *et al.*, "Radio frequency or microwave plasma reactors? Factors determining the optimum frequency of operation," *Journal of Vacuum Science & Technology B*, vol. 9, pp. 8-25, 1991.
- [71] M. Wertheimer and M. Moisan, "Comparison of microwave and lower frequency plasmas for thin film deposition and etching," *Journal of Vacuum Science & Technology A*, vol. 3, pp. 2643-2649, 1985.
- [72] K. Ostrikov, "Colloquium: Reactive plasmas as a versatile nanofabrication tool," *Reviews of modern physics*, vol. 77, p. 489, 2005.
- [73] A. Fridman and L. A. Kennedy, *Plasma physics and engineering*: CRC press, 2004.
- [74] D. Hash and M. Meyyappan, "Model based comparison of thermal and plasma chemical vapor deposition of carbon nanotubes," *Journal of applied physics*, vol. 93, pp. 750-752, 2003.
- [75] Z. L. Tsakadze, K. Ostrikov, J. D. Long, and S. Xu, "Self-assembly of uniform carbon nanotip structures in chemically active inductively coupled plasmas," *Diamond and Related Materials*, vol. 13, pp. 1923-1929, 10// 2004.
- [76] M. W. Lee, M. A. S. M. Haniff, A. S. Teh, D. C. Bien, and S. K. Chen, "Effect of Co and Ni nanoparticles formation on carbon nanotubes growth via PECVD," *Journal of Experimental Nanoscience*, vol. 10, pp. 1232-1241, 2015.
- [77] A. T. Chuang, B. O. Boskovic, and J. Robertson, "Freestanding carbon nanowalls by microwave plasma-enhanced chemical vapour deposition," *Diamond and related materials*, vol. 15, pp. 1103-1106, 2006.
- [78] Wu and Yang, "Effects of Localized Electric Field on the Growth of Carbon Nanowalls," *Nano Letters*, vol. 2, pp. 355-359, 2002/04/01 2002.
- [79] M. Y. Lone, A. Kumar, S. Husain, M. Zulfequar, and M. Husain, "Growth of single wall carbon nanotubes using PECVD technique: An efficient chemiresistor gas sensor," *Physica E: Low-dimensional Systems and Nanostructures*, vol. 87, pp. 261-265, 2017.
- [80] D. Q. Duy, H. S. Kim, D. M. Yoon, K. J. Lee, J. W. Ha, Y. G. Hwang, *et al.*, "Growth of carbon nanotubes on stainless steel substrates by DC-PECVD," *Applied Surface Science*, vol. 256, pp. 1065-1068, 11/30/ 2009.
- [81] C. Bower, W. Zhu, S. Jin, and O. Zhou, "Plasma-induced alignment of carbon nanotubes," *Applied Physics Letters*, vol. 77, pp. 830-832, 2000.
- [82] G. Amaratunga, A. Putnis, K. Clay, and W. Milne, "Crystalline diamond growth in thin films deposited from a CH₄/Ar rf plasma," *Applied Physics Letters*, vol. 55, pp. 634-635, 1989.

- [83] J. J. Wang, M. Y. Zhu, R. A. Outlaw, X. Zhao, D. M. Manos, B. C. Holloway, *et al.*, "Free-standing subnanometer graphite sheets," *Applied Physics Letters*, vol. 85, pp. 1265-1267, 2004.
- [84] Z. Bo, S. Mao, Z. J. Han, K. Cen, J. Chen, and K. K. Ostrikov, "Emerging energy and environmental applications of vertically-oriented graphenes," *Chemical Society Reviews*, vol. 44, pp. 2108-2121, 2015.
- [85] M. Meyyappan, L. Delzeit, A. Cassell, and D. Hash, "Carbon nanotube growth by PECVD: a review," *Plasma Sources Science and Technology*, vol. 12, p. 205, 2003.
- [86] Y. Chen, Z. L. Wang, J. S. Yin, D. J. Johnson, and R. Prince, "Well-aligned graphitic nanofibers synthesized by plasma-assisted chemical vapor deposition," *Chemical physics letters*, vol. 272, pp. 178-182, 1997.
- [87] Y. Wu, P. Qiao, T. Chong, and Z. Shen, "Carbon Nanowalls Grown by Microwave Plasma Enhanced Chemical Vapor Deposition," *Advanced Materials*, vol. 14, pp. 64-67, 2002.
- [88] M. Chhowalla, K. Teo, C. Ducati, N. Rupesinghe, G. Amaratunga, A. Ferrari, *et al.*, "Growth process conditions of vertically aligned carbon nanotubes using plasma enhanced chemical vapor deposition," *Journal of Applied Physics*, vol. 90, pp. 5308-5317, 2001.
- [89] S. Vizireanu, S. Stoica, C. Luculescu, L. Nistor, B. Mitu, and G. Dinescu, "Plasma techniques for nanostructured carbon materials synthesis. A case study: carbon nanowall growth by low pressure expanding RF plasma," *Plasma Sources Science and Technology*, vol. 19, p. 034016, 2010.
- [90] D. H. Seo, A. E. Rider, Z. J. Han, S. Kumar, and K. K. Ostrikov, "Plasma Break-Down and Re-Build: Same Functional Vertical Graphenes from Diverse Natural Precursors," *Advanced Materials*, vol. 25, pp. 5638-5642, 2013.
- [91] M. V. Jacob, R. S. Rawat, B. Ouyang, K. Bazaka, D. S. Kumar, D. Taguchi, *et al.*, "Catalyst-free plasma enhanced growth of graphene from sustainable sources," *Nano letters*, vol. 15, pp. 5702-5708, 2015.
- [92] D. H. Seo, S. Yick, Z. J. Han, J. H. Fang, and K. K. Ostrikov, "Synergistic Fusion of Vertical Graphene Nanosheets and Carbon Nanotubes for High-Performance Supercapacitor Electrodes," *ChemSusChem*, vol. 7, pp. 2317-2324, 2014.
- [93] S. Chugh, R. Mehta, N. Lu, F. D. Dios, M. J. Kim, and Z. Chen, "Comparison of graphene growth on arbitrary non-catalytic substrates using low-temperature PECVD," *Carbon*, vol. 93, pp. 393-399, 2015.
- [94] X. Song, J. Liu, L. Yu, J. Yang, L. Fang, H. Shi, *et al.*, "Direct versatile PECVD growth of graphene nanowalls on multiple substrates," *Materials Letters*, vol. 137, pp. 25-28, 2014.

- [95] J. Sun, Y. Chen, X. Cai, B. Ma, Z. Chen, M. K. Priyadarshi, *et al.*, "Direct low-temperature synthesis of graphene on various glasses by plasma-enhanced chemical vapor deposition for versatile, cost-effective electrodes," *Nano Research*, vol. 8, pp. 3496-3504, 2015.
- [96] Y. S. Kim, K. Joo, S.-K. Jerng, J. H. Lee, E. Yoon, and S.-H. Chun, "Direct growth of patterned graphene on SiO₂ substrates without the use of catalysts or lithography," *Nanoscale*, vol. 6, pp. 10100-10105, 2014.
- [97] S. Ghosh, K. Ganesan, S. Polaki, T. Mathews, S. Dhara, M. Kamruddin, *et al.*, "Influence of substrate on nucleation and growth of vertical graphene nanosheets," *Applied Surface Science*, 2015.
- [98] K. Prasad, C. D. Bandara, S. Kumar, G. P. Singh, B. Brockhoff, K. Bazaka, *et al.*, "Effect of precursor on antifouling efficacy of vertically-oriented graphene nanosheets," *Nanomaterials*, vol. 7, p. 170, 2017.
- [99] G. Ruan, Z. Sun, Z. Peng, and J. M. Tour, "Growth of graphene from food, insects, and waste," *ACS nano*, vol. 5, pp. 7601-7607, 2011.
- [100] B. Ouyang, Y. Zhang, Z. Zhang, H. J. Fan, and R. S. Rawat, "Green synthesis of vertical graphene nanosheets and their application in high-performance supercapacitors," *RSC Advances*, vol. 6, pp. 23968-23973, 2016.
- [101] D. Wei, L. Peng, M. Li, H. Mao, T. Niu, C. Han, *et al.*, "Low Temperature Critical Growth of High Quality Nitrogen Doped Graphene on Dielectrics by Plasma-Enhanced Chemical Vapor Deposition," *ACS nano*, 2015.
- [102] M. Li, D. Liu, D. Wei, X. Song, D. Wei, and A. T. S. Wee, "Controllable Synthesis of Graphene by Plasma-Enhanced Chemical Vapor Deposition and Its Related Applications," *Advanced Science*, vol. 3, 2016.
- [103] M. Zhu, J. Wang, B. C. Holloway, R. Outlaw, X. Zhao, K. Hou, *et al.*, "A mechanism for carbon nanosheet formation," *Carbon*, vol. 45, pp. 2229-2234, 2007.
- [104] Y. S. Kim, J. H. Lee, Y. D. Kim, S.-K. Jerng, K. Joo, E. Kim, *et al.*, "Methane as an effective hydrogen source for single-layer graphene synthesis on Cu foil by plasma enhanced chemical vapor deposition," *Nanoscale*, vol. 5, pp. 1221-1226, 2013.
- [105] R. Kato, S. Minami, Y. Koga, and M. Hasegawa, "High growth rate chemical vapor deposition of graphene under low pressure by RF plasma assistance," *Carbon*, vol. 96, pp. 1008-1013, 2016.
- [106] C. Riccardi, R. Barni, M. Fontanesi, and P. Tosi, "Gaseous precursors of diamond-like carbon films in CH₄/Ar plasmas," *Chemical Physics Letters*, vol. 329, pp. 66-70, 2000.

- [107] J. Kim, M. Ishihara, Y. Koga, K. Tsugawa, M. Hasegawa, and S. Iijima, "Low-temperature synthesis of large-area graphene-based transparent conductive films using surface wave plasma chemical vapor deposition," *Applied physics letters*, vol. 98, p. 091502, 2011.
- [108] L. Cui, J. Chen, B. Yang, D. Sun, and T. Jiao, "RF-PECVD synthesis of carbon nanowalls and their field emission properties," *Applied Surface Science*, vol. 357, pp. 1-7, 2015.
- [109] M. Zhu, R. Outlaw, M. Bagge-Hansen, H. Chen, and D. Manos, "Enhanced field emission of vertically oriented carbon nanosheets synthesized by C₂H₂/H₂ plasma enhanced CVD," *Carbon*, vol. 49, pp. 2526-2531, 2011.
- [110] M. Cai, R. A. Outlaw, R. A. Quinlan, D. Premathilake, S. M. Butler, and J. R. Miller, "Fast response, vertically oriented graphene nanosheet electric double layer capacitors synthesized from C₂H₂," *Acs Nano*, vol. 8, pp. 5873-5882, 2014.
- [111] S. Ghosh, K. Ganesan, S. Polaki, S. Ilango, S. Amirthapandian, S. Dhara, *et al.*, "Flipping growth orientation of nanographitic structures by plasma enhanced chemical vapor deposition," *RSC Advances*, vol. 5, pp. 91922-91931, 2015.
- [112] Z. Yue, I. Levchenko, S. Kumar, D. Seo, X. Wang, S. Dou, *et al.*, "Large networks of vertical multi-layer graphenes with morphology-tunable magnetoresistance," *Nanoscale*, vol. 5, pp. 9283-9288, 2013.
- [113] A. Obraztsov, A. Zolotukhin, A. Ustinov, A. Volkov, Y. Svirko, and K. Jefimovs, "DC discharge plasma studies for nanostructured carbon CVD," *Diamond and Related Materials*, vol. 12, pp. 917-920, 2003.
- [114] K. Teii, S. Shimada, M. Nakashima, and A. T. H. Chuang, "Synthesis and electrical characterization of n-type carbon nanowalls," *Journal of Applied Physics*, vol. 106, pp. -, 2009.
- [115] R. Thomas and G. M. Rao, "Synthesis of 3-dimensional porous graphene nanosheets using electron cyclotron resonance plasma enhanced chemical vapour deposition," *RSC Advances*, vol. 5, pp. 84927-84935, 2015.
- [116] F.-J. Wang, L.-N. Deng, and J.-H. Deng, "Facile synthesis of differently shaped, ultrathin, and aligned graphene flakes without a catalyst for highly efficient field emission," *Applied Surface Science*, vol. 355, pp. 218-225, 2015.
- [117] Z. Tsakadze, K. Ostrikov, J. Long, and S. Xu, "Self-assembly of uniform carbon nanotip structures in chemically active inductively coupled plasmas," *Diamond and related materials*, vol. 13, pp. 1923-1929, 2004.
- [118] S. Vizireanu, B. Mitu, C. Luculescu, L. Nistor, and G. Dinescu, "PECVD synthesis of 2D nanostructured carbon material," *Surface and Coatings Technology*, vol. 211, pp. 2-8, 2012.

- [119] C. Yang, H. Bi, D. Wan, F. Huang, X. Xie, and M. Jiang, "Direct PECVD growth of vertically erected graphene walls on dielectric substrates as excellent multifunctional electrodes," *Journal of Materials Chemistry A*, vol. 1, pp. 770-775, 2013.
- [120] J. Wang, M. Zhu, R. A. Outlaw, X. Zhao, D. M. Manos, and B. C. Holloway, "Synthesis of carbon nanosheets by inductively coupled radio-frequency plasma enhanced chemical vapor deposition," *Carbon*, vol. 42, pp. 2867-2872, // 2004.
- [121] B. Boskovic, V. Golovko, M. Cantoro, B. Kleinsorge, A. Chuang, C. Ducati, *et al.*, "Low temperature synthesis of carbon nanofibres on carbon fibre matrices," *Carbon*, vol. 43, pp. 2643-2648, 2005.
- [122] S. Hofmann, B. Kleinsorge, C. Ducati, and J. Robertson, "Controlled low-temperature growth of carbon nanofibres by plasma deposition," *New journal of Physics*, vol. 5, p. 153, 2003.
- [123] S. Hofmann, C. Ducati, J. Robertson, and B. Kleinsorge, "Low-temperature growth of carbon nanotubes by plasma-enhanced chemical vapor deposition," *Applied Physics Letters*, vol. 83, pp. 135-137, 2003.
- [124] T.-o. Terasawa and K. Saiki, "Growth of graphene on Cu by plasma enhanced chemical vapor deposition," *Carbon*, vol. 50, pp. 869-874, 3// 2012.
- [125] S. Pineda, F. F. Borghi, D. H. Seo, S. Yick, M. Lawn, T. van der Laan, *et al.*, "Multifunctional graphene micro-islands: Rapid, low-temperature plasma-enabled synthesis and facile integration for bioengineering and genosensing applications," *Biosensors and Bioelectronics*, vol. 89, pp. 437-443, 2017.
- [126] K. B. Teo, D. B. Hash, R. G. Lacerda, N. L. Rupesinghe, M. S. Bell, S. H. Dalal, *et al.*, "The significance of plasma heating in carbon nanotube and nanofiber growth," *Nano Letters*, vol. 4, pp. 921-926, 2004.
- [127] B. Lewis and J. C. Anderson, *Nucleation and growth of thin films*: Academic Press, 1978.
- [128] S. Y. Kim, W. S. Choi, J.-H. Lee, and B. Hong, "Substrate temperature effect on the growth of carbon nanowalls synthesized via microwave PECVD," *Materials Research Bulletin*, vol. 58, pp. 112-116, 2014.
- [129] S. M. Ubnoske, A. S. Raut, B. Brown, C. B. Parker, B. R. Stoner, and J. T. Glass, "Perspectives on the growth of high edge density carbon nanostructures: transitions from vertically oriented graphene nanosheets to graphenated carbon nanotubes," *The Journal of Physical Chemistry C*, vol. 118, pp. 16126-16132, 2014.

- [130] I. B. Denysenko, S. Xu, J. D. Long, P. P. Rutkevych, N. A. Azarenkov, and K. Ostrikov, "Inductively coupled Ar/CH₄/H₂ plasmas for low-temperature deposition of ordered carbon nanostructures," *Journal of Applied Physics*, vol. 95, pp. 2713-2724, 2004.
- [131] S. Ghosh, S. R. Polaki, N. Kumar, S. Amirthapandian, M. Kamruddin, and K. K. Ostrikov, "Process-specific mechanisms of vertically oriented graphene growth in plasmas," *Beilstein journal of nanotechnology*, vol. 8, pp. 1658-1670, 2017.
- [132] N. Mutsukura, K. Kobayashi, and Y. Machi, "Plasma sheath thickness in radio-frequency discharges," *Journal of Applied Physics*, vol. 68, pp. 2657-2660, 1990.
- [133] N. Mutsukura, Y. Fukasawa, Y. Machi, and T. Kubota, "Diagnostics and control of radio-frequency glow discharge," *Journal of Vacuum Science & Technology A*, vol. 12, pp. 3126-3130, 1994.
- [134] H. Wei, K. Leou, M. Wei, Y. Lin, and C. Tsai, "Effect of high-voltage sheath electric field and ion-enhanced etching on growth of carbon nanofibers in high-density plasma chemical-vapor deposition," *Journal of applied physics*, vol. 98, p. 044313, 2005.
- [135] J. S. Burgess, B. R. Matis, J. T. Robinson, F. A. Bulat, F. K. Perkins, B. H. Houston, *et al.*, "Tuning the electronic properties of graphene by hydrogenation in a plasma enhanced chemical vapor deposition reactor," *Carbon*, vol. 49, pp. 4420-4426, 2011.
- [136] J. Gao, X. Song, J. Hu, S. Guo, L. Fang, F. Wu, *et al.*, "Superhydrophobic graphenic carbon nanowalls fabricated by one-step PECVD," *Materials Letters*, vol. 184, pp. 273-277, 2016.
- [137] A. Malesevic, R. Vitchev, K. Schouteden, A. Volodin, L. Zhang, G. Van Tendeloo, *et al.*, "Synthesis of few-layer graphene via microwave plasma-enhanced chemical vapour deposition," *Nanotechnology*, vol. 19, p. 305604, 2008.
- [138] A. Yoshimura, H. Yoshimura, S. C. Shin, K.-i. Kobayashi, M. Tanimura, and M. Tachibana, "Atomic force microscopy and Raman spectroscopy study of the early stages of carbon nanowall growth by dc plasma-enhanced chemical vapor deposition," *Carbon*, vol. 50, pp. 2698-2702, 2012.
- [139] K. Yu, P. Wang, G. Lu, K.-H. Chen, Z. Bo, and J. Chen, "Patterning vertically oriented graphene sheets for nanodevice applications," *The Journal of Physical Chemistry Letters*, vol. 2, pp. 537-542, 2011.
- [140] L. Jiang, T. Yang, F. Liu, J. Dong, Z. Yao, C. Shen, *et al.*, "Controlled synthesis of large-scale, uniform, vertically standing graphene for high-performance field emitters," *Advanced Materials*, vol. 25, pp. 250-255, 2013.

- [141] Y. Li and N. Chopra, "Progress in Large-Scale Production of Graphene. Part 1: Chemical Methods," *JOM*, vol. 67, pp. 34-43, 2015.
- [142] Y. Li and N. Chopra, "Progress in Large-Scale Production of Graphene. Part 2: Vapor Methods," *JOM*, vol. 67, pp. 44-52, 2015.
- [143] M. Kumar and Y. Ando, "Chemical vapor deposition of carbon nanotubes: a review on growth mechanism and mass production," *Journal of nanoscience and nanotechnology*, vol. 10, pp. 3739-3758, 2010.
- [144] K. Norinaga and O. Deutschmann, "Detailed kinetic modeling of gas-phase reactions in the chemical vapor deposition of carbon from light hydrocarbons," *Industrial & engineering chemistry research*, vol. 46, pp. 3547-3557, 2007.
- [145] S. Ravi and S. Vadukumpully, "Sustainable carbon nanomaterials: recent advances and its applications in energy and environmental remediation," *Journal of Environmental Chemical Engineering*, vol. 4, pp. 835-856, 2016.
- [146] M.-M. Titirici, R. J. White, N. Brun, V. L. Budarin, D. S. Su, F. del Monte, *et al.*, "Sustainable carbon materials," *Chemical Society Reviews*, vol. 44, pp. 250-290, 2015.
- [147] J. Deng, Y. You, V. Sahajwalla, and R. K. Joshi, "Transforming waste into carbon-based nanomaterials," *Carbon*, vol. 96, pp. 105-115, 2016.
- [148] L. Sun, C. Tian, M. Li, X. Meng, L. Wang, R. Wang, *et al.*, "From coconut shell to porous graphene-like nanosheets for high-power supercapacitors," *Journal of Materials Chemistry A*, vol. 1, pp. 6462-6470, 2013.
- [149] J. Gong, J. Liu, X. Wen, Z. Jiang, X. Chen, E. Mijowska, *et al.*, "Upcycling waste polypropylene into graphene flakes on organically modified montmorillonite," *Industrial & Engineering Chemistry Research*, vol. 53, pp. 4173-4181, 2014.
- [150] P. Ghosh, T. Soga, R. A. Afre, and T. Jimbo, "Simplified synthesis of single-walled carbon nanotubes from a botanical hydrocarbon: Turpentine oil," *Journal of alloys and compounds*, vol. 462, pp. 289-293, 2008.
- [151] E. Ruiz-Hitzky, M. Darder, F. M. Fernandes, E. Zatile, F. J. Palomares, and P. Aranda, "Supported graphene from natural resources: easy preparation and applications," *Advanced Materials*, vol. 23, pp. 5250-5255, 2011.
- [152] M. Kumar and Y. Ando, "Single-wall and multi-wall carbon nanotubes from camphor—a botanical hydrocarbon," *Diamond and Related Materials*, vol. 12, pp. 1845-1850, 2003.
- [153] P. R. Somani, S. P. Somani, and M. Umeno, "Planer nano-graphenes from camphor by CVD," *Chemical Physics Letters*, vol. 430, pp. 56-59, 2006.

- [154] R. A. Afre, T. Soga, T. Jimbo, M. Kumar, Y. Ando, M. Sharon, *et al.*, "Carbon nanotubes by spray pyrolysis of turpentine oil at different temperatures and their studies," *Microporous and mesoporous materials*, vol. 96, pp. 184-190, 2006.
- [155] R. A. Afre, T. Soga, T. Jimbo, M. Kumar, Y. Ando, and M. Sharon, "Growth of vertically aligned carbon nanotubes on silicon and quartz substrate by spray pyrolysis of a natural precursor: Turpentine oil," *Chemical physics letters*, vol. 414, pp. 6-10, 2005.
- [156] P. Ghosh, R. A. Afre, T. Soga, and T. Jimbo, "A simple method of producing single-walled carbon nanotubes from a natural precursor: Eucalyptus oil," *Materials Letters*, vol. 61, pp. 3768-3770, 2007.
- [157] S. S. Kawale, S. Bhardwaj, D. Kshirsagar, C. Bhosale, M. Sharon, and M. Sharon, "Thin Films of Carbon Nanomaterial from Natural Precursor by Hot Wire CVD," *Fullerenes, Nanotubes, and Carbon Nanostructures*, vol. 19, pp. 540-549, 2011.
- [158] M. Sevilla and A. Fuertes, "Graphitic carbon nanostructures from cellulose," *Chemical Physics Letters*, vol. 490, pp. 63-68, 2010.
- [159] S. Sharma, G. Kalita, R. Hirano, S. M. Shinde, R. Papon, H. Ohtani, *et al.*, "Synthesis of graphene crystals from solid waste plastic by chemical vapor deposition," *Carbon*, vol. 72, pp. 66-73, 2014.
- [160] K. V. Manukyan, S. Rouvimov, E. E. Wolf, and A. S. Mukasyan, "Combustion synthesis of graphene materials," *Carbon*, vol. 62, pp. 302-311, 2013.
- [161] A. K. Ray, R. K. Sahu, V. Rajinikanth, H. Bapari, M. Ghosh, and P. Paul, "Preparation and characterization of graphene and Ni-decorated graphene using flower petals as the precursor material," *Carbon*, vol. 50, pp. 4123-4129, 2012.
- [162] K. Bazaka, M. V. Jacob, and K. Ostrikov, "Sustainable Life Cycles of Natural-Precursor-Derived Nanocarbons," *Chemical reviews*, 2016.
- [163] D. Seo, A. Rider, S. Kumar, L. Randeniya, and K. Ostrikov, "Vertical graphene gas-and bio-sensors via catalyst-free, reactive plasma reforming of natural honey," *Carbon*, vol. 60, pp. 221-228, 2013.
- [164] D. H. Seo, S. Yick, S. Pineda, D. Su, G. Wang, Z. J. Han, *et al.*, "Single-Step, Plasma-Enabled Reforming of Natural Precursors into Vertical Graphene Electrodes with High Areal Capacitance," *ACS Sustainable Chemistry & Engineering*, vol. 3, pp. 544-551, 2015.
- [165] J. Shah, J. Lopez-Mercado, M. G. Carreon, A. Lopez-Miranda, and M. L. Carreon, "Plasma Synthesis of Graphene from Mango Peel," *ACS Omega*, vol. 3, pp. 455-463, 2018.

Chapter 3

RF Plasma Polymerization of Orange oil and Characterization of the Polymer Thin films

In order to implement polymer thin films in real applications a deep insight in the materials fundamental properties are essentially required. This chapter outlined the fabrication of polymer thin films from *Citrus sinensis* essential oil through RF plasma polymerization process and its characteristic properties. A set of samples were fabricated at various input RF power and the influence of RF power on the structural, morphological, chemical and mechanical properties were studied using appropriate characterization techniques. The outcomes of this study was reported in *S. Alancherry, K. Bazaka and M.V. Jacob, "RF plasma polymerization of orange oil and characterization of polymer thin films", J. Polymers and the environment, (2018), 26 (7), 2925-33.*

3.1 Introduction

Polymer thin films have attracted considerable research attention for their potential to advance the performance and reduce the cost of organic electronic devices, such as organic thin film transistors (OTFTs), organic photovoltaics (OPV) and organic light emitting diodes (OLEDs) [1-3]. In organic devices various types of polymeric materials are used including organic conductors, organic semiconductors and insulators. Unlike inorganic semiconductors, polymers possess weak van der Waals forces between molecules which make them flexible and hence well-suited to flexible or foldable devices [4]. Also, polymers afford easy processing conditions, versatile properties and economic viability compared to semiconductors commonly used in microelectronics. Even though significant progress has been made in increasing power conversion efficiency (>11%) of solar cells, mobility in OTFTs, and power efficiency and response time in high efficiency OLED displays, with several of these technologies being available commercially [2, 5], these technologies are yet to reach their full potential.

Plasma polymerization has emerged as one of the promising polymer thin film fabrication techniques owing to the flexible processing and unique properties of resulting plasma polymer thin films. From a process point of view, plasma polymerization is free from organic solvents and offers an easy tailoring of the physical and chemical properties of the polymer film through retention of functional groups, etching, functionalization and cross linking [6, 7]. With regard to the properties, plasma polymers exhibit a smooth, pinhole free nature with conformity, mechanical and thermal stability and good adhesion with the substrate [8]. A large body of literature has been published on the process optimization and structure-property correlation of plasma polymers derived from a variety of monomers [8-11], reporting a wide range of properties ranging from conductors to insulators [12, 13], variable refractive index [14], and hydrophilic to hydrophobic surfaces [15, 16].

Polymers derived from bio-renewable resources are very promising owing to their environmental friendliness, biodegradability and biocompatibility [17-19]. However, processing required to convert the bio-renewable resource into useful high-quality polymers typically necessitates the use of a catalyst (e.g., acid catalyst, bio-catalyst, and metal-catalyst), and is complex, multistep and time consuming [20]. On the other hand, plasma polymerization offers alternate reaction paths and

reaction mechanisms, enabling direct, one-step conversion of virtually any type of monomer [21, 22]. Highly volatile at ambient temperature and pressure, rich in hydrocarbon compounds and featuring a wide range of chemical functionalities, essential oils and their derivatives are suitable precursors for fabrication of high-quality thin films using plasma polymerization [23]. Previous studies have shown plasma polymers derived from individual components of essential oils have attractive electronic and biomedical properties [24, 25]. However, isolation of individual components may increase the complexity and expense associated with the use of this natural carbon resource.

Citrus sinensis essential oil (here after called as orange oil) is a multicomponent system principally composed of monoterpenes (97.52%), aldehydes (0.75%) and alcohols (0.58%). The major monoterpene component is limonene (94.14%) followed by myrcene (1.66%), α -pinene (0.48%) and sabinene (0.48%). Decanal (0.38%) and linalool (0.40%) are identified as the main aldehyde and alcohol components, respectively [26]. Hence, the present study investigates the synthesis and characterization of polymer thin films derived directly from multicomponent orange essential oil as-extracted from orange peel. The structural, optical, surface and mechanical properties of the films and their dependence on processing conditions, such as deposition time and applied RF power were investigated.

3.2 Experimental

The present study used a custom-made tubular plasma polymerization apparatus for fabricating plasma polymer thin films. The electromagnetic signals of frequency of 13.56 MHz is used and capacitively coupled into the system via external copper electrodes. The inter-electrode distance and the distance between monomer and the electrode were optimised to attain the best plasma stability and kept same throughout the deposition. The radio frequency power level was varied from 10 to 75 W and the films were deposited at different time intervals, i.e. 2, 5, and 10 min. The depositions were performed at pressure of 0.2 mbar. Orange essential oil obtained from Australian Botanical Products was used as the precursor. Orange essential oil predominantly composed of monoterpene limonene along with feeble percentage of alcohols and aldehydes. For each deposition, same amount of monomer (5 ml) was placed into the monomer flask, which was then evacuated prior to placement of the substrate within the polymerization cell to remove residual air. The monomer was released into the chamber

throughout deposition. Flow rate was estimated to be $32 \text{ cm}^3\text{min}^{-1}$ by the procedure outlined by Gengenbach and Griesser [27].

FTIR spectroscopy was employed to determine the chemical structure of the polymer thin films using a Perkin-Elmer Spectrum 2000 FTIR Spectrometer. Spectra were obtained in transmission mode in the region of $4000\text{--}600 \text{ cm}^{-1}$. The surface chemistry of the polymer films was analysed by X-ray photoelectron spectroscopy [28]. XPS spectrum was recorded by Specs SAGE 150 spectroscope equipped with monochromatic Al $K\alpha$ X-ray source ($h\nu=1486.6 \text{ eV}$). The spectra were recorded at a take-off angle 90° from a circular area of diameter 5 mm. The C1s peak with binding energy 285.0 eV used as the reference to eliminate the surface charging effects. The atomic concentrations were calculated using Casa XPS software. Optical properties and thickness of the films were examined over the wavelength range 200–1000 nm using a variable angle spectroscopic ellipsometer (model M-2000, J. A. Woollam Co., Inc.). Ellipsometric parameters Ψ and Δ were collected at three different angles of incidence, $\phi = 55^\circ, 60^\circ, \text{ and } 65^\circ$. In addition, the transmission data was also collected. Ψ and Δ were used to derive the optical constants based on a model of the sample built in the J.A. Woollam Inc. analysis software (WVASE32) via regression analysis. The absorption spectrum was measured using a UV-vis spectrometer (Avantes AvaSpec 2048, UV-vis spectrometer, Broomfield, CO) and the band gap was calculated using Tauc plot. Analysis of the surface morphology was undertaken using the NT–MDT NTEGRA Prima atomic force microscope in tapping mode.

Nanoindentation experiments were performed to characterise the mechanical properties of orange oil polymer thin films. Hysitron Triboscope head attached to NT–MDT NTEGRA Prima atomic force microscope was used to carry out the indentations. A Berkovich indenter (70.3° equivalent semi opening angle) was used and the instrument was calibrated using fused silica. A series of seven indentations were performed with loads ranging from 200 to 1000 μN and constant loading time of 3 s, holding time 3 s and unloading time 5 s, respectively. The indentation process was monitored and the load–displacement curves were obtained. The mechanical properties were derived from the contact area and load–displacement curve as proposed by Oliver and Pharr [29].

3.3 Results and Discussion

The diverse properties exhibited by plasma polymers make them an excellent candidate material for electronic and optoelectronic applications. Plasma polymers possess branched, randomly terminated and highly cross-linked structures due to the considerable fragmentation and rearrangement of molecular species that occurs during the deposition process. Hence these polymers display different properties compared to conventional polymer thin films [30-32]. For instance, plasma polymers show high dielectric constant compared to conventional polymers, with potential applications as gate dielectric material in TFTs [33]. Plasma polymerized dichlorotetramethyldisiloxane (pp-DCTMDS) exhibited a very high dielectric constant ($\sim 7-10$) owing to the presence of highly polarizable $-Cl$ functional group, and showed good gate dielectric performance [34]. Similarly, the layered structure created by the plasma polymerization of vinyl acetic acid and allyl amine demonstrated enhanced gate dielectric performance, characterized by high dielectric constant (5.7–6.2) attributed to the retention of polar $-COO^-$ and $-NH_3^+$ groups [35, 36]. Plasma polymer films deposited from O_2 /hexamethyldisiloxane and silicone– SiO_2 also displayed tunable dielectric properties, good interfacial characteristics with channel layers and flexibility [37, 38]. In addition, O_2 /hexamethyldisiloxane hybrid films were characterised by good transmittance of $\geq 90\%$, and low water vapour transmission rate (WVTR) of $3.6 \times 10^{-6} \text{ gm}^{-2} \text{ day}^{-1}$, suggesting they can be used as encapsulating layers for solar cells [39].

Polymers derived from bio-renewable resources, such as essential oils and plant extracts, have the potential to deliver the same valuable properties characteristic of polymers at lower economic and environmental costs, as well as enable the development of biodegradable and biocompatible materials and devices [19, 25]. Using minimally-refined input materials, e.g. essential oil rather than individual component, is particularly attractive for both reducing the cost and environmental impact of the polymer synthesis.

3.3.1 Film thickness

In order to determine the effect of deposition time on film thickness, films were fabricated at deposition times 2, 5 and 10 min at each RF power level. The Ψ and Δ values were measured using variable angle spectroscopic ellipsometer and the film thickness was calculated using optical model with Cauchy dispersion relation [40]. The transmission spectra of the polymer films at normal incidence was also collected to determine a transparent region and Cauchy model is applied to this wavelength region (400–1000nm). An initial values for the dispersion parameters $A=1.534$ and $B=0.009$ were assumed and fitted along with the thickness to estimate the best possible values for the same. It is observed that the film thickness increased linearly with deposition time, which is in good agreement with previous reported studies [41, 42]. For the deposition power of 10 W, 2 min deposition leads to a thickness of 135 nm, which increases to 675 nm for 10 min deposition, corresponding to a deposition rate of 67.5 nm/min. The samples deposited at other power levels showed similar trend of increase in film thickness with deposition time, with estimated deposition rates of 57.5 nm/min, 45.5 nm/min, and 39.5 nm/min for 25, 50 and 75 W respectively. The decrease in deposition rate with power can be explained by the competitive ablation-polymerization concept, where the process of ablation is predominant at higher RF power due to the increased rate of high energy ion bombardment [43].

3.3.2 Chemical characterization

Structurally, plasma polymers are considered to be amorphous in nature and possess a different chemical composition and chemical bonding compared with conventional counterpart polymers [44]. In order to get an insight into the chemical composition, FTIR spectra of both the films and the orange essential oil were recorded and showed in *Figure 3.1*. The major vibration peaks were assigned based on the work by Coates [45]. With regards to the FTIR spectrum of orange oil, strong bands at ~ 2920 , 2965, 2856 and 2835 cm^{-1} can be assigned to the asymmetric stretching (ν_a) and symmetric (ν_s) stretching vibrations of saturated C–H bonds. The asymmetric (δ_a) and symmetric (δ_s) bending vibrations of C–H bonds are observed at wavenumbers 1453, 1436 cm^{-1} and 1376 cm^{-1} , respectively. The vibrational peaks observed above 3000 cm^{-1} can be associated with the unsaturated C–H stretching

from =C–H and =CH₂ bonds. Whereas the peak formed around 2725 cm⁻¹ represents the C–H stretching vibration from aldehyde functional group and the corresponding C=O vibrations formed around lower wavenumber 1732 cm⁻¹. The medium intensity peak located at 1644 cm⁻¹ arose from the C=C stretching vibrations. The small peaks on either side may indicate the presence of C=C bonds conjugated with second unsaturated site. The several weak intensity peaks observed between 1300–900 cm⁻¹ may be produced from =CH bending, C–H skeletal vibration or C–H out of plane bending vibrations [46]. The two prominent peaks formed at lower wavenumbers are at 887 cm⁻¹ and 797 cm⁻¹ and can be attributed to C–H out of plane bending vibrations from mono-substituted and tri-substituted =C–H bonds [47].

Upon exposure to plasma, the reactant molecules dissociate into low molecular species (ions, free radicals, and excited species) and photons through inelastic collisions of the electrons, which gain energy from the plasma field. In general, the electron collision produces significant amounts of free radicals than ions. These radicals serve as reactive sites to form bonds with other free radicals and neutral species. Apart from electronic collisions, the vacuum ultraviolet radiation from plasma ($\lambda \sim 100\text{--}200$ nm) will result in H-abstraction, C–C bond scission, double bond formation, radical formation and oxidation [8]. However, free radicals and neutral species are considered to be contributing to polymer growth, whereas ions provide adsorbing sites for the free radicals through high energy bombardment [48].

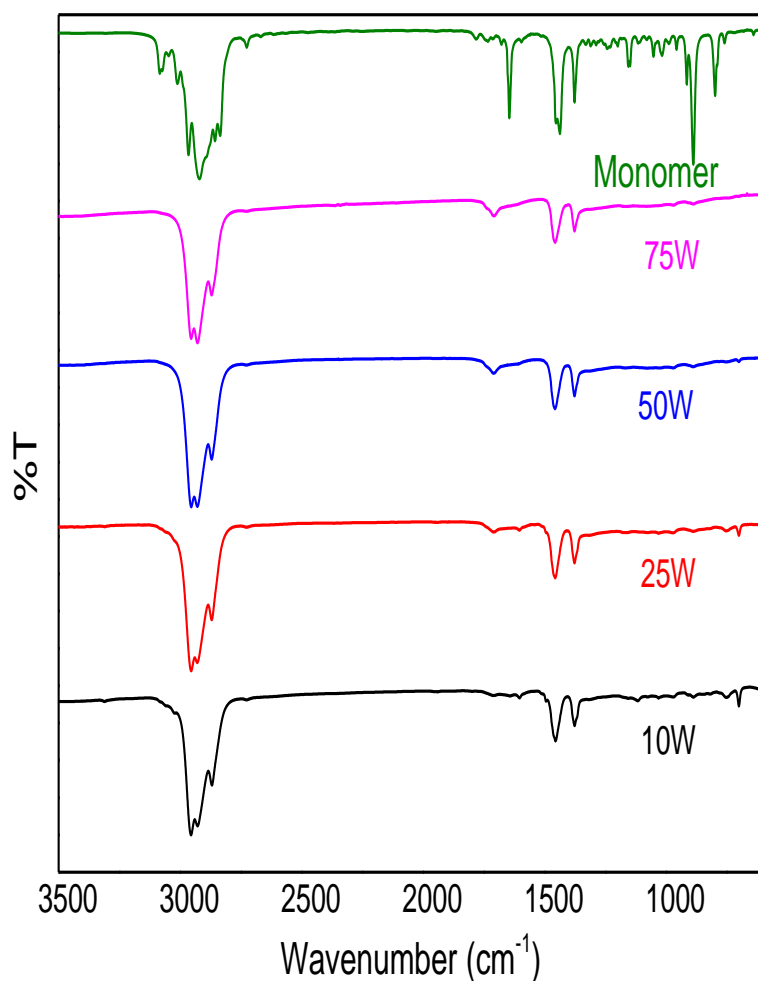


Figure 3.1 FTIR spectra of orange oil and plasma polymerized orange oil thin films fabricated at different RF input powers.

A comparison between FTIR spectra of orange oil before and after plasma exposure shows significant changes in the vibrational features. Most importantly, considerable reduction in the number of vibrational peaks was observed in the plasma polymerized orange oil polymer films. In the higher wave number region, the quartet indicating the saturated C–H stretching vibrations reformed to triplet. Also, the unsaturated C=C bonds became saturated, revealed by the disappearance of =C–H and C=C stretching vibrations. However, the samples fabricated at 10 W have retained very low yet discernible peaks of functional groups present in the original precursor, indicating potential retention of these moieties from the precursor material. By increasing the RF input power, higher dissociation of molecules is achieved, which lowers the likelihood of original precursor chemistry being retained in the polymer. Strong bands at 2954 and 2928 cm^{-1} arise from the asymmetric stretching vibrations of C–H bonds in methyl ($-\text{CH}_3$) group. The next strong intense band at 2870 cm^{-1} corresponds to symmetric

stretching vibrations. The methyl C–H asymmetric bend appeared around 1456 cm^{-1} and vibrational peak at 1376 cm^{-1} indicates the corresponding symmetric bending vibration. The weak peak at 1708 cm^{-1} related to carboxylic C=O stretch. The peak associated with O–H stretching vibration is very weak and broad (not seen in the spectrum) and occurs around 3455 cm^{-1} . The band assignments for orange oil and plasma polymerized orange oil polymer thin film are summarised in Table 3.1.

Table 3.1 Vibrational band assignments. Vibrational modes: ν_s = symmetric stretching, ν_a = asymmetric stretching, ν = stretching, δ_s =symmetric bending, δ_a =asymmetric bending, ω = out of plane bending

Group frequency (cm^{-1})	Relative intensity	Band assignment
<i>Orange oil</i>		
3083,3068,3043 and 3010	weak	$\nu(\text{C-H})$ unsaturated
2965, 2920	strong	$\nu_a(\text{C-H})$
2856, 2835	strong	$\nu_s(\text{C-H})$
2725, 1732	weak	$\nu(\text{C-H})$ and $\nu(\text{C=O})$ from aldehyde
1644	medium	$\nu(\text{C=C})$
1453, 1436	medium to strong	$\delta_a(\text{C-H})$
1376	medium	$\delta_s(\text{C-H})$
1300 to 950	weak	$\omega(\text{C-H})$ or $\omega(\text{C-H})$
957 and 914	weak	$\delta(\text{C-H})$ unsaturated
887 and 797	strong, medium	$\omega(\text{C-H})$ unsaturated
<i>Plasma polymer</i>		
2954 and 2928	strong	$\nu_a(\text{C-H})$
2870	medium	$\nu_s(\text{C-H})$
1708	weak	$\nu(\text{C=O})$
1456	weak	$\delta_a(\text{C-H})$
1376	weak	$\delta_s(\text{C-H})$

The elemental composition of the plasma reformed orange oil polymer film was further confirmed by performing the XPS analysis. A representative XPS spectrum (survey scan) of the polymer thin film fabricated at 10W in put RF power is presented in *Figure 3.2a*. The wide scan spectrum clearly detect the presence of carbon and oxygen at binding energies around 282 eV and 531 eV respectively. In addition, a minor intensity peak was also noticed about 396 eV attributed to nitrogen possibly arise from the air contamination. Furthermore, atomic fractions have calculated and carbon identified as the dominating element contributed to 86.86% of the total atomic concertation followed by oxygen 10.55% and nitrogen 2.60%.

Figure 3.2b depicts the high-resolution C1s XPS spectrum for the same sample. The C1s spectrum was fitted with four different component peaks each of which corresponding to different possible bonding environments of the carbon atoms like hydrocarbons C–C/ C–H (BE= 285.0 eV) and functional groups such as ether C–O (BE= 286.4 eV), carbonyl C=O (BE= 287.7 eV), and ester O–C=O (BE= 289.1 eV). From the fitting, the relative concentration of the different carbon bonding states with respect to the total carbon concentration within the sample was quantified. In the present case, the major contribution arise form from the hydrocarbon species holding 86.89% of the total carbon concertation. The second leading contribution came from ethers, 10.74% and the rest is estimated from carbonyl, 2.37%. Compared to high C 1s peak, high-resolution O 1s appeared to be symmetric and devoid of any distortion or fine structure to perform fitting. However, it is presumed that the O 1s peak resulted from the C–O bonds in functional groups.

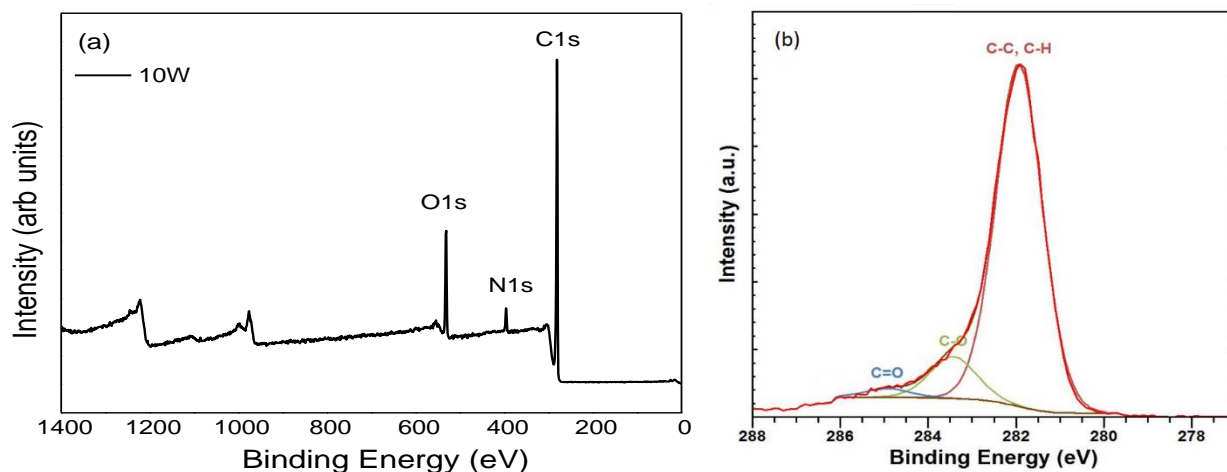


Figure 3.2 (a) XPS survey spectrum of orange oil polymer thin film fabricated at 10W RF power (b) Curve fitting for the high-resolution C 1s spectrum.

3.3.3 Optical properties

Optical properties of orange oil thin films deposited at different RF power levels (10, 25, 50 and 75W) are shown in Figure 3.3. The refractive index (Figure. 3.3a) and extinction coefficient (Figure 3.3b) were calculated from the Ψ and Δ values (wavelength from 200–1000 nm, and angle of incidence $\varphi = 55\text{--}65^\circ$ with 5° interval) by constructing an optical model that incorporated Cauchy dispersion layer, followed by Gaussian harmonic oscillator. The Cauchy dispersion relation describes the relationship between the refractive index and wavelength within the transparent wavelength region. To understand the absorption behaviour of the films, the film transmission data at normal incidence was measured using the ellipsometer and shown in Figure 3.3c. Irrespective of the deposition power, the films were found to be transparent (transparency $\sim 90\%$) above 380 nm. The refractive index profiles for samples deposited at various RF power (Figure 3.3a) resemble each other in shape and exhibited a similar behaviour. For samples fabricated at 10 W and 25 W, the refractive index varied from 1.67 to 1.54, whereas for 50 W and 75 W samples, the refractive index changes from 1.65 to 1.54 within measured spectral range. Even though a very small change in refractive index is observed within UV wavelength region (200–380 nm), it is not noticeable in the visible wavelength range. Furthermore, within UV range, the dispersion of refractive index was more prominent and attributed to the absorption in this the region. A refractive index of 1.55 is measured at 500 nm for all the samples and found to be

slightly higher than glass ($n \sim 1.5$). *Figure 3.3b* shows the extinction coefficients for the same set of samples within the same wavelength region. The plot reveals that the extinction coefficients are relatively high within the UV region and approach zero as the wavelength increases. High optical transparency and refractive index similar to that of glass suggest possible applications for these polymers as protective coating for organic devices and lenses.

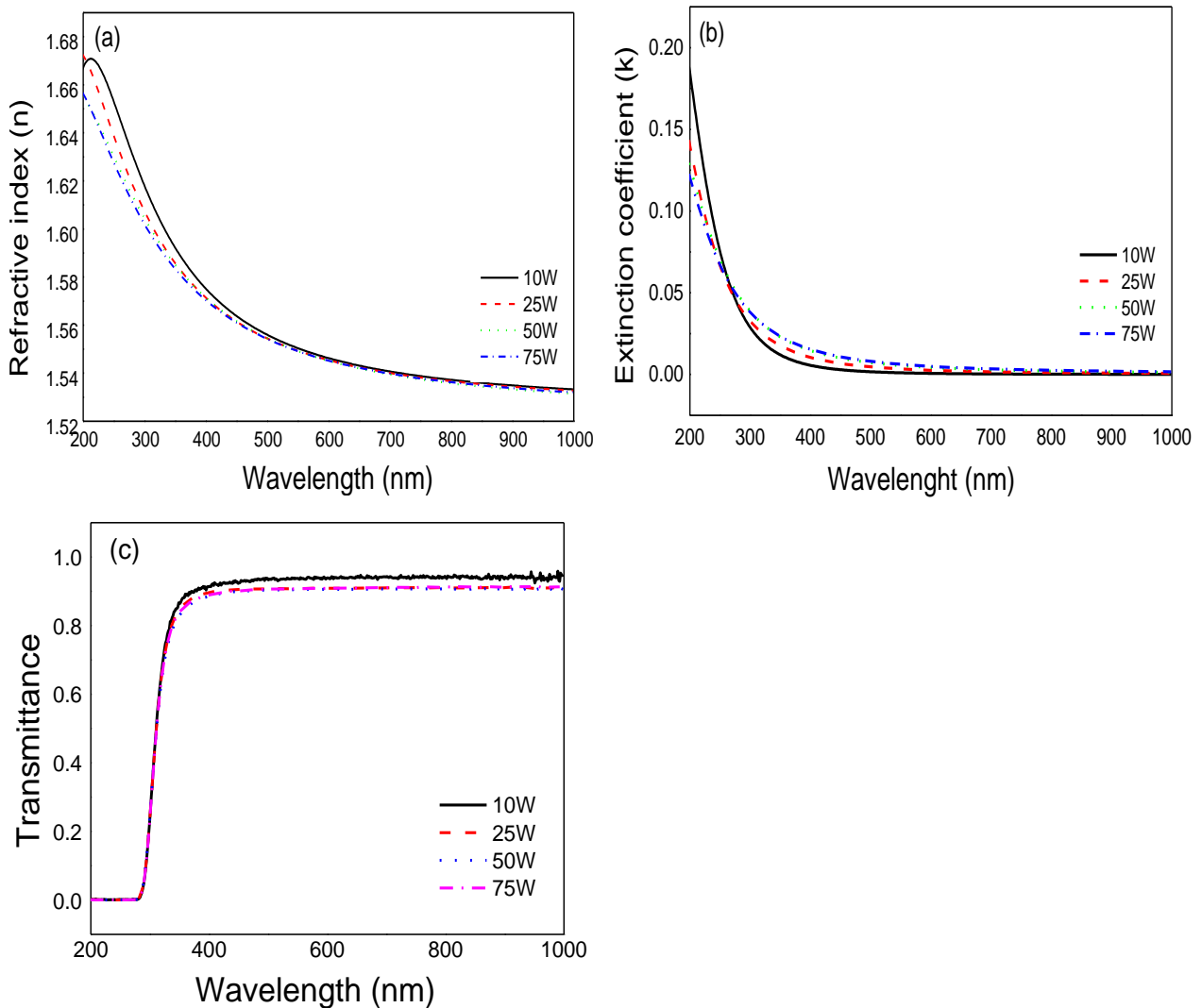


Figure 3.3 Refractive index (a), extinction coefficient (b), and (c) transmittance of polymer thin films derived from orange oil within the range 200-1000nm.

3.3.4 Optical band gap

In order to study the absorption behaviour and to determine the optical band gap of the polymer thin films, UV-visible absorption spectra were collected (plotted in *Figure 3.4*) and analysed. Irrespective of the deposition power, all the samples showed a strong single absorption peak around

295 nm. However, a difference in peak intensity was observed due to the difference in film thickness. In general, the absorption within 200–800 nm region is associated with transition of electrons from Π (bonding) to Π^* (antibonding) or from nonbonding to Π^* antibonding orbitals. Furthermore, the latter transition produces two absorption peaks and hence the absorption peak here can be assigned to Π – Π^* electronic transition. The UV-vis data also confirms that polymer thin films are transparent in the visible region. The absorption band can be used to determine the optical band gap of the material using the relation [49]

$$\alpha h\nu = A(h\nu - E_g)^m \quad (1.1)$$

where A is a constant, E_g is the optical band gap, α is the absorption coefficient (determined from the absorbance values), and m denotes the type of transmission such as direct allowed and forbidden ($m=1/2$ and $m=3/2$), indirect allowed and forbidden ($m=2$ and $m=3$) [50]. Tauc plots were generated with MATLAB program and the most linear plot is identified for different m values. It is observed that $m=1/2$ gives the most linear plot, indicating that the nature of electronic transition is direct allowed. The band gap is calculated from the plot and obtained within the range 3.55 to 3.64 eV. However, as the RF power increased, a slight decrease in optical band gap is noticed. The band gap values are observed within the insulating region, and hence the films can be implemented as flexible insulating layers in organic electronics.

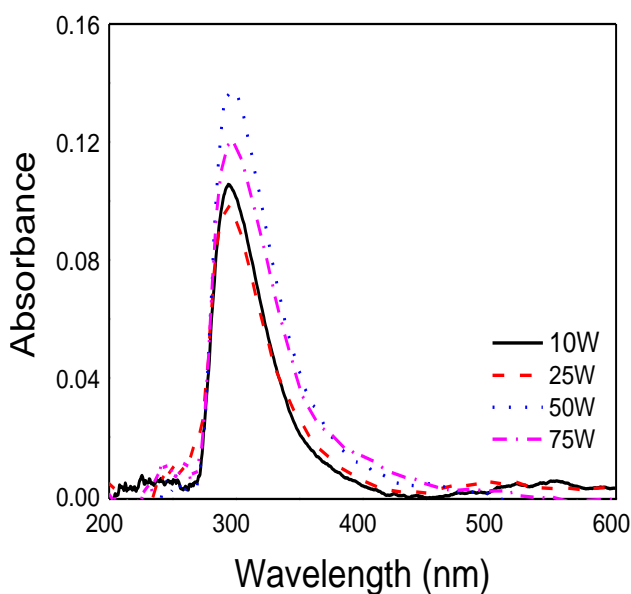


Figure 3.4 UV-vis absorption spectra of orange oil polymer thin films.

3.3.5 Surface topography

The surface topography of polymer thin films may affect the range of potential applications, and need to be precisely controlled to put in to real applications [51]. For instance, surface defects, pinholes and roughness will determine the quality of interface, which is of particular significance for the performance of electronics multilayer structures [52]. In order to obtain a quantitative description of surface topography, atomic force microscopic images were taken for samples fabricated at different RF powers (*Figure 3.5*).

The AFM images ($3\ \mu\text{m} \times 3\ \mu\text{m}$) reveal the defect-free and pinhole-free nature of film surfaces comprising peaks and valleys. At a glance, the films showed nearly similar topography except the sample made at 50 W, which exhibited comparatively broad peaks than other samples. In addition to average surface roughness (R_a), other topographical parameters, such as surface skewness (R_{sk}) and coefficient of kurtosis (R_{ku}) were determined to get a better understanding of the surface nature. It is observed that the surface roughness of the samples showed an increasing tendency upon increasing the RF power up to 50 W but then decreased for film made at 75 W RF power (Table 3.2). The average surface roughness increased from 0.62 nm to 2.19 nm with an increase in deposition power from 10 to 50 W. However, samples fabricated at 75 W showed a lower surface roughness (1.14 nm) than films made at 50W. Furthermore, one-way ANOVA test was employed to define the statistical significance of increase in surface roughness. The analysis was significant as determined by one-way ANNOVA, $F(3,16) = 123.5161$, $p < 0.001$. The statistical test resulted with a lower p value ($p < 0.001$) compared to the alpha level 0.05 used, and the $F_{\text{statistics}}$ value (123.5161) found to be greater than the F_{critical} (3.2388) which confirm that the roughness values are statistically different. The increase in the surface roughness with the deposition power can be attributed to the high energy bombardment of the energetic ions during the deposition process. The symmetry of the surface profile is represented by the statistical amplitude distribution function surface skewness (R_{sk}) which gives the variation of symmetry of the surface profile over a mean line. Ideally, a symmetrical distribution of peaks leads to zero R_{sk} . Here, the $R_{sk} > 0$ and hence the peak distribution is asymmetric, indicating the surface is dominated by peaks rather than valleys. The coefficient of kurtosis (R_{ku}) is the second distribution function that describes the surface

sharpness relative to a normal distribution. Normal distribution has a kurtosis of 3 and higher value indicates spiked surface. The samples under study exhibited a low $R_{sk} < 3$ which reveal that the surface is nearly flat. The good morphological features provide better interface characteristics and hence suggested prospective applications as gate dielectric layers in OTFTs and as buffer layers in various thin film device structures [53].

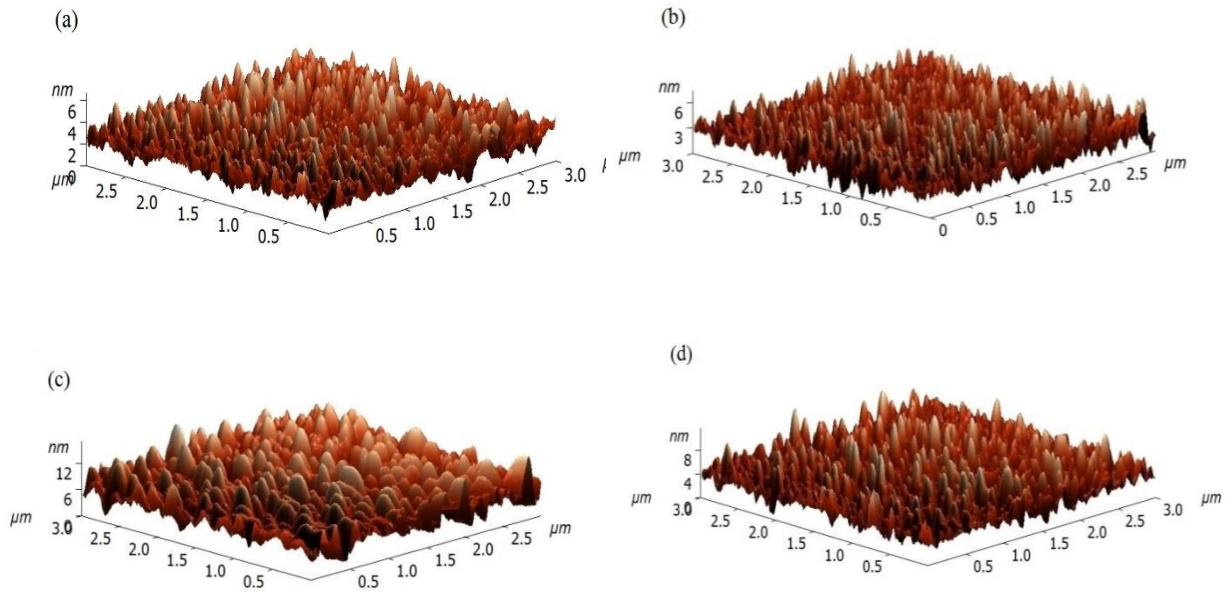


Figure 3.5 Representative AFM images ($3\mu\text{m} \times 3\mu\text{m}$) of plasma derived orange oil thin films deposited at different RF powers (a) 10 W, (b) 25 W, (c) 50 W and (d) 75 W.

Table 3.2 Surface properties of orange oil thin films.

Topographical parameters	10W	25W	50W	75W
Average surface roughness R_a (nm)	0.62	0.76	2.19	1.14
Root mean square R_q (nm)	0.79	0.96	2.49	1.51
Surface skewness R_{sk}	0.73	0.70	0.17	0.85
Coefficient of kurtosis R_{kur}	0.81	0.85	-0.24	0.97

3.3.6 Nanoindentation

The mechanical properties of the films were studied using nanoindentation technique. *Figure 3.6* is the representative image for the typical load-displacement curve recorded at a load of 1000 μN and AFM image of orange oil thin film fabricated at 25 W after indentation with different loads. The mechanical properties such as hardness and elastic modulus of the orange oil thin films were calculated by the method proposed by Oliver and Pharr and tabulated in Table 3.3 [29]. From the measurements, it can be seen that the hardness of the films increased with the deposition power. An increase in the hardness from 0.50 GPa to 0.78 GPa is noted for the polymer films when the deposition power increased from 10 to 75 W. Again, there was a statistically significant difference between hardness values as determined by the one-way ANNOVA, $F(3,24)=17.01596$, $p<0.001$. The alpha level was less than 0.05 and calculated $F_{\text{statistics}}$ value (17.01596) exceeds the F_{critical} value (3). The improvement in hardness can be attributed to the enhancement in degree of crosslinking with deposition power. In addition, under the same load, films fabricated at higher deposition power had smaller maximum depth and contact area values (Table 3.3). The elastic modulus found to increase from 10.26 GPa (10 W) to 10.33 GPa (25 W), but then decreased for 50 and 75 W samples. However, it is important to note that thus-estimated values for polymer films can be subject to several uncertainties. Most importantly, the exact determination of contact area is difficult as method does not account for the pile-up or sink-in, both of which may occur during indentation and thus lead to overestimation of hardness and elastic modulus [29, 54]. Also, the accuracy of modulus and hardness values further depend on the selection of correction factor β . Hence, the listed hardness and elastic modulus may vary from the actual values.

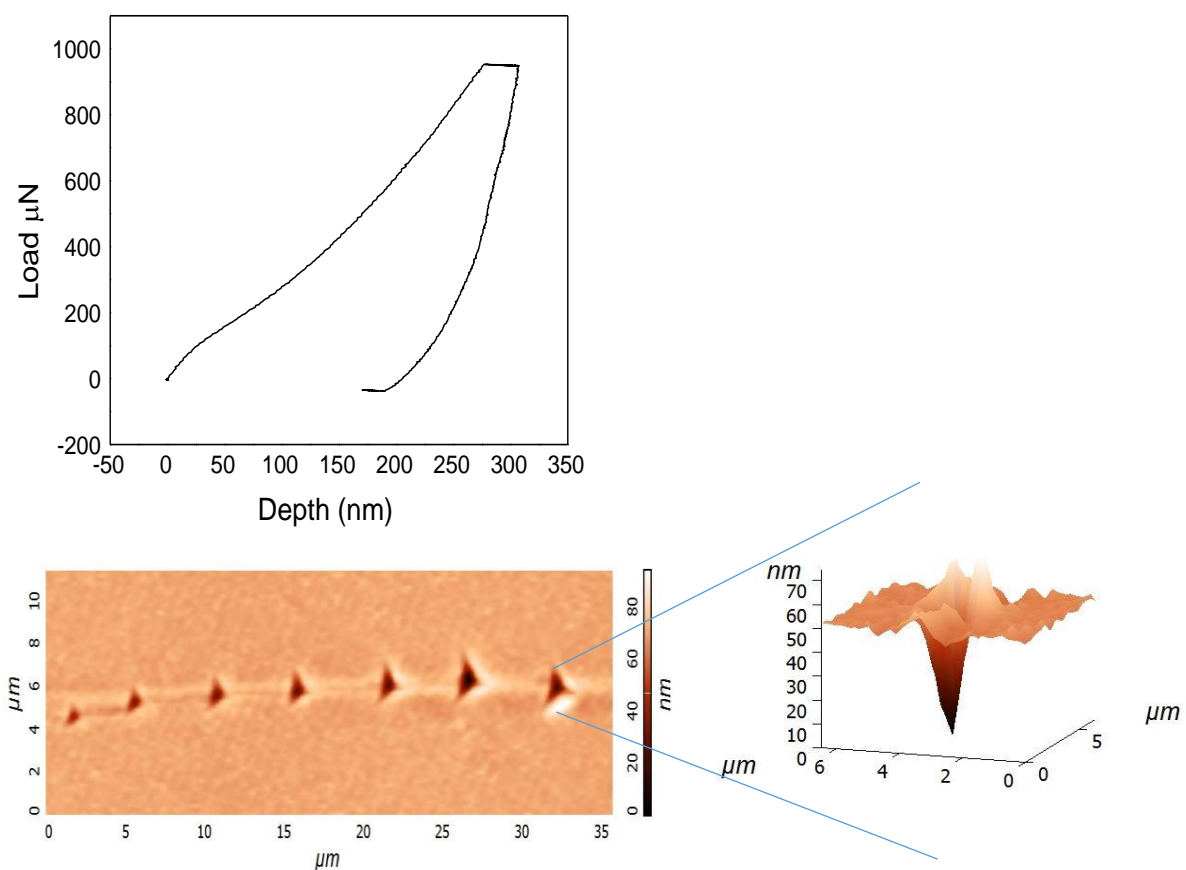


Figure 3.6 Typical loading and unloading curve (maximum load 1000 μN) and AFM image of orange oil polymer thin film fabricated at 25 W and indented with different loads.

Table 3.3 Mechanical properties of orange oil thin films.

RF power (W)	Hardness (GPa)	Elasticity (GPa)	Max depth (nm)	Contact area (nm^2)
10	0.50	10.26	180.48	1.02×10^6
25	0.58	10.33	166.98	9.27×10^5
50	0.68	9.74	156.81	7.62×10^5
75	0.78	9.38	148.64	6.49×10^5

3.4 Conclusion

Polymer thin films from orange essential oil were successfully synthesised through RF plasma polymerization technique by varying the RF power and the structural, optical, topographical and mechanical properties were studied. Under different RF power, the films were transparent in the visible region and exhibited a refractive index ~ 1.55 at 500 nm. The optical absorption is found to be direct allowed transition and the optical band gap falls within the insulating region. The topographical characteristics showed dependence on RF power, with an increase in average surface roughness with increase in deposition power. However, the 50 W sample exhibited a higher surface roughness (2.01 nm) compared to the 75 W sample (1.17 nm). The nanoindentation studies revealed that the film hardness increased upon increasing the deposition power. The film exhibited a lower hardness of 0.50 GPa at 10 W which increased to 0.78 GPa for 75 W sample. Hence, by controlling the input RF energy, the surface and mechanical properties of the orange oil film can be tailored without affecting optical properties of the films. The obtained properties suggest that these films can be implemented as insulating layers or as encapsulation coatings for flexible organic thin film devices.

REFERENCES:

- [1] B. Nketia-Yawson, H. S. Lee, D. Seo, Y. Yoon, W. T. Park, K. Kwak, *et al.*, "A Highly Planar Fluorinated Benzothiadiazole-Based Conjugated Polymer for High-Performance Organic Thin-Film Transistors," *Advanced Materials*, vol. 27, pp. 3045-3052, 2015.
- [2] Z. Zheng, S. Zhang, J. Zhang, Y. Qin, W. Li, R. Yu, *et al.*, "Over 11% Efficiency in Tandem Polymer Solar Cells Featured by a Low-Band-Gap Polymer with Fine-Tuned Properties," *Advanced Materials*, vol. 28, pp. 5133-5138, 2016.
- [3] C. Sekine, Y. Tsubata, T. Yamada, M. Kitano, and S. Doi, "Recent progress of high performance polymer OLED and OPV materials for organic printed electronics," *Science and Technology of Advanced Materials*, vol. 15, pp. 1-15, 2014.
- [4] M. S. White, M. Kaltenbrunner, E. D. Głowacki, K. Gutnichenko, G. Kettlgruber, I. Graz, *et al.*, "Ultrathin, highly flexible and stretchable PLEDs," *Nature Photonics*, vol. 7, pp. 811-816, 2013.
- [5] X. Xu, Y. Yao, B. Shan, X. Gu, D. Liu, J. Liu, *et al.*, "Electron Mobility Exceeding $10 \text{ cm}^2 \text{ V}^{-1} \text{ s}^{-1}$ and Band-Like Charge Transport in Solution-Processed n-Channel Organic Thin-Film Transistors," *Advanced Materials*, vol. 28, pp. 5276-5283, 2016.
- [6] M. Wertheimer, "Plasma Processing and Polymers: A Personal Perspective," *Plasma Chemistry and Plasma Processing*, vol. 34, pp. 363-376, 2014/05/01 2014.
- [7] B. Akhavan, K. Jarvis, and P. Majewski, "Development of oxidized sulfur polymer films through a combination of plasma polymerization and oxidative plasma treatment," *Langmuir*, vol. 30, pp. 1444-1454, 2014.
- [8] J. Friedrich, "Mechanisms of Plasma Polymerization – Reviewed from a Chemical Point of View," *Plasma Processes and Polymers*, vol. 8, pp. 783-802, 2011.
- [9] A. Michelmore, D. A. Steele, D. E. Robinson, J. D. Whittle, and R. D. Short, "The link between mechanisms of deposition and the physico-chemical properties of plasma polymer films," *Soft Matter*, vol. 9, pp. 6167-6175, 2013.
- [10] O. Kylián, A. Choukourov, and H. Biederman, "Nanostructured plasma polymers," *Thin Solid Films*, vol. 548, pp. 1-17, 2013.
- [11] C. D. Easton and M. V. Jacob, "Solubility and adhesion characteristics of plasma polymerized thin films derived from *Lavandula angustifolia* essential oil," *Journal of applied polymer science*, vol. 115, pp. 404-415, 2010.

- [12] L. Wen, D.-C. Jeong, A. Javid, S. Kim, J.-D. Nam, C. Song, *et al.*, "Conductive polythiophene-like thin film synthesized using controlled plasma processes," *Thin Solid Films*, vol. 587, pp. 66-70, 2015.
- [13] J. Ahmad, K. Bazaka, K. Vasilev, and M. V. Jacob, "Electrical conduction in plasma polymerized thin films of γ -terpinene," *Journal of Applied Polymer Science*, vol. 132, p. 42318, 2015.
- [14] H. Jiang, K. O'Neill, J. Grant, S. Tullis, K. Eyink, W. Johnson, *et al.*, "Variable refractive index polymer thin films prepared by plasma copolymerization," *Chemistry of materials*, vol. 16, pp. 1292-1297, 2004.
- [15] J. Berndt, H. Acid, E. Kovacevic, C. Cachoncinlle, T. Strunskus, and L. Boufendi, "Deposition and tuning of nanostructured hydrocarbon deposits: From superhydrophobic to superhydrophilic and back," *Journal of Applied Physics*, vol. 113, p. 063302, 2013.
- [16] B. Akhavan, K. Jarvis, and P. Majewski, "Evolution of Hydrophobicity in Plasma Polymerised 1, 7-Octadiene Films," *Plasma Processes and Polymers*, vol. 10, pp. 1018-1029, 2013.
- [17] A. A. Kehail, V. Boominathan, K. Fodor, V. Chalivendra, T. Ferreira, and C. J. Brigham, "In Vivo and In Vitro Degradation Studies for Poly (3-hydroxybutyrate-co-3-hydroxyhexanoate) Biopolymer," *Journal of Polymers and the Environment*, pp. 1-12, 2016.
- [18] S. Islam, M. R. Bhuiyan, and M. Islam, "Chitin and Chitosan: Structure, Properties and Applications in Biomedical Engineering," *Journal of Polymers and the Environment*, pp. 1-13, 2016.
- [19] P. A. Wilbon, F. Chu, and C. Tang, "Progress in renewable polymers from natural terpenes, terpenoids, and rosin," *Macromolecular rapid communications*, vol. 34, pp. 8-37, 2013.
- [20] R. T. Mathers, "How well can renewable resources mimic commodity monomers and polymers?," *Journal of Polymer Science Part A: Polymer Chemistry*, vol. 50, pp. 1-15, 2012.
- [21] A. Michelmore, P. Gross-Kosche, S. A. Al-Bataineh, J. D. Whittle, and R. D. Short, "On the effect of monomer chemistry on growth mechanisms of nonfouling PEG-like plasma polymers," *Langmuir*, vol. 29, pp. 2595-2601, 2013.
- [22] K. Bazaka, M. V. Jacob, and K. Ostrikov, "Sustainable Life Cycles of Natural-Precursor-Derived Nanocarbons," *Chemical reviews*, vol. 116, pp. 163-214, 2016.
- [23] A. Al-Jumaili, K. Bazaka, and M. V. Jacob, "Retention of Antibacterial Activity in Geranium Plasma Polymer Thin Films," *Nanomaterials*, vol. 7, p. 270, 2017.

- [24] M. V. Jacob, K. Bazaka, M. Weis, D. Taguchi, T. Manaka, and M. Iwamoto, "Fabrication and characterization of polyterpenol as an insulating layer and incorporated organic field effect transistor," *Thin Solid Films*, vol. 518, pp. 6123-6129, 2010.
- [25] K. Bazaka, M. V. Jacob, V. K. Truong, R. J. Crawford, and E. P. Ivanova, "The effect of polyterpenol thin film surfaces on bacterial viability and adhesion," *Polymers*, vol. 3, pp. 388-404, 2011.
- [26] Z. Shen, V. Mishra, B. Imison, M. Palmer, and R. Fairclough, "Use of adsorbent and supercritical carbon dioxide to concentrate flavor compounds from orange oil," *Journal of agricultural and food chemistry*, vol. 50, pp. 154-160, 2002.
- [27] T. R. Gengenbach and H. J. Griesser, "Deposition conditions influence the postdeposition oxidation of methyl methacrylate plasma polymer films," *Journal of Polymer Science Part A: Polymer Chemistry*, vol. 36, pp. 985-1000, 1998.
- [28] K. S. Siow, L. Britcher, S. Kumar, and H. J. Griesser, "Deposition and XPS and FTIR analysis of plasma polymer coatings containing phosphorus," *Plasma Processes and Polymers*, vol. 11, pp. 133-141, 2014.
- [29] W. C. Oliver and G. M. Pharr, "Measurement of hardness and elastic modulus by instrumented indentation: Advances in understanding and refinements to methodology," *Journal of materials research*, vol. 19, pp. 3-20, 2004.
- [30] C. Zhang, J. Wyatt, and D. Weinkauff, "Carbon dioxide sorption in conventional and plasma polymerized methyl methacrylate thin films," *Polymer*, vol. 45, pp. 7665-7671, 2004.
- [31] J. Wang, K. Neoh, and E. Kang, "Comparative study of chemically synthesized and plasma polymerized pyrrole and thiophene thin films," *Thin Solid Films*, vol. 446, pp. 205-217, 2004.
- [32] A. Al-Jumaili, S. Alancherry, K. Bazaka, and M. V. Jacob, "The electrical properties of plasma-deposited thin films derived from *Pelargonium graveolens*," *Electronics*, vol. 6, p. 86, 2017.
- [33] J.-S. Lim, P.-K. Shin, B.-J. Lee, and S. Lee, "Plasma polymerized methyl methacrylate gate dielectric for organic thin-film transistors," *Organic Electronics*, vol. 11, pp. 951-954, 2010.
- [34] Y. Xu, P. R. Berger, J. Cho, and R. B. Timmons, "Pulsed plasma polymerized dichlorotetramethyldisiloxane high-k gate dielectrics for polymer field-effect transistors," *Journal of applied physics*, vol. 99, p. 014104, 2006.
- [35] W.-J. Yoon, D. Bhattacharyya, R. B. Timmons, and P. R. Berger, "Plasma-polymerized multistacked bipolar gate dielectric for organic thin-film transistors," *Organic Electronics*, vol. 11, pp. 1767-1771, 2010.

- [36] D. Bhattacharyya, W. J. Yoon, P. R. Berger, and R. B. Timmons, "Plasma-Polymerized Multistacked Organic Bipolar Films: A New Approach to Flexible High- κ Dielectrics," *Advanced Materials*, vol. 20, pp. 2383-2388, 2008.
- [37] C. H. Tsai, Y. S. Li, I. Cheng, and J. Z. Chen, "O₂/HMDSO-Plasma-Deposited Organic–Inorganic Hybrid Film for Gate Dielectric of MgZnO Thin-Film Transistor," *Plasma Processes and Polymers*, vol. 11, pp. 89-95, 2014.
- [38] L. Han, K. Song, P. Mandlik, and S. Wagner, "Ultraflexible amorphous silicon transistors made with a resilient insulator," *Applied Physics Letters*, vol. 96, p. 042111, 2010.
- [39] Y.-S. Li, C.-H. Tsai, S.-H. Kao, I.-W. Wu, J.-Z. Chen, C.-I. Wu, *et al.*, "Single-layer organic–inorganic-hybrid thin-film encapsulation for organic solar cells," *Journal of Physics D: Applied Physics*, vol. 46, p. 435502, 2013.
- [40] J. Woollam, "Guide to Using WVASE32 Spectroscopic Ellipsometry Data Acquisition and Analysis Software. JA Woollam Co," ed: Inc, 2005.
- [41] J. Ahmad, K. Bazaka, and M. V. Jacob, "Optical and surface characterization of radio frequency plasma polymerized 1-isopropyl-4-methyl-1, 4-cyclohexadiene thin films," *Electronics*, vol. 3, pp. 266-281, 2014.
- [42] C. D. Easton, M. V. Jacob, and R. A. Shanks, "Fabrication and characterisation of polymer thin-films derived from cineole using radio frequency plasma polymerisation," *Polymer*, vol. 50, pp. 3465-3469, 2009.
- [43] G. P. Lopez and B. D. Ratner, "Substrate temperature effects on film chemistry in plasma deposition of organics. I. Nonpolymerizable precursors," *Langmuir*, vol. 7, pp. 766-773, 1991.
- [44] F. F. Shi, "Recent advances in polymer thin films prepared by plasma polymerization synthesis, structural characterization, properties and applications," *Surface and Coatings Technology*, vol. 82, pp. 1-15, 1996.
- [45] J. Coates, "Interpretation of infrared spectra, a practical approach," in *Encyclopedia of analytical chemistry*, R. A. Meyers, Ed., ed. Chichester: John Wiley & Sons Ltd, 2000.
- [46] R. B. Zapata, A. L. Villa, C. M. de Correa, and C. T. Williams, "In situ Fourier transform infrared spectroscopic studies of limonene epoxidation over PW-Amberlite," *Applied Catalysis A: General*, vol. 365, pp. 42-47, 2009.
- [47] H. Schulz, B. Schrader, R. Quilitzsch, and B. Steuer, "Quantitative analysis of various citrus oils by ATR/FT-IR and NIR-FT Raman spectroscopy," *Applied spectroscopy*, vol. 56, pp. 117-124, 2002.

- [48] A. Michelmore, D. A. Steele, J. D. Whittle, J. W. Bradley, and R. D. Short, "Nanoscale deposition of chemically functionalised films via plasma polymerisation," *RSC Advances*, vol. 3, pp. 13540-13557, 2013.
- [49] J. Tauc, "Optical properties and electronic structure of amorphous Ge and Si," *Materials Research Bulletin*, vol. 3, pp. 37-46, 1968.
- [50] Z. Z. You and G. J. Hua, "Refractive index, optical bandgap and oscillator parameters of organic films deposited by vacuum evaporation technique," *Vacuum*, vol. 83, pp. 984-988, 2009.
- [51] J. Tang, C. Lee, M. Chan, and S. Lee, "Enhanced electrical properties of pentacene-based organic thin-film transistors by modifying the gate insulator surface," *Applied Surface Science*, vol. 254, pp. 7688-7692, 2008.
- [52] S. E. Fritz, T. W. Kelley, and C. D. Frisbie, "Effect of dielectric roughness on performance of pentacene TFTs and restoration of performance with a polymeric smoothing layer," *The Journal of Physical Chemistry B*, vol. 109, pp. 10574-10577, 2005.
- [53] J. Li, D. Liu, Q. Miao, and F. Yan, "The application of a high-k polymer in flexible low-voltage organic thin-film transistors," *Journal of Materials Chemistry*, vol. 22, pp. 15998-16004, 2012.
- [54] M. R. VanLandingham, J. S. Villarrubia, W. F. Guthrie, and G. F. Meyers, "Nanoindentation of polymers: an overview," in *Macromolecular symposia*, 2001, pp. 15-44.

Chapter 4

Towards Sophisticated Morphology Control of Natural Resource-derived Vertical Graphenes: Experimental and Simulation Insights

Strong interest in vertically-oriented graphemes largely stems from their unique surface morphology, which makes them well suited for such applications as field emitters, gas and biomolecule sensors, and electrodes in supercapacitors to name but a few. Recently, minimally-processed raw and waste biomass have been discussed as a promising low-cost, abundant source of carbon for the synthesis of these materials via plasma-enhanced chemical vapour deposition (PECVD). However, the extent to which the multicomponent chemical nature of such a precursor would affect the ability to control the structural and morphological features of graphenes using traditional control mechanisms such as RF power, hydrogen flow rate and deposition duration is not well understood. In this chapter, the evolution of surface morphology of graphene derived from cold-pressed *Citrus sinensis* oil, via catalyst-free radio frequency PECVD is investigated using experimental analysis, standard characterisation techniques such as Raman spectroscopy, scanning electron microscopy and X-ray photoelectron spectroscopy, and numerous advanced analytical techniques such as distributions of fractal dimensions, 2D FFT transforms, Hough transformation spectra and others. Detailed growth simulations by an ad hoc model based on a large number of interaction elemental processes was implemented to insure deep insight into the processes. *S. Alancherry, M. Jacob, K. Prasad, J. Joseph, O. Bazaka, R. Neupane, O. Varghese, O. Baranov, S. Xu, I. Levchenko, and K. Bazaka, "Towards Sophisticated Morphology Control of Natural Resource-derived Vertical Graphenes: Experimental and Simulation Insights", has been submitted to Journal of Materials Chemistry A.*

4.1 Introduction

Among graphene-based materials, surface-grown vertically oriented graphene nanosheets or nanoflakes hold promise for a wide range of applications, which include but not limited to field emitters [1, 2], gas and biomolecule sensors [3, 4], biotechnological devices [5, 6], catalysis [7, 8], electrodes in supercapacitors [9, 10], and lithium ion batteries [11, 12], materials for storage [13, 14], nanoscale electronic devices [15, 16] and materials for space technologies [17-19]. These applications rely on several inherent properties of this type of graphene [20, 21]. These include vertical orientation of flakes on the surface, excellent mechanical stability, open intersheet space that allows exceptionally high surface contact area for ion and atom diffusion and transport, superior in-plane conductivity for charge transport [14, 22] and exposed long and sharp edges that enable high chemical reactivity [21, 23] as well as facilitate mechanical killing of pathogenic bacteria [24].

The specific performance of this network of self-supported graphene layers is highly dependent on its structural and morphological characteristics, including dimensions of the flakes, sharpness and length of the edges, degree of 3D interconnectivity between individual sheets, spacing between sheets, presence of structural defects and doping, and others [23, 25, 26]. Typically, these characteristics are controlled during material synthesis by tuning the processing conditions such as temperature, residence time, and gas chemistry (e.g. ratio of methane to hydrogen) and flow rate, and by using post-fabrication treatments, such as using plasma to sharpen and thin the edges [27, 28].

Recently, there has been a growing interest in the use of minimally-processed raw and waste biomass resources as precursors for the synthesis of graphene and other nanoscale materials [29-31], with the primary objective to reduce the environmental footprint of this family of materials and reduce the cost and complexity of their synthesis [32]. Materials from food waste and oils to plant and animal matter have been converted to graphenes with some success, with most examples using catalytic thermal chemical vapour deposition (CVD) where temperatures in excess of 1000 °C are used to break down the precursor into carbon atoms, which are then reassembled into graphene sheets on the surface of nickel or copper catalyst support [33]. This synthesis route is lengthy (reaching several hours) [34, 35],

and most often results in the formation of horizontal graphene sheets which then have to be transferred from the substrate [36].

Plasma enhanced chemical vapour deposition (PECVD) presents a far more attractive environment for the growth of vertically-oriented carbon nanostructures, providing a wide range of possible control mechanisms for the synthesis and assembly of structures with diverse geometry and chemical characteristics. These controls include conventional mechanisms, such as controlling gas chemistry, substrate temperature, and time of treatment, as well as those unique to plasma environment, such as presence of highly chemically-reactive species [37, 38], e.g. energetic electrons and ions, and electric fields, and the ability to control fluxes of energy and matter using external electric and magnetic fields [39]. The plasma sheath and the intense ion fluxes that originate at the sheath region direct the incoming carbon bearing species to the tips of the growing nanoassemblies, strongly favouring vertical over lateral growth [40]. Importantly, in PECVD, it is possible to grow vertically-oriented graphenes directly on the substrate of choice, e.g. silicon wafer, in the absence of conventional catalytic support. Furthermore, it is possible to use these various control mechanisms for the synthesis and post-processing within the same technological run.

There is a growing body of evidence that suggests PECVD to be highly amenable to fabrication of large-area vertically-oriented graphenes at scales needed to realise real-life devices, including directly from natural resources, particularly from inherently volatile precursors such as essential oils that produce vapours without the need for heating or carrier gas [41, 42].

However, while these results are certainly promising, our understanding of the major processes that govern graphene morphology at these larger scales is limited, particularly in the context of the use of chemically-complex, multi-component precursors [43]. Indeed, the effects of plasma process parameters on nucleation, propagation and termination stages of vertical graphene growth are conventionally described in terms of *nanoflake height*, *nanoflake length*, and *nanoflake surface density* [44]. However, at larger scales of cm, these traditional parameters may not provide adequate representation of long-order characteristics of vertically-oriented graphenes yet these long-order morphological features may define how the graphene network would behave.

In this chapter, a comprehensive characterization of short and long-order morphological features of arrays of vertically-oriented graphenes as a single system is conducted, to understand the extent to which the multicomponent chemical nature of carbon precursor would affect the structural and morphological features and evolution of surface morphology of graphenes using traditional control mechanisms. A catalyst free radio frequency PECVD have used where RF power (i), hydrogen flow rate (ii), and deposition duration (iii) were varied. A low-value 'green' product, i.e. cold-pressed *Citrus sinensis* oil, which is a by-product of orange juice production by centrifugation was selected as a model precursor.

The remainder of the chapter is organized as follows. Firstly, the core principles of growing complex nanostructures in plasmas is described. Then, the experimental setup used to synthesise the arrays of vertical graphene nanoflakes in low-temperature plasma is outlined. Next, the results of the Raman characterization that reflects the chemical properties and structural characteristics of individual nanoflakes. Then the results of a comprehensive characterization of the morphological features of the arrays as a single system, which is the main focus of this chapter. Finally, successfully related the experimental results to a model that allows simulation of nanoflake growth and modelling of principal characteristics of thus-produced graphenes.

4.2. Methods

4.2.1 Framework for growth processes in plasmas

Figure 4.1 illustrates the core framework for growing complex nanostructures in plasmas, which is based on a step-by-step transition from plasma-enhanced treatment of millimeter- through micrometer- to nanometer size areas, with each consecutive stage using features formed or grown during the previous stage. Fundamentally, each stage comprises three main phases, which can be classified in accordance with the rate of change in the geometrical shape of the treated surface. The first phase is associated with events that transform the base surface into a substrate suitable for material growth. Since there is typically no geometry change that is required at this phase, and the main purpose of the phase is to change atomic bonding characteristics of the surface to increase e.g. the likelihood of adhesion

interactions, this phase is called “functionalization” and is described as a change in material structure without changing its geometry. Examples of events that take place during this phase include generation of vacancies and interstitial atoms; formation of precipitates transformed to screw and edge dislocations; ballistic mixing and thermal segregation of material phases; heating and grain coalescence, which are used later as adsorption sites; and others. The second stage covers all the processes of additive growth of structures on the base surface. For the case of vertically-oriented graphenes, this phase describes the growth of graphene sheets orthogonal to the surface of the substrate. Next phase, denoted as “trimming”, includes processes that result in removal of excess material, such as atoms of amorphous carbon (α -C). Then, next cycle of the construction can begin, and the possible transition is shown by the arrow pointed from the stage 1 to stage 2 in *Figure 4.1*. During this phase, the surface or sharp edges of vertically-oriented graphene sheets can serve as the base on which nanostructure growth can take place. This sequential growth is in good agreement with experimentally observed evolution of nanocrystalline carbon film morphology, which involved a sequence of such phases as formation of diamond-like particles on the surface, formation of ultra-thin graphite flakes parallel to the surface, nucleation and growth of vertically-oriented graphene sheets on stacked horizontal flakes, growth vertically-oriented graphene sheets accompanied by a continuing decrease in the structural defect density, and, lastly, nucleation of carbon nanotubes on the surface of vertically-oriented flakes driven by the internal stress generated at the tips of these flakes [45]. In principle, these nanotubes can also be trimmed and undergo the following doping or tree-like structure modification.

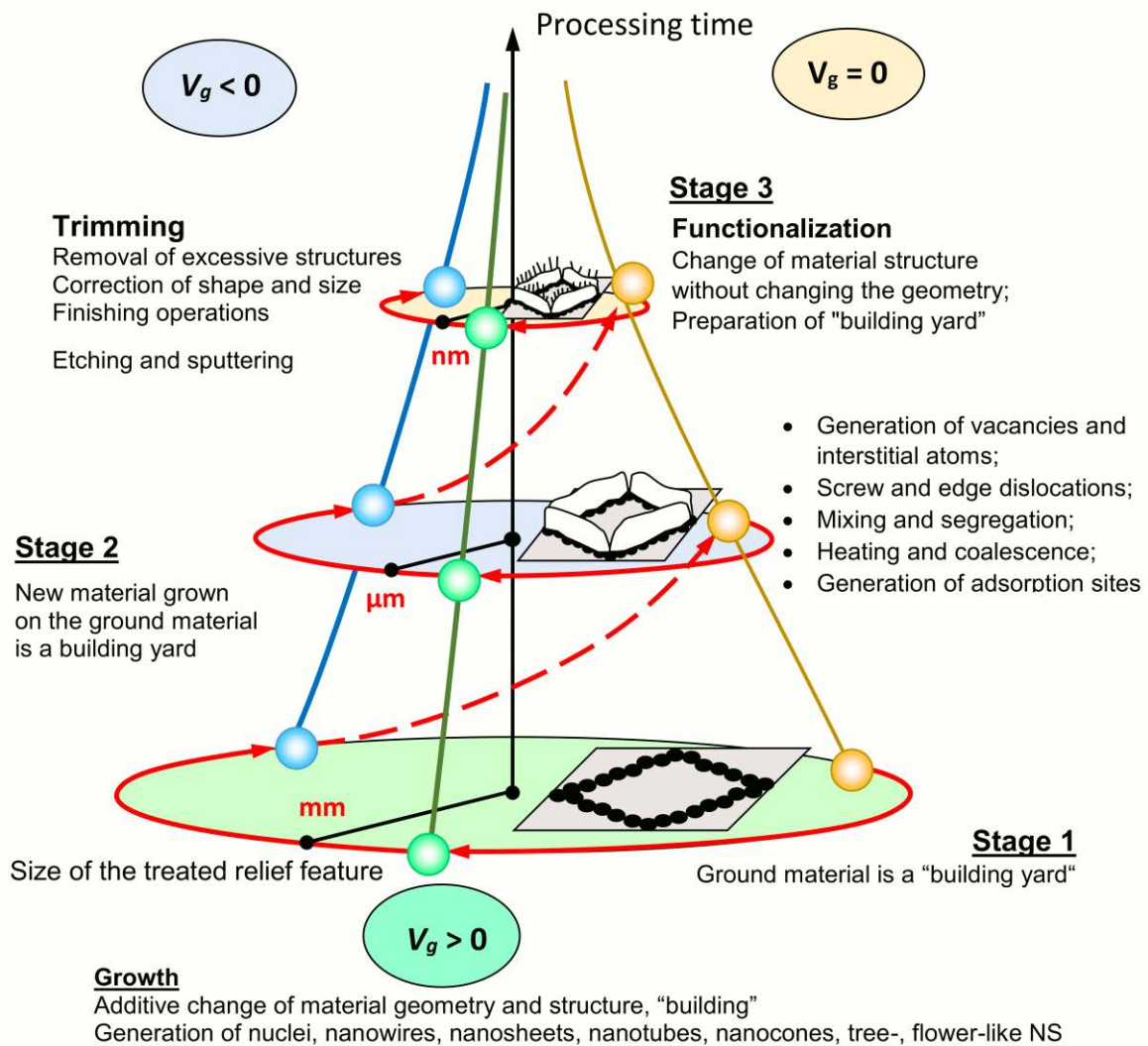


Figure 4.1 A strategy for growing complex nanostructures based on a step-by-step transition from plasma-enhanced treatment of millimetre- through micrometre- to nanometre-size areas. Each stage comprises three main phases classified according to the rate of change in the geometrical shape of the treated surface. The first phase is associated with that transform the base surface into a substrate suitable for material growth; the second stage covers all the processes of additive growth of structures on the base surface. For the case of vertically-oriented graphenes, this phase describes the growth of graphene sheets orthogonal to the surface of the substrate. The third phase, denoted as "trimming", includes processes that result in removal of excess material, such as atoms of amorphous carbon (α -C). Then, next cycle of the construction can begin, and the possible transition is shown by the arrow pointed from the stage 1 to stage 2.

4.2.2 Experimental

The fabrication of graphene was carried out using a custom-made quartz tube RF-PECVD system. *Figure 4.2* depicts the schematic of the experimental set-up. Silicon wafers (N-type) with a size of 1 cm × 1 cm coated with 500 nm-thick thermally oxidized SiO₂ layer were used as substrates for graphene growth. Prior to loading into the deposition reactor, substrates were cleaned by sonication with acetone (5 min), isopropanol (5 min) and finally dried with N₂ gas. Cleaned silicon substrates were loaded into an alumina boat and arranged at the middle of the reactor. The tube was then pumped down to a base pressure of 0.03 mbar and the substrate was heated up to 750 °C. Following this, hydrogen gas was flown into the system at a flow rate of 10 sccm, and the system pressure was adjusted to 0.3 mbar. The RF energy from *Navio* RF generator (13.56 MHz, 1.2 kW max) was capacitively coupled to the quartz tube reactor via an impedance matching network and two external copper electrodes. Prior to deposition of graphene, plasma was ignited at 500 W and silicon substrates were pre-etched for 1 min to remove any contaminants from the substrate surface. Cold-pressed *Citrus sinensis* oil (hereafter referred to as orange oil) was acquired from Australian botanical products, Australia, and used as the precursor source without further modification. Highly volatile at room temperature and pressure, orange essential oil is primarily composed of limonene (94.14%) and other monoterpenes, e.g. myrcene (1.66%), α -pinene (0.48%) and sabinene (0.48%) [46], making the oil a rich source of hydrocarbon compounds. For each deposition, 3 ml of essential oil was used and the vapour flow was controlled using a needle valve.

To study the evolution of short- and long-order morphological features of arrays of vertically-oriented graphenes as a single system, the study assumed some initial set of plasma process parameters as follows:

- *Phase 1*: Input RF power varied from 300 W to 500 W to study the effect of deposition power. The process kept the hydrogen flow rate at 10 sccm, deposition temperature at 750 °C and duration of deposition at 4 min.

- *Phase 2:* The RF power fixed at a single value and the hydrogen flow rate was varied gradually from 10 to 50 sccm. The growth temperature and duration were retained same as in Phase 1.
- *Phase 3:* The RF power and hydrogen flow rate were fixed, and the deposition time varied successively from 2 min to 8 min. The deposition temperature remained at 750 °C.

The structural evolution of all the samples grown under various plasma conditions was investigated by confocal laser Raman spectroscopy (*Witec*, 532 nm laser). The morphology of graphene samples were analysed by scanning electron microscope (Carl Zeiss, EV018, Germany). The elemental analysis was done using X-ray photoelectron spectroscopy (XPS) (Physical Electronics Model 5700 with an Al x-ray source). A Multipak™ software was used for data processing. The morphology was characterised by the Gwyddion© visualization and analysis free software (released by GPL license).

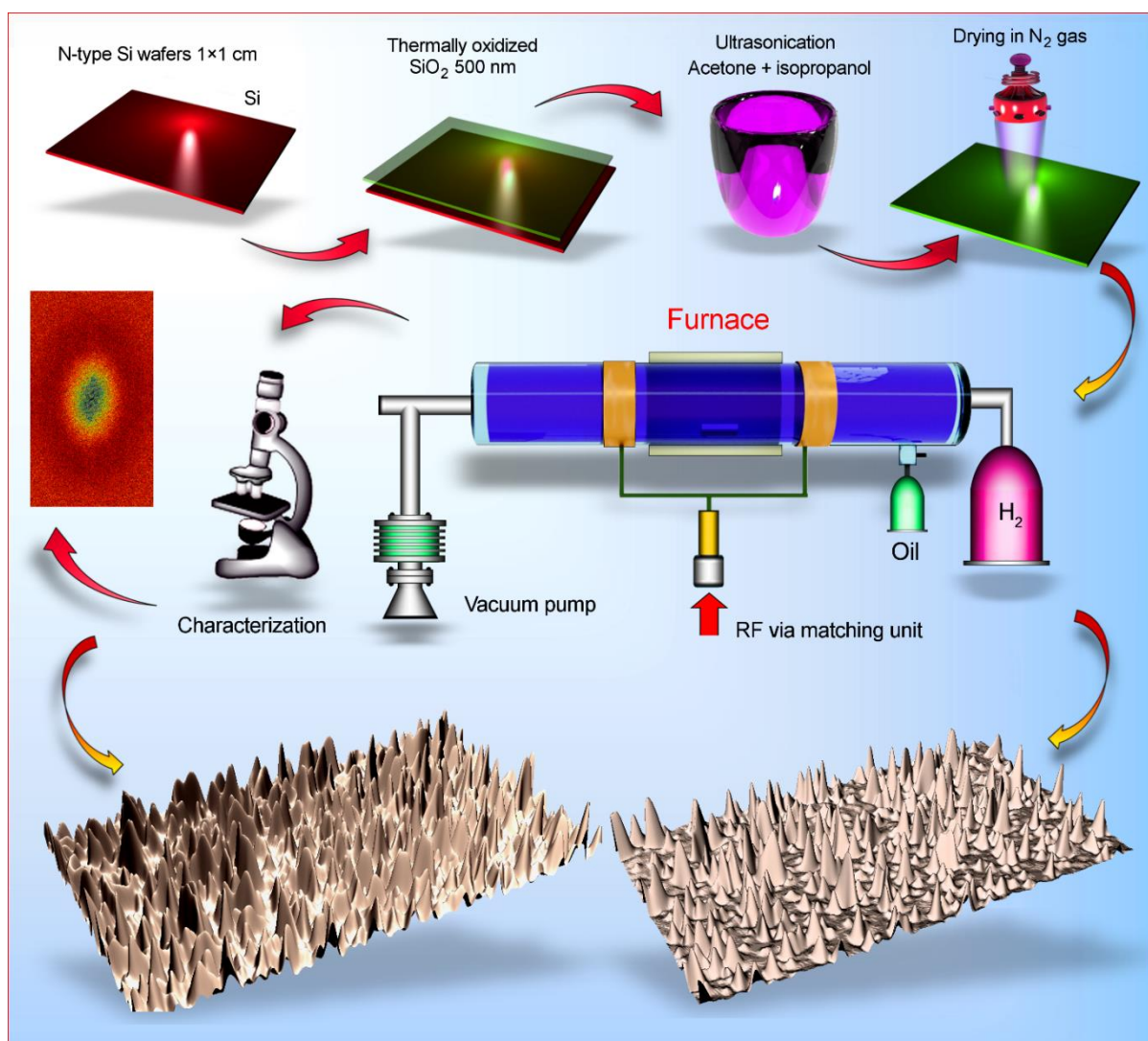


Figure 4.2 Top panel: Experimental set-up for growth of networks of vertically-oriented graphene nanosheets in low-temperature plasmas. Surface characterization was performed using traditional suit of microscopy and spectroscopy methods, and analytical approaches to investigate various morphological characteristics such as fractal dimensions, Minkowski connectivity, and others. Bottom panel: Three-dimensional morphology patterns of the dense (left) and rarefied (right) arrays of vertical graphenes.

4.3 Experimental Results and Discussion

4.3.1 Effect of RF power, gas flux and growth time on structure of graphene

The input RF energy influences the growth of graphene mainly in two ways. Most importantly, an increase in RF power enhances the electric field intensity within the plasma, which triggers an acceleration of charged entities (electrons and ions) and creates a large number of reactive species through highly energetic inelastic plasma collisions [47, 48]. Besides, the electric field acting normal to the substrate is critical to the formation of nucleation sites on the substrate and to the stacking of growth species in vertical direction [49]. On the other hand, it is also noted that higher RF power elevates the atomic hydrogen concentration in the plasma volume that causes competitive etching of the deposited carbon to become a dominant process, hence leading to a decline in the growth rate [49, 50]. Therefore, for efficient growth, the input RF power need to be precisely controlled.

Figure 4.3a represents Raman spectra of graphene samples fabricated at three different RF powers of 300, 400 and 500 W. Irrespective of the deposition power, Raman spectra of all samples show three distinct peaks indexed around 1335 cm^{-1} , 1570 cm^{-1} and 2675 cm^{-1} attributed to the fundamental D, G and 2D bands indicating the formation of multilayer graphene. The D' peak is intercalated along with the G peak and forms a shoulder around 1604 cm^{-1} . Apart from this, the spectra also show small intensity D+G and 2D' peaks at respective wave numbers of 2930 cm^{-1} and 3230 cm^{-1} . The relative intensity ratios of these bands were calculated and plotted in *Figure 4.3d*. The I_D/I_G ratio remains low at ~ 0.65 for all these samples that represented a low defect structure mainly composed of sp^2 -hybridized carbon atoms. Nevertheless, an increase in I_D/I_G was noticed with increasing RF power, probably due to the disorder that arises from the high-energy ionic collisions. On the other hand, with the increase in RF power, the I_{2D}/I_G ratio decreased from 0.91 to 0.78, indicating the formation of a few layer graphene.

The atomic species of hydrogen plays two key roles in the growth of graphene. First, as an initiator to trigger the dehydrogenation of carbon bearing free radicals that flourish the plasma volume with active species. Second, as an etching agent that etches away the amorphous carbon and cleaves

“weak” carbon-carbon bonds from the surface of growing graphene. During the growth, these two processes compete with each other and serve as a control for the rate and mechanism of graphene growth.

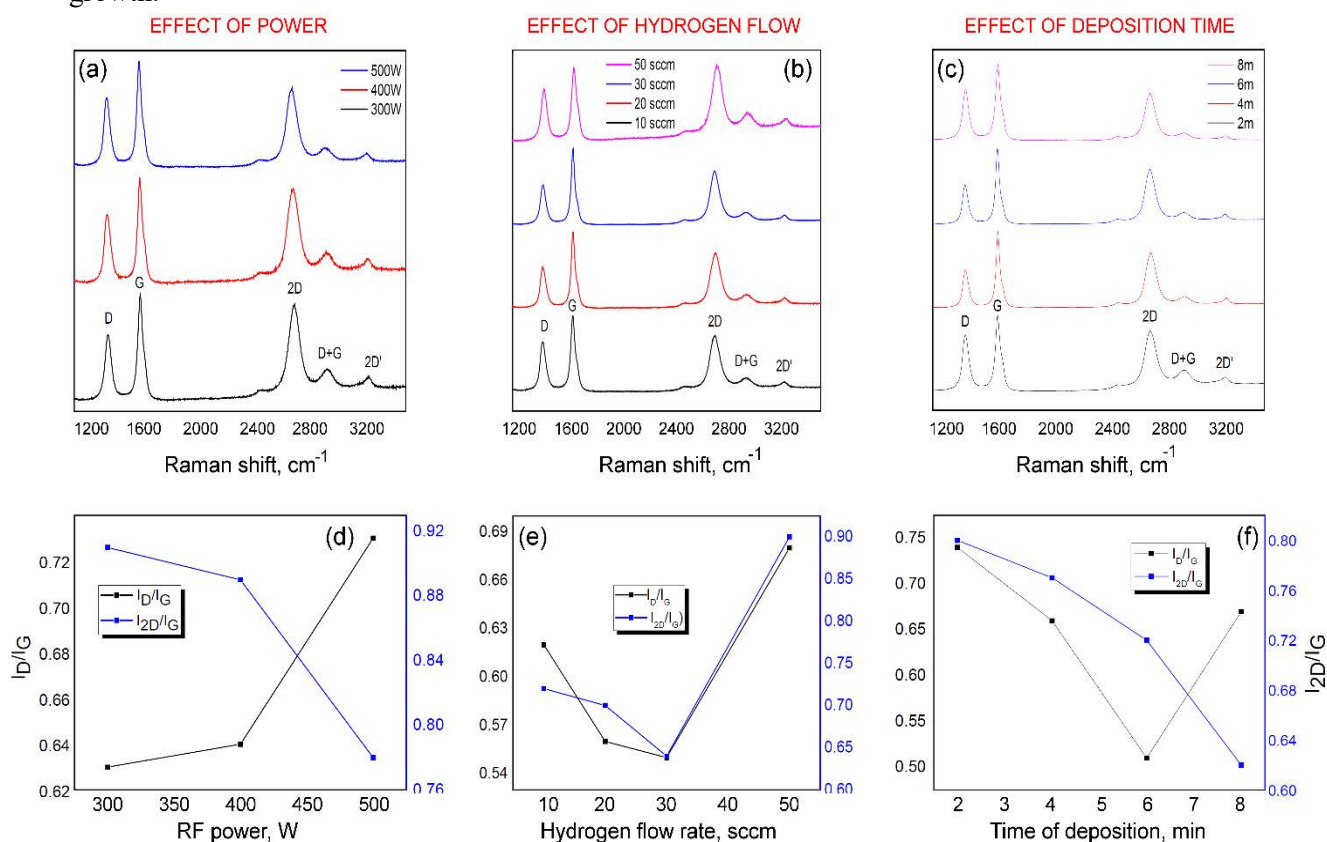


Figure 4.3. Raman characterization of vertically-oriented graphene nanoflakes synthesizes in plasma. (a-c) Raman spectra of graphene samples fabricated at different RF power (300, 400, and 500 W), hydrogen flow rates (10, 20, 30, and 50 sccm), and time of deposition (2, 4, 6, and 8 min). (d-f) Peak intensity ratios from the Raman spectra for the same samples, fabricated at different RF power, hydrogen flow rate, and time of deposition.

The Raman spectra of graphene samples did not differ considerably with the initial increase in hydrogen flow rate and showed all the characteristics D, G and 2D peaks at wave numbers of $\sim 1334 \text{ cm}^{-1}$, 1566 cm^{-1} and 2669 cm^{-1} , respectively (Figures 4.3b and 4.3e). However, the samples fabricated at 50 sccm exhibited an enlarged and slightly right shifted ($\sim 2690 \text{ cm}^{-1}$) 2D peak compared to the rest of the samples. The band intensity ratio I_D/I_G remained low for all samples (between 0.56 and 0.68), indicative of a low defect structure. It can also be inferred that the initial increase in hydrogen (up to 30 sccm) brought about only a very slight change in I_{2D}/I_G ratio, with the change becoming significantly

more prominent upon further increase in hydrogen flow. This increase in I_{2D}/I_G at 50 sccm may be a result of a lower thickness of the produced samples due to higher level of etching.

A sequence of depositions was performed by gradually varying the deposition duration from 2 to 8 min under 500 W input RF power and 30 sccm hydrogen to reveal the different growth stages of orange oil derived graphene. A lower deposition time is deliberately included to get an insight into the very early stages of nanostructure growth. *Figure 4.3c* denotes the corresponding Raman spectra showing the characteristic D, G and 2D bands formed at respective wave numbers of $\sim 1340\text{ cm}^{-1}$, 1563 cm^{-1} and 2670 cm^{-1} . It is worth noting that D+G ($\sim 2924\text{ cm}^{-1}$) and 2D' ($\sim 3214\text{ cm}^{-1}$) peaks acquire a relatively noticeable intensity at a lower deposition time, but diminished successively after longer periods of deposition. Interestingly, even a very short time of deposition (2 min) leads to the growth of graphene nanostructures and reveals the efficacy of PECVD in producing graphene structures. *Figure 4.3f* plots the extracted band intensity ratios for the same samples. As observed in the above cases, I_D/I_G does not show a regular trend, being relatively high for the samples made at 2 min (0.74) and low for 6 min sample (0.51). In contrast, the I_{2D}/I_G ratio consistently dropped from 0.80 to 0.62 with an increase in duration of deposition, most likely due to the improvement in thickness.

Representative XPS spectra of the fabricated graphene nanosheets is presented in *Figure 4.4*. The survey scan (*Figure 4.4a*) shows a single strong peak located at a binding energy (BE) of $\sim 284.5\text{ eV}$, unambiguously assigned to C1s peak that explicitly confirm that the resulted structure is predominantly composed of carbon atoms. In addition to this, a minor intensity peak is also observed around $BE \sim 532.45\text{ eV}$ corresponding to O1s peak, which most likely arises due to the exposure of graphene to air. The atomic concentration of carbon and impurity oxygen was estimated to be 98.69% and 0.94%, respectively. With the optimized process conditions, the elemental analysis detected only the presence of carbon that effectively reveals the efficacy of RF-PECVD in converting the multicomponent orange essential oil into high purity graphene. The high resolution XPS scan of C1s band is given in *Figure 4.4b*. Upon peak deconvolution, the narrow C1s peak was fitted with three peaks, as can be seen in the figure. A major intensity peak and minor intensity peak were obtained at binding energies ~ 284.8 and 285.4 eV , respectively, corresponding to the sp^2 and sp^3 hybridized carbon

in the graphene nanostructure. The fraction of sp^2 -hybridized carbon is higher than that of sp^3 carbon, which demonstrates the high quality of thus-synthesized vertical graphene. A very low intensity peak was observed around $BE \sim 290.9$ eV, corresponding to the shake-up energy loss feature.

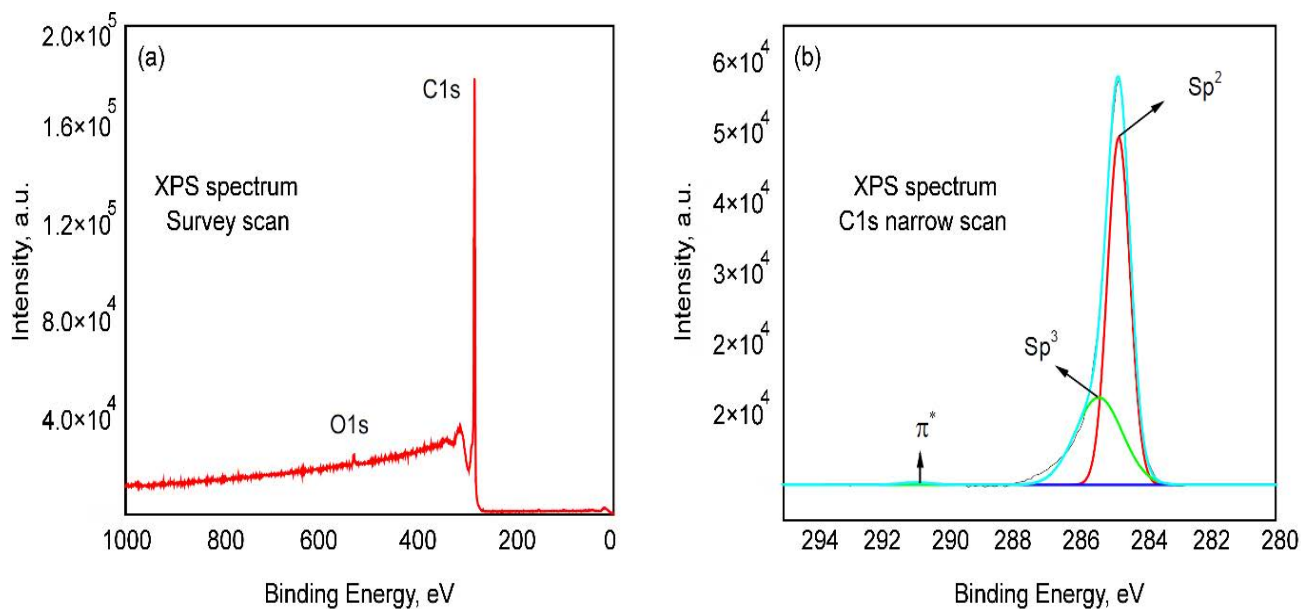


Figure 4.4 XPS spectra of vertically-oriented graphenes produced in PECVD (a) survey scan and (b) C1s high resolution scan fitted with sp^2 , sp^3 and shake-up features.

4.3.2. Effect of RF power on the morphological characteristics of graphene array

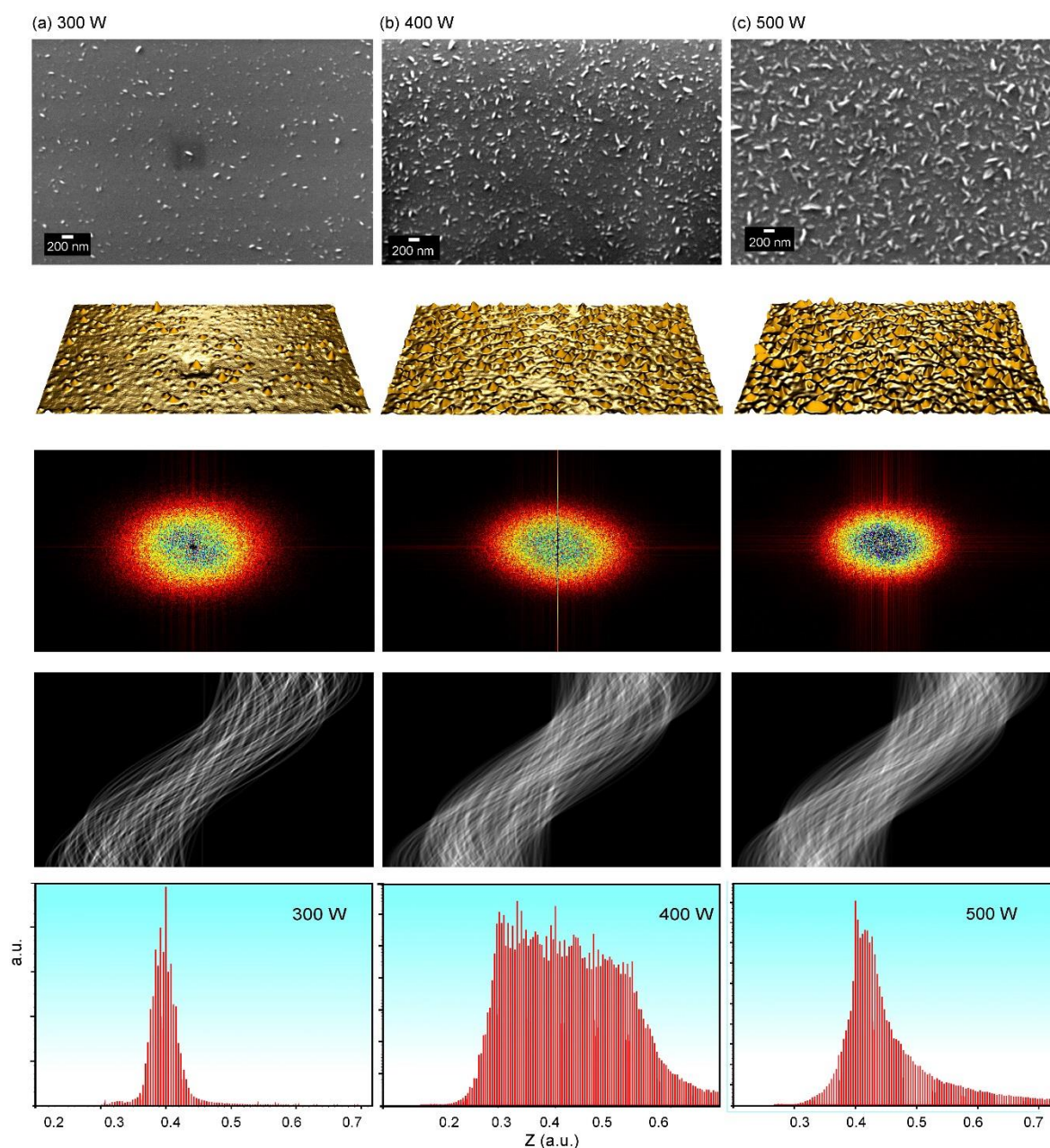


Figure 4.5 Control of the graphene patterns morphology by varying input power. Image illustrates (from top to bottom) SEM images, 3D reconstructions, 2D FFT transforms, Hough transformation spectra and heights distributions of the arrays of graphene nanoflakes grown at 300 W (a), 400 W (b), and 500 W (c) discharge power. Low density of graphene nanoflakes can be observed for 300 W, with much higher density obtained for 400 W, and even higher density of flakes for samples fabricated at 500 W. Fourier and Hough transformation spectra show a notable change with an increase in power, thus highlighting a change in the morphology with the density of nanoflakes. Growth at 10 sccm, 750 °C, 4 min. Bottom images show the spectra of heights distributions, with notably wider distribution obtained at 400 W.

Figure 4.5 presents a comprehensive characterization of the morphological structure and characteristics of graphene arrays fabricated at different RF power levels, i.e. 300 W (left panel, a), 400 W (central panel, b), and 500 W (right panel, c), at the fixed hydrogen flow rate of 10 sccm and temperature of 750 °C. SEM images of graphene samples prepared under the same plasma process conditions but different powers are shown in the upper line, with the 3D reconstructions below. None of the images showed a fully developed vertical graphene structure. Instead, sparsely distributed vertically-oriented graphene flakes resembling the early growth phase were observed. The spatial distribution of vertically-oriented graphene edges found to be noticeably affected by the input RF energy. The graphene flakes formed at a lower power were less in number, smaller in size and scattered further apart (*Figure 4.5a*). The height distribution reveals the particularities of growth at the low power, which are evidenced by a sharp narrow peak located at 0.4 a.u. on the height axis. It can conclude that the process involved a rather short nucleation time, followed by the growth period when the growth rate was almost the same. This behaviour can be explained by a low effect of the ion bombardment experienced by the substrate at 300 W, which results in a prolonged time of diffusion of the adsorbed particle along the surface and preferential attachment to existing adsorption sites, rather than dissociation and generation of new sites. In this case, we conclude that the adsorption sites are generated within the short period of time, and then they serve as a sink for the rest of the adsorbed particles.

Nevertheless, these flakes appeared to be the initial nucleation sites before the onset of vertical graphene wall growth. As the power was increased to 400 W, more flakes with less interspacing are formed (*Figure 4.5b*). Interestingly, when the RF power increased further to 500 W the growth rate was enhanced, with flake size increasing both in lateral and vertical directions. The improvement in the growth rate with RF power can be attributed to the enhanced decomposition rate of orange essential oil components and their subsequent substrate surface diffusion to take part in the growth process. Similar observations have been reported by Yang et al. [49] in growing vertical graphene from CH₄ precursor. In contrast to the case of 300 W, a manifestation of a prolonged nucleation stage, followed by the growth stage are evident. By considering the linear dependence of the growth rate on time, it is possible to conclude that the nucleation time occupies about $[(0.6-0.3)/0.6] \times 100 \% = 50 \%$ of the processing time,

since the distribution is characterized by a plateau with a sharp rise at 0.3 a.u. and a sharp drop at 0.6 a.u. The distribution obtained at 500 W looks similar to the distribution at 300 W, yet is slightly wider, while the reason is quite different from the low power operation mode. It is assumed that there is an interference between the neighbouring vertically-oriented graphene sheets for the 500 W mode, when the capturing areas (which are the domains on the substrate surface which provide the adatoms for the particular vertically-oriented graphene sheets) of the highest and longest graphenes becomes superimposed due to the very quick growth. During this process, the growth of the highest graphenes is terminated due to the lack of the building material, while the smaller graphenes continue their growth thus removing the difference in sizes with the largest graphenes. Hence, the distribution with the plateau obtained at the intermediate power of 400 W, transforms to the peaked distribution again. By considering the obtained results, it should be stressed that the distributions do demonstrate the ability to control the nucleation stage by changing the applied power, since the transition from 300 W to 400 W results in a change from short-to long nucleation time, yet the following increase in power to 500 W does not change the nucleation to the short time mode, and the observation for 500 W is explained by coincidence of the time of observation and the time of the growth interference. Intentionally, the present study fixed the RF power at 500W for the rest of the experiments in order keep the growth at lower plasma conditions.

Fourier and Hough transformations were used to better assess both short-and long-range ordering in the fabricated and selected samples, aiming to verify the high quality of the produced graphene arrays, and to test these assessment methods for specific graphene growth applications. For this purpose, the SEM images of the selected samples were inverted, and generated the 2D FFT (two-dimensional Fourier Transform) and Hough patterns. The 2D FFT and Hough spectra for the three sample types are shown in *Figure 4.5*, central horizontal line. These spectra highlight differences in the morphology, with a much more distinct and clear structure for the first and third sample groups (this also corresponds to the heights distributions).

Another method for the ordering estimation is the Hough transformation, which is being used to search for certain shapes in the pattern. In the case of PECVD growth of graphenes, apparent

differences can be noticed in the spectra shown in *Figure 4.5* for all three sample types. These differences could indicate the ordering in the graphene patterns, since the perfect structure of the defect-free pseudo-crystal features many linearly ordered flakes. Sample 2 appears to be the worse one with respect to the long-scale ordering of the graphene flakes.

In this research work, two functionals were used, namely the Minkowski connectivity (the Euler-Poincaré characteristic) and fractal dimension (FD), to quantify the degree of connectivity and randomness in several different networks of vertically-aligned few-layered graphene flakes grown on a solid substrate [51]. We demonstrate that the Minkowski connectivity and fractal dimension essentially depend on the morphological features of graphene patterns, and thus could be used as morphological descriptors to differentiate between various graphene flake configurations on surfaces and hence, provide a quantitative measure to correlate the geometrical configuration of the pattern with its physical properties.

Minkowski functionals are statistical measures used to characterize geometrical structure and morphology of a system composed of many objects irregularly distributed in the two- and three-dimensional space. These measures have been previously successfully used to relate the structural characteristic with the physical parameters of such systems. For example, Minkowski functionals were capable of predicting fluid phase distribution in porous media [52], provide an estimation of percolation threshold [53], assess mechanical and transport properties [54, 55], permeability [56] and strength [57] of complex systems with stochastically distributed objects. Minkowski functionals have also been proposed as useful to characterize morphology of MoO₃ nanosheet networks [58] and surface roughness features along hetero-interfaces that support electromagnetic wave excitations, morphologies and geometrical properties of thin films [59], large nanotube networks [60], complex networks inlaying the surface such as carbon interconnections [61] and other similar patterns. Specifically, Minkowski connectivity describes the measure of the amount of connections in the pattern by analysing the relationship of connected and disconnected pixels in an image. In a general case, ξ is defined [62],

$$\xi(\theta) = \frac{N_W - N_B}{N}, \quad (4.1)$$

where θ is the threshold, i.e. parameter running over the entire interval between the lightest and darkest hints in the image; N_W and N_B are the numbers of continuous (percolated) clusters of pixels above and below the threshold θ , respectively; and N is the total number of pixels. As can be seen from the equation, ξ is a characteristic of properties which depend on the interconnection of nanostructures in network, such as percolation threshold, conductivity and others related to the transfer of gas, heat, electrons etc. between the nanostructures [63].

Fractal dimensions is one more morphological descriptor often used to characterize morphological features and degree of order/randomness in the complex arrays and networks [60, 64]. Importantly, fractal dimension can be correlated with the physical properties of the patterns, such as thermal conductivity for porous media [65], hydraulic conductivity [66] and complex conductivity [67]. It has also been demonstrated that the films with a significant fractal character exhibit intense surface-enhanced Raman spectra (SERS) [68]. In the classical formulation, the fractal dimension ψ is the limit of logarithmic ratio of the number of self-similar objects $N(l)$ and length scale l/l , i.e.

$$\psi(Z) = \lim_{l \rightarrow 0} \left(\frac{\log N(l)}{\log(1/l)} \right), \quad (4.2)$$

where Z is the current height of the network or hint threshold for the image [69]. Geometrically, the fractal dimension ψ can be interpreted as the power of stretched factor k which return the area increase; i.e. if the area was increased by the factor of k , the area increase is $\delta = k^\psi$. Apparently, for the continued (not fractalized) surface with $\psi = 2$, this will return $\delta = 2^2 = 4$, as expected. For the fractalized surface, ψ can exceed 2, that is, a fractalized surface cannot be considered as flat.

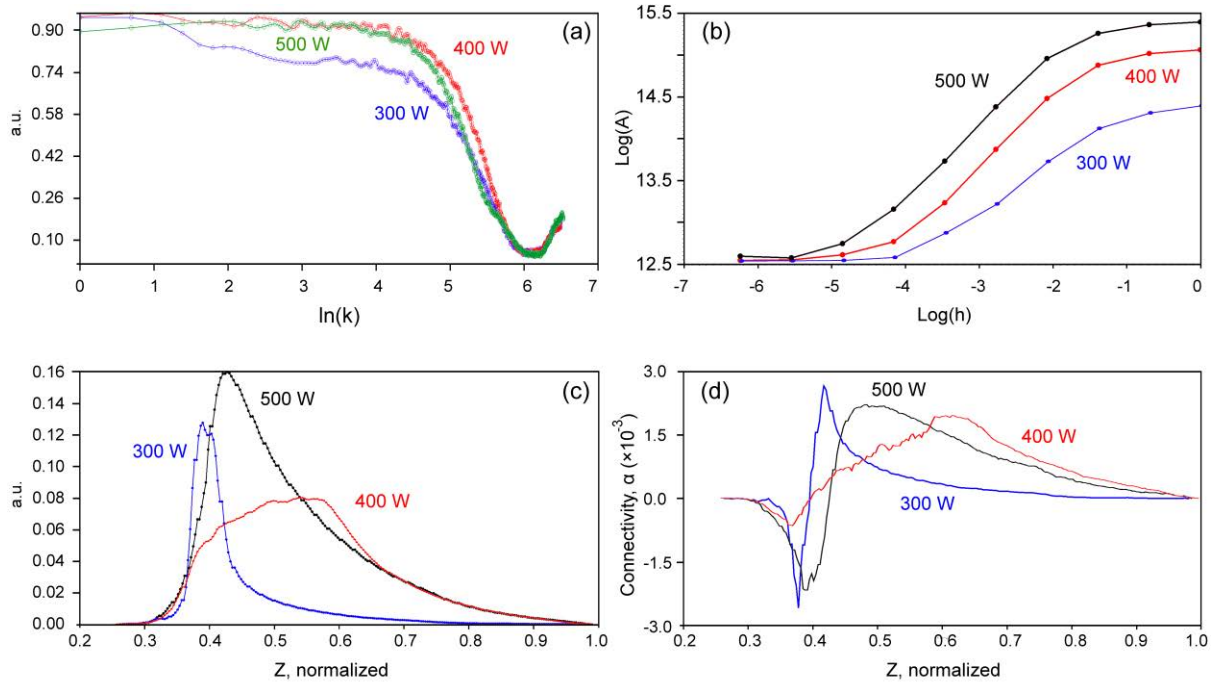


Figure 4.6. Fractal dimensions calculated as a power spectrum [70] (a) and by triangulation [68] (b). (c, d): Minkowski boundaries distribution (c) and Minkowski connectivity (d) as morphological descriptors.

Figures 4.6a and 4.6b show the fractal dimensions, power spectrum (a) and calculated by triangulation (b) [71, 72]. An increase in input power results in slight variations of spectra, but a significant change in the value of fractal dimension elucidates an essential change in the morphological structure. Fractal dimension increases with input power, suggesting that new fragments are being nucleated and developed at the elevated input power probably due to an increase in ion energy and fluxes. Figures 4.6c and 4.6d show the Minkowski boundaries distribution (c) and Minkowski connectivity (d) as morphological descriptors. A wide boundary distribution at 400 W agrees well with the wide heights distribution for 400 W shown in Figure 4.5. Narrow boundary distributions for 300 W are due to the weakly developed structures formed at this input power, and for 500 W—due to the narrower heights distribution. This analysis shows that during the growth, pattern goes through a complex morphological transformation.

4.3.3. Effect of hydrogen flow rate on the morphological characteristics of graphene array

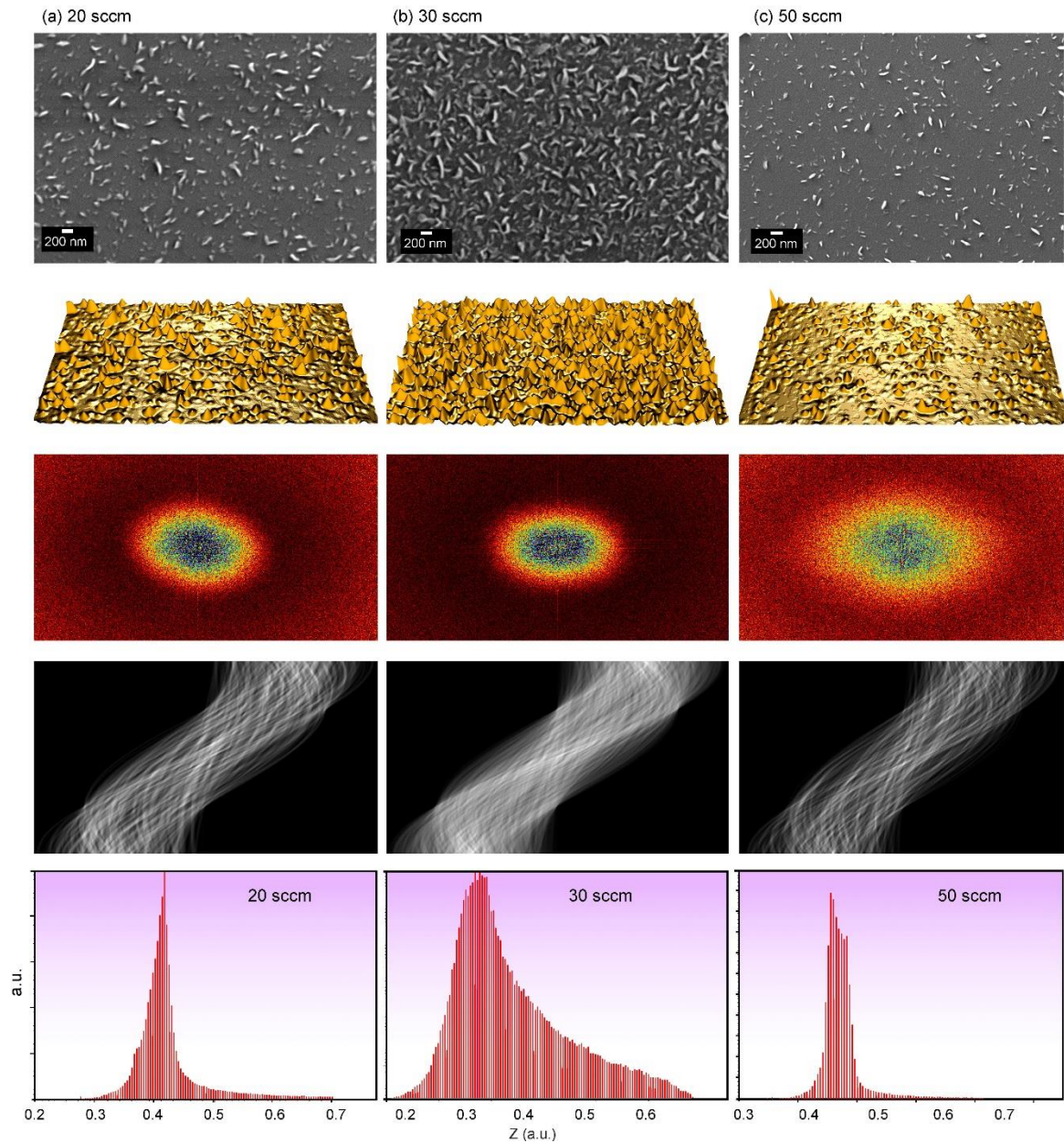


Figure 4.7 Evolution of graphene morphology as a function of gas flux (see caption of similar figure 4.5 for more details). SEM images, 3D reconstruction, and 2D FFT transform of the arrays of graphene nanoflakes grown at 20 sccm (a), 30 sccm (b), and 50 sccm (c) gas flux. Low density of graphene nanoflakes for 20 sccm, much higher density for 30 sccm, and even lower density for 50 sccm is noted. 2D FFT transform spectra show notable changes with increasing hydrogen flux, thus highlighting a change in morphology with the density of nanoflakes. Very narrow height distributions were obtained for 20 and 50 sccm (lower histograms). Growth at 500 W, 750 °C, 4 min.

SEM analysis suggests that an increase in hydrogen concentration accelerates the vertical growth up until 30 sccm, but decreases the growth thereafter (*Figure 4.7*). This trend can be interpreted by the dual role played by hydrogen in graphene growth, as explained in the above section. During the initial increase in the amount of available hydrogen (from 10 to 30 sccm), hydrogen acts like a catalyst to promote rapid dissociation of essential oil components and gives rise to a greater amount of carbon-bearing building blocks that take part in the flake growth. In contrast, at the hydrogen flow rate above this value, the etching process dominates (*Figure 4.7c*). Furthermore, it effectively decreases the C/H ratio and hinders the successful supply of carbon species to the site of graphene growth. This is in good agreement with the Raman results, where a sudden increase in I_{2D}/I_G was noted, indicating the lower thickness of the resulted structure. These results suggest that while graphene can be grown with various hydrogen flow rates, 30 sccm was found to be most favourable for the present case.

A comparison with the SEM image in *Figure 4.5* (500 W, 10 sccm, 4 min) shows that the dependence of the length of vertical graphenes on the flow ratio is strongly nonlinear. One can see a dense array of vertically-oriented graphene structures at 10 sccm, less dense at 20 sccm, very dense at 30 sccm, and a rather sparse array at 50 sccm. At the same time, the heights distribution obtained for samples produced at 30 sccm is similar to the interference growth observed at 10 sccm, which confirms the similarity of the growth conditions. In contrast to the results obtained with the varied power (*Figure 4.5*), no obvious plateau was observed with the varied flow ratio, yet we may conclude the presence of the plateau for 20 and 50 sccm cases for the observation time above 4 min (here one can see the initial stage of a very slow nucleation and growth), as well as for 10 and 30 sccm at the time less than 4 min (where one can observe the interference growth when the largest sheets do not grow while the smaller sheets still grow).

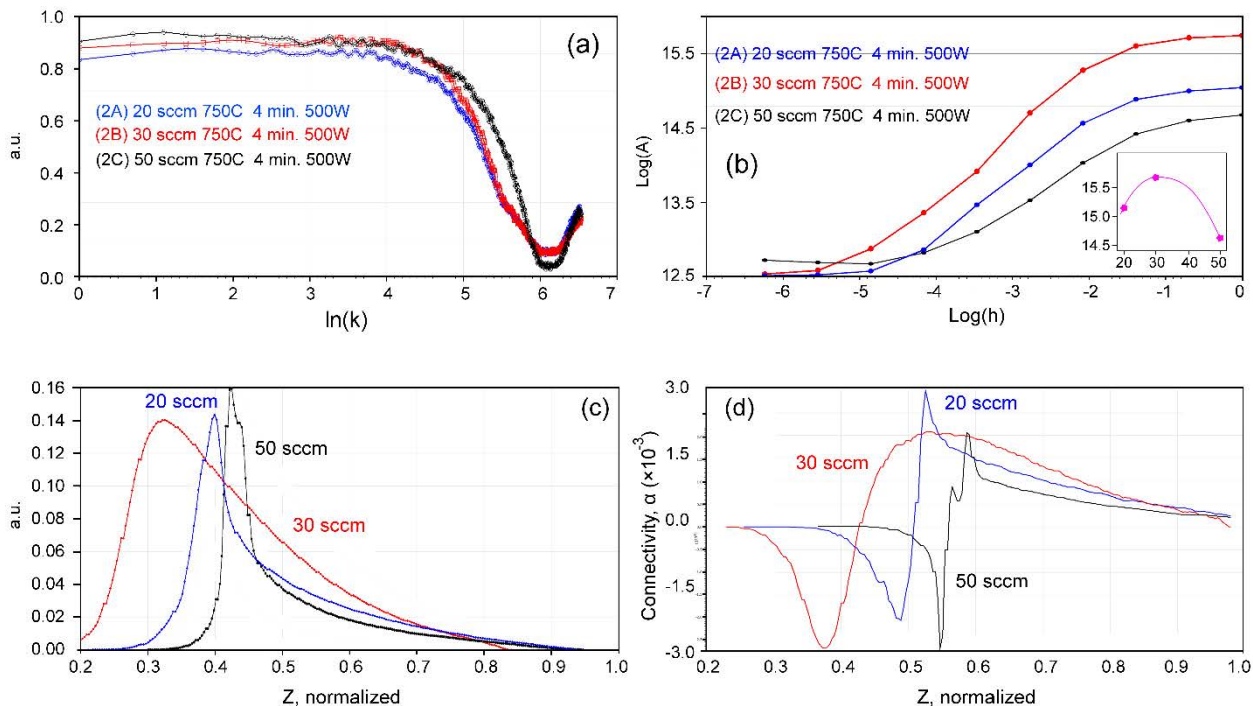


Figure 4.8 Spectrum of the fractal dimensions (power spectrum) does not significantly depend on the reactive gas supply (a); complex dependence of a triangulation-calculated fractal dimension on gas flux (b), with the highest values reached at 30 sccm (b). Indeed, the relevant SEM images shows simple-shaped nanoflakes. Insets illustrates the dependence of maximum values of fractal dimension on gas flow. Minkowski boundaries distribution (c) and Minkowski connectivity (d) show narrow spectra for 50 sccm, and well-developed patterns for 30 sccm of hydrogen flow.

Lower fractal dimensions were found for low and high gas fluxes, while the highest value of fractal dimension was obtained at medium (30 sccm) flux. It is evident that a proper balance between the growth of the already nucleated structures, and nucleation of new structures is important to form well-developed structures with high fractal dimensions (Figure 4.8).

4.3.4. Effect of deposition time on the morphological characteristics of graphene arrays

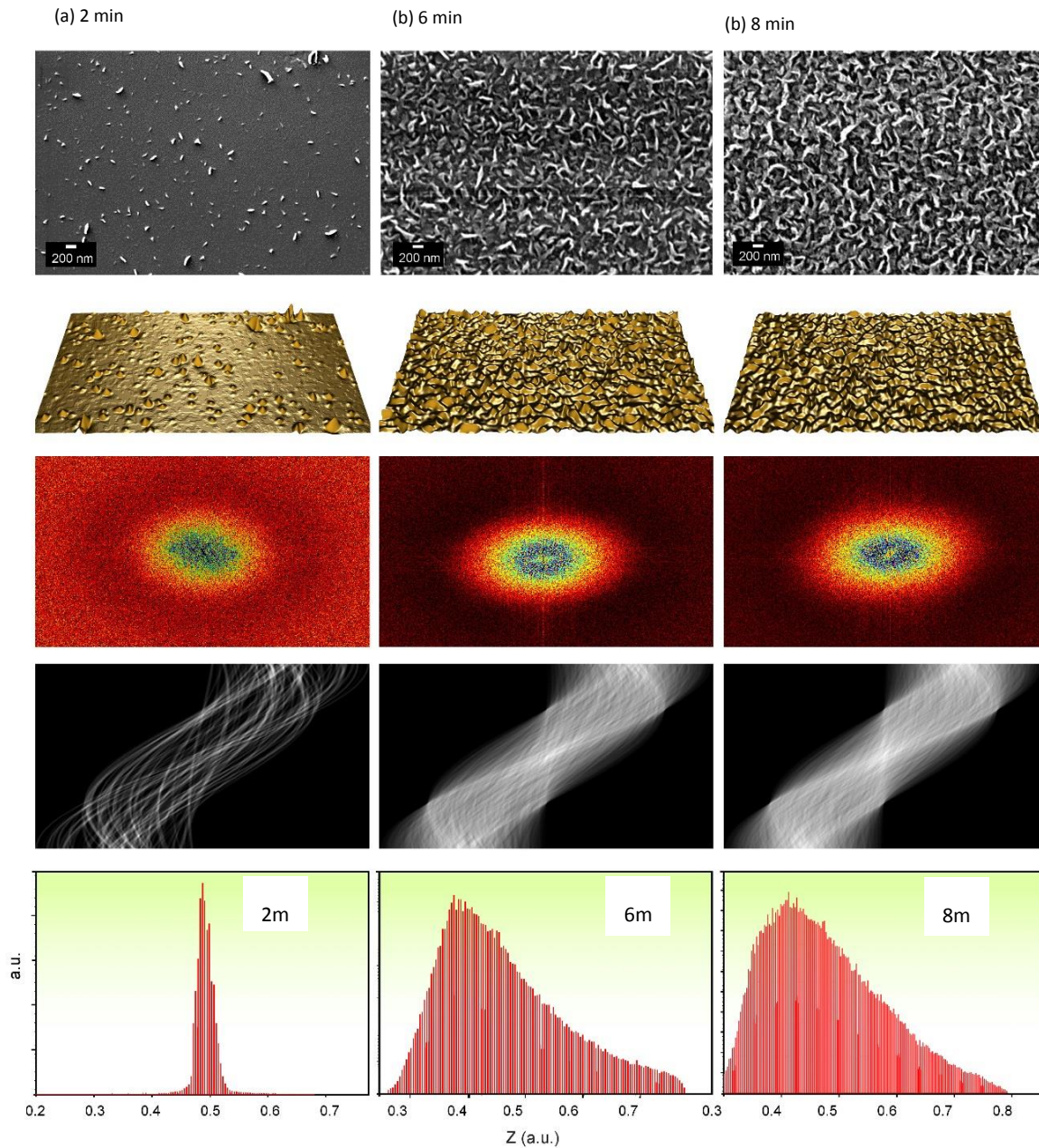


Figure 4.9. Influence of growth time on evolution of morphology (see caption of similar figure 4.5 for more details). SEM images, 3D-reconstruction, and 2D FFT transform of the arrays of graphene nanoflakes grown at 2 min (a), 6 min (b), and 8 min (c). The density of graphene flakes increases with time. 2D FFT transform spectra show a notable change with deposition time increasing from 2 to 5 min, thus highlighting change of the morphology with the density of nanoflakes. Growth at 500 W, 750 °C, 30 sccm.

The SEM images displayed in *Figure 4.9* illustrate the morphology of graphene samples where the time of deposition was varied. As indicated by *Figure 4.9a*, the early growth of graphene is likely to involve evolution of base layers parallel to the substrate surface likely composed of nanocrystalline graphene sheets that possess initial nucleation sites for vertical growth. With an increase in deposition duration, nucleation sites begin to proliferate and act as the seeds to start the vertical growth. These observations are in good agreement with two phase growth mechanism of vertical graphene reported by previous studies [73, 74].

As time progressed further, with the arrival of more carbon-bearing reactive species, these seeds grow larger, predominantly in vertical direction caused by the combined effect of plasma sheath and the induced polarization of the graphitic layers. In the present study, the deposition time was optimized to 6 min at which point the whole surface was completely covered with vertically-oriented interconnected carbon nanostructures with thin edges (*Figure 4.9b*). However, longer deposition duration (8 min) tends to lead to agglomeration of individual free-standing walls. The heights distributions exhibit the initial stage of growth with the short nucleation time (*Figure 4.9a*), and two final stages of growth, when the capture areas on the surface are being superimposed (interference growth) (*Figure 4.9b,c*)

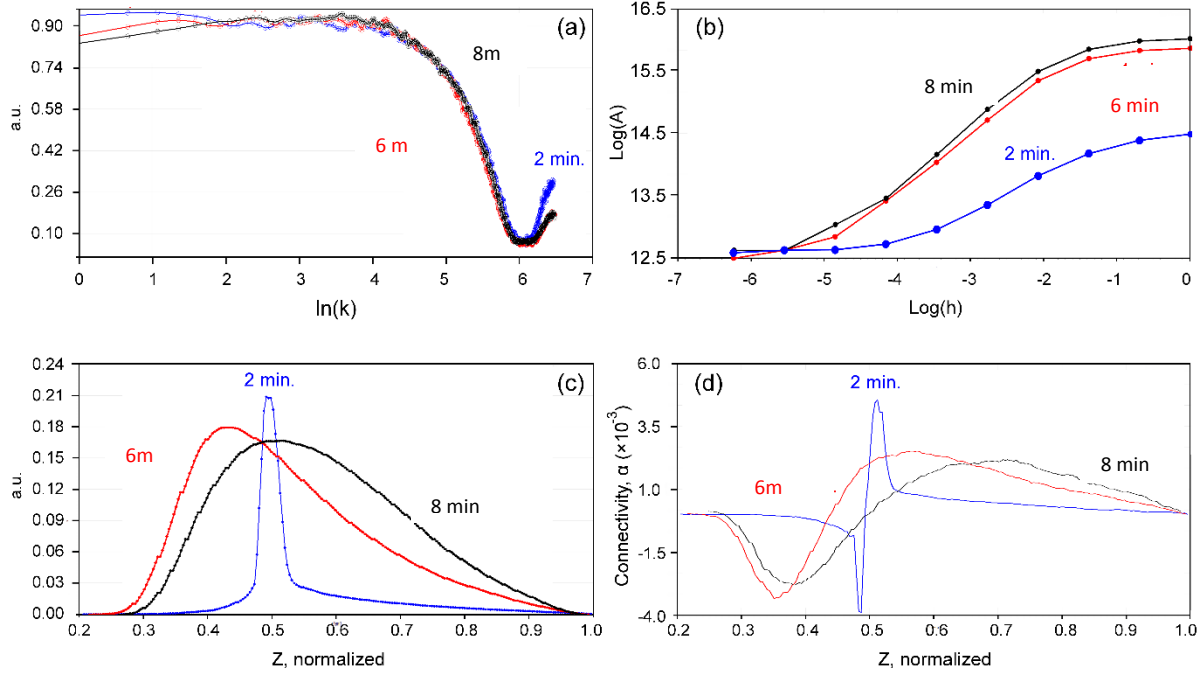


Figure 4.10 Spectrum of fractal dimensions (power spectrum) does not significantly depend on the time of deposition (a); complex dependence of fractal dimension (calculated by triangulation) on time of deposition (b), with the lowest values obtained after 2 min (b). Minkowski boundaries distribution (c) and Minkowski connectivity (d) show the widest distribution for the longer (8 minutes) process.

4.4 Simulations: Insights into Growth Process

4.4.1. Model and technique

A multi-parameter model is used to look deeper into the processes that directly, physically and chemically, relate the formation of the highly-controllable morphology with the key parameters of the process. A schematic of the dependencies of the growth characteristics considered in this model is shown in Figure 4.11. The main species necessary for the vertical graphene growth are delivered by pressurizing a processing reactor with carbon precursor gas ($P_{C_xH_y}$) and molecular hydrogen (P_{H_2}) at a total gas pressure P . When supplying the discharge power to the gas mixture, a transition from gas to plasma occurs, and this enriches the mixture with ions (mostly hydrogen) and electrons. The charged particles interact with a substrate mounted in the reactor, and a negative space charge sheath with a potential drop U_s is formed between the plasma and the substrate. Neutral species also interact with the

substrate, and a number of carbon precursor (n_{CxHy}) and hydrogen (n_{H2}) molecules are adsorbed on the substrate surface with the adsorption energies of $\varepsilon_{aCxHy(\alpha)}$ and $\varepsilon_{aH2(\alpha)}$, respectively.

The molecules can dissociate through a thermal process at the substrate temperature T_s yet the dissociation energies ε_{disH2} and $\varepsilon_{disCxHy}$ are rather high to neglect this route without a catalyst on the surface. The ion bombardment changes the adsorption energies as comparing to the values calculated or measured for the ideal surface because of large number of defects generated due to the kinetic energy of the ions. The value of the energy depends not only on the sheath potential drop U_s , but also on the total gas pressure P , since at the interactions with the neutral gas species, a charge exchange is possible, so the mean ion energy ε_i can differ from the maximal value of U_s . The ion energy acts as a powerful catalyst for the surface reactions – the adsorbed molecules are decomposed, and the radical and atomic species diffuse easily along the substrate surface due to the ion mixing; we describe the diffusion with the potential barriers of $\varepsilon_{dCHx(\alpha)}$ and $\varepsilon_{dH(\alpha)}$, respectively.

As a result of the diffusion, the species collide and some stable densities of the adsorbed atomic hydrogen $n_{H(\alpha)}$ and carbon-containing radicals $n_{CHx(\alpha)}$ are obtained on the substrate. Then, the ion bombardment promotes a formation of a layer of amorphous carbon (α -C) on the substrate, and a large number of seeds for the future vertical graphene growth is generated as a result of the nucleation process (that is not considered in this model). This model consider the stage of the growth when the adsorbed carbon precursor radical reaches the sharp edge of the seed during the diffusion along the substrate surface, and starts the diffusion along the seed edge with the energy of the diffusion activation $\varepsilon_{dCHx(E)}$. It should be mentioned that the sharp edges generate rather strong local electric field due to the charge re-distribution, so they also are subjected to intense ion bombardment. When an ion hits the radical on the seed edge, the energy ε_{xi} is gained, which facilitates the process of dissociation of the carbon-containing radical, and the carbon atom is released and attached to the seed edge—the seed grows and develops into a vertical graphene sheet. Due to the dissociation on the edges, a sink term is added into the diffusion equation, which describes the number density $n_{CHx(E)}$ of the carbon-containing radicals along the edge. The non-uniformity of the shape of vertical graphene forces us to imply two components of the ion flux extracted from the plasma to the substrate: while we treat the substrate with the average

4.4.2 Density of radicals of the precursor gas on a substrate surface

Carbon-containing radicals play a vital role in the discussed mechanism of vertical graphene growth, and the substrate surface either in its initial state or once covered by amorphous carbon (α -C) is the place where the radicals are generated. The radicals are originated from the molecules of hydrogen and carbon-containing precursors adsorbed on the substrate and exposed to the bombardment by predominantly hydrogen ions extracted from plasma. During this process, the adsorbed species dissociate through a non-thermal process driven by the kinetic energy of the ions. The products of the dissociation diffuse along the surface and collide, thus making the recombination process possible. Generally, ion bombardment affects greatly the adsorption of molecules, their dissociation, as well as diffusion of the atoms and carbon-containing radicals.

The densities $n_{C_xH_y}$ and n_{H_2} of C_xH_y and H_2 molecules on a surface of the substrate ($z = 0$) are expressed in a form of Langmuir adsorption isotherm at a suggestion of the small densities ($n_{C_xH_y}/n_0 \ll 1$, and $n_{H_2}/n_0 \ll 1$) [77]

$$\frac{n_{C_xH_y}}{n_0} = \frac{P_{C_xH_y}}{P_{0C_xH_y} + P_{C_xH_y}}, \quad \frac{n_{H_2}}{n_0} = \frac{P_{H_2}}{P_{0H_2} + P_{H_2}}. \quad (4.3)$$

Where $P_{C_xH_y}$ and P_{H_2} are the partial pressure of the precursor and hydrogen gases, Pa; $P_{0C_xH_y}$ and P_{0H_2} are the constants which do not depend on the pressures $P_{C_xH_y}$ and P_{H_2} ; and n_0 is a surface density of the adsorption nodes. The constants are found using the following equations:

$$P_{0C_xH_y} = \left(\frac{M_C + 4M_H}{2\pi h^2}\right)^{3/2} (k_B T_s)^{5/2} \exp\left(-\frac{e\epsilon_{aC_xH_y(\alpha)}}{k_B T_s}\right), \quad P_{0H_2} = \left(\frac{2M_H}{2\pi h^2}\right)^{3/2} (k_B T_s)^{5/2} \exp\left(-\frac{e\epsilon_{aH_2(\alpha)}}{k_B T_s}\right), \quad (4.4)$$

where M_C and M_H are the masses of carbon and hydrogen atoms (here we assume that methane is the carbon-containing molecule), kg; k_B is the Boltzmann constant; e is the electron charge; T_s is the substrate temperature; $\epsilon_{aH_2(\alpha)}$, and $\epsilon_{aC_xH_y(\alpha)}$ are the adsorption energies of the hydrogen and carbon precursor molecules.

The partial pressure of the precursor and hydrogen are expressed as

$$P_{C_xH_y} = \frac{\phi_{C_xH_y}}{\phi_{H_2} + \phi_{C_xH_y}} P, \quad P_{H_2} = \frac{\phi_{H_2}}{\phi_{H_2} + \phi_{C_xH_y}} P, \quad (4.5)$$

where $\phi_{C_xH_y}$ and ϕ_{H_2} are the flows of the precursor gas and hydrogen, sccm; and P is the total gas pressure in the chamber, Pa (we suppose that no other gases are present in the vessel).

4.4.3 Density of hydrocarbon radicals and atomic hydrogen on substrate surfaces

The adsorption energy of the carbon precursor molecule is changed from $\varepsilon_{aC_xH_y(\alpha)}$ to $\varepsilon_{aCH_x(\alpha)}$ after the ion-induced dissociation, and C_xH_y molecule is transformed into CH_x radical.

The number density of the precursor radicals n_{CH_x} on the substrate surface depends on the rate of dissociation of the adsorbed precursor and hydrogen on the surface. To describe a process of the radical generation, a balance between the processes of the radical generation and loss of the adsorbed molecules is considered; the rates of the density growth are described by the equations:

$$\frac{dn_{H_2}}{dt} = -n_{H_2} \left(a_0^2 \frac{j_i}{e} \frac{n_{H_2}}{n_0} + \nu_0 \exp\left(-\frac{e\varepsilon_{disH_2}}{k_B T_s}\right) \right) + n_H \frac{n_H}{n_0} \nu_0 \exp\left(-\frac{e\varepsilon_{dH(\alpha)}}{k_B T_s}\right), \quad (4.6)$$

$$\begin{aligned} \frac{dn_{C_xH_y}}{dt} = & -n_{C_xH_y} \left(a_0^2 \frac{j_i}{e} \frac{n_{C_xH_y}}{n_0} + \nu_0 \exp\left(-\frac{e\varepsilon_{disC_xH_y}}{k_B T_s}\right) \right) + n_H \frac{n_{CH_x}}{n_0} \nu_0 \left(\exp\left(-\frac{e\varepsilon_{dH(\alpha)}}{k_B T_s}\right) + \right. \\ & \left. \exp\left(-\frac{e\varepsilon_{dCH_x(\alpha)}}{k_B T_s}\right) \right), \end{aligned} \quad (4.7)$$

where ν_0 is the lattice vibration frequency, $\nu_0 = \frac{2k_B T_s}{h}$, h is the Plank's constant; j_i is an average density of ion current extracted to a substrate from plasma; n_{H_2} and $n_{C_xH_y}$ are the surface densities of the adsorbed molecules of hydrogen and carbon precursor; ε_{disH_2} and $\varepsilon_{disC_xH_y}$ are the dissociation energies of the adsorbed hydrogen and hydrocarbon gas; n_H and n_{CH_x} are the surface densities of the hydrogen atoms and hydrocarbon radicals; $\varepsilon_{dH(\alpha)}$ and $\varepsilon_{dCH_x(\alpha)}$ are the diffusion activation energies of hydrogen atoms and hydrocarbon radicals.

The first summand in both equations (4.6) and (4.7) describes the decrease in the number densities of the adsorbed molecules due to the dissociation caused by the ion bombardment (j_i) and

temperature (T_s), while the second summand in both equations describes the increase in the number density due to the recombination of atoms and radicals (which are generated after the ion and thermal induced dissociation of the molecules) on the surface.

For the steady mode, the derivatives equal zero, and the stationary surface densities of the species are determined:

$$n_H = n_0 \left(\frac{P_{H_2}}{P_{O_{H_2}} + P_{H_2}} \right)^{1/2} \left(\frac{j_i a_0^2}{e v_0} \frac{P_{H_2}}{P_{O_{H_2}} + P_{H_2}} \exp\left(\frac{e \varepsilon_{dH}(\alpha)}{k_B T_s}\right) + \exp\left(-\frac{e(\varepsilon_{disH_2} - \varepsilon_{dH}(\alpha))}{k_B T_s}\right) \right)^{1/2}, \quad (4.8)$$

$$n_{0CHx} = \frac{\frac{P_{CH_4}}{P_{O_{CH_4}} + P_{CH_4}} \left(\frac{P_{O_{H_2}} + P_{H_2}}{P_{H_2}} \right)^{1/2} \left(\frac{j_i}{e v_0} \frac{P_{CxHy}}{P_{O_{CxHy}} + P_{CxHy}} + \frac{1}{a_0^2} \exp\left(-\frac{e \varepsilon_{disCxHy}}{k_B T_s}\right) \right)}{\left(\frac{j_i a_0^2}{e v_0} \frac{P_{H_2}}{P_{O_{H_2}} + P_{H_2}} \exp\left(-\frac{e \varepsilon_{dH}(\alpha)}{k_B T_s}\right) + \exp\left(-\frac{e(\varepsilon_{disH_2} + \varepsilon_{dH}(\alpha))}{k_B T_s}\right) \right)^{1/2} \left(1 + \exp\left(-\frac{e(\varepsilon_{dCHx}(\alpha) - \varepsilon_{dH}(\alpha))}{k_B T_s}\right) \right)}. \quad (4.9)$$

As it can be seen, the density of the hydrocarbon radicals depends on the precursor gas and hydrogen pressures, temperature of the substrate, and density of the ion current to the substrate surface.

4.4.4 Ion energy and density of ion current as the factors determining surface sputtering

In spite of the positive effect caused by the ion energy, which is expressed in activation and functionalization of the processed surface, high value of this parameter may result in intensive sputtering of the graphene surface thus terminating the whole growth process. Since the high ion energy intensifies the sputtering processes, low ion energy usually is required to grow graphene nanostructures, and for the plasma source applied in the processing chamber, when growing the graphene structures in low-pressure plasmas (RF, MW), a substrate is usually either under the floating potential or is grounded; here the specific ion energy is determined by the discharge conditions:

$$\varepsilon_i \approx \varepsilon_s, \quad (4.10)$$

where ε_s is the energy gained by the ion in the plasma sheath, and the energy ε_s does not exceed the values from a few eV to a few tens of eV.

After the calculation of the ion energy, for the specified energy range the sputter yield can be found as

$$Y = Y_0 \left(\frac{\varepsilon_i}{U_0} \right)^k, \quad (4.11)$$

where Y_0 , U_0 , and k are constants. For the narrow ranges of the ion energy the linear dependence is rather good fit, i.e. the above expression with $k=1$.

4.4.5 Rate of vertical graphene growth

The carbon radicals n_{CH_x} diffuse along the substrate surface, and some of them are adsorbed by the graphene flake side or edge during the diffusion, at which stage the adsorption energy is changed from $\varepsilon_{aCH_x(\alpha)}$ to $\varepsilon_{aCH_x(S)}$ or $\varepsilon_{aCH_x(E)}$, respectively (Ref. *Figure 4.12*). We consider that the energy $\varepsilon_{aCH_x(S)}$ is very small due to the perfect crystalline structure, so adsorption of the radical by the side surface of the flake results in quick evaporation of the radical. If the radical is adsorbed by the defect graphene edge, the adsorption energy is increased ($\varepsilon_{aCH_x(\alpha)} \rightarrow \varepsilon_{aCH_x(E)}$), and the radical can diffuse along the edge for rather long time with low probability of evaporation or transition to the side surface of the vertical graphene sheet ($\varepsilon_{aCH_x(G)} \gg \varepsilon_{aCH_x(S)}$) [80]. Because of the ion bombardment the radical on the flake edge dissociates and releases a carbon atom, which attaches to the graphene edge thus enabling vertical graphene growth.

The rate of the growth due to a presence of the carbon species delivered from the substrate surface through the diffusion for the side edge of the VG sheet at a coordinate z is [81];

$$V_{vg-dif}(z) = \frac{n_{CH_x}(z) j_{iR}}{n_0 e} a_0^3 \exp\left(-\frac{e(\varepsilon_{x-dis}-\varepsilon_{xi})}{k_B T_s}\right) = \frac{n_{CH_x}(z) j_{iR}}{n_0 e} a_0^3 \exp\left(-\frac{e\varepsilon_{x-dis}(1-\alpha_\varepsilon)}{k_B T_s}\right), \quad (4.12)$$

where $n_{CH_x}(z)$ is a density of CH_x radicals at the edge of VG at a coordinate z , a_0 is the lattice parameter of vertical graphene, m; n_0 is the surface density of carbon atoms (density of adsorption nodes), $n_0 = a_0^{-2}$; $\exp(-e\varepsilon_{x-dis}/k_B T_s)$ is the probability for CH_x radical to dissociate by overcoming a potential barrier ε_{x-dis} (eV) which is the energy of CH_x dissociation at the substrate temperature T_s , K; k_B is the Boltzmann constant; e is the electron charge; a_0^3 is the volume generated at the condition that the

reaction of dissociation of CH_x radical followed by generation of carbon atom took place; j_{iR}/e is the ion flux; n_{CH_x}/n_0 is a probability to find the radical CH_x in the adsorption node; $n_{\text{CH}_x}/n_0(j_{iR}/e) \exp[-e(\varepsilon_{x\text{-dis}} - \varepsilon_{xi})/k_B T_s]$ is a frequency per unit area of dissociation of CH_x radicals in the node due to the energy ε_{xi} gained as a result of the interaction with the bombarding ion, $\varepsilon_{x\text{-dis}} \geq \varepsilon_{xi}$ (a case when $\varepsilon_{x\text{-dis}} < \varepsilon_{xi}$ is considered as sputtering), $\alpha_\varepsilon = \varepsilon_{xi}/\varepsilon_{x\text{-dis}}$ is a ratio of the energy ε_{xi} gained by CH_x radical as a result of ion bombardment to the energy $\varepsilon_{x\text{-dis}}$ of dissociation of the radical.

The sputtering results in a negative rate of the vertical graphene side edge for any coordinate z :

$$V_{vg\text{-sput}}(z) = -Y \frac{j_{iR}}{e} a_0^3, \quad (4.13)$$

where $Y a_0^3$ is the volume removed at the condition that carbon layer is affected by the ion flux j_{iR}/e ; Y is the sputter yield.

Hence, for the side edge of the vertical graphene with a coordinate z , the resulting growth rate is:

$$V_{vg\text{-}w}(z) = \frac{dW_{vg}(z,t)}{dt} = V_{vg\text{-}ion}(z) + V_{vg\text{-}sput}(z) = \frac{n_{\text{CH}_x}(z)}{n_0} \frac{j_{iR}}{e} a_0^3 \exp\left(-\frac{e\varepsilon_{x\text{-dis}}(1-\alpha_\varepsilon)}{k_B T_s}\right) - Y \frac{j_{iR}}{e} a_0^3. \quad (4.14)$$

where W_{vg} is the half-width of the vertical graphene sheet.

The distribution $n_{\text{CH}_x}(z)$ is determined by solving the diffusion equation, which describes the stationary mode of the diffusion of the carbon precursor radicals from the substrate surface

$$D_{\text{CH}_x} \frac{\partial^2 n_{\text{CH}_x}}{\partial z^2} = -\frac{n_{\text{CH}_x}(z)}{n_0} \frac{j_{iR}}{e} \exp\left(-\frac{e\varepsilon_{x\text{-dis}}(1-\alpha_\varepsilon)}{k_B T_s}\right), \quad (4.15)$$

And the diffusion coefficient is

$$D_{\text{CH}_x} = D_{0\text{CH}_x} \exp\left(-\frac{e\varepsilon_{d\text{CH}_x(E)}}{k_B T_s}\right) = \frac{\nu_0 a_0^2}{2} \exp\left(-\frac{e\varepsilon_{d\text{CH}_x(E)}}{k_B T_s}\right) = \frac{k_B T_s}{h} a_0^2 \exp\left(-\frac{e\varepsilon_{d\text{CH}_x(E)}}{k_B T_s}\right), \quad (4.16)$$

where $\varepsilon_{d\text{CH}_x(E)}$ is the activation energy for the diffusion of the radicals along the VG edge, eV; $D_{0\text{CH}_x}$ is a diffusion coefficient.

It is assumed that in the model the surface features such as vertical graphene seeds or sheets cause re-distribution of the local electric field above the substrate surface and generation of a very strong

electric field which, in turn, results in the strong focusing of ions extracted from plasma to the sharp edges of vertical graphene [44, 82], so the ion current densities to the side edge j_{iR} and top edge j_{iL} are [83];

$$j_{iR} = f_{iR}j_i, \quad j_{iL} = f_{iL}j_i, \quad (4.17)$$

where f_{iR} and f_{iL} are the coefficients of the ion flux enhancement because of the focusing to the VG side and top edge, respectively; j_i is the average density of the ion current extracted from the plasma to the substrate, A/m².

General solution of equation (4.15) is [79];

$$n_{CH_x}(z) = A \cos \left[\left(\frac{j_{iR}}{eD_{CH_x}n_0} \exp \left(-\frac{e\varepsilon_{x-dis}(1-\alpha_\varepsilon)}{k_B T_s} \right) \right)^{1/2} z \right] + B \sin \left[\left(\frac{j_{iR}}{eD_{CH_x}n_0} \exp \left(-\frac{e\varepsilon_{x-dis}(1-\alpha_\varepsilon)}{k_B T_s} \right) \right)^{1/2} z \right]; \quad (4.18)$$

by considering that the density of CH_x radicals should be n_{0CH_x} for $z=0$, the final expression is:

$$n_{CH_x}(z) = n_{0CH_x} \cos \left[\left(\frac{j_{iR}}{eD_{CH_x}n_0} \exp \left(-\frac{e\varepsilon_{x-dis}(1-\alpha_\varepsilon)}{k_B T_s} \right) \right)^{1/2} z \right]. \quad (4.19)$$

After the substitution, the dependence of the rate of the vertical graphene flake half-width and length on time t is:

$$\frac{dW_{vg}(z,t)}{dt} = \frac{n_{0CH_x} j_{iR}}{n_0 e} a_0^3 \exp \left(-\frac{e\varepsilon_{x-dis}(1-\alpha_\varepsilon)}{k_B T_s} \right) \cos \left[\left(\frac{j_{iR}}{eD_{CH_x}n_0} \exp \left(-\frac{e(\varepsilon_{x-dis}(1-\alpha_\varepsilon))}{k_B T_s} \right) \right)^{1/2} z \right] - Y \frac{j_{iR}}{e} a_0^3, \quad (4.20)$$

$$\frac{dL_{vg}(t)}{dt} = \frac{j_{iL}}{e} a_0^3 \frac{n_{0CH_x}}{n_0} \exp \left(-\frac{e\varepsilon_{x-dis}(1-\alpha_\varepsilon)}{k_B T_s} \right) \cos \left[\left(\frac{j_{iR}}{eD_{CH_x}n_0} \exp \left(-\frac{e(\varepsilon_{x-dis}(1-\alpha_\varepsilon))}{k_B T_s} \right) \right)^{1/2} L_{vg}(t) \right] - Y \frac{j_{iL}}{e} a_0^3, \quad (4.21)$$

with W_{0vg} and L_{0vg} as the initial half-width and length of the VG, m.

The exact solution of the above equation can be found [84];

$$W_{vg}(z, t) = \left(\frac{n_{0CHx}}{n_0} \exp\left(-\frac{e\varepsilon_{x-dis}(1-\alpha_\varepsilon)}{k_B T_s}\right) \cos[Az] - Y \right) \frac{j_R}{e} a_0^3 t + W_{0vg}, \quad (4.22)$$

$$L_{vg}(t) = \frac{2}{A} \arctg \left[\frac{\sqrt{D^2-C^2} (\exp(\sqrt{D^2-C^2}t)+1)(D-C)tg \frac{a_0 L_{0vg}}{2} + (\exp(\sqrt{D^2-C^2}t)-1)\sqrt{D^2-C^2}}{(D-C) (\exp(\sqrt{D^2-C^2}t)-1)(D-C)tg \frac{a_0 L_{0vg}}{2} + (\exp(\sqrt{D^2-C^2}t)+1)\sqrt{D^2-C^2}} \right], \left(\frac{D}{C}\right)^2 > 1; \quad (4.23)$$

where

$$A = \left(\frac{j_{iR}}{e D_{CHx} n_0} \exp\left(-\frac{e(\varepsilon_{x-dis}(1-\alpha_\varepsilon))}{k_B T_s}\right) \right)^{1/2}, \quad (4.24)$$

$$C = -AY \frac{j_{iL}}{e} a_0^3, \quad (4.25)$$

$$D = \frac{n_{0CHx}}{n_0} \frac{j_{iL}}{e} A a_0^3 \exp\left(-\frac{e\varepsilon_{x-dis}(1-\alpha_\varepsilon)}{k_B T_s}\right). \quad (4.26)$$

L_{0vg} is the initial length of the flake; n_0 is the surface density of carbon atoms (density of adsorption nodes) on the substrate surface; n_{0CHx} is a density of carbon-containing radicals on a surface of the substrate ($z = 0$); $\alpha_\varepsilon = \varepsilon_{xi} / \varepsilon_{x-dis}$ is a ratio of the energy ε_{xi} gained by carbon-containing radical as a result of ion bombardment to the energy ε_{x-dis} of dissociation of the radical; $\varepsilon_{dCHx(E)}$ is the energy of activation of diffusion of carbon-containing radicals along the flake edge; a_0 is the lattice parameter of graphene; T_s is the substrate temperature; k_B is the Boltzmann constant; e is the electron charge; Y is the sputter yield; A case when $\left(\frac{D}{C}\right)^2 < 1$ is not considered here since it corresponds to the mode when sputtering of the surface is a dominant process.

4.4.6 Numerical Procedure

The task of modelling the growth of vertical graphene is complicated by the fact that many parameters cannot be measured directly, and even theoretical results obtained for the conditions without the ion bombardment cannot be considered as reliable. That is why in our model we determined the main adsorption and diffusion activation energies by fitting the calculation results to the experimental

data. The energies of adsorption $\epsilon_{aH2(\alpha)}$ and $\epsilon_{aCH4(\alpha)}$ were determined from the condition of sustaining the densities of the species on the substrate surface at elevated temperatures (of about 1000 °C) at a value of about a few percent at least; the corresponding energies are $\epsilon_{aH2(\alpha)} = 1.5$ eV and $\epsilon_{aCxHy(\alpha)} = 2.8$ eV. The adsorption energy for carbon radical exceeds the value calculated for methane by density-functional theory (DFT) for adsorption on pristine graphene (0.45 eV), but is compared to the energy of adsorption on P-doped graphene (2.13 eV), and is much less than energy of adsorption on Al-doped graphene (3.28 eV) [85]. The energy of hydrogen adsorption on graphene is also much less than the energy obtained by DFT and Monte Carlo studies is about 0.1 eV [86], which can be attributed to the activation of the atomic bonds caused by the ion bombardment; the diffusion activation energies $\epsilon_{dH(\alpha)} = 1.6$ eV, $\epsilon_{dCHx(\alpha)} = 1.8$ eV, and $\epsilon_{dCHx(E)} = 0.57$ eV were determined also by the reason to fit the experimental results. Since the dissociation energies ϵ_{dH2} and ϵ_{dCH4} are rather high (4.52 eV and 4.95 eV, respectively) [87], the thermal dissociation does not affect the process of generation of hydrogen atoms and hydrocarbon radicals on the surface for the considered temperature range at the absence of a catalyst, so the plasma enhanced dissociation is the main driving force for the growth of vertical graphene.

4.4.7 Numerical results

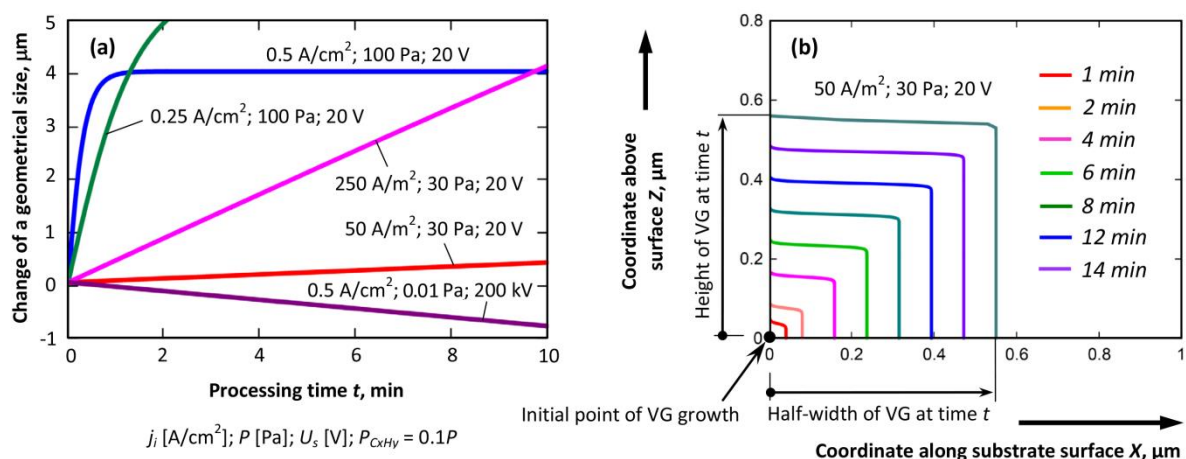


Figure 4.13 Dependence of a vertical graphene length on time under various growth conditions (a); time evolution of the vertical graphene shape at $T_s = 750$ °C.

Various growth characteristics obtained by use of equation (4.21) are shown in *Figure 4.13*. Principally, the dependence of the vertical graphene growth is described by a curve with a saturation, and the expression of the dependence is deduced from expression (4.23) at the limit for $t \rightarrow \infty$:

$$L_{vg}(\infty) = \frac{2}{a} \operatorname{arctg} \sqrt{\frac{D+C}{D-C}}. \quad (4.27)$$

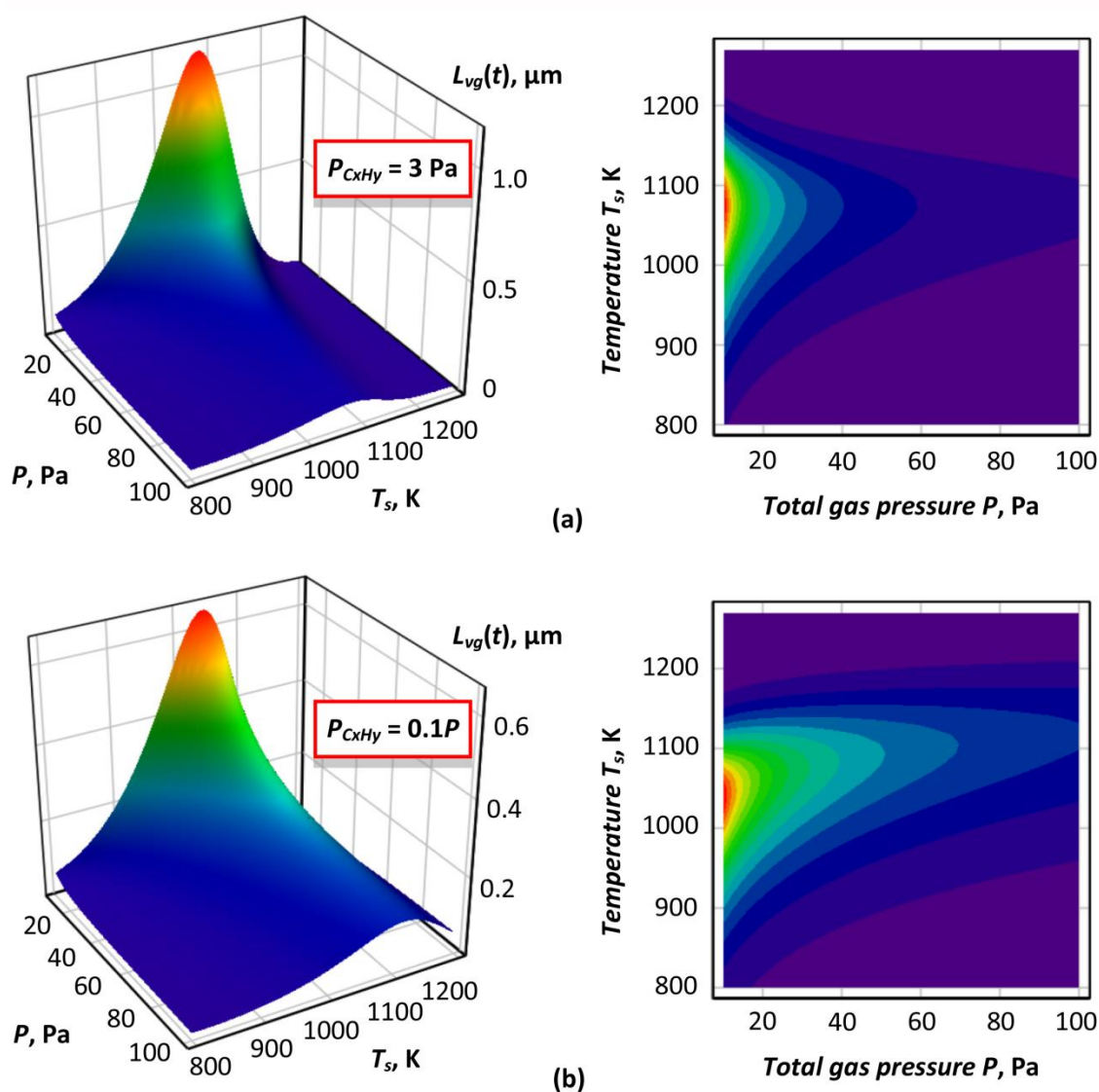


Figure 4.14 Surface plots $L_{vg}(P, T_s)$ of the vertical graphene length for the growth time $t = 6 \text{ min}$ and for different ratios of carbon precursor-to-total gas pressure: total gas pressure P is varied at a fixed pressure $P_{C_xH_y} = 3 \text{ Pa}$ of the carbon precursor (a), P is varied at a fixed ratio $P_{C_xH_y} : P = 0.1$ (b).

The saturation depends on the density of the ion current applied to the surface, and the higher is the current density the quicker the saturation occurs, and the lower is the maximum length of the VG structure. It should be noted that the dependencies calculated at 0.25-0.5 A/cm² are consistent with the experiments conducted by the use of microwave plasma sources where dense plasma is generated [88]. For the relatively low densities of the ion current obtained in the low-pressure RF plasma setups [89, 90], the linear part of the dependence is observed in the experiments, which is consistent with the experiments described in this chapter. All dependencies except one were calculated for the sheath voltage drop of about 20 V that is a fit to the floating potential developed on the isolated electrode exposed to the RF plasma, while the lower curve calculated for rather severe plasma conditions such as 200 kV of the sheath voltage drop at the total gas pressure of 0.01 Pa is shown to illustrate the sputtering possibilities of plasma yet the parameters are adjusted just to show the effect for the short time.

The shape of vertical graphene sheet calculated by the use of expressions (4.22) and (4.23) shows gradual evolution of the rectangular seed with almost constant length-to-width ratio of about 1:2, as it can be seen in *Figure 4.13b*. However, according to expression (4.22), the shape gradually changes, and the closer is vertical graphene to the saturation mode, the more cosine-like the VG shape is, since at the saturation point the vertical growth is stopped while the growth in width is not.

An interesting feature is revealed when calculating the surface plots of the vertical graphene length obtained for the same growth time of 6 min, but different pressure operation modes (*Figure 4.14*). When the carbon precursor pressure is fixed at 3 Pa, the maximum length of the VG structure can be as high as 1.2 μm, while for the fixed ratio $P_{C_xH_y} : P = 0.1$ the length does not exceed 0.7 μm for the whole field of the pressure and temperature parameters, which confirms the necessity of adjustment of the ratio to control the growth process.

4.4.8 Simulation results

The following discussion is aimed to establish the dependencies of short-and long-order morphological features on processing parameters by comparing the experimental data with the numerical results

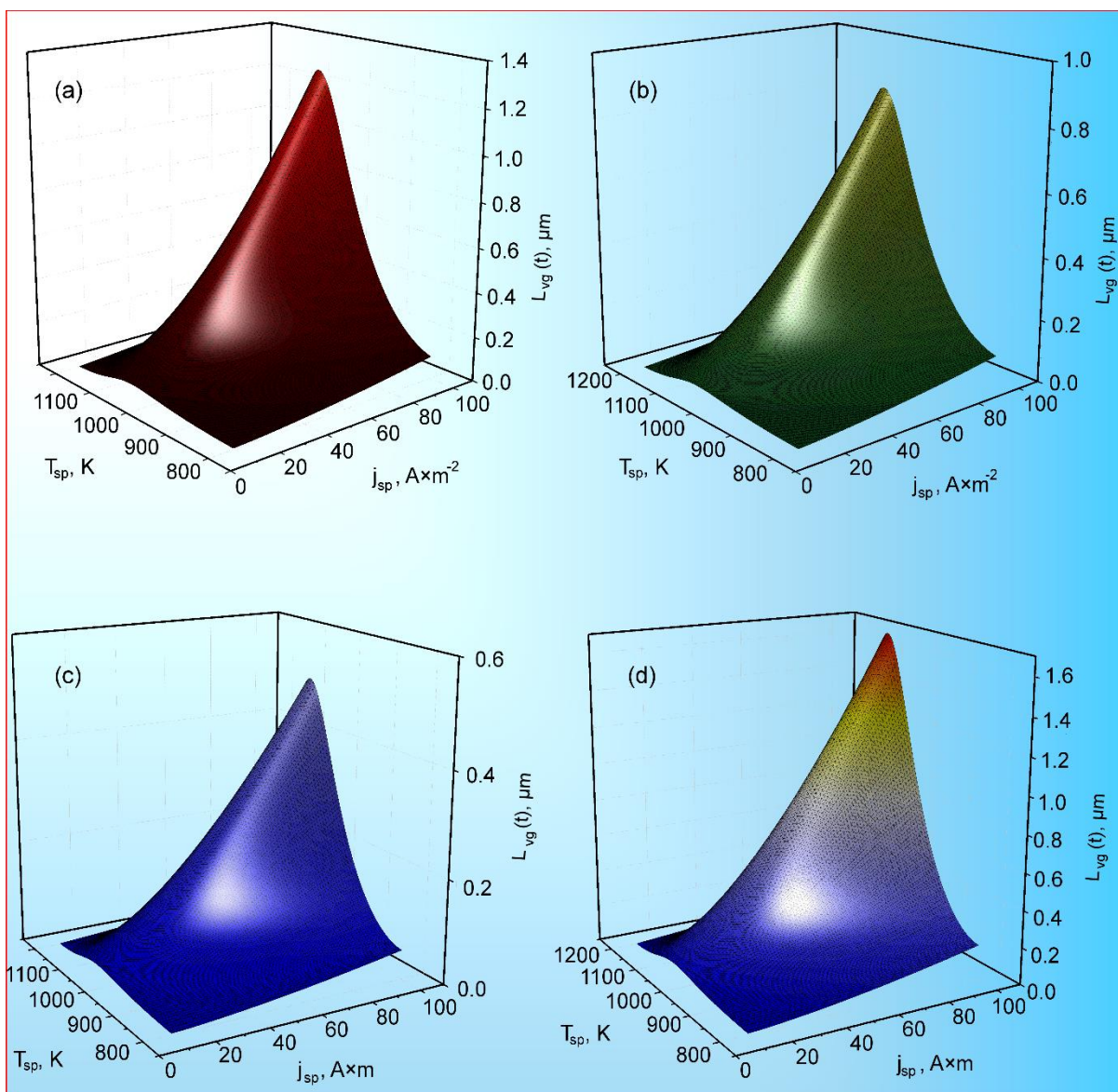


Figure 4.15 Surface plots $L_{vg}(j_i, T_s)$ of the vertical graphene flake length for different operation modes and moments of time t : a – hydrogen pressure 18 Pa (corresponds to hydrogen flow of 20 sccm), carbon precursor gas pressure 3 Pa, total gas pressure 21 Pa, time of growth 6 min; b – hydrogen pressure 27 Pa (hydrogen flow of 30 sccm), carbon precursor gas pressure 3 Pa, total gas pressure 30 Pa, time of growth 6 min; c – hydrogen pressure 45 Pa (hydrogen flow of 50 sccm), carbon precursor gas pressure 3 Pa, total gas pressure 48 Pa; time of growth 6 min; d – Hydrogen pressure 45 Pa (hydrogen flow of 50 sccm); carbon precursor gas pressure 3 Pa, total gas pressure 48 Pa, time of growth 20 min.

The graphs in *Figure 4.15* show the plot of graphene length as a function of the density of the ion current [A/m^2], which is considered as linearly dependent on the discharge power, and the substrate temperature [K] including the value 1023 K or 750 °C used in the experiment. The discharge power varied from 300 to 500 W in the experiment, and the density of the ion current in the range from 10 to 100 A/m^2 at the ion energy of 20 eV suitable for the sample under the floating potential and exposed to the low-pressure RF plasma was used in the calculations. The measured values of the vertical graphene structure length of about 0.25 μm obtained for the time of growth of 6 min was used as a reference point to fit the experimental data. The model describes the results shown in *Figure 4.9* (SEM images of the graphenes growth for 2, 6, 8min), as well as the results shown in *Figure 4.7c* (where the increase in the hydrogen flow results in the decrease of the nanostructure size). The decrease in the sizes with an increase in the hydrogen gas flow is explained by the recombination of the hydrocarbon radicals (which are considered as the main building blocks) with the hydrogen atoms—the higher is the hydrogen density, the higher is the recombination rate, and the lower is the hydrocarbon radical density.

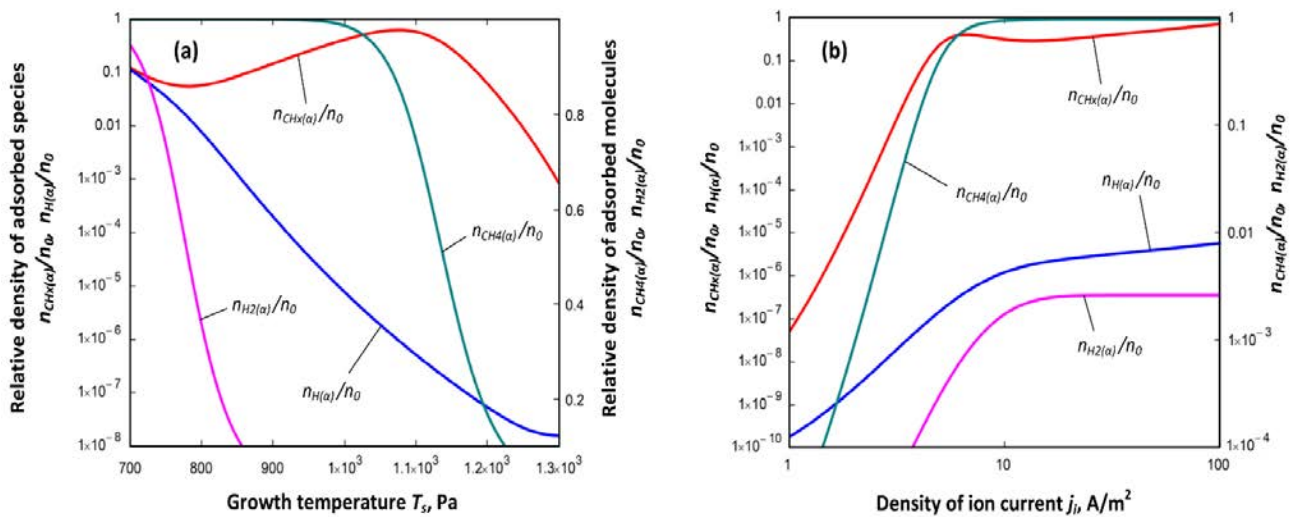


Figure 4.16 Relative densities of adsorbed species as a function of growth temperature at a fixed density of the ion current $j_i = 50 A/m^2$ (a), and the relative densities as a function of density of the ion current at the fixed growth temperature $T_s = 750$ °C (b); other parameters are: $P_{H_2} = 30 Pa$; $P_{C_xH_y} = 3 Pa$

Figure 4.15 highlights the importance of the direct ion flux for graphene growth. The growth is very slow when the ion current J_i is low, since the ion-induced decomposition of the adsorbed

molecules is not sufficient to create the necessary concentration of carbon radicals on the surface, even at a high adsorption energy. Moreover, a balance between adsorption and diffusion should be sustained to grow the nanostructures, as seen from the growth dependence on substrate temperature. In the case of low temperatures, concentration of the adsorbed molecules on surfaces can be high yet the growth is still slow due to a low mobility of the species. When the temperature is high, the growth is restricted by the low concentration of the molecules on the surface due to re-evaporation.

The results shown in *Figure 4.3* are explained by the assumed dependence of the surface state from the ion bombardment—the higher is the discharge power the higher is the density of the ion current, and the more intensive is the ion bombardment, which results in generation of the hydrocarbon radicals on the substrate surface. The calculations reveal the existence of a maximum of a dependence of the vertical graphene length on the growth temperature for the fixed density of the ion current. The maximum is explained by noting the dependence of the adsorption and diffusion on temperature. To obtain long vertical graphene sheets, we should deliver a large number of the carbon precursor radicals to the top of the flake, and make this delivery process as fast as possible.

For that, high density of the radicals should be sustained on the substrate surface to make a rather powerful source for the diffusion along the vertical graphene edges, and the diffusion should be fast. However, the density of the adsorbed species is decreased with the temperature increase, unlike the diffusion that is enhanced by high temperatures. Thus, the temperature maximum describes the optimal conditions to provide vertical graphene growth with high productivity. The presence of the ion flux is vital for the catalyst-free graphene growth, since two important processes are initiated by ions: generation of adsorption sites on the surface to reach the necessary concentration of molecules on the surface (i), and generation of carbon radicals, which is possible due to the ballistic effects during ion bombardment (ii). The model accounts for both of these processes by introducing adsorption energies and by adding the density of the ion flux j_i into the equations.

The relation between the energies of adsorption of the molecular hydrogen and carbon precursor gas also is important: since the energy for hydrogen molecules is lower than that for the precursor, the decrease of the hydrogen molecule density occurs earlier than that for methane—at

approximately 500 °C (*Figure 4.16a*) for H₂ and at 800 °C—for C_xH_y. Importantly, the molecular H₂ adsorption could be negligible at high temperatures without the effect of ion bombardment; however, the situation changes in the plasma environment, where strong ion bombardment is present. As a result, density of hydrocarbon radicals CH_x adsorbed on the surface changes the behaviour from decreasing initially to increasing until the high temperature maximum is reached at about 1000–1100 °C; the high temperature mode is usually utilized in growth of the vertical graphene. According to the calculation, the ion current is a much more effective tool to control the density of the adsorbed precursor radicals, since a change in the ion current density by two orders of magnitude (which can be conducted in plasma reactors) results in changing the density of adsorbed radicals by seven orders of magnitude, while the temperature control allows to change the density by three orders of magnitude (*Figure 4.16b*).

Thus the results of simulations show that the dependence of the vertical graphene length on the ion current density is monotonic for the entire range of parameters considered in this study. For the specific pressure range, ion energy is not restricted by the charge exchange collisions, so the sputter yield is almost constant. Moreover, ions promote adsorption of species on the surface of the growing nanostructures by generating a large number of defects and activating surface bonds. As a result, the adsorption energy increases, and hence the density of the adsorbed carbon precursor molecules elevates. However, when the growth is sustained at a high (about 10³–10⁴ Pa) pressure, the collision sheath should be considered. In this case, the charge exchange collisions lead to the formation of a directed flux of neutrals from the gas phase to the surface, wherein the processing flux energy can be adjusted by changing the gas pressure. Hence, the combination of the plasma power and gas pressure forms an additional control loop to adjust the growth of vertical graphenes to the specified conditions. Then, ions bombard the adsorbed molecules and decompose them, thus giving rise to the density of carbon precursor radicals, which are the main building blocks for the growth of vertical graphenes. Moreover, the bombardment also destroys carbon precursor molecules on the edges of vertical graphenes, thus promoting the release of carbon atoms to be incorporated into the lattice of the growing vertical graphene sheet. Thus, plasma is an environment that makes the growth of vertical graphene possible in the absence of any catalyst on the surface; where the sheets grow not via direct gas phase deposition of

building blocks onto graphene sheets but mainly under ion bombardment, with the thermal guided adsorption, diffusion, and dissociation complemented by ballistic effects.

4.5 Conclusion

Complex arrays of vertically-aligned few-layer graphene nanostructures were synthesized from orange essential oil through a single step, green, environmentally friendly catalyst-free RF-PECVD process, suggesting a set of plasma process conditions (duration of synthesis; power applied to the plasma discharge; gas flow rates) that maximise the development of highly-controllable, well-resolved graphene array morphologies. SEM, FEM, Raman and XPS techniques were used to study the morphology, and advanced analytical characterization methods (distributions of fractal dimensions calculated by triangulation and power spectrum methods, 2D FFT transforms, 3D reconstructions of the arrays, as well as Hough transformation spectra and heights distributions) were then utilized to analyse various geometrical and statistical parameters and characteristics of the arrays synthesised under various process conditions. Moreover, a specially developed model was then used to conduct a detailed multi-parameter simulation of the array formation on plasma, to reveal the major processes and drivers that govern and significantly influence the array morphology and other characteristics of large, complex patterns of the vertically-aligned few-wall graphene flakes. It was found that all the examined parameters of the reactive plasma environment significantly influence the array morphology and hence, could be used as efficient control knobs.

Specifically, narrow distributions of the graphene nanowalls were obtained at 300 and 500 W with much wider array synthesised at 400 W. This was confirmed by well-articulated Hough transformation spectra and 2D FFT transform patterns. The distributions of fractal dimensions calculated as power spectrum and by triangulation, as well as Minkowski boundaries distributions and connectivity also manifest the best array morphology obtained at 300 W. Similar results were obtained for the analysis of experiments conducted in 500 W discharge, with the most narrow height distributions and well-shaped Hough transformation spectra obtained for 20 and 50 sccm of gas supply. The spectra of the fractal dimensions have also confirmed that the arrays grown at 20 and 50 sccm feature the most articulated and regular morphology. The experiments on the array grown at various process durations

have demonstrated that the best result in terms of well-ordered morphology was obtained for short (about 2 min) processes, which are enabled by strong material and energy fluxes from active plasma environment; however, short process still results in a low-density graphene array. The analytical model was then used to provide a deep insight in these processes, based on a large number of elemental events (*Figure 4.11 and 4.12* illustrates a scheme of the interactions that were taken into account). The model has enabled detailed simulation of the major parameters in the graphene arrays, as well as parameters of intermedium processes which cannot be directly measured and assessed in the experiment (e.g., relative densities of adsorbed species as a function of growth temperature and density of the ion current, and the relative densities as a function of density of the ion current). The simulation results ensured important insights and deeper understanding of the processes that govern formation of the morphology, and have revealed several important facts, such that e.g. the ions promote the adsorption of species on the surface by generating a large number of defects and activating surface bonds; ions bombard the adsorbed molecules and decompose them, promoting re-nucleation; and ensure the release of carbon atoms to be incorporated into the lattice vertical graphenes.

REFERENCES:

- [1] S. Chen and W. Yang, "Flexible low-dimensional semiconductor field emission cathodes: fabrication, properties and applications," *Journal of Materials Chemistry C*, vol. 5, pp. 10682-10700, 2017.
- [2] I. Levchenko, S. Xu, G. Teel, D. Mariotti, M. Walker, and M. Keidar, "Recent progress and perspectives of space electric propulsion systems based on smart nanomaterials," *Nature communications*, vol. 9, p. 879, 2018.
- [3] I. Levchenko, K. Bazaka, M. Keidar, S. Xu, and J. Fang, "Hierarchical Multicomponent Inorganic Metamaterials: Intrinsically Driven Self-Assembly at the Nanoscale," *Advanced Materials*, vol. 30, p. 1702226, 2018.
- [4] Z. Zhu, "An overview of carbon nanotubes and graphene for biosensing applications," *Nano-Micro Letters*, vol. 9, p. 25, 2017.
- [5] V. K. Das, Z. B. Shifrina, and L. M. Bronstein, "Graphene and graphene-like materials in biomass conversion: paving the way to the future," *Journal of Materials Chemistry A*, vol. 5, pp. 25131-25143, 2017.
- [6] S. Gadipelli, Y. Lu, N. T. Skipper, T. Yildirim, and Z. Guo, "Design of hyperporous graphene networks and their application in solid-amine based carbon capture systems," *Journal of Materials Chemistry A*, vol. 5, pp. 17833-17840, 2017.
- [7] S. Navalón, J. R. Herance, M. Álvaro, and H. García, "General aspects in the use of graphenes in catalysis," *Materials Horizons*, vol. 5, pp. 363-378, 2018.
- [8] B. Qiu, M. Xing, and J. Zhang, "Recent advances in three-dimensional graphene based materials for catalysis applications," *Chemical Society Reviews*, vol. 47, pp. 2165-2216, 2018.
- [9] X. Hu, D. Bai, Y. Wu, S. Chen, Y. Ma, Y. Lu, *et al.*, "A facile synthesis of reduced holey graphene oxide for supercapacitors," *Chemical Communications*, vol. 53, pp. 13225-13228, 2017.
- [10] A. Abdelkader and D. Fray, "Controlled electrochemical doping of graphene-based 3D nanoarchitecture electrodes for supercapacitors and capacitive deionisation," *Nanoscale*, vol. 9, pp. 14548-14557, 2017.
- [11] S. Wang, H. Zhang, D. Zhang, Y. Ma, X. Bi, and S. Yang, "Vertically oriented growth of MoO₃ nanosheets on graphene for superior lithium storage," *Journal of Materials Chemistry A*, vol. 6, pp. 672-679, 2018.

- [12] Y.-W. Chi, C.-C. Hu, H.-H. Shen, and K.-P. Huang, "New approach for high-voltage electrical double-layer capacitors using vertical graphene nanowalls with and without nitrogen doping," *Nano letters*, vol. 16, pp. 5719-5727, 2016.
- [13] S. Liu, Y. Liu, W. Lei, X. Zhou, K. Xu, Q. Qiao, *et al.*, "Few-layered ReS₂ nanosheets vertically aligned on reduced graphene oxide for superior lithium and sodium storage," *Journal of Materials Chemistry A*, vol. 6, pp. 20267-20276, 2018.
- [14] X. Xia, S. Deng, D. Xie, Y. Wang, S. Feng, J. Wu, *et al.*, "Boosting sodium ion storage by anchoring MoO₃ on vertical graphene arrays," *Journal of Materials Chemistry A*, vol. 6, pp. 15546-15552, 2018.
- [15] N. Otero, C. Pouchan, and P. Karamanis, "Quadratic nonlinear optical (NLO) properties of borazino (B₃N₃)-doped nanographenes," *Journal of Materials Chemistry C*, vol. 5, pp. 8273-8287, 2017.
- [16] M. V. Jacob, D. Taguchi, M. Iwamoto, K. Bazaka, and R. S. Rawat, "Resistive switching in graphene-organic device: Charge transport properties of graphene-organic device through electric field induced optical second harmonic generation and charge modulation spectroscopy," *Carbon*, vol. 112, pp. 111-116, 2017.
- [17] I. Levchenko, M. Keidar, J. Cantrell, Y.-L. Wu, H. Kuninaka, K. Bazaka, *et al.*, "Explore space using swarms of tiny satellites," ed: Nature Publishing Group, 2018.
- [18] I. Levchenko, K. Bazaka, T. Belmonte, M. Keidar, and S. Xu, "Advanced Materials for Next-Generation Spacecraft," *Advanced Materials*, p. 1802201, 2018.
- [19] I. Levchenko, K. Bazaka, S. Mazouffre, and S. Xu, "Prospects and physical mechanisms for photonic space propulsion," *Nature Photonics*, vol. 12, p. 649, 2018.
- [20] S. Shen, W. Guo, D. Xie, Y. Wang, S. Deng, Y. Zhong, *et al.*, "A synergistic vertical graphene skeleton and S-C shell to construct high-performance TiNb₂O₇-based core/shell arrays," *Journal of Materials Chemistry A*, vol. 6, pp. 20195-20204, 2018.
- [21] P. Zhang, Q. Liao, H. Yao, H. Cheng, Y. Huang, C. Yang, *et al.*, "Three-dimensional water evaporation on a macroporous vertically aligned graphene pillar array under one sun," *Journal of Materials Chemistry A*, vol. 6, pp. 15303-15309, 2018.
- [22] J. Yun, Y. Zhang, Y. Ren, M. Xu, J. Yan, W. Zhao, *et al.*, "Tunable band gap of graphyne-based homo-and hetero-structures by stacking sequences, strain and electric field," *Physical Chemistry Chemical Physics*, 2018.

- [23] H. Zhang, W. Ren, C. Guan, and C. Cheng, "Pt decorated 3D vertical graphene nanosheet arrays for efficient methanol oxidation and hydrogen evolution reactions," *Journal of Materials Chemistry A*, vol. 5, pp. 22004-22011, 2017.
- [24] J. He, X. Zhu, Z. Qi, C. Wang, X. Mao, C. Zhu, *et al.*, "Killing dental pathogens using antibacterial graphene oxide," *ACS applied materials & interfaces*, vol. 7, pp. 5605-5611, 2015.
- [25] G. Sahoo, S. Ghosh, S. Polaki, T. Mathews, and M. Kamruddin, "Scalable transfer of vertical graphene nanosheets for flexible supercapacitor applications," *Nanotechnology*, vol. 28, p. 415702, 2017.
- [26] O. Baranov, I. Levchenko, J. M. Bell, M. Lim, S. Huang, L. Xu, *et al.*, "From nanometre to millimetre: A range of capabilities for plasma-enabled surface functionalization and nanostructuring," *Materials Horizons*, 2018.
- [27] R. Okamoto, K. Yamasaki, and N. Sasaki, "New potential model for atomic-scale peeling of armchair graphene: toward understanding of micrometer-scale peeling," *Materials Chemistry Frontiers*, vol. 2, pp. 2098-2103, 2018.
- [28] J. Lin, H. Jia, Y. Cai, S. Chen, H. Liang, X. Wang, *et al.*, "Modifying the electrochemical performance of vertically-oriented few-layered graphene through rotary plasma processing," *Journal of Materials Chemistry A*, vol. 6, pp. 908-917, 2018.
- [29] K. Bazaka, M. V. Jacob, D. Taguchi, T. Manaka, and M. Iwamoto, "Investigation of interfacial charging and discharging in double-layer pentacene-based metal-insulator-metal device with polyterpenol blocking layer using electric field induced second harmonic generation," *Chemical Physics Letters*, vol. 503, pp. 105-111, 2011.
- [30] K. Bazaka, M. V. Jacob, and B. F. Bowden, "Optical and chemical properties of polyterpenol thin films deposited via plasma-enhanced chemical vapor deposition," *Journal of Materials Research*, vol. 26, pp. 1018-1025, 2011.
- [31] J. Ahmad, K. Bazaka, and M. V. Jacob, "Optical and surface characterization of radio frequency plasma polymerized 1-isopropyl-4-methyl-1, 4-cyclohexadiene thin films," *Electronics*, vol. 3, pp. 266-281, 2014.
- [32] S. Yang, W. Li, S. Bai, and Q. Wang, "High-performance thermal and electrical conductive composites from multilayer plastic packaging waste and expanded graphite," *Journal of Materials Chemistry C*, vol. 6, pp. 11209-11218, 2018.
- [33] A. K. Ray, R. K. Sahu, V. Rajinikanth, H. Bapari, M. Ghosh, and P. Paul, "Preparation and characterization of graphene and Ni-decorated graphene using flower petals as the precursor material," *Carbon*, vol. 50, pp. 4123-4129, 2012.

- [34] G. Faggio, A. Capasso, G. Messina, S. Santangelo, T. Dikonimos, S. Gagliardi, *et al.*, "High-temperature growth of graphene films on copper foils by ethanol chemical vapor deposition," *The Journal of Physical Chemistry C*, vol. 117, pp. 21569-21576, 2013.
- [35] N. Lisi, T. Dikonimos, F. Buonocore, M. Pittori, R. Mazzaro, R. Rizzoli, *et al.*, "Contamination-free graphene by chemical vapor deposition in quartz furnaces," *Scientific reports*, vol. 7, p. 9927, 2017.
- [36] Y. Ding, R. Wu, I. H. Abidi, H. Wong, Z. Liu, M. Zhuang, *et al.*, "Stacking-Modes-Induced Chemical Reactivity Differences on CVD-Grown Trilayer Graphene," *ACS applied materials & interfaces*, 2018.
- [37] I. Levchenko, K. Ostrikov, J. Zheng, X. Li, M. Keidar, and K. Teo, "Scalable graphene production: perspectives and challenges of plasma applications," *Nanoscale*, 2016.
- [38] O. Baranov, S. Xu, K. Ostrikov, B. Wang, U. Cvelbar, K. Bazaka, *et al.*, "Towards universal plasma-enabled platform for the advanced nanofabrication: plasma physics level approach," *Reviews of Modern Plasma Physics*, vol. 2, p. 4, 2018.
- [39] O. Baranov, K. Bazaka, H. Kersten, M. Keidar, U. Cvelbar, S. Xu, *et al.*, "Plasma under control: Advanced solutions and perspectives for plasma flux management in material treatment and nanosynthesis," *Applied Physics Reviews*, vol. 4, p. 041302, 2017.
- [40] I. Levchenko, K. Bazaka, O. Baranov, R. M. Sankaran, A. Nomine, T. Belmonte, *et al.*, "Lightning under water: Diverse reactive environments and evidence of synergistic effects for material treatment and activation," *Applied Physics Reviews*, vol. 5, p. 021103, 2018.
- [41] M. V. Jacob, R. S. Rawat, B. Ouyang, K. Bazaka, D. S. Kumar, D. Taguchi, *et al.*, "Catalyst-free plasma enhanced growth of graphene from sustainable sources," *Nano letters*, vol. 15, pp. 5702-5708, 2015.
- [42] S. S. Shams, L. S. Zhang, R. Hu, R. Zhang, and J. Zhu, "Synthesis of graphene from biomass: a green chemistry approach," *Materials Letters*, vol. 161, pp. 476-479, 2015.
- [43] K. Bazaka, M. V. Jacob, and K. Ostrikov, "Sustainable Life Cycles of Natural-Precursor-Derived Nanocarbons," *Chemical reviews*, 2016.
- [44] Z. Bo, Y. Yang, J. Chen, K. Yu, J. Yan, and K. Cen, "Plasma-enhanced chemical vapor deposition synthesis of vertically oriented graphene nanosheets," *Nanoscale*, vol. 5, pp. 5180-5204, 2013.
- [45] V. Krivchenko, V. Dvorkin, N. Dzbanovsky, M. Timofeyev, A. Stepanov, A. Rakhimov, *et al.*, "Evolution of carbon film structure during its catalyst-free growth in the plasma of direct current glow discharge," *Carbon*, vol. 50, pp. 1477-1487, 2012.

- [46] Z. Shen, V. Mishra, B. Imison, M. Palmer, and R. Fairclough, "Use of adsorbent and supercritical carbon dioxide to concentrate flavor compounds from orange oil," *Journal of agricultural and food chemistry*, vol. 50, pp. 154-160, 2002.
- [47] E. Sandoz-Rosado, W. Page, D. O'Brien, J. Przepioski, D. Mo, B. Wang, *et al.*, "Vertical graphene by plasma-enhanced chemical vapor deposition: Correlation of plasma conditions and growth characteristics," *Journal of Materials Research*, vol. 29, pp. 417-425, 2014.
- [48] O. Baranov, I. Levchenko, S. Xu, J. Lim, U. Cvelbar, and K. Bazaka, "Formation of vertically oriented graphenes: what are the key drivers of growth?," *2D Materials*, vol. 5, p. 044002, 2018.
- [49] C. Yang, H. Bi, D. Wan, F. Huang, X. Xie, and M. Jiang, "Direct PECVD growth of vertically erected graphene walls on dielectric substrates as excellent multifunctional electrodes," *Journal of Materials Chemistry A*, vol. 1, pp. 770-775, 2013.
- [50] I. Levchenko, M. Keidar, S. Xu, H. Kersten, and K. Ostrikov, "Low-temperature plasmas in carbon nanostructure synthesis," *Journal of Vacuum Science & Technology B, Nanotechnology and Microelectronics: Materials, Processing, Measurement, and Phenomena*, vol. 31, p. 050801, 2013.
- [51] C. Munkel and D. W. Heermann, "Fractal dimensions of dynamically triangulated random surfaces," *Journal de Physique I*, vol. 2, pp. 2181-2190, 1992.
- [52] P. Lehmann, M. Berchtold, B. Ahrenholz, J. Tölke, A. Kaestner, M. Krafczyk, *et al.*, "Impact of geometrical properties on permeability and fluid phase distribution in porous media," *Advances in Water Resources*, vol. 31, pp. 1188-1204, 2008.
- [53] M. Rodríguez-Valverde, P. Ramón-Torregrosa, and M. Cabrerizo-Vílchez, "Estimation of percolation threshold of acid-etched titanium surfaces using Minkowski functionals," *Microscopy: Science, Technology, Applications and Education*, vol. 3, pp. 1978-1983, 2010.
- [54] C. Arns, M. Knackstedt, and K. Mecke, "Reconstructing complex materials via effective grain shapes," *Physical Review Letters*, vol. 91, p. 215506, 2003.
- [55] K. Mecke and C. Arns, "Fluids in porous media: a morphometric approach," *Journal of Physics: Condensed Matter*, vol. 17, p. S503, 2005.
- [56] H. Rajaram, L. A. Ferrand, and M. A. Celia, "Prediction of relative permeabilities for unconsolidated soils using pore-scale network models," *Water Resources Research*, vol. 33, pp. 43-52, 1997.
- [57] R. Monetti, J. Bauer, I. Sidorenko, D. Müller, E. Rummeny, M. Matsuura, *et al.*, "Assessment of the human trabecular bone structure using Minkowski Functionals," in *Medical Imaging*

- 2009: *Biomedical Applications in Molecular, Structural, and Functional Imaging*, 2009, p. 72620N.
- [58] D. Mariotti, H. Lindström, A. C. Bose, and K. K. Ostrikov, "Monoclinic β -MoO₃ nanosheets produced by atmospheric microplasma: application to lithium-ion batteries," *Nanotechnology*, vol. 19, p. 495302, 2008.
- [59] K. Michielsen and H. De Raedt, "Integral-geometry morphological image analysis," *Physics Reports*, vol. 347, pp. 461-538, 2001.
- [60] P. T. Lillehei, J.-W. Kim, L. J. Gibbons, and C. Park, "A quantitative assessment of carbon nanotube dispersion in polymer matrices," *Nanotechnology*, vol. 20, p. 325708, 2009.
- [61] I. Levchenko, K. Ostrikov, D. Mariotti, and V. Švrček, "Self-organized carbon connections between catalyst particles on a silicon surface exposed to atmospheric-pressure Ar+ CH₄ microplasmas," *Carbon*, vol. 47, pp. 2379-2390, 2009.
- [62] D. Legland, K. Kiêu, and M.-F. Devaux, "Computation of Minkowski measures on 2D and 3D binary images," *Image Analysis & Stereology*, vol. 26, pp. 83-92, 2011.
- [63] J.-F. Gouyet, *Physics and fractal structures*: Springer Verlag, 1996.
- [64] A. Van Put, A. Vertes, D. Wegrzynek, B. Treiger, and R. Van Grieken, "Quantitative characterization of individual particle surfaces by fractal analysis of scanning electron microscope images," *Fresenius' journal of analytical chemistry*, vol. 350, pp. 440-447, 1994.
- [65] J. Kou, Y. Liu, F. Wu, J. Fan, H. Lu, and Y. Xu, "Fractal analysis of effective thermal conductivity for three-phase (unsaturated) porous media," *Journal of applied physics*, vol. 106, p. 054905, 2009.
- [66] O. Bacchi, K. Reichardt, and N. Villa Nova, "Fractal scaling of particle and pore size distributions and its relation to soil hydraulic conductivity," *Scientia Agricola*, vol. 53, pp. 356-356, 1996.
- [67] C. Ruffet, Y. Gueguen, and M. Darot, "Complex conductivity measurements and fractal nature of porosity," *Geophysics*, vol. 56, pp. 758-768, 1991.
- [68] C. Douketis, Z. Wang, T. L. Haslett, and M. Moskovits, "Fractal character of cold-deposited silver films determined by low-temperature scanning tunneling microscopy," *Physical Review B*, vol. 51, p. 11022, 1995.
- [69] K. R. Mecke, "Additivity, convexity, and beyond: applications of Minkowski Functionals in statistical physics," in *Statistical Physics and Spatial Statistics*, ed: Springer, 2000, pp. 111-184.

- [70] F. De Nicola, P. Castrucci, M. Scarselli, F. Nanni, I. Cacciotti, and M. De Crescenzi, "Multi-fractal hierarchy of single-walled carbon nanotube hydrophobic coatings," *Scientific reports*, vol. 5, p. 8583, 2015.
- [71] N. Curien and J.-F. Le Gall, "Random recursive triangulations of the disk via fragmentation theory," *The Annals of Probability*, vol. 39, pp. 2224-2270, 2011.
- [72] N. Broutin and H. Sulzbach, "The dual tree of a recursive triangulation of the disk," *The Annals of Probability*, vol. 43, pp. 738-781, 2015.
- [73] H. Yoshimura, S. Yamada, A. Yoshimura, I. Hirose, K. Kojima, and M. Tachibana, "Grazing incidence X-ray diffraction study on carbon nanowalls," *Chemical Physics Letters*, vol. 482, pp. 125-128, 2009.
- [74] A. Yoshimura, H. Yoshimura, S. C. Shin, K.-i. Kobayashi, M. Tanimura, and M. Tachibana, "Atomic force microscopy and Raman spectroscopy study of the early stages of carbon nanowall growth by dc plasma-enhanced chemical vapor deposition," *Carbon*, vol. 50, pp. 2698-2702, 2012.
- [75] I. Levchenko, K. Ostrikov, K. Diwan, K. Winkler, and D. Mariotti, "Plasma-driven self-organization of Ni nanodot arrays on Si (100)," *Applied Physics Letters*, vol. 93, p. 183102, 2008.
- [76] R. Atif and F. Inam, "Modeling and simulation of graphene based polymer nanocomposites: advances in the last decade," *Graphene*, vol. 5, pp. 96-142, 2016.
- [77] C. Kittel and H. Kroemer, "Thermal Physics. WH Freeman," *New York*, 1980.
- [78] S. Stankovich, D. A. Dikin, G. H. Dommett, K. M. Kohlhaas, E. J. Zimney, E. A. Stach, *et al.*, "Graphene-based composite materials," *nature*, vol. 442, p. 282, 2006.
- [79] F. F. Chen, "Introduction to plasma physics and controlled fusion, Volume 1: Plasma physics," *Plenum Press, NY*, 1984.
- [80] M. Zhu, J. Wang, B. C. Holloway, R. Outlaw, X. Zhao, K. Hou, *et al.*, "A mechanism for carbon nanosheet formation," *Carbon*, vol. 45, pp. 2229-2234, 2007.
- [81] G. Filipič, O. Baranov, M. Mozetič, and U. Cvelbar, "Growth dynamics of copper oxide nanowires in plasma at low pressures," *Journal of Applied Physics*, vol. 117, p. 043304, 2015.
- [82] K. Davami, M. Shaygan, N. Kheirabi, J. Zhao, D. A. Kovalenko, M. H. Rummeli, *et al.*, "Synthesis and characterization of carbon nanowalls on different substrates by radio frequency plasma enhanced chemical vapor deposition," *Carbon*, vol. 72, pp. 372-380, 2014.

- [83] G. Filipič, O. Baranov, M. Mozetič, K. Ostrikov, and U. Cvelbar, "Uniform surface growth of copper oxide nanowires in radiofrequency plasma discharge and limiting factors," *Physics of Plasmas*, vol. 21, p. 113506, 2014.
- [84] V. F. Zaitsev and A. D. Polyanin, *Handbook of exact solutions for ordinary differential equations*: CRC press, 2002.
- [85] X.-P. Chen, N. Yang, J.-M. Ni, M. Cai, H.-Y. Ye, C. Wong, *et al.*, "Density-functional calculation of methane adsorption on graphenes," *IEEE Electron Device Lett*, vol. 36, pp. 1366-1368, 2015.
- [86] M. Gallouze, A. Kellou, and M. Drir, "Adsorption isotherms of H₂ on defected graphene: DFT and Monte Carlo studies," *International Journal of Hydrogen Energy*, vol. 41, pp. 5522-5530, 2016.
- [87] K. May, S. Dapprich, F. Furche, B. V. Unterreiner, and R. Ahlrichs, "Structures, C–H and C–CH₃ bond energies at borders of polycyclic aromatic hydrocarbons," *Physical Chemistry Chemical Physics*, vol. 2, pp. 5084-5088, 2000.
- [88] L. Jiang, T. Yang, F. Liu, J. Dong, Z. Yao, C. Shen, *et al.*, "Controlled synthesis of large-scale, uniform, vertically standing graphene for high-performance field emitters," *Advanced Materials*, vol. 25, pp. 250-255, 2013.
- [89] D. J. Cott, M. Verheijen, O. Richard, I. Radu, S. De Gendt, S. van Elshocht, *et al.*, "Synthesis of large area carbon nanosheets for energy storage applications," *Carbon*, vol. 58, pp. 59-65, 2013.
- [90] X. Song, J. Liu, L. Yu, J. Yang, L. Fang, H. Shi, *et al.*, "Direct versatile PECVD growth of graphene nanowalls on multiple substrates," *Materials Letters*, vol. 137, pp. 25-28, 2014.

Chapter 5

One-step Plasma-assisted Synthesis of Graphene from *Citrus sinensis* oil: Acetone Sensors and Evidence of Onion-like Structures

Citrus sinensis essential oil, a volatile aroma liquid composed of non-synthetic hydrocarbon compounds, was successfully reformed in a single-step, environmentally sustainable radio frequency plasma enhanced chemical vapor deposition into the ordered patterns of vertically oriented graphene nanosheets of complex structure incorporating the onion-like structures (multi-layer fullerenes), and their potential for gas sensing application is demonstrated in this chapter. Laser Raman spectroscopy, scanning and transmission electron microscopies, as well as sophisticated statistical and morphological analyses were used to probe deep into the structure of graphenes formed on four various conducting and insulating substrates. Highly promising for various applications such as sensing and catalysis, 3D nanoporous onion-like loop nanostructures were then unveiled, and the mechanism of their formation was suggested. The surface energy of the graphene patterns was then calculated by three different surface energy models. Finally, integration of *C. sinensis* oil derived graphene patterns into a chemiresistor prototype sensor has revealed a promising sensing activity towards acetone. S. Alancherry, K. Bazaka, I. Levchenko, A. Al-Jumaili, O. K. Varghese and M. V. Jacob, “One-step plasma assisted synthesis of graphene from *Citrus sinensis* oil for acetone gas sensors”, has been submitted to Carbon.

5.1 Introduction

Graphene, an atomically thin and hexagonally oriented lattice of sp^2 hybridized carbon atoms perpetuate the scientific interest over wide range of applications since inception. The 2-D crystalline carbon framework with its extraordinary carrier mobility [1], large surface-to-volume ratio, transparency [2], mechanical flexibility and robustness [3] extend its application potential to high frequency nano electronics [4], energy storage [5], photovoltaics [6], sensors [7], and transparent conductors [8]. Exhibiting a layer dependent physical properties, the current progress has enabled the fabrication of single, few layered graphene through a range of techniques such as micromechanical exfoliation [9], chemical vapor deposition (CVD) [10], epitaxial growth [11], and plasma enhanced chemical vapor deposition (PECVD) [12] along with the quality assessment [13]. However, most of these techniques either employ highly purified petroleum derived compressed precursor gases or require multistep solvent assisted process and hence consumes more energy, resources and money. Therefore, it is essential to identify novel bio renewable precursors and efficient fabrication techniques for the development of graphene at lower cost and minimal environmental impact.

The ever-increasing demand for graphene in advanced applications necessitate scalable and economically affordable growth on arbitrary substrates. As far as scalability is concerned, thermal CVD is promising for large area wafer-sized high quality graphene growth [14]. Nevertheless, CVD demanded high reaction temperature (900–1200°C) and long-lasting catalyst aided process that impose laborious post-growth graphene transfer procedure thus enhances the total production cost [15-17]. On the other hand, micromechanical exfoliation restricted to laboratory scale production and epitaxial growth required extremely high vacuum (10^{-4} to 10^{-9} Torr) and temperature (1200-1600°C) [18]. In this context, PECVD was recognized for single-step, non-precursor specific, catalyst-free and low temperature fabrication of graphene [19-21]. Since the first ever synthesis of few layers of graphene through PECVD by Wang and coworkers [22] much attention was focused in this area and recent studies have demonstrated very low temperature fabrication of graphene from hydrocarbon sources [23-25].

Recent investigations have revealed considerable advancements in the development of graphene from bio-renewable resources principally aimed to achieve the futuristic goal of implementing

sustainable technologies for safe future [20, 21]. Until now, different approaches such as thermal CVD, simultaneous carbonization and thermal exfoliation have been employed to convert various natural carbon sources like biomass, plant extracts, waste plastics, food/insect waste etc. to graphene nanostructures [26-28]. However, these techniques to some extent challenge the sustainability as the reformation process involve high temperature consumption, catalyst assistance and harsh chemical treatments. As an alternative approach that is more environmentally friendly and efficient, PECVD technique has been acknowledged, owing to its outstanding capability to break and rebuild virtually any type precursors to functional nanomaterials [21, 29, 30]. However only handful of literatures were published so far on the plasma assisted synthesis of graphene from non-conventional resources and hence there exist plenty of space to research.

Gas sensors play crucial role in various domains of industries, environment, agriculture and health for detecting dangerous gases and volatile organic compounds bio marking different diseases. Strongly defined by the delocalized electrons, carrier mobility of graphene can be significantly altered by the adsorption or desorption of molecules, therefore widely employed in gas sensing and biosensing applications [31, 32]. With its atomic thinness and low noise level graphene based sensors demonstrated exceptionally high sensitivity even towards single gas molecule [33, 34]. Driven by the huge surface-to-volume ratio a large body of literature have been published on graphene sensors for the selective detection of different gases such as NH_3 [35], NO_2 [34], CO_2 [36], CO [37], H_2S [38], $\text{C}_3\text{H}_6\text{O}$ [39] etc. in trace concentrations. Meanwhile, efforts are also devoted to enhance the performance of graphene based gas sensors by improving the sensitivity, reproducibility and cross sensing at room temperature and under humid conditions [34]. However, environmentally sustainable and economically feasible fabrication of graphene based gas sensors is yet challenging due to the high production cost imposed by expensive precursors and complex production techniques. To this end plasma derived graphene from natural resources are prospective candidates.

This chapter reports a simple and environmentally benign RF-PECVD fabrication of vertically oriented graphene nanostructures from a renewable precursor *C. sinensis* essential oil and its potential for gas sensing application. Firstly, through RF-PECVD vertical graphene nanostructures were

fabricated on different substrates such as copper, nickel, silicon and quartz. The extent to which the substrate influenced structural, topographical and chemical properties of plasma synthesized vertical graphene arrays were studied with the help of laser Raman spectroscopy, scanning electron microscopy, 2-D Fast Fourier Transform and X-ray photoelectron spectroscopy techniques. A set of three different surface energy model was employed to estimate the surface energy. Finally, a chemiresistor sensor prototype incorporated with *C. sinensis* essential oil derived graphene was fabricated and evaluated its sensing performance towards acetone gas.

5.2 Experimental

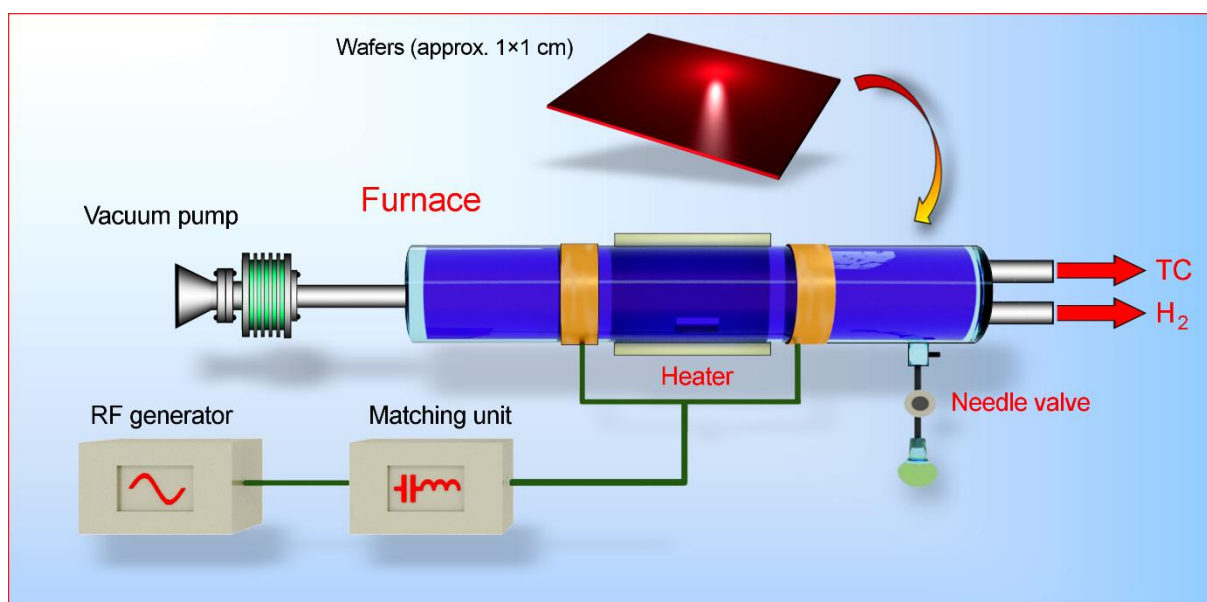


Figure 5.1 Custom-made quartz tube plasma enhanced chemical vapor deposition system.

The fabrication of graphene was carried out using a custom-made quartz tube RF-PECVD system. Figure 5.1 depicts the schematic of the experimental set up. Different substrates copper, nickel, quartz and Si/SiO₂ having size (1×1 cm) were selected for this study. Prior to deposition, the substrates were cleaned by sonicating with acetone (5 min), isopropanol (5 min) and finally dried with N₂ gas. Cleaned substrates were loaded into an alumina boat and arranged at the middle of the reactor. The tube was then pumped down to a base pressure 0.03 mbar and the substrate was heated up to 750°C. Following this, hydrogen gas was flown into the system at a flow rate 30 sccm and the system pressure

was adjusted to 0.3 mbar. The RF energy from *Navio* RF generator (13.56 MHz, 1.2 kW max) capacitively coupled to the quartz tube reactor via an impedance matching network and two external copper electrodes. Prior to deposition of graphene, plasma was ignited at 500W and the substrates were pre-etched for 1m to remove any contaminants remained on the surface. Subsequently, the *C.sinensis* vapor was fed into the reactor via needle valve and the deposition was carried out for 6 minutes. Confocal laser Raman spectroscopy (Witec, 532 nm laser) and scanning electron microscopy (Hitachi SU 5000) were used to investigate the structural and morphological features. The elemental analysis was carried out using X-ray photoelectron spectroscopy (Physical Electronics Model 5700 with an Al x-ray source). A MultipakTM software was used for data processing. The transmission electron microscopic images were obtained using a TEM. The contact angle measurements were performed using KSV 101 system. Surface energy was calculated using Owens, Wendt, Rabel and Kaelble (OWRK) approach, Van Oss Chaudhary and Good method and Neumann model.

The environmental response of the graphene films on quartz substrates were studied by exposing them to the test gas/vapor atmosphere and monitoring the resistance as a function of time. Circular platinum electrodes of thickness about 100 nm, diameter 1 mm with center to center spacing about 2 mm were formed on the surface of a graphene film by direct current (dc) sputtering. The sample was then loaded inside a stainless steel chamber fitted with a septum sealed port for injecting the gases or vapors of interest. Gas flushing lines also were connected to the chamber. Electrical contacts were taken from the platinum electrodes using platinum wires. The resistance was measured using a Picoammeter (Keithley 6487) interfaced with a computer. A constant 0.5 V was applied to measure the resistance. While a calibrated syringe was used to inject a known amount of gas/vapor into the chamber, argon was used to flush the chamber and remove the test gas environment. The argon flow was controlled by a mass flow controller (MKS Instruments). After loading the sample, the chamber was flushed with Ar till the baseline resistance was stabilized. This was followed by stopping the argon flow, sealing the chamber and injecting a known amount of test gas/vapor into the chamber. After the resistance reached a saturation level, the gas inlet and outlet were opened and the chamber was again

flushed with argon. The resistance was monitored the whole time using a computer. The sensitivity S was calculated using the relation

$$S = \frac{R_g - R_{air}}{R_{air}} 100\%$$

5.3 Results and Discussion

5.3.1 Raman characterization of plasma derived vertically oriented graphene

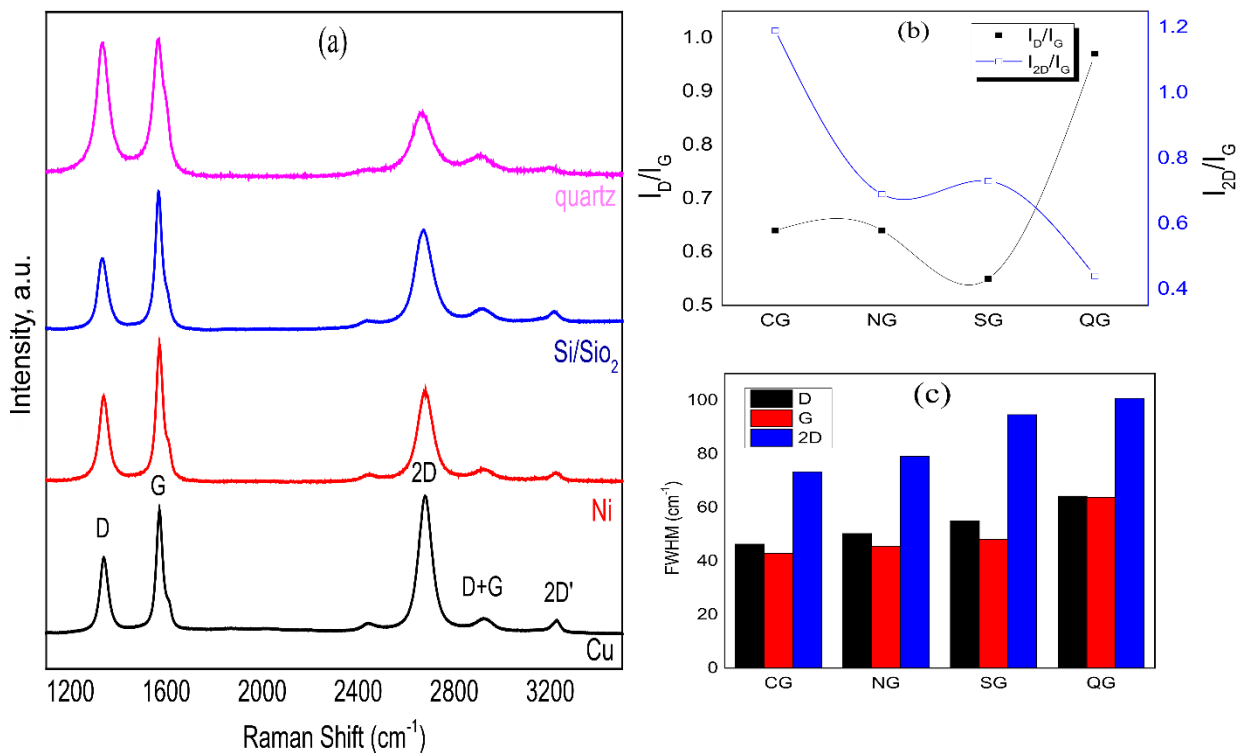


Figure 5.2 Raman characterization of plasma synthesized vertically-oriented graphene samples (a) Raman spectra of graphene deposited on copper, nickel, Si/SiO₂ and quartz substrates, (b) Band intensity ratios and (c) FWHM for D, G and 2D Raman bands for the same set of samples.

Raman spectroscopy is a well-established technique for identifying graphene and to characterize its structural features such as defects, number of layers, impurities, strain and atomic arrangement at the edges [40]. Figure 5.2a plots the Raman spectra for vertical graphene deposited on copper (CG), nickel (NG), Si/SiO₂ (SG) and quartz (QG) substrates and confirmed the formation of multi-layer graphene with the presence of unique vibrational D, G and 2D peaks. Even though the characteristics D, G and

2D peaks were formed at nearly similar wavenumbers changes have observed in peak intensity and broadening especially for the 2D band. The D peak observed at $\sim 1340 \text{ cm}^{-1}$, generated by the A_{1g} breathing mode vibrations of hexagonal carbon rings and accounts for the various defects such as edges, vacancies, grain boundaries, doped atoms, and change in hybridization (sp^2 to sp^3) that hinder the long range order of hexagonal honeycomb lattice [40, 41]. Compared to CG, NG and SG Raman spectrum obtained from QG exhibited relatively larger D band hence indicate structure that is more defective. The typical G peak located $\sim 1570 \text{ cm}^{-1}$, related to the doubly degenerate E_{2g} phonon mode at the Brillouin zone center, originated from the first order Raman scattering from the carbon-carbon stretching vibrations [42]. In addition, the symmetry breaking due to the finite size of sp^2 hybridized crystallites caused a shoulder peak ($\sim 1620 \text{ cm}^{-1}$) intercalated with G peak termed as D' [43]. The G peak attains more intensity with respect to increase in layer numbers as more carbon contributes to similar kind of vibrations [42, 44]. The 2D band situated around 2670 cm^{-1} resulted from the second order phonon vibrations at the Brillouin zone boundary and showed a significant variation in the peak intensity with respect to the substrates. The relative intensity ratios between the prominent D, G and 2D bands were extracted from the Raman spectra and plotted at *Figure 5.2b*. The I_D/I_G ratio remained low in the range 0.64–0.55 for CG, NG and SG representing a very low defected structure but obtained relatively high for QG (0.97). Apart from this, CG presented larger intensity 2D peak and the highest I_{2D}/I_G (1.19) ratio, QZ on the other hand displayed the smallest intensity 2D peak, and the lowest I_{2D}/I_G (0.44) ratio. The FWHM for D, G and 2D were projected at *Figure 5.2c* and noticed with a steady increase in peak broadening particularly for 2D band. The CG exhibited the lowest FWHM of 73.36 cm^{-1} and increased up to 100.79 cm^{-1} for QZ, which again confirms the defective nature of QZ.

5.3.2 Morphological features of vertically oriented graphene arrays on different substrates

Figure 5.3 (a-d) presents the SEM images, three-dimensional reconstructions and EDX spectra of as-grown CG, NG, SG and QG nanosheets, respectively. As can be seen, the PECVD of *C.sinensis* oil gives rise to densely packed interconnected vertically projected free-standing carbon nanowalls irrespective of the substrates. Morphologically, QG showed a maze-like appearance while the rest of the samples have petal-like network. In addition, CG, NG and SG seems to be structurally more rigid, well separated and less defected compared to QG. The difference in the SEM images with respect to substrates may plausibly arise due to the change in the nucleation and growth rate imposed by different substrates. Worth noting, that the substrates play no role in the dissociation of molecular species in PECVD, instead the plasma-substrate interaction and the surface diffusion of growth species differ for each substrate that caused difference in the surface topology [45]. As the growth occurred both on metallic and insulating substrates under the same plasma conditions and can be extended to arbitrary substrates which make the device fabrication less complicated and economically feasible by eliminating all intricacies (formation of wrinkles and retention of impurities etc.) associated with the post-synthesis graphene transfer [16, 17]. The EDX spectra was also recorded (*Figure 5.3, right column*) as a primary tool to get an insight of the chemical composition and the extent to which the PECVD process converted the multi-component *C.sinensis* oil into graphene nanostructure. The spectra detected carbon and oxygen along with substrate constituents.

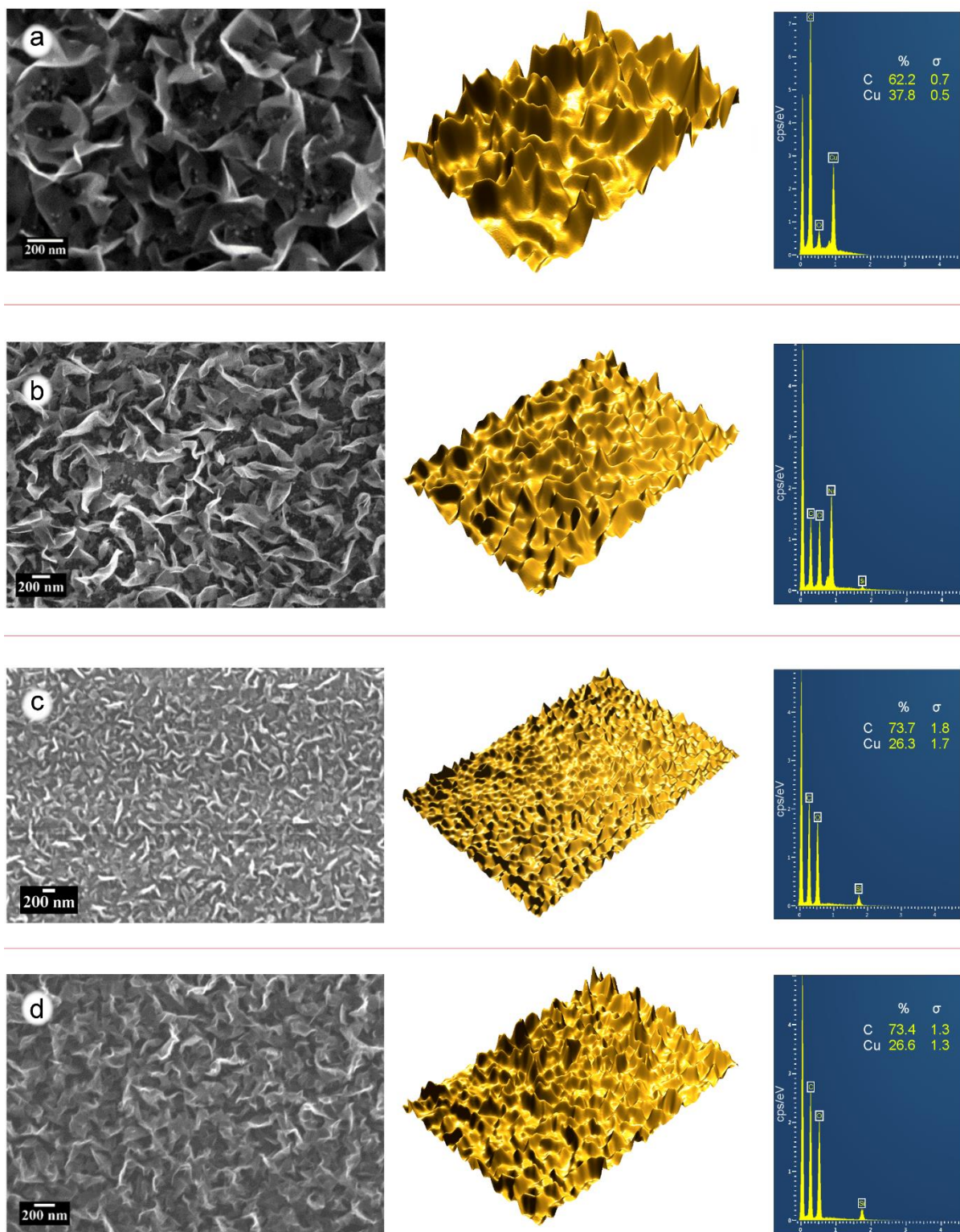


Figure 5.3 Morphological features of plasma derived vertically-oriented graphene nanostructures fabricated over different substrates. Scanning electron microscopic images (left column), three-dimensional representation of the relief (central column), and the energy dispersive X-ray diffraction spectrum (right column) for graphene patterns grown on (a) copper, (b) nickel, (c) Si/SiO₂ and (d) quartz substrates, respectively.

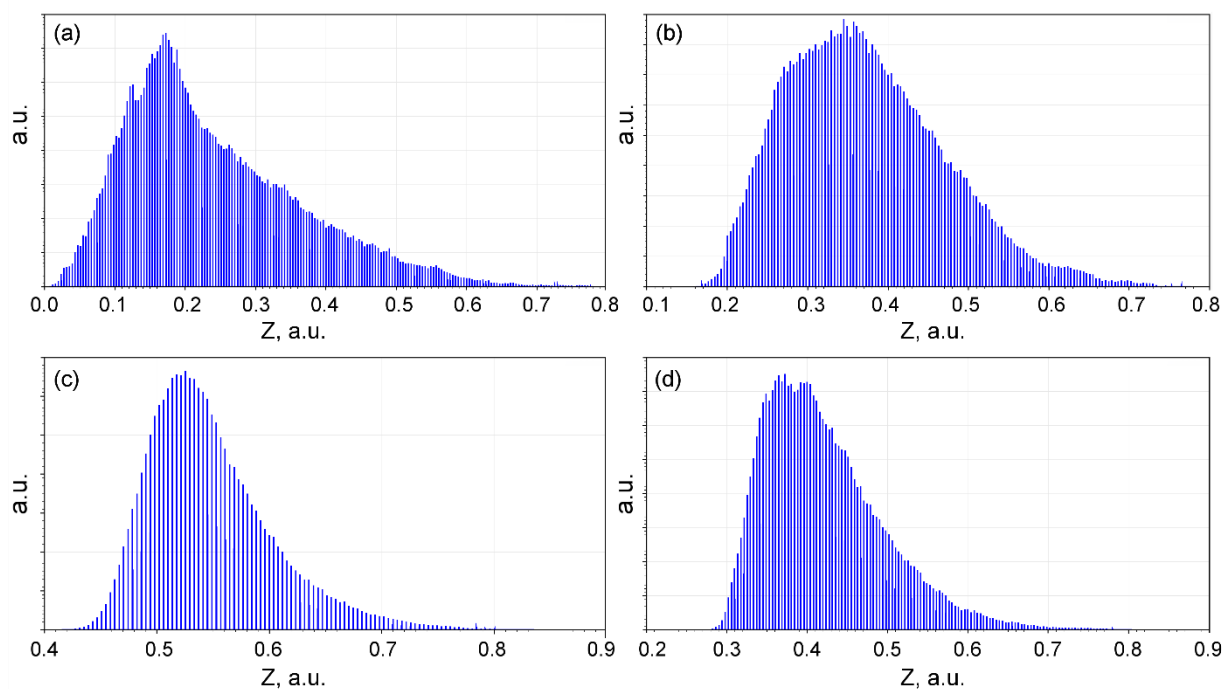


Figure 5.4 Morphological analysis of the four samples shown in Figure 5.3. Normalized height distribution functions of the vertically oriented graphene patterns on different substrates: (a) copper, (b) nickel, (c) Si/SiO₂ and (d) quartz. The pattern on Si/SiO₂ (c) demonstrates the most uniform distribution, followed by the array formed on quartz (d).

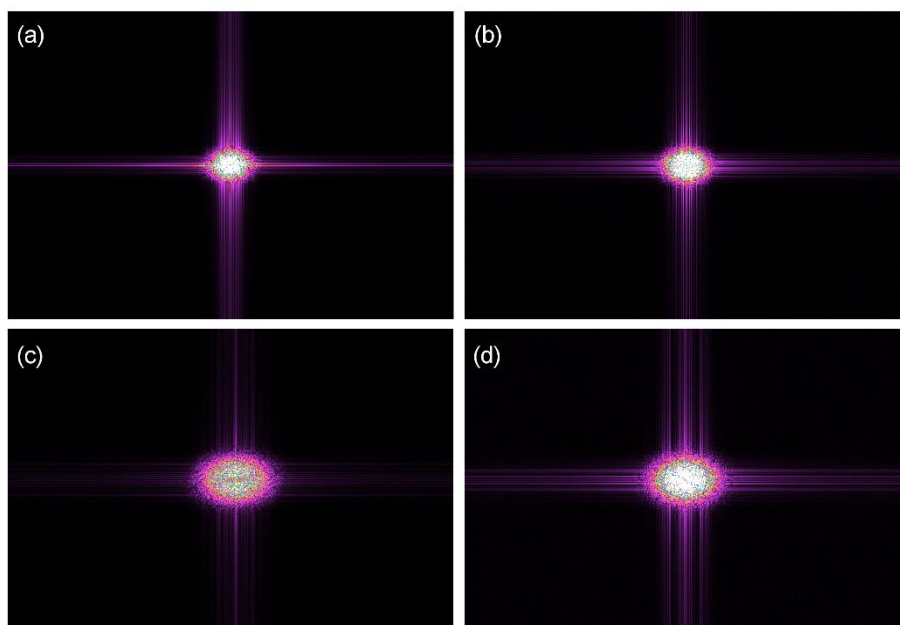


Figure 5.5 Morphological analysis of the four samples shown in Figure 5.3. 2D Fast Fourier Transform (2D FFT) spectra of the vertically-oriented graphene patterns on different substrates: (a) copper, (b) nickel, (c) Si/SiO₂ and (d) quartz. The pattern on Si/SiO₂ (c) demonstrates the most ordered (less noised) structure.

Figures 5.4 and 5.5 represent the further morphological analysis of the four samples shown in *Figure 5.3*. Normalized height distribution functions of the vertically-oriented graphene patterns on different substrates (*Figure 5.4*) reveals that the pattern grown on Si/SiO₂ (*Figure 5.4c*) demonstrates the most uniform distribution, followed by the array formed on quartz (*Figure 5.4d*). The Fast Fourier Transform (2D FFT, *Figure 5.5*) spectra of the vertically-oriented graphene patterns on different substrates also demonstrates the most ordered (less noised) structure for the pattern grown on Si/SiO₂.

5.3.3 Transmission electron microscopic studies

The TEM micrographs (*Figure 5.6*) from QG revealed the formation of closed loops and highly important onion-like carbon nanostructures resembling the multi-layer fullerenes. The size of the loop varies at different regions. To the best of our knowledge, post-synthesis techniques like Joule heating, electron beam irradiation and high temperature annealing have previously been reported that caused the formation of loops in graphene nanostructures whereby the creation of defects critically affected the curvature and physicochemical properties [46-48]. Chuvilin et al. [46] demonstrated that electron beam irradiation remove carbon atoms from the strained hexagonal graphene lattice and create pentagons that triggers the curving of graphene edges to bowl shaped fullerene structures. Similarly, non-hexagonal rings introduced into carbon nanotube structure through high energy ionic bombardment by post plasma treatments initiate bending of hexagonal nanosheets and reported to form onion-like nano-protuberance [49]. Strictly controlled by the annealing temperature Delgado et al. [47] observed a thermally induced loop formation produced by the defect annihilation mechanism upon high temperature treatments of graphitic nanoribbons. Worth noting that, plasma growth in fact simultaneously involve deposition of growth species and etching of the same from the ionic bombardments. Therefore, we assume that the high-energy ionic collisions during the plasma deposition process introduce defects in growing graphene lattice that induces curving of graphitic basal planes to eliminating dangling bonds and ultimately resulted in the loop formation. The loop formation was also noticed in CG and was given in the *Supporting Information, Figure S1*. Importantly, the onion-like structures demonstrate several exceptional properties, very important for various applications ranging from catalysis [50] to energy storage [51], electrodes in supercapacitors [52], rechargeable batteries [53, 54], and many others. Below

we will discuss briefly some plausible mechanism that may lead to the formation on onion-like structures in the plasma reactive environments.

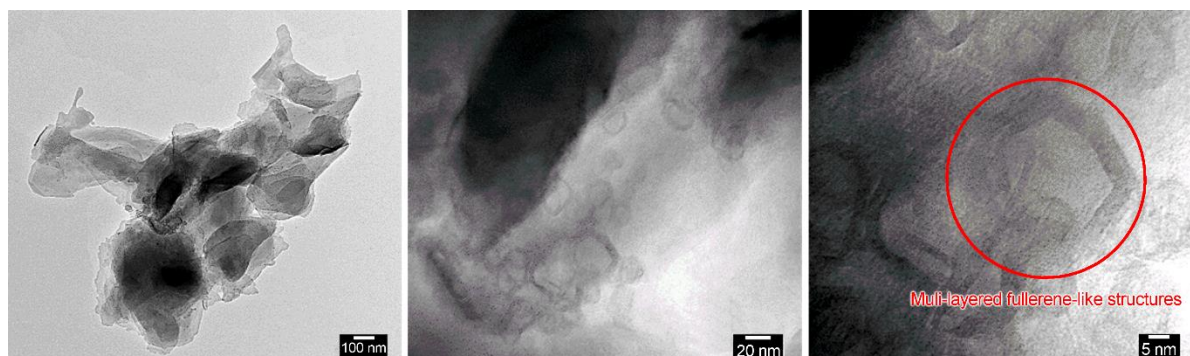


Figure 5.6 Representative transmission electron microscopic (TEM) images of graphene samples deposited on quartz substrates.

5.3.4 Plausible mechanism on nano-onions and nano-rings formation

Let us examine in short the possible mechanisms that could result in the formation of multi-layered fullerene-like nano-onions. As we have mentioned above, these structures are highly promising for various applications and a deeper understanding of the formation mechanisms, and hence the possibilities to control the structure, are required for efficient applications of these nanostructures. It should be mentioned that the two types of closed nanoparticles, namely surface-based nano-rings and nano-onions similar to multi-layered fullerenes, are possible. *Figure 5.7* illustrates the rings (a) and onions (multi-layered fullerenes) (b), both are important for the applications due to high specific surface area and specific surface energy.

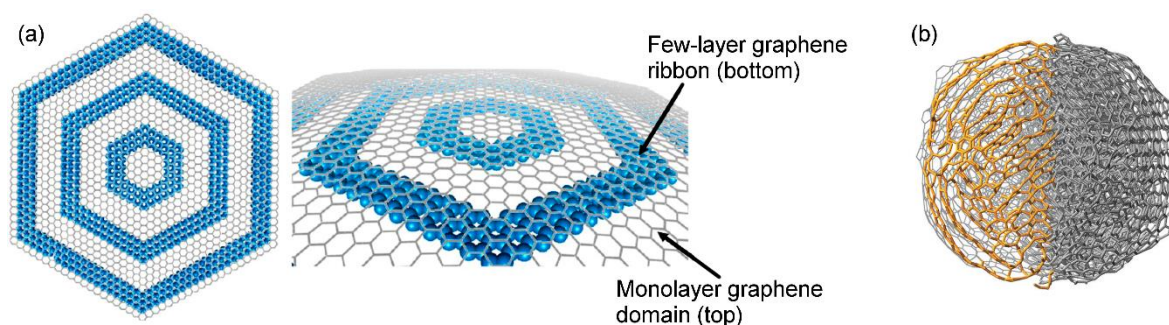


Figure 5.7 (a) Formation carbon rings on surface. This system is a combination of the topside monolayer graphene domain (gray) and the bottom side few-layer graphene ribbons (blue), are synthesized on Cu foils by heating in a H_2/CH_4 atmosphere at 1074 °C. Reprinted from [55]. Note that our structures were synthesized at much lower temperatures, due to strong activation by plasma-accelerated ions. (b) A model of three-dimensional onion-like structure. Reprinted from [51]. According to TEM observations (see also Figure S1 in the Supporting Information available), the structures close to onions shown in (b) were synthesized in this work.

Several sound mechanisms for both three- and two-dimensional structures were already discussed in the recent publications (see e.g. [51, 55]), with high temperatures and intense diffusion processes being considered as the key processes. However, while in the publications the onions of μm -scale sizes are demonstrated, our findings have revealed much smaller ('true nanoscale') structures that range from 10 to 20-30 nm in size (see TEM images in Figure 5.6, and Figure S1 in the SI available). In general, the formation and growth of similar structures is interpreted in terms of an initial nucleation (on copper or some other surface that does not feature high solubility of carbon) of small graphene nuclei, followed by the edge growth, formation of carbon ring (or multilayered structure), and repeated growth that eventually result in the formation of layered two- or three-dimensional structures of μm -scale size. Importantly, the heat process techniques require the temperatures of about 1000 °C for this kind of growth, while in our plasma-based technology we rely on much lower temperature due to strong activation by plasma-accelerated ions [56, 57]. Apart from the technological benefits and lower cost, such a process could potentially ensure much higher controllability [58] and lower level of damage to the crystalline lattice of both substrates and formed carbon nanostructures [59-61].

5.3.5 Elemental analysis of plasma synthesized vertical graphene

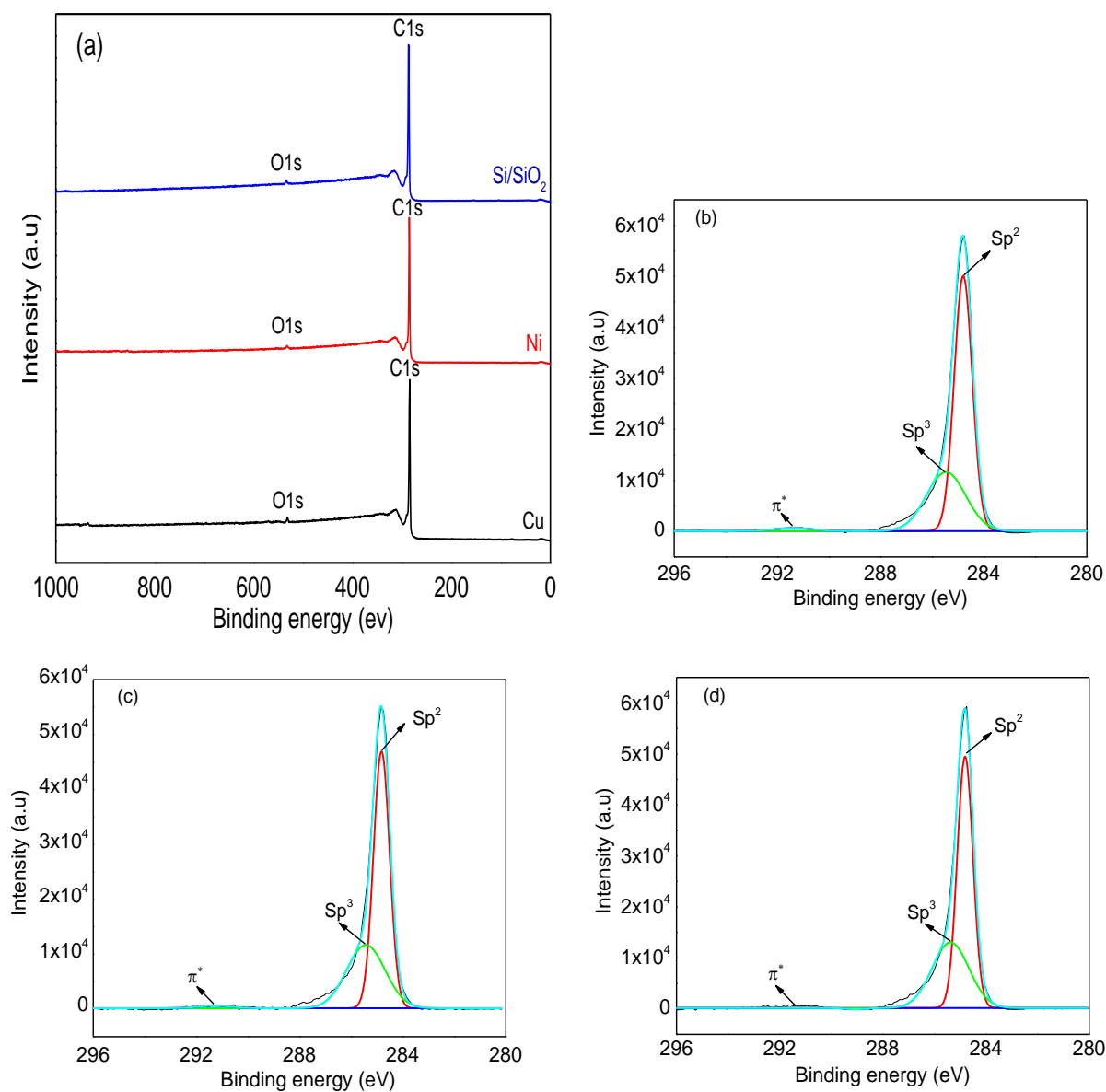


Figure 5.8 XPS spectra of vertically-oriented graphene samples grown on copper, nickel and silicon substrates (a) survey scan, (b-d) high resolution C1s scan.

The XPS spectra of graphene nanosheets derived from *C.sinensis* essential oil fabricated on different substrates was recorded and given in Figure 5.8. The survey scan of CG, NG and SG (Figure 5.8a) resemble each other, showed no apparent change in peak positions with respect to the substrates and located a single strong peak at binding energy (BE) of ~284.82eV assigned to C1s peak. In addition to this, a feeble intensity peak is formed around BE~532.45eV attributed to O1s peak, plausibly due to

the exposure of graphene samples with ambient air. The percentage of atomic concentration of carbon was estimated to 98.12, 99.27 and 98.69% for CG, NG and SG respectively. Likewise, the atomic percentage for impurity oxygen was also calculated and obtained between 1.54–0.66%. The elemental analysis confirms that the RF-PECVD and the process conditions are well enough to break and reassemble the multi-component *C. sinensis* oil into high pure graphene nanostructure (dominated by carbon element) over different conducting and insulating substrates. *Figure 5.8b-d* depict the high-resolution XPS scan of C1s band from CG, NG and SG samples. The deconvoluted C1s peak contained a major intensity band at BE~284.8 that corresponding to sp² hybridized carbon and a medium intensity band at BE~285.4 eV related with sp³ hybridized carbon in the graphene nanostructure. In addition, a very feeble peak was observed around BE~291.3 eV, corresponds to the shake-up energy loss feature.

5.3.6 Contact angle measurements and surface energy studies

Surface energy is an important surface property determining the interactions of solid surface with its surroundings. As graphene exhibit exceptionally high surface area, the interactions with the nearby environment became significant. The surface energy play critical role in the graphene–substrate adhesion and surface adsorption of biomolecules, living cells and bacteria, determining the electronic and biomedical applications of graphene [62, 63]. Hence, it is important to have a good knowledge on surface properties of graphene to make use of the excellent material properties in real applications

As most of the practical applications depends on the wettability, number of studies have been reported regarding the contact angle measurements of graphene. The wettability shows large dependence to the chemical composition and the geometric structure of the solid surface [64-66]. Exhibiting hydrophobic behavior a range of water contact angle values has reported for graphene, of which the horizontal graphene showed water contact angle within the range 90–96° [67, 68]. Moreover the contact angle was found affected by the supporting substrate [69]. Though, a high water contact angle of 127° reported for planar graphene, but challenged by researchers and theoretically arrived at a value of the order 95-100° for single layer graphene [68]. On the other hand, vertically oriented graphene exhibited highly hydrophobic behavior that originated from the combined effect of 3-D porous structure, non-polar surface nature, surface chemistry, and roughness effect [70]. Recent study by

Mohan et al. [20] reported a very high water contact angle of 135° for as-grown graphene derived from *M. alternifolia* extracts. A WCA of 152.0° was reported by Dong et al. [71] for chemically modified, microwave plasma derived vertical graphene formed on patterned silicon substrates. There are few studies reporting the tailoring the wettability of vertical graphene through controlled plasma exposure [63, 65]. Although, number of studies have been published on the WCA measurements, only a handful are extended to the surface energy analysis [72-75].

The most common way to measure the surface energy/wetting properties of graphene with reference to a liquid is by measuring the contact angle of the liquid droplet on the graphene surface. The calculation of solid surface tension from contact angle measurement is based on Young's equation described as

$$\gamma_s = \gamma_{sl} + \gamma_l \cos \theta, \quad (5.1)$$

where γ_s is the solid surface tension, γ_l is the liquid surface tension, γ_{sl} is the solid-liquid interfacial tension and θ is the contact angle. Worth noting that, the surface energy measurements depend on a particular model and selected based on the nature of surface. For non-polar surfaces, it is more likely to employ methods that do not lay on specific molecular interactions and vice versa [76]. Likewise, in order to measure the surface energy, the test liquid surface tension should be equal or greater than the expected solid surface tension, otherwise complete wetting occurs and liquid spread over the solid surface instantaneously [77].

Based on the contact angle measurements, different surface energy calculation methods such as Zisman's critical tension, acid-base approximation, Fowkes approach, Neumann method, Owens-Wendet, Berthelots approximation etc. have been developed and detailed elsewhere [75, 77, 78]. In fact, the calculated surface energy have explicit dependence on the surface energy model, and unlikely to predict the most accurate method. The present study, have chosen Neumann approach, Owens, Wendt, Rabel and Kaelble (OWRK) approach and van-Oss-Chaudhury-Good relation to calculate the surface energy of plasma synthesized vertically oriented graphene synthesized from *C.sinensis* essential oil.

The contact angles measured for SG using water, glycerol, formamide, ethyleneglycol, dimethylsulphoxide (DSMO) and diiodomethane (DIM) are tabulated along with surface tension components in Table 5.1. The as-fabricated vertically oriented graphene presented strong hydrophobic nature and displayed a high water contact angle of 129°. The second highest contact angle was measured for glycerol, 107.3°. The remaining liquids formamide, ethylene glycol, dimethyl sulfoxide and diiodomethane exhibited successively decreasing contact angle, 94.54°, 81.39°, 64.40° and 39.5° respectively (refer *Figure 5.9* and table 5.1).

Table 5.1 Polar and dispersive surface energy components and average contact angle measured for different solvents.

Solvent	Contact angle (Degrees)	Surface tension (mJ/m ²)	Surface tension components (mJ/m ²)		
			γ_1	γ_1^+	γ_1^-
Water	129.04	72.8	21.8	25.5	25.5
Glycerol	107.03	64.0	34.0	3.9	57.4
Formamide	94.54	57.5	38.5	2.3	39.6
Ethylene glycol	81.39	48.0	29.0	1.9	47.0
DSMO	64.40	43.6	35.6	0.5	32.0
DIM	39.50	50.8	50.8	-	-

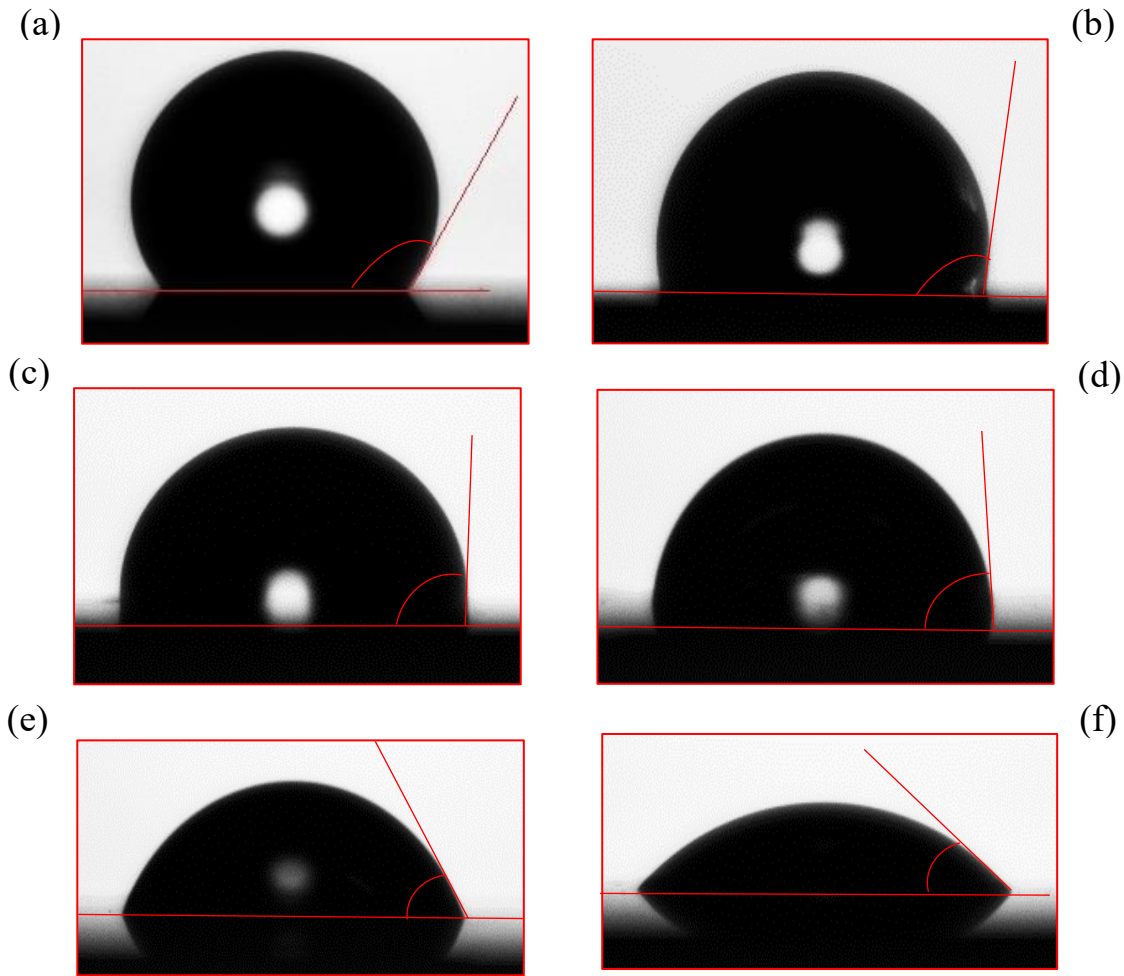


Figure 5.9 contact angle measurements on vertical graphene patterns formed on Si/SiO₂ substrates for six different test liquids, (a) water (129.04°), (b) glycerol (107.03°), (c) formamide (94.54°), (d) ethylene glycol (81.39°), (e) DSMO (64.40°) and (f) DIM (39.50°).

Van Oss Chaudhary and Good method (OCG) approach

The Van Oss Chaudhary and Good method (OCG) approach postulates that the total surface energy of a solid or liquid can be expressed as the sum of the Lifshitz-van der Waals (LW) and Lewis acid-base components.

$$\gamma_i = \gamma_i^{LW} + 2\sqrt{\gamma_i^+ \gamma_i^-}, \quad (5.2)$$

where γ_i denote the total surface tension, γ_i^{LW} represents the Lifshitz-van der Waals interaction and γ_i^+, γ_i^- corresponds to electron donor (+) and electron acceptor (-) components at the solid-liquid interface. For any solid liquid system the OCG relation described as

$$(1 + \cos\theta) \frac{\gamma_l}{2} = \sqrt{\gamma_s^d \gamma_l^d} + \sqrt{\gamma_s^+ \gamma_l^-} + \sqrt{\gamma_s^- \gamma_l^+} \quad (5.3)$$

The surface energy can be determined by solving a set of three simultaneous equations obtained by substituting contact angles and surface tension parameters for at least three solvents. A non-polar liquid ($\gamma_l^+ = \gamma_l^- = 0$) was inducted so that only Lifshitz-van der Waals interactions come into play during the course of measurements enabling the calculation of the LW parameter (dispersive component) for the solid [79]. Nevertheless, this method largely depend on the combination of liquids used and some resulted in unphysical values.

Table 5.2 combines the calculated surface tension values for seven liquid combinations obtained for SG samples. The Lifshitz-van der Waals component estimated as 39.69 mJ/m² using polar liquid diiodomethane. For majority of the liquid combinations the donor component (γ_s^-) dominates over the acceptor component (γ_s^+) revealing slightly monopolar nature of graphene surface. In addition, the total contribution from the acid base interactions found to be much lower compared to the Lifshitz-van der Waals interactions and therefore predicted that the principal contribution of graphene surface energy derive from dispersive forces. The estimated surface energy for different liquid combinations using OCG method ranges between 41-35 mJ/m².

Table 5.2. Surface tension components graphene nanosheets using OCG method for different liquid combinations

Liquid combinations	Dispersion component γ_l (mJ/m ²)	Polar components (mJ/m ²)		Surface energy γ_s (mJ/m ²)
		γ_s^+	γ_s^-	
W/EG/DIM	39.69	0.13	7.82	41.73
W/GLY/DIM	39.69	1.97	3.09	44.61
W/FMID/DIM	39.69	2.68	2.33	44.69
W/DMSO/DIM	39.69	0.24	7.13	42.33
GLY/DMSO/DIM	39.69	0.018	58.85	37.61
EG/DMSO/DIM	39.69	0.44	1.72	41.43
FMID/DSMO/DIM	39.69	0.20	104.77	35.46

Neumann surface energy model

The second approach, Neumann surface energy model was based on the equation of state theory [80]:

$$\cos\theta = -1 + 2\sqrt{\frac{\gamma_s}{\gamma_l}} e^{\beta(\gamma_s - \gamma_l)^2}, \quad (5.4)$$

where γ_s and γ_l represent the solid and liquid surface tension and β a constant coefficient specific solid surface. The Eq. 4 can be rewrite as

$$\ln\left[\gamma_l\left(\frac{1+\cos\theta}{2}\right)^2\right] = -2\beta(\gamma_s - \gamma_l)^2 + \ln(\gamma_s). \quad (5.5)$$

Neumann model calculate the surface energy by plotting the left hand side of Eq.5.5 against γ_l and fitting the generated parabolic curve with a second order polynomial to obtain the β and the γ_s . *Figure 5.10a* displays the Neumann plot created for the vertical graphene samples fabricated on silicon substrates (SG) using five different liquids. The generated parabolic curve was described by the

equation $y = -0.00225 X^2 + 0.19276 X - 1.13467$, from which the surface energy was calculated as 41.91 mJ/m².

Owens, Wendt, Rabel and Kaelble (OWRK) Approach

The OWRK model derived by assuming the total surface tension of solid and liquid as the sum of dispersive (γ^d) and polar components (γ^p). The dispersive component originates from the specific molecular interactions between the solid-liquid interface whereas the polar component resulted from all other interactions (hydrogen bonding, dipole-dipole interactions, dipole-induced dipole interactions etc.) arise due to non-London forces [78]. For any solid-liquid system the OWRK model was derived as

$$\left[\frac{1 + \cos\theta}{2} \right] X \left[\frac{\gamma_l}{\sqrt{\gamma_l^d}} \right] = \sqrt{\gamma_s^p} X \sqrt{\frac{\gamma_l^p}{\gamma_l^d}} + \sqrt{\gamma_s^d} \quad (5.6)$$

where γ , γ^d , and γ^p represent the surface tension and the respective dispersive and polar components. The subscript s and l stands for solid and liquid phases. Eq. 5.6 can be associated to the general equation for a straight line, $y = mx + c$. where y is the LHS of Eq.5.6 and x is the square root of the ratio between polar and dispersive components of the liquids (RHS). A linear regression plot between LHS and RHS of Eq.5.6 resulted in a straight line whose square of the slope and y ordinate gave the polar (γ_s^p) and dispersive (γ_s^d) component of the solid surface tension. To minimize the error, the present study used contact angle values from five test liquids. The linear fitting resulted in a straight line, $y = -2.188748x + 6.22286$ (Figure 5.10b) and the polar and dispersion components were obtained as 4.79 mJ/m² and 38.72 mJ/m² respectively. Therefore, OWRK method estimated the total surface energy as 43.51 mJ/m². The observation resulted from OCG method that dispersion component exceeds polar component was further confirmed by the similar observation obtained from the OWRK approach.

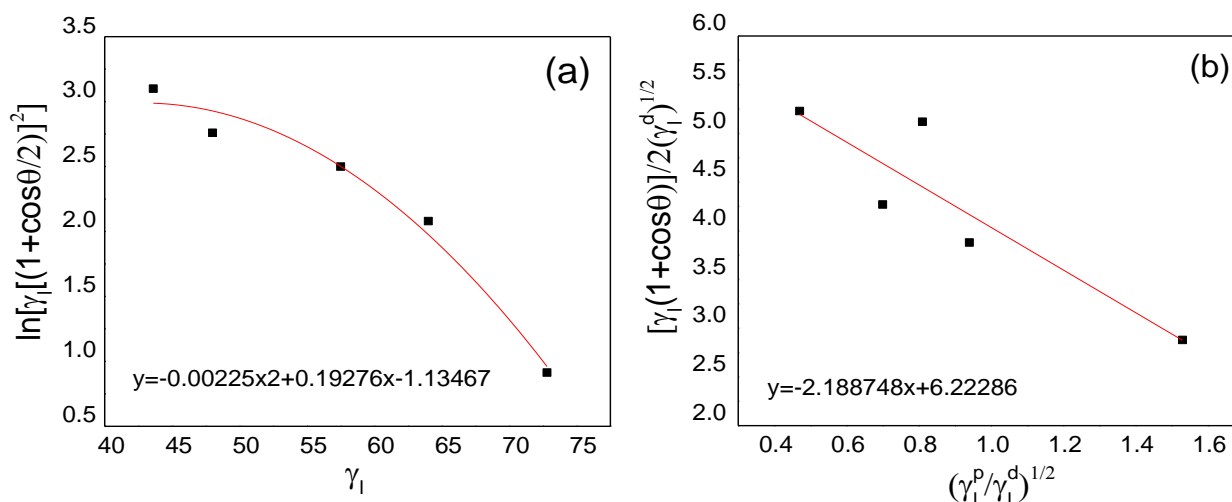


Figure 5.10 Surface energy studies of vertically oriented graphene samples fabricated on silicon substrates. Surface energy plots obtained from (a) calculated by Neumann surface energy model and (b) Owens, Wendt, Rabel and Kaelble (OWRK) Approach.

5.4 C. sinensis derived vertically oriented graphene and gas sensing properties

Acetone detection grabbed immense research interest as a noninvasive medical tool for its capability to mark early stage detection of diabetes mellitus [81]. Extensively used in industries, acetone gas also raise potential threat to human health due to its highly volatile nature and needs to be traced for facilitating a healthy and safe workplace environment. With the growing concerns, metal-oxide based sensors are vastly explored to detect acetone ranging from minute concentrations 0.6-2000 ppm, but restricted by the elevated operating temperature (200-400°C) and rigid nature [82]. On the other hand, sensors based on graphene and graphene oxide are widely recognized for its ease of fabrication, better sensing performance and flexibility. Recent study by Chia and coworkers [39] demonstrated a room temperature resistive-type monolayer graphene sensor showing enhanced reversible acetone sensitivity (100-1000 ppb). Hybrid structures formed by inducting metal oxide nanoparticles like $ZnFe_2O_4$ [83], SnO_2 [81], WO_3 [84], ZnO [85] etc. into graphene structure were also gained immense research attention for enhanced acetone sensing performance.

The acetone gas sensing performance of sensor integrated with *C. sinensis* derived vertically oriented graphene presented in Figure 5.11. In the chemiresistive type sensor, as-fabricated graphene acts as excellent channel material connecting the electrodes whose conductivity changes when subjected to test gas. Upon exposure to acetone gas the resistance of the sensor device increased as depicted by

Figure 5.11a, demonstrating the acetone sensing activity. However, the sensor device could not achieved the initial base resistance after truing the acetone supply off probably due to the incomplete removal of the test gas. Apart from good response to acetone, the chemiresistor sensor device exhibited sensing towards ammonia (NH_3) and hydrogen sulfide (H_2S) gases, shown in Figure 5.11b. Among the three gases tested, the device showed highest sensitivity towards acetone. The change in resistance towards H_2S and NH_3 were feeble and hence displayed relatively low sensitivity. As can be seen from Figure 5.11b, on supplying acetone and ammonia, the sensor device resistance increased and noticed with a positive sensitivity whereas H_2S decreased the resistance hence revealed a negative sensitivity. It can also be observed that the desorption process was gradual and the base resistance was upshifted compared to the initial base resistance after closing the acetone supply due to the retention acetone gas molecules.

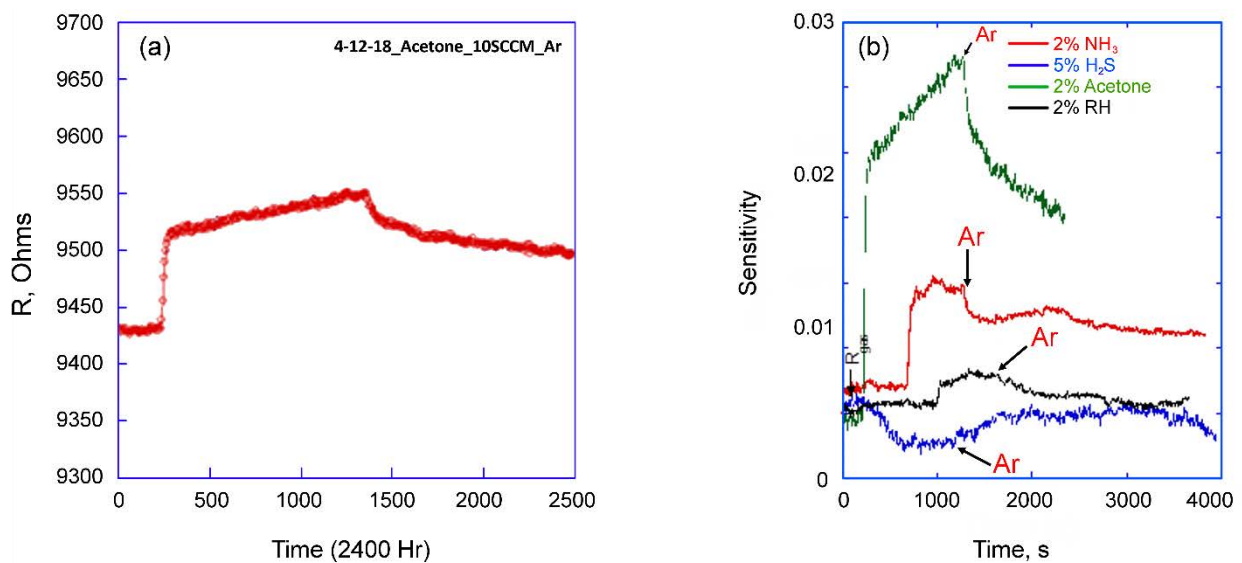


Figure 5.11 The response of the orange oil reformed graphene chemiresistive device towards acetone (a) and the selectivity of the device towards various gases (b).

5.5 Conclusion

In summary, the fabrication of vertically-aligned graphene nanosheets from *C. sinensis* essential oil on different metallic and insulating substrates through one-step environmentally benign RF-PECVD technique has been successfully demonstrated. These films predominantly composed of carbon atoms, exhibited a network of interconnected vertical graphene walls having maze-like and petal-like morphologies. The normalized height distribution and 2D-FFT profiles demonstrated that among the different substrates used, vertically-oriented graphene arrays on silicon substrates exhibited the most uniform and less noised distribution. The formation of ‘true nanoscale’ closed loops resembling multilayer fullerene was unveiled using TEM analysis and a mechanism for the formation was proposed. As-fabricated graphene measured with a high water contact angle of 129° signifying the hydrophobic behavior of the surface and the surface energy was estimated in the range 41-35 mJ/m². Finally, we fabricated a sensor device incorporated with *C.sinensis* oil derived vertical graphene and evaluated the performance towards acetone detection.

REFERENCES:

- [1] S. Morozov, K. Novoselov, M. Katsnelson, F. Schedin, D. Elias, J. Jaszczak, *et al.*, "Giant intrinsic carrier mobilities in graphene and its bilayer," *Physical Review Letters*, vol. 100, p. 016602, 2008.
- [2] R. Nair, P. Blake, A. Grigorenko, K. Novoselov, T. Booth, T. Stauber, *et al.*, "Fine structure constant defines visual transparency of graphene," *Science*, vol. 320, pp. 1308-1308, 2008.
- [3] C. Lee, X. Wei, J. W. Kysar, and J. Hone, "Measurement of the Elastic Properties and Intrinsic Strength of Monolayer Graphene," *Science*, vol. 321, pp. 385-388, July 18, 2008 2008.
- [4] C.-H. Yeh, Y.-W. Lain, Y.-C. Chiu, C.-H. Liao, D. R. Moyano, S. S. Hsu, *et al.*, "Gigahertz flexible graphene transistors for microwave integrated circuits," *ACS nano*, vol. 8, pp. 7663-7670, 2014.
- [5] Z. S. Wu, Z. Liu, K. Parvez, X. Feng, and K. Müllen, "Ultrathin Printable Graphene Supercapacitors with AC Line-Filtering Performance," *Advanced Materials*, vol. 27, pp. 3669-3675, 2015.
- [6] Y. Song, X. Li, C. Mackin, X. Zhang, W. Fang, T. s. Palacios, *et al.*, "Role of interfacial oxide in high-efficiency graphene–silicon Schottky barrier solar cells," *Nano letters*, vol. 15, pp. 2104-2110, 2015.
- [7] S. S. Varghese, S. Lonkar, K. Singh, S. Swaminathan, and A. Abdala, "Recent advances in graphene based gas sensors," *Sensors and Actuators B: Chemical*, vol. 218, pp. 160-183, 2015.
- [8] H. Sung, N. Ahn, M. S. Jang, J. K. Lee, H. Yoon, N. G. Park, *et al.*, "Transparent Conductive Oxide-Free Graphene-Based Perovskite Solar Cells with over 17% Efficiency," *Advanced Energy Materials*, vol. 6, 2016.
- [9] M. Yi and Z. Shen, "A review on mechanical exfoliation for the scalable production of graphene," *Journal of Materials Chemistry A*, vol. 3, pp. 11700-11715, 2015.
- [10] W. Fang, A. L. Hsu, Y. Song, and J. Kong, "A review of large-area bilayer graphene synthesis by chemical vapor deposition," *Nanoscale*, vol. 7, pp. 20335-20351, 2015.
- [11] G. R. Yazdi, T. Iakimov, and R. Yakimova, "Epitaxial graphene on SiC: A review of growth and characterization," *Crystals*, vol. 6, p. 53, 2016.
- [12] M. Li, D. Liu, D. Wei, X. Song, D. Wei, and A. T. S. Wee, "Controllable Synthesis of Graphene by Plasma-Enhanced Chemical Vapor Deposition and Its Related Applications," *Advanced Science*, vol. 3, 2016.

- [13] C. M. Nolen, G. Denina, D. Teweldebrhan, B. Bhanu, and A. A. Balandin, "High-throughput large-area automated identification and quality control of graphene and few-layer graphene films," *Acs Nano*, vol. 5, pp. 914-922, 2011.
- [14] S. Bae, H. Kim, Y. Lee, X. Xu, J.-S. Park, Y. Zheng, *et al.*, "Roll-to-roll production of 30-inch graphene films for transparent electrodes," *Nature nanotechnology*, vol. 5, pp. 574-578, 2010.
- [15] K. S. Kim, Y. Zhao, H. Jang, S. Y. Lee, J. M. Kim, K. S. Kim, *et al.*, "Large-scale pattern growth of graphene films for stretchable transparent electrodes," *Nature*, vol. 457, pp. 706-710, 2009.
- [16] G. Lupina, J. Kitzmann, I. Costina, M. Lukosius, C. Wenger, A. Wolff, *et al.*, "Residual metallic contamination of transferred chemical vapor deposited graphene," *ACS nano*, vol. 9, pp. 4776-4785, 2015.
- [17] A. Pirkle, J. Chan, A. Venugopal, D. Hinojos, C. Magnuson, S. McDonnell, *et al.*, "The effect of chemical residues on the physical and electrical properties of chemical vapor deposited graphene transferred to SiO₂," *Applied Physics Letters*, vol. 99, p. 122108, 2011.
- [18] W. Lu, J. J. Boeckl, and W. C. Mitchel, "A critical review of growth of low-dimensional carbon nanostructures on SiC (0 0 0 1): impact of growth environment," *Journal of Physics D: Applied Physics*, vol. 43, p. 374004, 2010.
- [19] Z. Bo, Y. Yang, J. Chen, K. Yu, J. Yan, and K. Cen, "Plasma-enhanced chemical vapor deposition synthesis of vertically oriented graphene nanosheets," *Nanoscale*, vol. 5, pp. 5180-5204, 2013.
- [20] M. V. Jacob, R. S. Rawat, B. Ouyang, K. Bazaka, D. S. Kumar, D. Taguchi, *et al.*, "Catalyst-free plasma enhanced growth of graphene from sustainable sources," *Nano letters*, vol. 15, pp. 5702-5708, 2015.
- [21] K. Bazaka, M. V. Jacob, and K. Ostrikov, "Sustainable Life Cycles of Natural-Precursor-Derived Nanocarbons," *Chemical reviews*, 2016.
- [22] J. Wang, M. Zhu, R. A. Outlaw, X. Zhao, D. M. Manos, and B. C. Holloway, "Synthesis of carbon nanosheets by inductively coupled radio-frequency plasma enhanced chemical vapor deposition," *Carbon*, vol. 42, pp. 2867-2872, // 2004.
- [23] S. Pekdemir, M. S. Onses, and M. Hancer, "Low temperature growth of graphene using inductively-coupled plasma chemical vapor deposition," *Surface and Coatings Technology*, vol. 309, pp. 814-819, 2017.

- [24] D. Wei, L. Peng, M. Li, H. Mao, T. Niu, C. Han, *et al.*, "Low Temperature Critical Growth of High Quality Nitrogen Doped Graphene on Dielectrics by Plasma-Enhanced Chemical Vapor Deposition," *ACS nano*, 2015.
- [25] R. M. Gómez, L. Mart, E. Lopez-Elvira, C. Munuera, Y. Huttel, and M. García-Hernández, "Direct Synthesis of Graphene on Silicon Oxide by low temperature Plasma Enhanced Chemical Vapor Deposition," *Nanoscale*, 2018.
- [26] G. Ruan, Z. Sun, Z. Peng, and J. M. Tour, "Growth of graphene from food, insects, and waste," *ACS nano*, vol. 5, pp. 7601-7607, 2011.
- [27] A. K. Ray, R. K. Sahu, V. Rajinikanth, H. Bapari, M. Ghosh, and P. Paul, "Preparation and characterization of graphene and Ni-decorated graphene using flower petals as the precursor material," *Carbon*, vol. 50, pp. 4123-4129, 2012.
- [28] L. Sun, C. Tian, M. Li, X. Meng, L. Wang, R. Wang, *et al.*, "From coconut shell to porous graphene-like nanosheets for high-power supercapacitors," *Journal of Materials Chemistry A*, vol. 1, pp. 6462-6470, 2013.
- [29] D. H. Seo, S. Yick, D. Su, G. Wang, Z. J. Han, and K. K. Ostrikov, "Sustainable process for all-carbon electrodes: Horticultural doping of natural-resource-derived nano-carbons for high-performance supercapacitors," *Carbon*, vol. 91, pp. 386-394, 2015.
- [30] D. H. Seo, S. Yick, Z. J. Han, J. H. Fang, and K. K. Ostrikov, "Synergistic Fusion of Vertical Graphene Nanosheets and Carbon Nanotubes for High-Performance Supercapacitor Electrodes," *ChemSusChem*, vol. 7, pp. 2317-2324, 2014.
- [31] S. Mao, G. Lu, K. Yu, Z. Bo, and J. Chen, "Specific protein detection using thermally reduced graphene oxide sheet decorated with gold nanoparticle-antibody conjugates," *Advanced materials*, vol. 22, pp. 3521-3526, 2010.
- [32] D. Khatayevich, T. Page, C. Gresswell, Y. Hayamizu, W. Grady, and M. Sarikaya, "Selective Detection of Target Proteins by Peptide-Enabled Graphene Biosensor," *Small*, vol. 10, pp. 1505-1513, 2014.
- [33] F. Schedin, A. Geim, S. Morozov, E. Hill, P. Blake, M. Katsnelson, *et al.*, "Detection of individual gas molecules adsorbed on graphene," *Nature materials*, vol. 6, pp. 652-655, 2007.
- [34] Y. H. Kim, S. J. Kim, Y.-J. Kim, Y.-S. Shim, S. Y. Kim, B. H. Hong, *et al.*, "Self-activated transparent all-graphene gas sensor with endurance to humidity and mechanical bending," *ACS nano*, vol. 9, pp. 10453-10460, 2015.

- [35] Q. Feng, X. Li, J. Wang, and A. M. Gaskov, "Reduced graphene oxide (rGO) encapsulated Co₃O₄ composite nanofibers for highly selective ammonia sensors," *Sensors and Actuators B: Chemical*, vol. 222, pp. 864-870, 2016.
- [36] X. Fan, K. Elgammal, A. D. Smith, M. Östling, A. Delin, M. C. Lemme, *et al.*, "Humidity and CO₂ gas sensing properties of double-layer graphene," *Carbon*, vol. 127, pp. 576-587, 2018.
- [37] Y. Tang, Z. Liu, Z. Shen, W. Chen, D. Ma, and X. Dai, "Adsorption sensitivity of metal atom decorated bilayer graphene toward toxic gas molecules (CO, NO, SO₂ and HCN)," *Sensors and Actuators B: Chemical*, vol. 238, pp. 182-195, 2017.
- [38] Z. Song, J. Liu, Q. Liu, H. Yu, W. Zhang, Y. Wang, *et al.*, "Enhanced H₂S gas sensing properties based on SnO₂ quantum wire/reduced graphene oxide nanocomposites: Equilibrium and kinetics modeling," *Sensors and Actuators B: Chemical*, vol. 249, pp. 632-638, 2017.
- [39] C.-M. Yang, T.-C. Chen, Y.-C. Yang, M. Meyyappan, and C.-S. Lai, "Enhanced acetone sensing properties of monolayer graphene at room temperature by electrode spacing effect and UV illumination," *Sensors and Actuators B: Chemical*, vol. 253, pp. 77-84, 2017.
- [40] A. Eckmann, A. Felten, A. Mishchenko, L. Britnell, R. Krupke, K. S. Novoselov, *et al.*, "Probing the nature of defects in graphene by Raman spectroscopy," *Nano letters*, vol. 12, pp. 3925-3930, 2012.
- [41] A. C. Ferrari and D. M. Basko, "Raman spectroscopy as a versatile tool for studying the properties of graphene," *Nature nanotechnology*, vol. 8, pp. 235-246, 2013.
- [42] Y. Hao, Y. Wang, L. Wang, Z. Ni, Z. Wang, R. Wang, *et al.*, "Probing Layer Number and Stacking Order of Few-Layer Graphene by Raman Spectroscopy," *small*, vol. 6, pp. 195-200, 2010.
- [43] D. Seo, S. Kumar, and K. Ostrikov, "Control of morphology and electrical properties of self-organized graphenes in a plasma," *Carbon*, vol. 49, pp. 4331-4339, 2011.
- [44] S. Kurita, A. Yoshimura, H. Kawamoto, T. Uchida, K. Kojima, M. Tachibana, *et al.*, "Raman spectra of carbon nanowalls grown by plasma-enhanced chemical vapor deposition," *Journal of Applied Physics*, vol. 97, pp. -, 2005.
- [45] S. Chugh, R. Mehta, N. Lu, F. D. Dios, M. J. Kim, and Z. Chen, "Comparison of graphene growth on arbitrary non-catalytic substrates using low-temperature PECVD," *Carbon*, vol. 93, pp. 393-399, 2015.
- [46] A. Chuvilin, U. Kaiser, E. Bichoutskaia, N. A. Besley, and A. N. Khlobystov, "Direct transformation of graphene to fullerene," *Nature chemistry*, vol. 2, p. 450, 2010.

- [47] J. Campos-Delgado, Y. Kim, T. Hayashi, A. Morelos-Gómez, M. Hofmann, H. Muramatsu, *et al.*, "Thermal stability studies of CVD-grown graphene nanoribbons: Defect annealing and loop formation," *Chemical Physics Letters*, vol. 469, pp. 177-182, 2009.
- [48] E. Cruz-Silva, A. R. Botello-Méndez, Z. M. Barnett, X. Jia, M. Dresselhaus, H. Terrones, *et al.*, "Controlling edge morphology in graphene layers using electron irradiation: from sharp atomic edges to coalesced layers forming loops," *Physical review letters*, vol. 105, p. 045501, 2010.
- [49] T. Feng, J. Zhang, Q. Li, X. Wang, K. Yu, and S. Zou, "Effects of plasma treatment on microstructure and electron field emission properties of screen-printed carbon nanotube films," *Physica E: Low-dimensional Systems and Nanostructures*, vol. 36, pp. 28-33, 2007.
- [50] G. Centi, K. Barbera, S. Perathoner, N. K. Gupta, E. E. Ember, and J. A. Lercher, "Onion-Like Graphene Carbon Nanospheres as Stable Catalysts for Carbon Monoxide and Methane Chlorination," *ChemCatChem*, vol. 7, pp. 3036-3046, 2015.
- [51] M. Zeiger, N. Jäckel, V. N. Mochalin, and V. Presser, "carbon onions for electrochemical energy storage," *Journal of Materials Chemistry A*, vol. 4, pp. 3172-3196, 2016.
- [52] N. Jäckel, D. Weingarth, M. Zeiger, M. Aslan, I. Grobelsek, and V. Presser, "Comparison of carbon onions and carbon blacks as conductive additives for carbon supercapacitors in organic electrolytes," *Journal of Power Sources*, vol. 272, pp. 1122-1133, 2014.
- [53] Y. Shi, Y. Wang, J. I. Wong, A. Y. S. Tan, C.-L. Hsu, L.-J. Li, *et al.*, "Self-assembly of hierarchical MoS_x/CNT nanocomposites (2 < x < 3): towards high performance anode materials for lithium ion batteries," *Scientific reports*, vol. 3, p. 2169, 2013.
- [54] J. Bartelmess and S. Giordani, "Carbon nano-onions (multi-layer fullerenes): chemistry and applications," *Beilstein journal of nanotechnology*, vol. 5, pp. 1980-1998, 2014.
- [55] Z. Yan, Y. Liu, J. Lin, Z. Peng, G. Wang, E. Pembroke, *et al.*, "Hexagonal graphene onion rings," *Journal of the American Chemical Society*, vol. 135, pp. 10755-10762, 2013.
- [56] J. Fang, I. Aharonovich, I. Levchenko, K. Ostrikov, P. G. Spizzirri, S. Rubanov, *et al.*, "Plasma-enabled growth of single-crystalline SiC/AlSiC core-shell nanowires on porous alumina templates," *Crystal Growth & Design*, vol. 12, pp. 2917-2922, 2012.
- [57] I. Levchenko, K. Bazaka, M. Keidar, S. Xu, and J. Fang, "Hierarchical Multicomponent Inorganic Metamaterials: Intrinsically Driven Self-Assembly at the Nanoscale," *Advanced Materials*, vol. 30, p. 1702226, 2018.

- [58] K. Bazaka, O. Baranov, U. Cvelbar, B. Podgornik, Y. Wang, S. Huang, *et al.*, "Oxygen plasmas: a sharp chisel and handy trowel for nanofabrication," *Nanoscale*, vol. 10, pp. 17494-17511, 2018.
- [59] O. Baranov, K. Bazaka, H. Kersten, M. Keidar, U. Cvelbar, S. Xu, *et al.*, "Plasma under control: Advanced solutions and perspectives for plasma flux management in material treatment and nanosynthesis," *Applied Physics Reviews*, vol. 4, p. 041302, 2017.
- [60] O. Baranov, I. Levchenko, S. Xu, J. Lim, U. Cvelbar, and K. Bazaka, "Formation of vertically oriented graphenes: what are the key drivers of growth?," *2D Materials*, vol. 5, p. 044002, 2018.
- [61] I. Levchenko, K. Bazaka, O. Baranov, R. M. Sankaran, A. Nomine, T. Belmonte, *et al.*, "Lightning under water: Diverse reactive environments and evidence of synergistic effects for material treatment and activation," *Applied Physics Reviews*, vol. 5, p. 021103, 2018.
- [62] Y. Yang, A. M. Asiri, Z. Tang, D. Du, and Y. Lin, "Graphene based materials for biomedical applications," *Materials Today*, vol. 16, pp. 365-373, 2013.
- [63] J. Lin, H. Jia, Y. Cai, S. Chen, H. Liang, X. Wang, *et al.*, "Modifying the electrochemical performance of vertically-oriented few-layered graphene through rotary plasma processing," *Journal of Materials Chemistry A*, vol. 6, pp. 908-917, 2018.
- [64] Y. Tian and L. Jiang, "Wetting: Intrinsically robust hydrophobicity," *Nature materials*, vol. 12, pp. 291-292, 2013.
- [65] L. Zhang, Z. Sun, J. L. Qi, J. Shi, T. Hao, and J. Feng, "Understanding the growth mechanism of vertically aligned graphene and control of its wettability," *Carbon*, vol. 103, pp. 339-345, 2016.
- [66] H. Li and X. C. Zeng, "Wetting and interfacial properties of water nanodroplets in contact with graphene and monolayer boron–nitride sheets," *ACS nano*, vol. 6, pp. 2401-2409, 2012.
- [67] Z. Li, Y. Wang, A. Kozbial, G. Shenoy, F. Zhou, R. McGinley, *et al.*, "Effect of airborne contaminants on the wettability of supported graphene and graphite," *Nature materials*, vol. 12, pp. 925-931, 2013.
- [68] F. Taherian, V. Marcon, N. F. van der Vegt, and F. Leroy, "What is the contact angle of water on graphene?," *Langmuir*, vol. 29, pp. 1457-1465, 2013.
- [69] J. Rafiee, X. Mi, H. Gullapalli, A. V. Thomas, F. Yavari, Y. Shi, *et al.*, "Wetting transparency of graphene," *Nature materials*, vol. 11, p. 217, 2012.
- [70] C. Yang, H. Bi, D. Wan, F. Huang, X. Xie, and M. Jiang, "Direct PECVD growth of vertically erected graphene walls on dielectric substrates as excellent multifunctional electrodes," *Journal of Materials Chemistry A*, vol. 1, pp. 770-775, 2013.

- [71] J. Dong, Z. Yao, T. Yang, L. Jiang, and C. Shen, "Control of superhydrophilic and superhydrophobic graphene interface," *Scientific reports*, vol. 3, p. 1733, 2013.
- [72] A. Kozbial, Z. Li, C. Conaway, R. McGinley, S. Dhingra, V. Vahdat, *et al.*, "Study on the surface energy of graphene by contact angle measurements," *Langmuir*, vol. 30, pp. 8598-8606, 2014.
- [73] A. I. Aria, P. R. Kidambi, R. S. Weatherup, L. Xiao, J. A. Williams, and S. Hofmann, "Time evolution of the wettability of supported graphene under ambient air exposure," *The Journal of Physical Chemistry C*, vol. 120, pp. 2215-2224, 2016.
- [74] Y. J. Shin, Y. Wang, H. Huang, G. Kalon, A. T. S. Wee, Z. Shen, *et al.*, "Surface-energy engineering of graphene," *Langmuir*, vol. 26, pp. 3798-3802, 2010.
- [75] S. Wang, Y. Zhang, N. Abidi, and L. Cabrales, "Wettability and surface free energy of graphene films," *Langmuir*, vol. 25, pp. 11078-11081, 2009.
- [76] C. Rulison, "So you want to measure surface energy," *A tutorial designed to provide basic understanding of the concept solid surface energy, and its many complications*, TN306/CR, pp. 1-16, 1999.
- [77] R. Deshmukh and A. Shetty, "Comparison of surface energies using various approaches and their suitability," *Journal of Applied Polymer Science*, vol. 107, pp. 3707-3717, 2008.
- [78] D. Y. Kwok and A. W. Neumann, "Contact angle measurement and contact angle interpretation," *Advances in colloid and interface science*, vol. 81, pp. 167-249, 1999.
- [79] M. Żenkiewicz, "Methods for the calculation of surface free energy of solids," *Journal of Achievements in Materials and Manufacturing Engineering*, vol. 24, pp. 137-145, 2007.
- [80] A. Neumann, R. Good, C. Hope, and M. Sejpal, "An equation-of-state approach to determine surface tensions of low-energy solids from contact angles," *Journal of Colloid and Interface Science*, vol. 49, pp. 291-304, 1974.
- [81] S.-J. Choi, B.-H. Jang, S.-J. Lee, B. K. Min, A. Rothschild, and I.-D. Kim, "Selective detection of acetone and hydrogen sulfide for the diagnosis of diabetes and halitosis using SnO₂ nanofibers functionalized with reduced graphene oxide nanosheets," *ACS applied materials & interfaces*, vol. 6, pp. 2588-2597, 2014.
- [82] A. Mirzaei, S. Leonardi, and G. Neri, "Detection of hazardous volatile organic compounds (VOCs) by metal oxide nanostructures-based gas sensors: A review," *Ceramics International*, vol. 42, pp. 15119-15141, 2016.

- [83] F. Liu, X. Chu, Y. Dong, W. Zhang, W. Sun, and L. Shen, "Acetone gas sensors based on graphene-ZnFe₂O₄ composite prepared by solvothermal method," *Sensors and Actuators B: Chemical*, vol. 188, pp. 469-474, 2013.
- [84] J. Kaur, K. Anand, A. Kaur, and R. C. Singh, "Sensitive and selective acetone sensor based on Gd doped WO₃/reduced graphene oxide nanocomposite," *Sensors and Actuators B: Chemical*, vol. 258, pp. 1022-1035, 2018.
- [85] P. Wang, D. Wang, M. Zhang, Y. Zhu, Y. Xu, X. Ma, *et al.*, "ZnO nanosheets/graphene oxide nanocomposites for highly effective acetone vapor detection," *Sensors and Actuators B: Chemical*, vol. 230, pp. 477-484, 2016.

Chapter 6

Conclusion and future work

In recent years, environmentally benign synthesis of carbon nanostructures (CNSs) has been recognized as an indispensable part of carbon nanomaterial research to address the growing environmental concerns associated with the production and implementation of nanomaterials for various advanced applications. The research and developments in this sector stem around the identification of abundant, cheap and renewable precursor materials along with the development of an appropriate technique that convert them to sustainable CNSs with better yield and performance. Noteworthy is that precursor chemistry plays a crucial role in the purity and properties of CNSs and various naturally derived sources such as waste plastics, biomass, plant extracts, food and animal waste etc. been recognized to this end. Nevertheless, efforts are afoot in search of plentiful and low cost materials to cater the huge demand. In the meantime, among the various processes developed for the breaking and reassembling various naturally derived and conventional precursors into functional nano materials, plasma enhanced chemical vapor deposition (PECVD) has emerged as the most efficient technique owing to its unique features and thus gained considerable impetus to minimize the environmental impacts and production cost.

In this thesis, an environmentally friendly RF-PECVD for the synthesis of vertical graphene nanostructures from a non-conventional resource is developed. *Citrus sinensis* essential oil, a non-synthetic renewable carbon feed stock derived from waste orange peels was selected as the processor source. The process was optimized for a range of plasma process parameters and the structural, morphological, chemical and surface properties of resulted graphene nanostructures were studied at length. Laser Raman spectroscopy and scanning electron microscopy (SEM) was used as the primary analysis tool to understand the structural and morphological evolution. A comprehensive characterization of the morphological features was done in depth using SEM, Fourier and Hough transformation, Minkowski connectivity and fractal dimensions to shed light into the morphological

transformations occurred at various plasma conditions. Besides, thorough theoretical simulated modelling of the growth of vertical graphene nanostructures is carried out at different operational modes. Furthermore, from an application point of view a gas sensor was fabricated and established to study the sensing activity towards acetone. The major finding of this thesis are as follows:

6.1 Low power RF plasma discharge: Plasma polymer thin films and fundamental properties

Polymer thin films were successfully fabricated from *C.sinensis* essential oil using RF-PECVD technique under different input RF power (10–75W) and their fundamental properties were investigated in chapter 3. The optical properties, mainly the refractive index (n), extinction coefficient (k), and the optical band gap (E_g) were determined from VASE and UV-Vis spectroscopy measurements. The films exhibited a refractive index of 1.55 (500nm) and found to be to be optically transparent in the visible region. The UV-vis spectrum showed an absorption peak around 295nm and the corresponding Tauc plot measured an optical band gap around 3.60. The FTIR measurements determined the characteristic bond vibrational frequencies and revealed the hydrocarbon rich nature of the fabricated polymer thin films. The XPS detected dominant carbon C1s peak (282 eV), feeble oxygen peak O1s (531 eV) and impurity nitrogen peak (396 eV). In addition, the atomic fraction of carbon, oxygen and nitrogen were estimated as 86.86%, 10.50% and 2.60% respectively. The AFM images unveiled the pinhole free thin films, which can be used for encapsulation layers. The average surface roughness showed a dependence to the deposition power and varied between 0.62 to 2.19 nm. To investigate the mechanical properties nanoindentation technique was employed and the hardness of the material was found to be increased from 0.50 to 0.78 GPa with the deposition power.

6.2 One-step plasma fabrication of vertical graphene: Characterization and control of morphology

Using RF-PECVD, vertically oriented graphene nanostructures were successfully fabricated from *C.sinensis* essential oil and the process optimization and comprehensive morphological characterizations were investigated in chapter 4. The evolution of structure and morphology was studied

as a function of plasma process parameters (i) input RF power (300-500W), (ii) hydrogen flow rate (10-50 sccm) and (iii) deposition duration (2-8m). The structural growth of graphene nanostructures fabricated under different plasma process conditions were explored by Raman spectroscopy. Raman spectrum of graphene samples confirmed the formation of low defect few-layered graphene, indicated by the characteristic vibrational features D (1335 cm^{-1}), G (1570 cm^{-1}) and 2D (2675 cm^{-1}) peaks and their corresponding band intensity ratios. The XPS survey scan detected dominant C1s peak (98.69%) at BE~284.5 eV unequivocally declared the predominance of elemental carbon in the resulted nanostructure produced from multicomponent *C.sinensis* precursor. Finally, the morphological growth at different process conditions was comprehensively characterized and illustrated the complex morphological transformations occurred with respect to the change in selected plasma process parameters.

RF power and morphological characteristics: The input RF power markedly control the spatial distribution of vertically erected graphene edges unveiled by the SEM analysis. A low density of distribution at 300W, higher distribution at 400W and much higher distribution at 500W was observed. In addition, the spectra of height distribution emphasized that RF power demonstrated the ability to govern the nucleation stage from short to long nucleation time. The Fourier and Hough transformation profiles displayed considerable changes that further revealed the complex morphological changes with successive increase in RF power. Besides, the fractal dimension analysis presented an increasing trend with RF power, mainly caused by the creation of new molecular fragments and their subsequent nucleation at the growth sites. Minkowski boundary distributions also found to be different, narrow at 300W, wide at 400W and narrow at 500W and in good agreement with the height distribution patterns.

Hydrogen flow rate and morphological characteristics: The density distribution of graphene nan flakes with subsequent increase in hydrogen flow rate was nonlinear and transformed through a dense (10 sccm), less dense (20 sccm), much dense (30 sccm) to rather light arrays of distributions (50 sccm). Different Fourier and Hough transformation profiles were also obtained for these samples. The Fractal dimensions were low at both lower (10 sccm) and higher (50 sccm) flow ratios, but the maximum value was obtained at 30sccm. The spectra of the fractal dimensions have confirmed that the

arrays grown at 20 and 50 sccm feature the most articulated and regular morphology. These analyses succinctly described the catalytic and etchant role played by the atomic hydrogen at lower and higher concentrations respectively.

Deposition duration: The SEM images at respective growth duration 2, 6 and 8min depicted a sequential growth of vertical graphene nanostructures from the early growth phase comprise of parallel nanocrystalline graphite layers to the final stage having completely grown non-agglomerated vertical graphene nanowalls. As observed in the previous cases, the set of sophisticated morphological analysis further showed that the morphology exhibited notable changes with deposition duration. Spectrum of fractal dimensions (calculated by triangulation) exhibited a complex dependence to deposition time whereas the power spectrum does not significantly depend on time of deposition. Minkowski boundaries distribution and Minkowski connectivity showed the widest distribution for the longer (8 minutes) process.

Finally, a multi-parameter model was employed that correlated the vertical graphene morphology with the key process parameters and intermedium processes that cannot be directly measured and assessed in the experiment. The growth parameters such as length of the vertical graphene sheet (L_{vg}) and half width of vertical graphene sheet (W_{vg}) were simulated for different operation modes. The modelling unveiled deep understanding on various processes (ion induced surface adsorption of molecular species, ion induced defect generation and surface activation etc.) that control the growth of vertical graphene nanostructures.

6.3 One-step plasma fabrication of vertical graphene: Growth on different substrates, properties and acetone gas sensing

With the optimized process, chapter 5 extended the vertical graphene growth to copper (CG), nickel (NG), quartz (QG) and Si/SiO₂ (SG) substrates and investigated how the substrate influenced the structure, morphology and chemical properties of *C.sinensis* derived graphene. With respect to the substrates, the Raman spectrum of CG, NG, QG and SG exhibited D, G and 2D peaks that formed at nearly same wavenumbers but differed in the peak intensity and peak broadening. Among the different

substrates QG denoted as more defective ($I_D/I_G=0.97$) whereas CG, NG and SG found to be less defective ($I_D/I_G=0.64-0.55$). Similarly, CG exhibited the highest I_{2D}/I_G (1.19) and QZ displayed the lowest I_{2D}/I_G (0.44). Under the same plasma conditions, different substrates gave the unique morphological features of vertical graphene arrays having Maze-like (QZ) and petal-like (CG, QG and SG) morphologies. Among the different samples studied, Fast Fourier Transform (2D FFT) spectra and height distribution profile of vertically-oriented graphene pattern on Si/SiO₂ presented the most ordered structure. The elemental concentration was calculated from XPS analysis. The C1s peak was formed at binding energy 284.5 eV and the atomic percentage was calculated 98.12% (CG), 99.27% (NG) and 98.6% (SG). The formation of unique onion-like closed loops within the graphene layers was unveiled by TEM analysis. These were previously observed in carbon nanotubes, but not in graphene.

Contact angle measurements were carried out to study the surface properties. Interestingly, the vertical graphene surface behaved as hydrophobic in nature and measured with a water contact angle of 129°. The surface energy was estimated using three different techniques Van Oss Chaudhary and Good method approach (41-35 mJ/m²), Neumann surface energy model (38.72 mJ/m²), Owens, Wendt, Rabel and Kaelble Approach (43.51 mJ/m²).

Finally, *C.sinensis* derived vertical graphene proved to be a good candidate for gas sensors and established the sensing activity towards acetone gas.

Overall, this research assisted to develop thin layers of plasma polymer thin films to few layer graphene with very novel and unique features in graphene. In a nutshell, the outcomes of this thesis significantly strengthen up the ongoing research activities in the development of vertical graphene nanostructures from bio-resources. Furthermore, it open up new avenues for Australian essential oil industry through recognition as precursors for high-end nanomaterials apart from their conventional applications.

6.4 Recommendations for future work

This research provided an efficient method for the synthesis of vertically oriented graphene from essential oils (*C.sinensis*) through green chemistry approach and revealed the structural, morphological and chemical properties of resulted graphene nanostructure.

Through comprehensive morphological characterization and theoretical modelling, the role of various plasm process parameters in architecting the unique vertical graphene morphology was clearly established. Likewise, it will be very interesting to look deep in to the plasma chemistry of *C.sinensis* oil plasma and establish its relationship with plasma process parameters. Therefore, investigations on different molecular species created during the ignition of plasma using mass spectroscopy will be important.

In fact, sustainability is subject to debate, and indeed a challenge for material scientists to make the complete cycle (i.e. precursor selection-process-nanomaterial-device fabrication) ecofriendly. In this respect, this research can be extended to analyze the constituent species in the plasma exhaust.

This research also outlined the straightaway fabrication of a sensor incorporated with *C.sinensis* oil derived graphene and its sensing activity to evaluate the performance in real application. However, present study utilized pristine *C.sinensis* reformed graphene for the sensor fabrication and testing. Meanwhile, the sensors fabricated out of hybrid structures (i.e. graphene incorporated with nanoparticles and metal oxide semiconductors) are better choices that improve the sensitivity, reversibility and sensing at room temperature and harsh environments. Hence, an efficient strategy that would dope the *C.sinensis* oil graphene with various metal oxide semiconductors or nanoparticles should be developed and further investigate for the fundamental material properties and sensing performance.

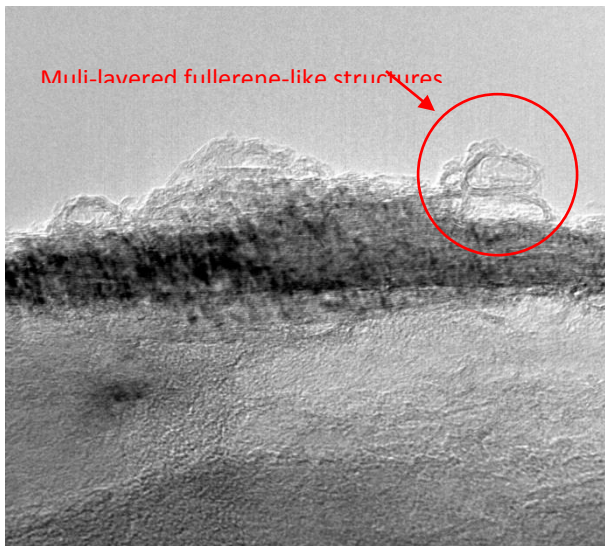
Last but not the least there are plenty of other applications such as electrode material for supercapacitors and batteries, anticorrosion coating and antibacterial coatings to which vertical graphene nanostructures are potential candidates. Hence expanding the investigation into these

applications will further enhance the scope of essential oil derived graphene to energy, environmental and biological research sectors.

APPENDIX A

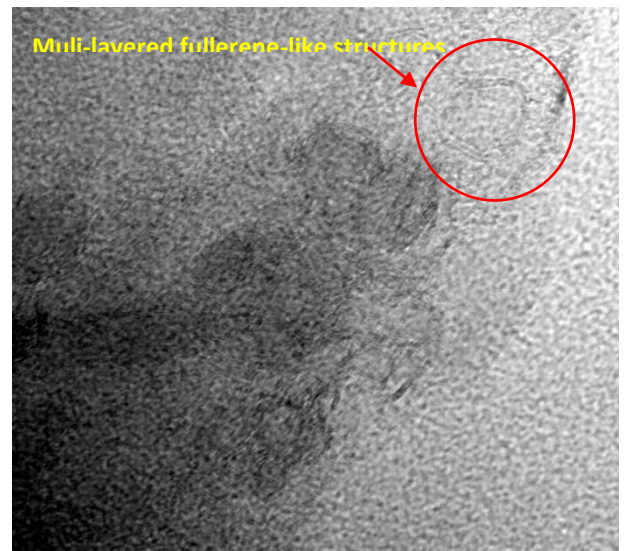
Figure S1. TEM images

Additional evidence of onion-like multi-layered fullerene structures formed over copper substrates



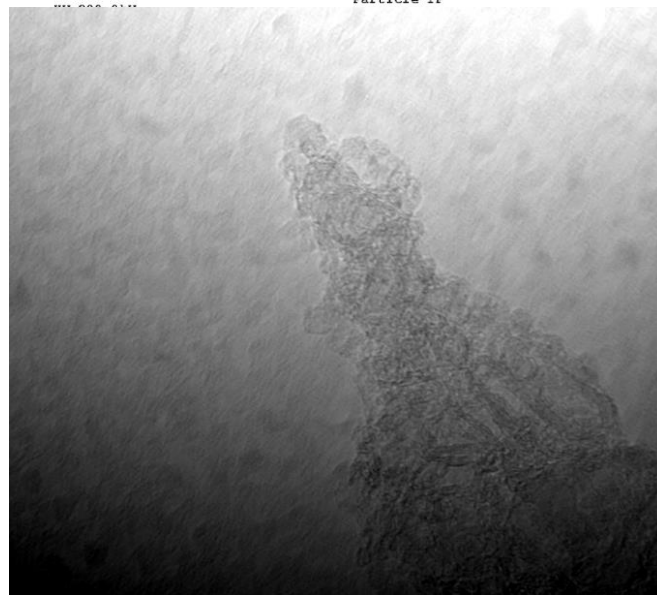
CG - A_031
Particle 4B-4
Cal: 0.040010 nm/pix
2: 37: 43 PM 12/18/2017

5 nm



CG - A_009
Particle 1F

5 nm
HV=200.0kV
Direct Mag: 500000x



CG - A_016
Particle 1I-2
Cal: 0.040010 nm/pix
2: 17: 23 PM 12/18/2017

5 nm
HV=200.0kV
Direct Mag: 500000x